DE-AC21-94MC31224--99

DOE/mc/31224--99

Naturally Fractured Tight Gas Reservoir Detection Optimization

Final Report
November 19, 1997

Work Performed Under Contract No.: DE-AC21-94MC31224

For
U.S. Department of Energy
Office of Fossil Energy
Federal Energy Technology Center
P.O. Box 880
Morgantown, West Virginia 26507-0880

By
Blackhawk Geometrics, Inc.
301 Commercial Road, Suite B
Golden, Colorado 80401

Disclaimer

DISCLAIMER

Portions of this document may be illegible in electronic image products. Images are produced from the best available original document.

1. EXECUTIVE SUMMARY

The principal objective of this project was to investigate and recommend cost-effective seismic technologies for characterizing the spatial distribution of gas-producing natural fractures. In this study, these techniques were evaluated in the Wind River Basin, Wyoming, for the naturally fractured gas-producing Lower Fort Union formation and its cap rock, the Waltman shale. The specific methods investigated were:

- 3D P-wave (three-dimensional compressional wave), two-azimuth seismic reflection over a 37-mi^2 area.
- 9C VSP (nine-component vertical seismic profile: downhole recording of three components of ground motion from surface compressional and orthogonal shear-wave sources).
- 3D-3C (P and P-to-S converted wave) four-azimuth seismic reflection, over a 2-mi^2 area centered within the larger 3D P-wave survey.

Seismic processing was aimed at revealing the *azimuthal anisotropy* recorded in the seismic reflections of the target formations. For the 3D-P survey, this was achieved by separating the seismic data in the early pre-processing stages into two subsets, one with source-receiver azimuths within 45° of the dominant regional fracture trend and the other in the orthogonal direction. All subsequent data analysis was done independently for the two azimuth-limited volumes. For the smaller 3D-3C survey, more sophisticated P- and S-wave velocity analyses were performed using four-azimuth separation.

The cost of the technology outlined herein has been an important consideration throughout this work, leading to greater emphasis on the less expensive 3D P-wave multi-azimuth techniques over the costlier shear-wave methods, and within the P-wave methods, to tests using fewer rather than more azimuths. The shear-wave data were used mainly for calibration and verification of the P-wave results. Furthermore, the 3D P-wave survey covered a much larger area than the other experiments, and hence, provided more wells for comparison to known gas production.

A variety of travel-time, amplitude, and frequency attributes formed from the 3D-P two-azimuth seismic data were analyzed. Two statistical techniques were used to rank the attributes as indicators of gas production by comparing attribute values at 19 wells in the 37-mi^2 survey area to the estimated ultimate gas recovery (EUR) at those wells. The best general correlations, found using a 300-ms (1500-ft) averaging window below the top of the Lower Fort Union formation, are:

- Fracture-parallel reflectivity and azimuthal difference in reflectivity.
- Fracture-parallel frequency and azimuthal difference in frequency.
- Fracture-perpendicular velocity and azimuthal ratio in velocity.

Although the best correlations are achieved by considering differences between azimuths, most of the information is contained in the fracture-parallel direction for reflectivity and frequency and in the fracture-perpendicular direction for velocity. The last attribute is optimal for mapping relative fracture density, as slower velocity perpendicular to the dominant fracture direction is associated with higher fracture density. The ratio of fracture-perpendicular to fracture-parallel velocity is used to remove any lateral variations in background velocity and highlight the relative fracture density alone (Fig 1.1).

We interpret the lower coherence of frequency and reflectivity in the fracture-perpendicular direction to indicate that strong scattering degrades the information in these raypaths. This inference is further supported by the judgement that structural and stratigraphic interpretation was better on the fracture-parallel reflectivity, in spite of having approximately half the fold of the fracture-perpendicular volume and shorter offsets also. Decreases in reflectivity correlated with pay are interpretable as decreases in impedance contrasts of local gas-charged sand bodies with respect to surrounding shales, whereas the increase in frequency with pay requires a more complex permeability anisotropy model. Using a neural network, the seismic azimuthal variations in reflectivity, frequency, and velocity were combined with the dominant geological attribute (structural altitude on the trapping anticline) to map the estimated potential for commercial gas pay throughout the survey area (Fig. 1.2). The improved drilling success using these methods is expected to save up to $100 million at this site.

P-wave velocity anisotropy within the 3D-3C survey was analyzed using two-azimuth interval velocities (similar to the 3D-P) and continuous interpolation from four-azimuth measurements (Fractogram). S-wave anisotropy (S1 or fast shear-wave direction) was determined from converted waves in four-azimuth data. The two-azimuth 3D-3C anisotropy differed strongly from the two-azimuth 3D-P, probably because of bias in the former introduced by the lack of prestack time migration in the presence of faulted and dipping units. Anisotropy in the Fractogram also appears to correlate with structure, suggesting further remnant biases in unmigrated data. The VSP provided local confirmation of the dominant anisotropy direction for the Waltman, but the LFU results were ambiguous, again probably due to incomplete processing (here, layer stripping).

The 3D-P two-azimuth anisotropy for the Waltman and LFU compared favorably to the mean direction and relative magnitudes in S1 and the Fractogram, in spite of some differences in layer definitions. Although significant local differences are present, the two-azimuth 3D-P anisotropy agrees well with the four-azimuth methods when the former exceeds about 8%. In regions of lower two-azimuth anisotropy, S1 correlates better with the two-azimuth directions, but the Fractogram is the better match at higher anisotropy.

For cost-effective seismic evaluation of fracture density, we recommend that:

1) 3D P-wave acquisition is all-azimuth, wide-angle (offset), preferably with point sources and circular geophone arrays;
2) Processing is in as many azimuths as allowed by cost;
3) A 9C VSP is acquired at a key well, preferably one with known azimuths of fractures azimuth and/or in-situ stress, to document the fast shear-wave polarization direction for comparison to the P-wave survey. The processing must include layer stripping.

For refined prediction of gas yield in fractured reservoirs, we recommend:

1) Exploit higher sensitivity of reflection attributes at large incidence angles (offsets) to better distinguish gas from water. This may require a new paradigm for amplitude-variation-with offset (AVO) modeling.
2) Improve mapping of seismic attributes to gas yield (e.g., as in neural network) by fully integrating seismic data with well logs in three dimensions, particularly those new logging tools like nuclear magnetic resonance that may best distinguish gas from water.

Figure 1.1 P-wave seismic anisotropy (ratio of NS/EW velocities) of the 37-mi2 study area in the Wind River Basin. Velocity anisotropy is principally sensitive to fracture density; here low velocity ratio indicates high density of EW-trending fractures.

Figure 1.2 Gas-Prospectivity Map constructed from neural network using structural altitude of reservoir and seismic anisotropy in velocity, reflectivity, and frequency. The 80% output level (yellow and red tones) predicts commercial wells in the test data with 70-90% accuracy.

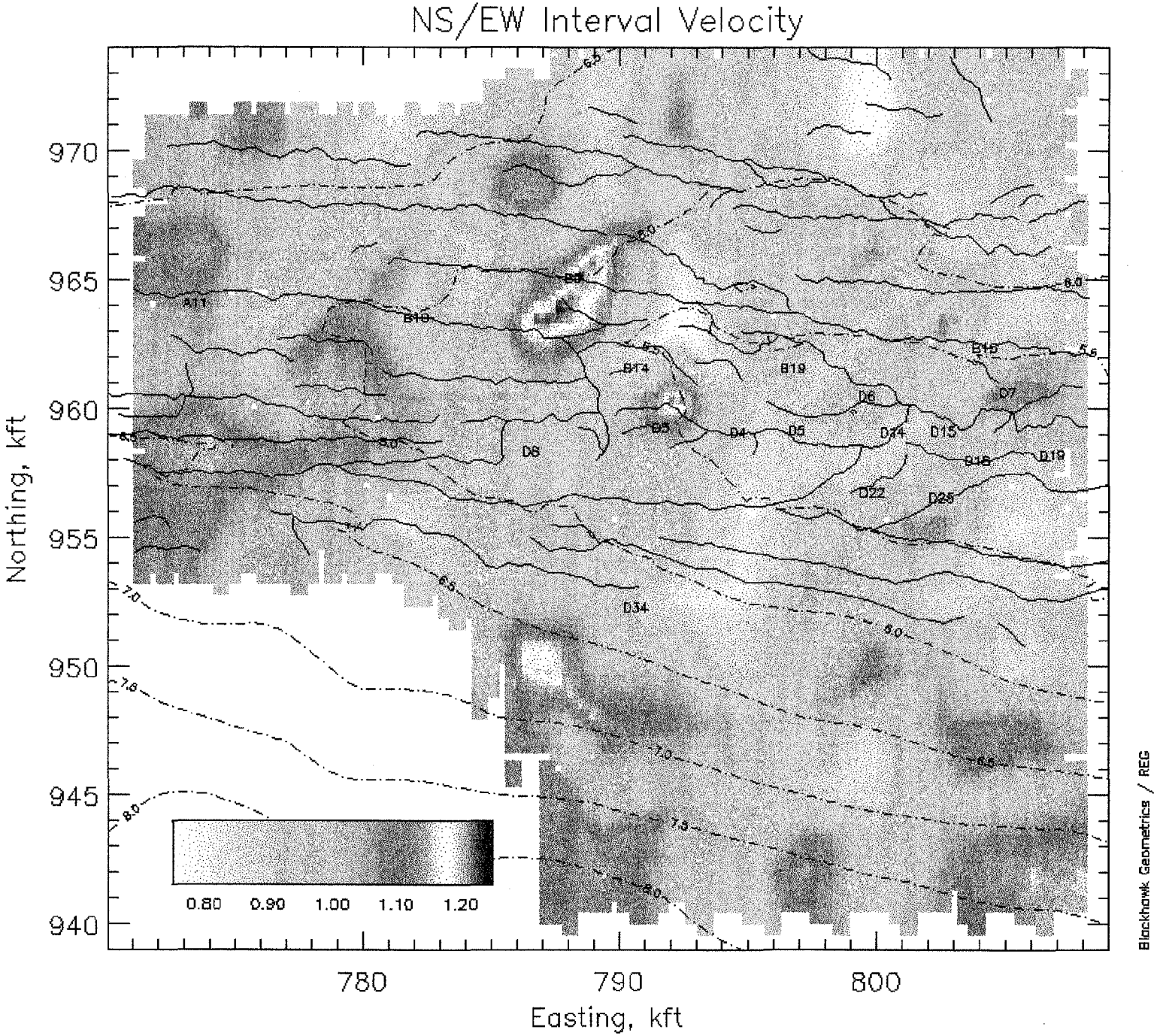

Fig. I.1. Velocity Anisotropy in Top of Reservoir Interval

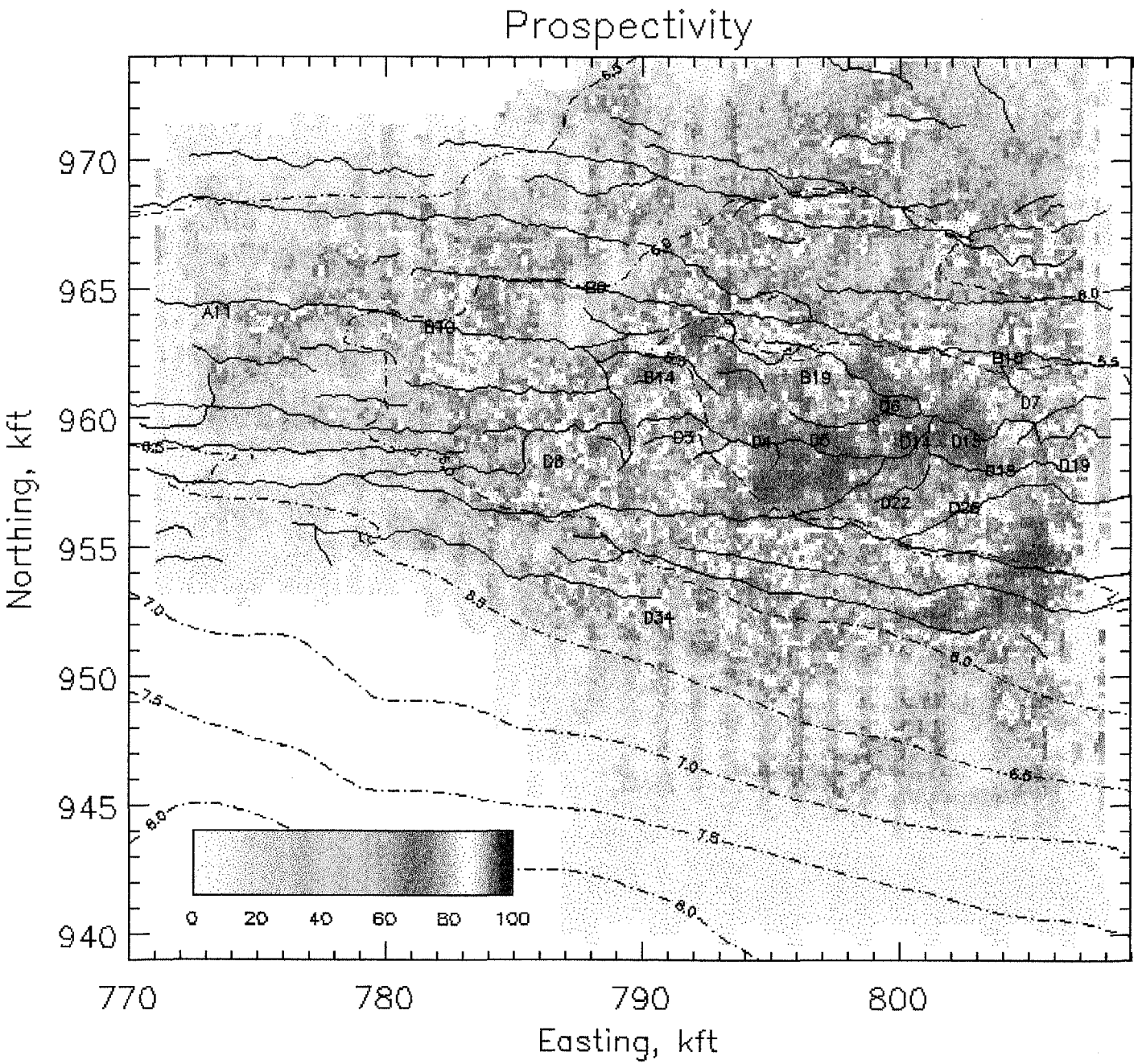

Fig. 1.2: Relative Commercial–Well Likelihood Using Seismic and Geology

TABLE OF CONTENTS

2. ACKNOWLEDGMENTS

Dr. Heloise B. Lynn (Lynn, Inc.), Principal Investigator, performed much of the data analysis and wrote a draft of this report. Dr. Richard Bates (formerly of Blackhawk Geosciences, now at St. Andrew's University, Scotland) was a Co-Investigator throughout much of the project and coordinated the 3D-3C seismic survey. Blackhawk Geometrics is grateful to both of these scientists for their efforts. Richard Van Dok (Western Geophysical) led the seismic data processing. Stewart Squires (formerly of Palantir Exploration) provided quality assurance and additional interpretation. Michele Simon (formerly of Lynn, Inc.), Wallace Beckham (Lynn, Inc.), and Dave Phillips (formerly of Blackhawk Geometrics) also contributed to this project.

We are particularly indebted to the Field Operator of the test site for providing seismic, geological, and engineering data, and especially for access to talented and knowledgeable geoscientists.

We thank our Department Of Energy (DOE) Program Managers, Royal Watts (retired) and Bill Gwilliam, for their support and guidance.

Robert E. Grimm, Ph.D.
Senior Geophysicist
Blackhawk Geometrics, Inc.

3. INTRODUCTION

3.1. Purpose of DOE-Funded Research into Seismic Detection of Fractures

This DOE-funded research into seismic detection of natural fractures is one of six projects within the DOE's Detection and Analysis of Naturally Fractured Gas Reservoirs Program, a multidisciplinary research initiative to develop technology for prediction, detection, and mapping of naturally fractured gas reservoirs. Through this program, the DOE hopes to expand current levels of industry development and production efficiency of natural gas from the extensive tight gas resource base of the United States (U.S.), which is expected to continue to grow in importance to the U.S. domestic energy supply. The demonstration of successful seismic techniques to locate subsurface zones of high fracture density and to guide drilling orientation for enhanced fracture permeability will enable better returns on investments in the development of the vast gas reserves held in tight formations beneath the Rocky Mountains.

3.2. Approach: Characterization of Seismic Anisotropy

The seismic techniques used in this project were designed to capture the azimuthal anisotropy within the seismic response. This seismic anisotropy is the result of the symmetry in the rock fabric created by aligned fractures and/or unequal horizontal stresses. These results may be compared and related to other lines of evidence to provide cross-validation. We undertook investigations along the following lines:

1. Characterization of the seismic anisotropy in three-dimensional, P-wave seismic data.
2. Characterization of the seismic anisotropy in a nine-component (P- and S-sources, three-component receivers) vertical seismic profile.
3. Characterization of the seismic anisotropy in three-dimensional, P-to-S converted wave seismic data (P-wave source, three-component receivers).
4. Description of geological and reservoir-engineering data that corroborate the anisotropy: natural fractures observed at the target level and at the surface, estimation of the maximum horizontal stress in situ, and examination of the flow characteristics of the reservoir.

Each of these factors contributes to the overall understanding of this particular reservoir, and in addition gives insight into a more general understanding of seismic responses to azimuthally anisotropic media. The type of knowledge gained through investigation of each factor, and the methods of investigation, are discussed below.

3.2.1. Seismic Anisotropy in a Vertically Fractured Reservoir

When fractures are vertical, the resulting symmetry is termed TIH, or transverse isotropy with a horizontal axis of symmetry. Vertical fractures are a common response to horizontal geological deviatoric stresses, which in turn can be ultimately related to plate-tectonic driving forces. Although fractures of other orientations may be present, vertical fractures are the most straightforward to detect seismically and, therefore, may provide clues to the overall distribution of fractures and reservoir yield.

Seismic P-wave velocity, frequency, amplitude, and attenuation are all affected by variable physical properties of rocks (e.g., Sheriff and Geldart, 1995). If *azimuthal dependence* of these characteristics is observed, then vertical, aligned fractures are a possible explanation. Specifically, a medium with aligned pores or fractures may exhibit a response consistent with variations in compliance in the fracture-perpendicular azimuth, and a response more consistent with matrix rock properties in the fracture-parallel azimuth. Most published examples of P-wave seismic field data that exhibit azimuthal anisotropy have been interpreted using these guidelines. This conventional interpretation of P-wave azimuthal anisotropy is based largely on the theoretical work of Crampin (1985), who examined azimuthal velocity dependence of both P-waves and S-waves in anisotropic media, and Thomsen (1986a,b), who derived mathematical expressions to describe weak anisotropy as it affects the velocities of seismic waves. Recent theoretical studies of seismic-wave attenuation support this interpretation (Akbar et al., 1993; Pointer et al., 1996). In these models, attenuation of P-waves propagating perpendicular to elongated pores is always greater than the attenuation for propagation parallel to the pore orientation. The azimuthal difference in attenuation is augmented for low frequencies and for gas-saturated rocks. However, an alternate model using different physical assumptions predicts greatest attenuation in the direction of highest permeability, i.e., parallel to cracks (Gelinsky and Shapiro, 1994, 1996).

3.2.1.1. S-wave Anisotropy

Shear waves transmitted through TIH material exhibit birefringence or "shear wave splitting", which has been extensively documented (see Sheriff and Geldart, 1995, for a summary). On entering a TIH medium, a shear wave will split into two component waves: a "fast" wave S1, polarized along the rock's seismically-fast direction, (usually parallel to cracks), and a "slow" wave S2, polarized in the rock's seismically slow direction (usually perpendicular to cracks). This phenomenon has been used extensively for characterization of naturally fractured reservoirs (Lynn and Thomsen, 1990; Mueller, 1991; Winterstein and Meadows, 1991; Queen et al., 1992). Crampin (1994) has also demonstrated the use of the magnitude of shear-wave birefringence as a direct indicator of fracture density.

3.2.1.2. P-wave Anisotropy

S-wave anisotropy in response to fractured media has been well documented compared to the relative paucity of published literature on P-wave azimuthal anisotropy: in general, this may be attributed to the higher sensitivity to fractures of S-waves over P-waves. Despite this recognized P-wave methods offer several advantages, the most important of which is decreased cost compared to S-wave techniques. Acquisition of a 3D P-wave multi-azimuth seismic survey costs run approximately thirty to fifty percent of the cost of a similar-sized 3D, three-component (3C, or P-S converted-wave) survey, and approximately twenty to forty percent of the cost of full nine-component recording (Lynn et al, 1996 and Kendall and Davis, 1996). In addition, there are factors unrelated to cost driving the current interest in fracture characterization from P-wave seismic. P-wave reflections respond to the rock properties *and* the material saturating the rock pores or fractures, whereas S-S reflection data contain information about the rock frame and are essentially unaffected by the material in the rock void space. Therefore, investigations using primarily P-wave seismic data include evaluation for the presence of gas as well as evaluation for fracture azimuth and relative fracture density.

In one of the first published examples of P-wave anisotropy related to fracturing (Garrotta, 1989), azimuthal differences in the far-offset reflection arrival times at Silo Field, Wyoming, were used for a qualitative evaluation of the fracture orientation. Far-offset arrivals travel more horizontal paths and, thus, will be more greatly delayed by vertical fractures. Spatial variations in the intensity of the arrival-time anisotropy were also detectable. Johnson (1995) recently recorded azimuthal differences in P-wave AVO response related to gas-filled fractures in a pre-Tertiary reservoir. Johnson found that the P-wave AVO response measured on seismic lines perpendicular to the strike of natural fractures were almost an order of magnitude greater than the AVO response measured in the fracture-parallel direction, suggesting AVO as a potential means of evaluating the direction and relative density of gas-filled natural fractures. Johnson's results are consistent with the results of recently completed DOE-sponsored project DE-AC21-92MC28135, where P-wave AVO gradient differences at the intersection of fracture-parallel and fracture-perpendicular 2D lines, in the Bluebell-Altamont field, Uinta Basin, Utah, were documented (Lynn et al, 1995).

Diverse field case studies show that azimuthal anisotropy resulting from the additional ordered compliance in rock layers with aligned vertical gas-filled fractures, is measurable in both S-wave and P-wave seismic data. The relation between S-wave azimuthal (velocity) anisotropy and relative fracture density is documented; therefore the relation between P-wave azimuthal anisotropy and S-wave azimuthal anisotropy is a crucial piece of information that provides a link between the P-wave anisotropy and the fracture density. This information link is central to the Wind River project: P-wave multi-azimuth seismic data were calibrated to S-wave seismic data to derive a relationship between the P-wave azimuthal anisotropy and the relative fracture density.

3.2.1.3. Modeling the Seismic Response

Modeling of reflection amplitude variations with offset and azimuth (AVOA) are used to interpret the seismic data recorded in the 3D P-wave field experiment. As documented in Appendix C of this report, paraxial ray-tracing was used to quantify the effects of acquisition bias (different offset ranges in different azimuths), large-scale structure, background azimuthal anisotropy in the target interval and layer anisotropy in the cap shale, on the AVO response (Grimm and Lynn, 1997). The paraxial ray-tracing method used the target reflector structure, the geometry of the 3D P-wave seismic survey, and representative P and S velocity profiles to calculate full synthetic seismograms for the top LFU surface.

AVO modeling of shale/brine sand and shale/gas sand reflections for typical shales and sands of the Lower Fort Union sequence was also used to aid in the interpretation. Modeling of the response from the top and base of these sequences was utilized to develop criteria to distinguish brine from gas sand from attributes averaged over large time intervals of the LFU.

3.2.2. Supporting Geological and Engineering Data

Geological evidence of fractures is important for "ground truth" support of the fracture characteristics interpreted from the seismic data. The results of several geologic studies undertaken by us and the field operator provide documentation of the natural fractures which are critical for gas production in the field.

- Fracture orientation in outcrop and downhole.
- The maximum horizontal stress σ_{HMAX} or σ_1 is considered to be a controlling factor on the strike of open vertical fractures and, hence, the permeability anisotropy. There is also evidence to indicate a relationship between the maximum horizontal stress direction and the azimuth of the fast (S1) shear wave component (Queen and Rizer, 1990; Queen et al., 1992).
- Flow anisotropy or permeability anisotropy has been documented in many fields that depend on fracture permeability for production (Heffer and Lean, 1993; Heffer and Koutsabeloulis, 1995).

4. GEOLOGICAL AND RESERVOIR-ENGINEERING BACKGROUND

4.1. Introduction

The naturally fractured gas field under study is located in the northeastern corner of the Wind River Basin about 100 miles west of Casper (Fig. 4.1). The field lies in a large, Laramide-age, east-west trending anticline, approximately 20x10 miles in size. The natural-gas accumulation covers portions of several townships and is encompassed by two Federal Drilling Units. The eastern Federal Drilling Unit, which covers the crest of the producing structure, is the focus of this study, and the operator of this Federal Drilling Unit is the Field Operator in the project. The Federal Government is the mineral owner of 83% of the Unit and receives a 12.5% royalty on those acres in production.

The first exploration drilling in the area took place in the late 1940's. However, major development of natural gas reserves did not begin until the mid-1960's and large portions of the various producing formations remain undeveloped. Production is established throughout much of the Phanerozoic section from the Mississippian Madison to the Tertiary Lower Fort Union (LFU). The latter is the target formation of this study. Approximately 132 BCF of gas have been produced to date from LFU reservoirs with an estimated ultimate recovery up to 2800 BCF.

Following a more detailed review of the geology and hydrocarbon production, we present several lines of evidence for the characteristics of naturally occurring fractures in the study area. These data are necessary to determine parameters for the multi-azimuth seismic processing and may also be used for posterior confirmation of the seismic results.

Figure 4.1 Schematic map of the Wind River Basin showing location of DOE Project.

4.2. Stratigraphy

The stratigraphy of the LFU has been described in detail by Schmitt (1975) and Keefer (1965). Briefly, the LFU comprises the section from 5,500 ft to 10,000 ft (Fig. 4.2) and is composed of sands and shales deposited primarily in fluvial, lacustrine, and associated continental environments. This cyclical deposition resulted in multiple, thin beds with comparatively limited lateral extent. Episodic, tectonically controlled downcutting and variable directions of sediment sources contributed further heterogeneity. Typical sands show low porosity and low permeability due to clay-filled matrix. Such poor sorting and resulting tight reservoirs are generally expected in higher-energy, near-source continental environments compared to marine environments. Petrophysical interpretations of wireline logs within the LFU are often difficult due in part to the non-marine origin of the rocks.

Figure 4.2 Generalized stratigraphic column of study area. Lower Ft. Union formation is reservoir of interest here; Waltman shale is cap rock.

4.3. Structure

The large Laramide-age gas-producing structure has no surface expression; the local topography consists of gently rolling hills. The overall anticlinal structure has been deduced from composite 2D seismic data (Fig. 4.3), although there no seismically mapped faults in the LFU prior to 3D seismic. Growth of the anticline is interpreted to have begun as early as middle Cretaceous, as north-south shortening was accommodated by folding and reverse faulting. A large thrust fault cores the anticline (Fig. 4.4), but does not penetrate the LFU, and thus does not inhibit geophysical imaging. Isochore maps from the top LFU to the base Lewis Shale (Kennell, 1985) support early growth of the structure during Upper Cretaceous Meeteetse and Lance deposition (Dunleavy and Gilbertson, 1986). Maximum growth of the anticline took place during the Paleocene and Eocene, generating a structure approximately 20 miles long and 10 miles wide. A key geophysical feature at this field is the lower apparent velocity of the Waltman Shale overlying the target LFU sandstones, which results in a time-sag in the Lower Ft. Union reflectors over the crest of the anticline.

A balanced cross-section perpendicular to the anticline, based on a 2D seismic line with well control, shows that most of the fold is also intensely faulted (Field Operator, personal communication, 1997: this figure cannot be reproduced in detail here due to industry confidentiality, but the general features are sketched in Fig. 4.4). The main low-angle south-vergent thrust deep beneath the anticline has superimposed upon it several antithetic (north-vergent) high-angle reverse faults. Some faults with antithetic orientation have normal displacements, suggesting fault reactivation. The crest of the anticline is characterized by a dense cluster of steeply dipping faults. Fault dips appear to match senses with the anticline limbs, i.e., they diverge from the crestal region. Some faults on the south side are joined with the antithetic reverse faults, again suggesting reactivation. The crestal faults on the north limb are mostly normal and sole into a master subhorizontal detachment in the lower Lance formation. While many details of this cross-section are doubtless interpretative, its overall character suggests that the dominant fault geometry was imposed during shortening and that many faults were reactivated during unloading, partially collapsing the anticline.

Alternatively, subvertical fractures parallel to anticline strike could be due to flexural extension near the crest of the fold. The dominance of shortening structures lower in the fold might indicate a neutral plane within the fold, thus supporting a flexural origin. However, thickening of lithologic units (particularly the Waltman shale) in the balanced cross-section indicates that shortening occurred near the crest also. Subvertical fractures perpendicular to anticline strike would also likely be contemporaneous with shortening, formed by extension perpendicular to the maximum compressive stress.

Figure 4.3 Map view of reservoir anticlinal structure.

Figure 4.4 Cross-section of anticline showing basal thrust fault and shallower, steeply dipping normal faults.

4.4. Hydrocarbon Geology and Production

The primary sources for gas in the LFU are thought to be carbonaceous shales and humic coals within the section (Meissner, 1984). The Waltman shale, which overlies the LFU in the study area, appears to be a relatively immature source rock around the Wind River Basin, and has not contributed significant hydrocarbons to the field accumulation. The Waltman shale is important to the field as the cap rock for gas in the underlying LFU. Recent DOE-funded work (Johnson, R., of the USGS, Denver, at 1995 and 1997 Contractor's Review Meetings) has documented chemical differences in the gases above and below the Waltman Shale. This has been interpreted to indicate that the Waltman Shale is an effective seal. Where the Waltman shale is absent, in the adjacent Federal Drilling Unit to the west, there is no production from the LFU.

The cumulative production from the field as of 1993 was 437 BCF of gas, of which 30% (132 BCF) has been produced from the LFU section. Ten wells with significant LFU production average 13.5 MMCF of gas per day. The gas in place in the LFU within the field has been recently estimated at 2.7 TCF (Johnson et al, 1996).

More than 100 wells have penetrated the LFU within the field area in the structural crest and flanking environments. These wells show the LFU sandstones to be typically low-porosity, low-permeability, and clay-filled such that production rates are unlikely to be controlled by matrix porosity and permeability alone. Genetically, there are no differences between productive LFU sandstones deposited on-structure and unproductive sandstones of the same formation deposited off-structure. In combination with structural altitude on the anticline trap, in-situ natural fracturing is thought to be responsible in large part for gas production from the LFU. Operators in the past have not been concerned with analyzing the fracture system within the field because of multitude of productive sandstones and the ease of establishing production in parts of the anticline's crest. However, it now appropriate to understand this fracture system to optimize field development.

Deposition of some reservoir rocks was very heterogeneous, which can frustrate reservoir characterization and predictability of production. The crest of the anticline is heavily faulted and fractured. Gas production is generally improved by fracturing; however, large-offset faults can also compartmentalize or disrupt reservoir units.

Section 9.3 gives some background into how geophysics is presently used in reservoir development and management at the Wind River site, and some suggestions for further implementation.

4.5. Evidence for Naturally Occurring Fractures

Evidence of natural fractures in situ within the target LFU formation is found in borehole imaging logs and cores. The operator's long experience in drilling and completion practices in the field is replete with evidence of fracture-related occurrences, such as abrupt losses or gains in drilling mud, drilling cutting samples containing calcite or quartz crystals (suggesting growth into fracture voids), and sudden torquing of the bit or catastrophic increase in penetration rate while drilling through the LFU. In-situ stress and flow characteristics of the reservoir give additional clues to fracture direction. Direct evidence of fracturing is also found in surface fractures near the field area. Furthermore, seismic imaging itself can be used to map the overall fault population.

4.5.1. Borehole Imaging

Borehole-imaging logs in six wells (Fig. 4.5) yield direct, in situ evidence of natural fractures. These data included formation microscanner image logs and ultrasonic borehole image logs. These logs provide high-resolution images of the borehole walls, upon which the strike and dip of fractures are interpretable from their characteristic sine-wave shapes in plane projection (Fig. 4.6). In addition, cores from the LFU in several wells on the crest of the structure have been analyzed for evidence of natural fractures, and a report on the core study was made available. Most fractures are steeply dipping and strike roughly east-west.

Figure 4.5 Azimuth of fractures observed in boreholes and seismically mapped faults at top of LFU.

Figure 4.6 Formation microscanner image (FMI) log in well D5, lower part of LFU. Fractures are steeply dipping and strike NE and ENE.

4.5.2. Mapping of Fractures on Outcrop

Direct measurements of natural fractures can also be made at the surface. Lineament analysis of the LFU was performed at the nearest outcrop to the seismic field site, the Castle Gardens area (about 25 miles south of the seismic site). Generally, the LFU dips to the north here at 10°-25°.

Mapping was performed along five adjacent traverse lines and at six other, more widely separated, locations (Fig. 4.7). All five of the adjacent traverse lines were oriented N30E, which is approximately perpendicular to the local strike of the LFU (N60W). This general trend is disturbed by a plunging, north-south striking anticline between Locations 5 and 6. The traverse lines ranged in length from 550 ft to 1400 ft. A description of the geology was made and the following fracture data recorded: (1) position at which fracture intersected traverse line, (2) strike, (3) dip, (4) length, and (5) nature of termination.

Only structures in the prominently outcropping sandstones could be mapped; the fine-grained siltstones and mudstones of the LFU are eroded and visible only at the base of sandstone bodies. No significant offset was observed along fractures in the survey area. The mean of all fracture strikes from the traverses is N60W (Fig. 4.8), the same as the strike of the sandstone bodies. Most fractures dip at a high angle (80°-90°). At the six separated outcrop locations, perpendicular traverse lines were also mapped. Here the dominant fracture strikes are N55W and N35E (Fig. 4.9). The second dominant direction is likely the result of both additional sampling in the perpendicular direction and the greater number of fractures perpendicular to strike due to the plunging anticline.

The most common termination was other fractures, followed by bedding planes. Mapped fracture length varied from 1 ft-100 ft (typically 3 ft-40 ft). Terminations could not be identified in about one-third of the fractures. The cumulative length-frequency plots (Fig. 4.10) for the five traverse lines, the six outcrop locations, and all data are log-log straight lines, indicating a power-law relationship (the small-length rollover is either a sampling artifact or a measure of the smallest fractures that can form). The cumulative power-law slopes vary from -1.11 to -1.17. If there were an equal probability of total fracture length per length bin, the cumulative slope would be -1. Therefore, the total fracture length per length bin appears to be nearly constant, i.e., the total length of many short fractures approximately equals that of a few long fractures.

The spatial distribution of fractures along the five traverse lines was also analyzed utilizing Barton's (1995) one-dimensional sampling and analysis of fracture networks. The traverse lines were divided into a series of adjacent segments each 2 ft in length. The number of segments which were occupied by at least one fracture was recorded and the measurement repeated in geometrically increasing bin sizes. The relationship between occupied cells and reciprocal size also follows a power law that may be interpreted in terms of a fractal dimension. For linear sampling, a fractal dimension of 0 indicates clumping at a single point, 0.5 is a random distribution, and 1 reflects even spacing. The fractal dimension of all fractures plotted (0.553) indicates that the spacing is uncorrelated. The fractal dimension of the northwest fractures, however, indicates some clumping (0.363).

In summary, mapping of the reservoir formation in outcrop indicates that the dominant fracture azimuth N60W is still in reasonable agreement with those determined in the subsurface of the field area some 25 miles away. The total fracture length is roughly equally distributed between long and short fractures. The spatial distribution of the dominant fracture system is more-or-less random on the outcrop scale; although, the orthogonal system may tend to slight clumping.

Figure 4.7 Locations of surface fracture mapping.

Figure 4.8 Fracture strikes for all traverse lines.

Figure 4.9 Fracture strikes for all outcrop locations.

Figure 4.10 Cumulative frequency of fracture lengths.

Figure 4.11 Fractal plot of fracture spacing.

4.5.3. In-Situ Stress

Heffer and Lean (1993) showed a strong correlation between preferred directions of fluid movement and the local orientation of the modern-day major horizontal principal stress, and suggested the correlation was due to the influence of open natural fractures. Heffer and Koutsabeloulis (1995) tested this result with coupled modeling of fluid flow (waterfloods) and geomechanical deformation, supporting the conclusion of the earlier work.

In the majority of field cases published to date, there is a clear correspondence between σ_{HMAX} and the azimuth of fast shear-wave polarization S1, reinforcing to the value of shear waves for fracture and stress characterization. The limited published accounts of P-wave anisotropy in the literature have dealt with the correspondence between the principal azimuths of P-wave anisotropy and the dominant fracture orientation, which implies only a correspondence with stress only if the strain (fractures) formed under the contemporary stress field.

It has been suggested that borehole ellipticity can be used as an indicator of unequal horizontal stresses, causing one axis of the borehole to be elongated by spalling or "breakouts" (Gough and Bell, 1981). The spalling occurs in the minimum stress azimuth, which allows an estimate of the maximum horizontal compressive stress direction in the orthogonal direction (Zoback et al, 1985). However, other factors such as proximity to faulting can influence local stresses and hence the borehole ellipticity; therefore breakouts should be interpreted with caution. Borehole Ovality Logs, multi-arm caliper logs or reports of such logs documenting borehole ellipticity within the LFU section in four wells over the crest of the structure were made available during the first year of the project.

The maximum horizontal stress direction interpreted from these data (Fig. 4.12) show a dominant east-west trend (±25°). This is consistent with the azimuth of faulting as interpreted from the seismic data and the dominant fracture azimuth as interpreted from the borehole imaging logs. The east-west horizontal stress trend suggests that the maximum horizontal permeability in the field is also aligned east-west. The consistency of the present-day maximum horizontal stress azimuth and the fracture/fault azimuth implies that there has been no major rotation of the stress field since the time of formation of the faults.

Figure 4.12 Azimuth of maximum horizontal stress from borehole data, superimposed on structure and faulting on top LFU.

4.5.4. Flow Characteristics of the Reservoir

Flow or permeability anisotropy is often aligned with the principal horizontal stress axis σ_{HMAX} and the dominant open fracture orientation. However, it is difficult to acquire hard documentation of permeability anisotropy due to the time and expense of interference or tracer tests. Although there is no direct measurement of permeability anisotropy at the field site, there are recent wells that have encountered virgin or near-virgin pressures throughout the entire LFU section, suggesting compartmentalization of the reservoir and a non-isotropic flow pattern in the LFU. In addition, gains and losses of drilling mud might be used as evidence for permeability anisotropy when compared to the directions of other wells. More data is required to reach firm conclusions. Furthermore, stratigraphic detection techniques such as coherency maps may also help to determine whether pressure compartmentalization may be due in part to lateral discontinuity of sand bodies.

4.5.5. Structural Interpretation of 3D Seismic Data: Faulting at Top LFU

Seismic indications of faulting through the LFU are clearly evident in the 3D seismic data (Fig. 4.13). We estimate these faults have throws of between 50 ft to 350 ft, based on reasonable seismic interval velocities. The faults with the most vertical displacement are those bounding the structural crest on either side. The faults appear to have normal displacement, are near-vertical and trend dominantly east-west (refer to Figs. 4.5 or 4.12). The detailed distribution of fault azimuths and lengths shows the mean azimuth to be N95E and the dominant length 10-20 kft (Fig. 4.14).

The exact occurrence of faults inferred from the 3D seismic data should, however, be viewed with some skepticism (Field Operator, personal communication, 1997), due to fault-shadow effects: where a strong impedance contrast is displaced by a fault, a cascading zone of amplitude disruption is commonly visible in the seismic record below (Fagin, 1996). Therefore faults in overlying units (e.g., Waltman) could influence the apparent record of faulting in the LFU. Such anomalies will collapse in prestack depth-migrated data, but this expensive processing was not performed for this study. Nonetheless, the general distribution and trend of faults in the data is likely valid.

Figure 4.13 Seismic cross-section over crest of anticline and interpreted faults.

Figure 4.14 Distribution of seismically mapped fault lengths and azimuths. Dominant strike is N95E, lengths 10-20 kft.

4.5.6. Conclusions: Fracture Azimuths and Implications for Seismic Acquisition and Processing

The essence of multiazimuth seismic analysis is to divide the source-to-receiver raypaths into two or more groups based on the ray azimuth or direction, process these groups independently, and compare the results for differences that may be interpreted as anisotropy. The wide variety of data discussed above is consistent with a dominant fracture strike approximately east-west. From the discussion of seismic anisotropy above, we therefore expect a fast shear wave (S1) direction EW, as well as the direction of maximum P-wave velocity. Variations in other attributes (e.g., reflectivity, frequency) may also be related to the principal directions NS and EW. In a two-azimuth approach, therefore, source-receiver azimuths should be divided into those within ±45° of east and those within ±45° of north. The Fractogram, used for the 3D-3C survey, uses four azimuths, but computes these from an EW reference also.

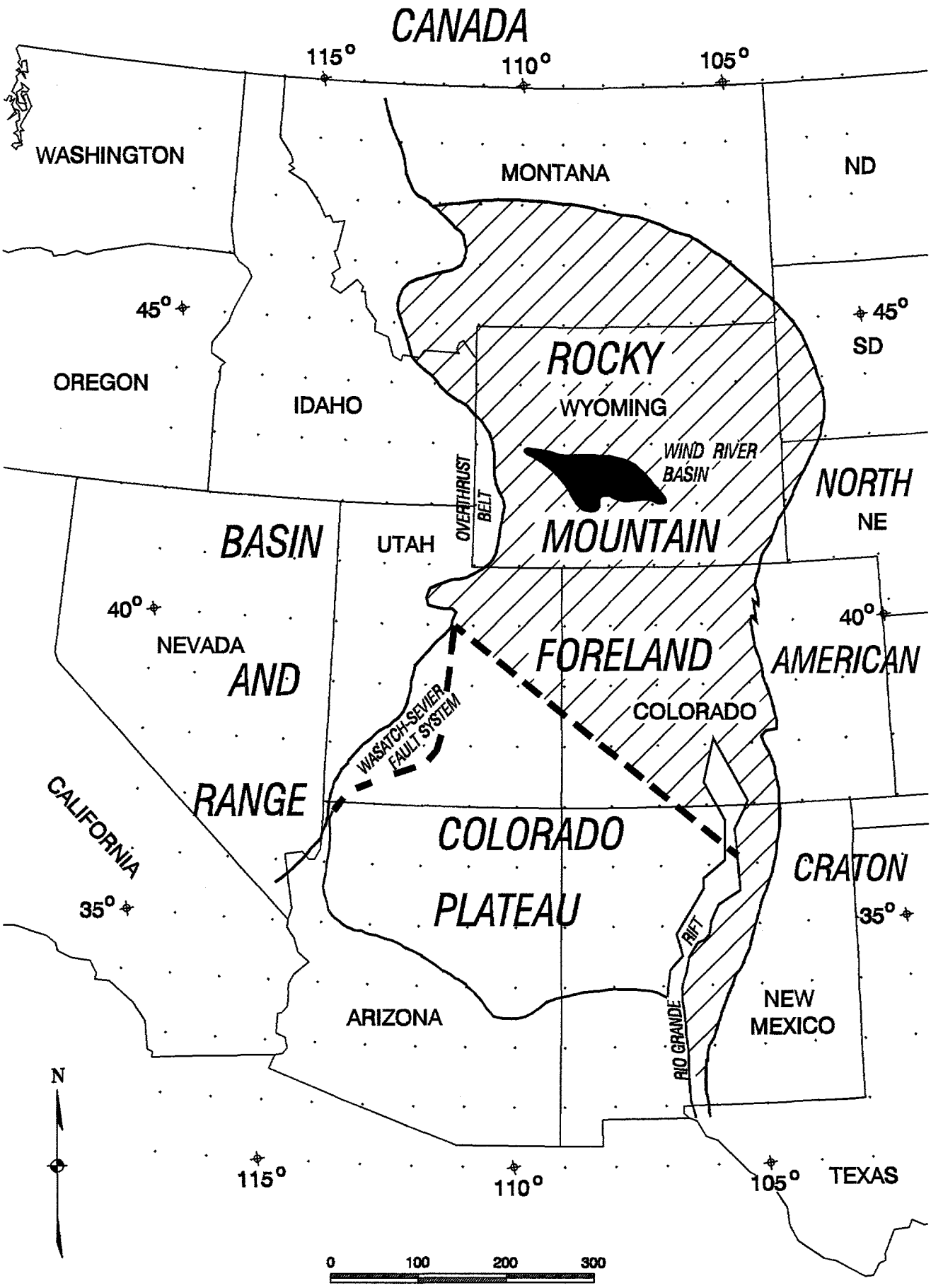
CANADA
115°
110°
105°
WASHINGTON
MONTANA
ND
45°
45°
SD
OREGON
IDAHO
ROCKY
WYOMING
WIND RIVER
BASIN
OVERTHRUST
BELT
NORTH
NE
BASIN
UTAH
MOUNTAIN
40°
40°
NEVADA
FORELAND
AMERICAN
AND
WASATCH-SEVIER
FAULT SYSTEM
COLORADO
CALIFORNIA
RANGE
COLORADO
CRATON
PLATEAU
35°
35°
RIFT
NEW
MEXICO
ARIZONA
RIO GRANDE
N
115°
110°
105°
TEXAS
0
100
200
300
Scale in Miles

Figure 4-1

Wind River Basin
Generalized Stratigraphic Chart

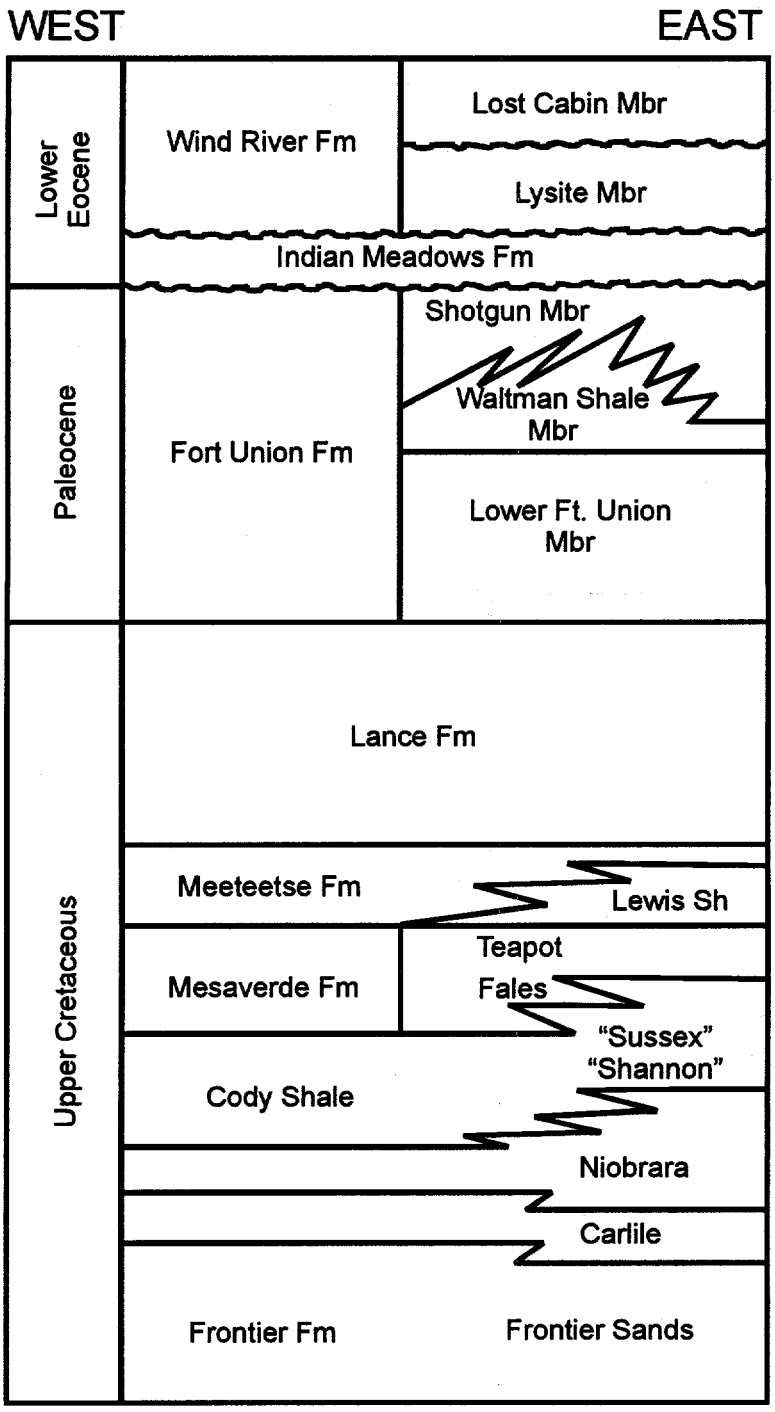

Figure 4-2

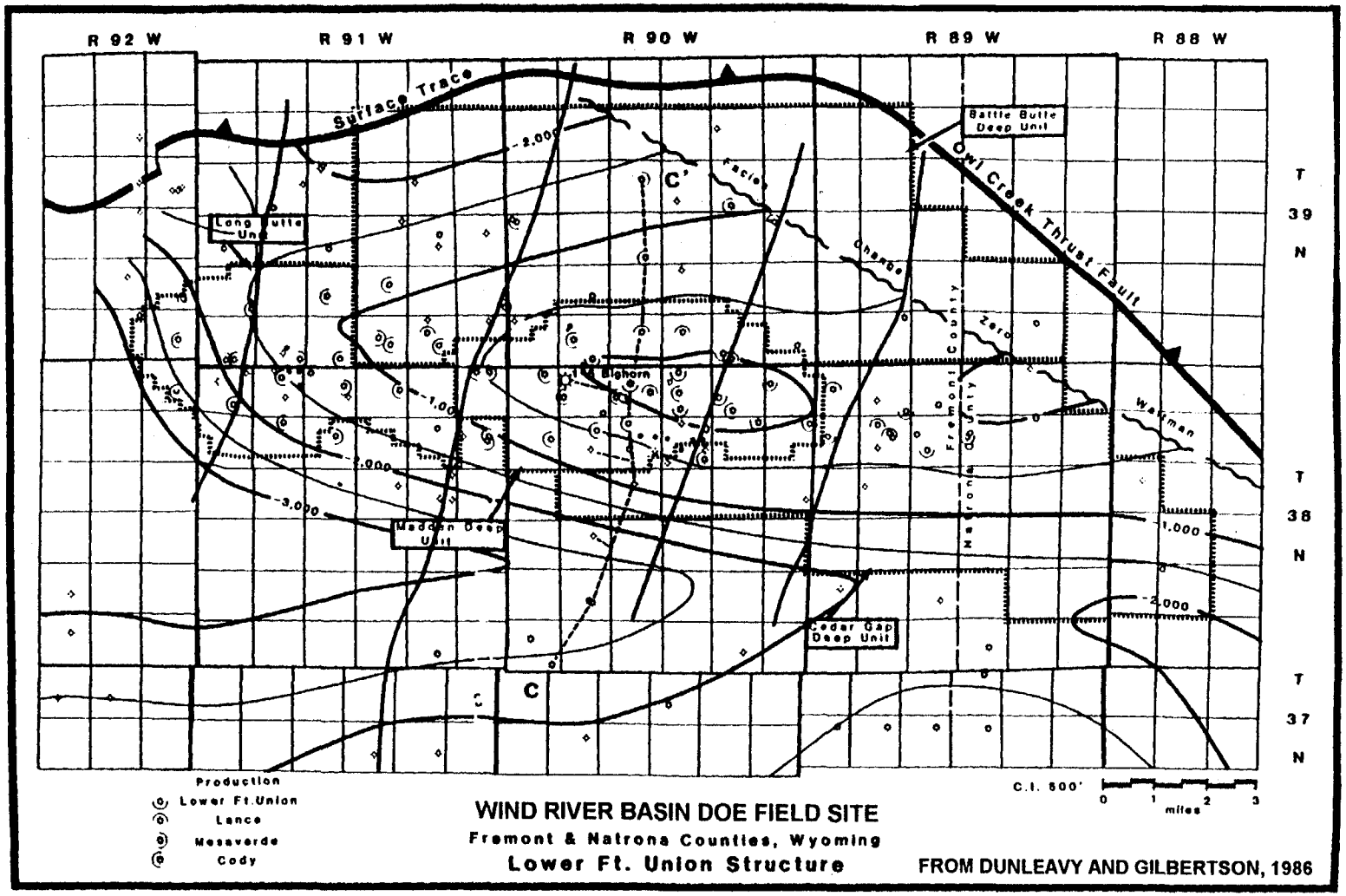

LOWER FORT UNION STRUCTURE MAP OF THE FIELD AREA. CONTOUR INTERVAL 500 FT

Figure 4-3

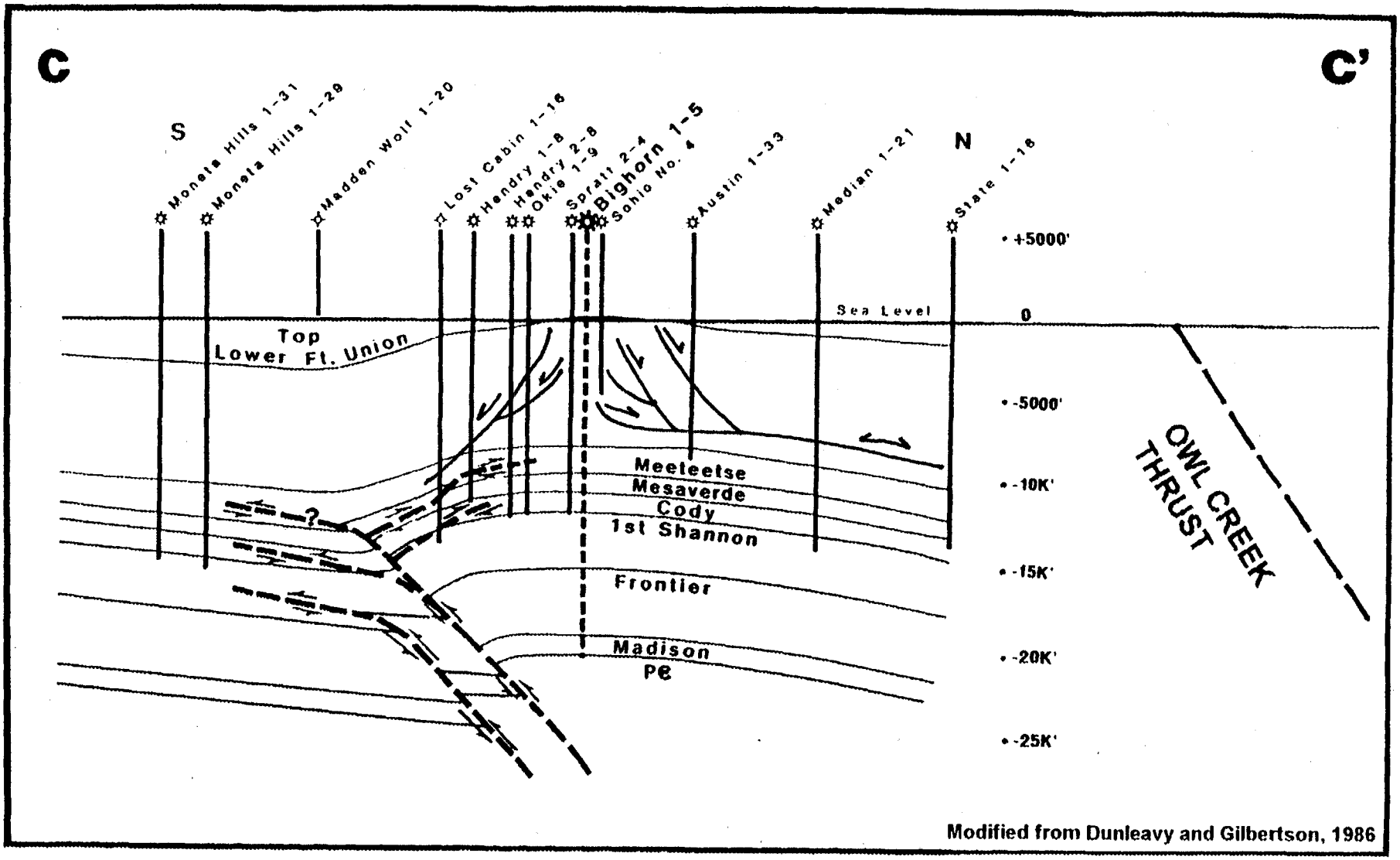

0 1M 2M 3M 4M 5MILES

Schematic structural cross section of DOE field

Figure 4-4

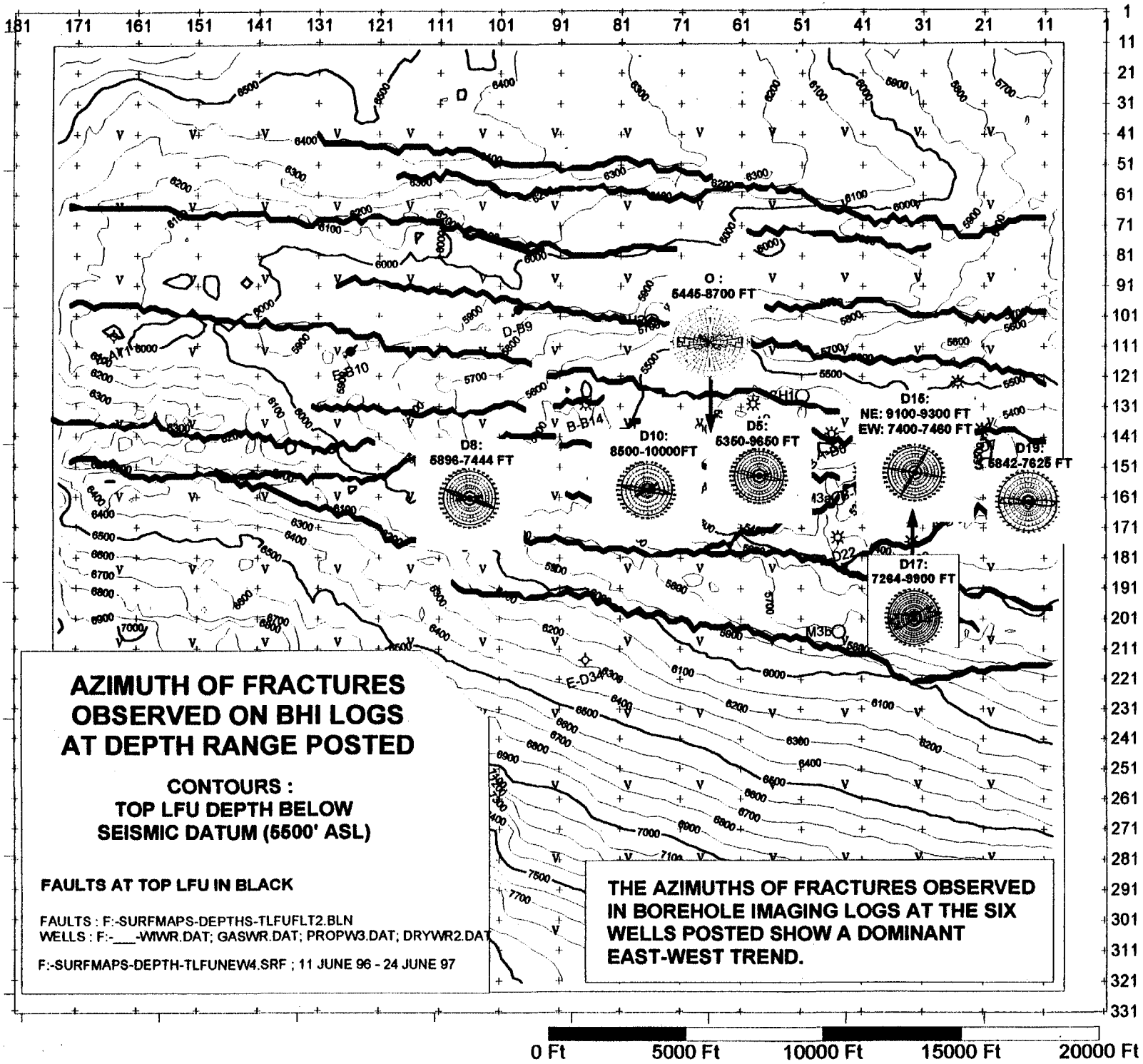
181 171 161 151 141 131 121 111 101 91 81 71 61 51 41 31 21 11
1 11 21 31 41 51 61 71 81 91 101 111 121 131 141 151 161 171 181 191 201 211 221 231 241 251 261 271 281 291 301 311 321 331
N
O :
5445-8700 FT
D15:
NE: 9100-9300 FT
EW: 7400-7460 FT
D8:
5896-7444 FT
D10:
8500-10000FT
D5:
5350-9650 FT
D19:
5842-7625 FT
D17:
7264-9900 FT
AZIMUTH OF FRACTURES
OBSERVED ON BHI LOGS
AT DEPTH RANGE POSTED
CONTOURS :
TOP LFU DEPTH BELOW
SEISMIC DATUM (5500' ASL)
FAULTS AT TOP LFU IN BLACK
FAULTS : F:-SURFMAPS-DEPTHS-TLFUFLT2.BLN
WELLS : F:-___-WIWR.DAT; GASWR.DAT; PROPW3.DAT; DRYWR2.DAT
F:-SURFMAPS-DEPTH-TLFUNEW4.SRF ; 11 JUNE 96 - 24 JUNE 97
THE AZIMUTHS OF FRACTURES OBSERVED IN BOREHOLE IMAGING LOGS AT THE SIX WELLS POSTED SHOW A DOMINANT EAST-WEST TREND.
0 Ft
5000 Ft
10000 Ft
15000 Ft
20000 Ft

Figure 4-5

WELL D-5: FMI DISPLAY SHOWS FRACTURES IN LFU FORMATION

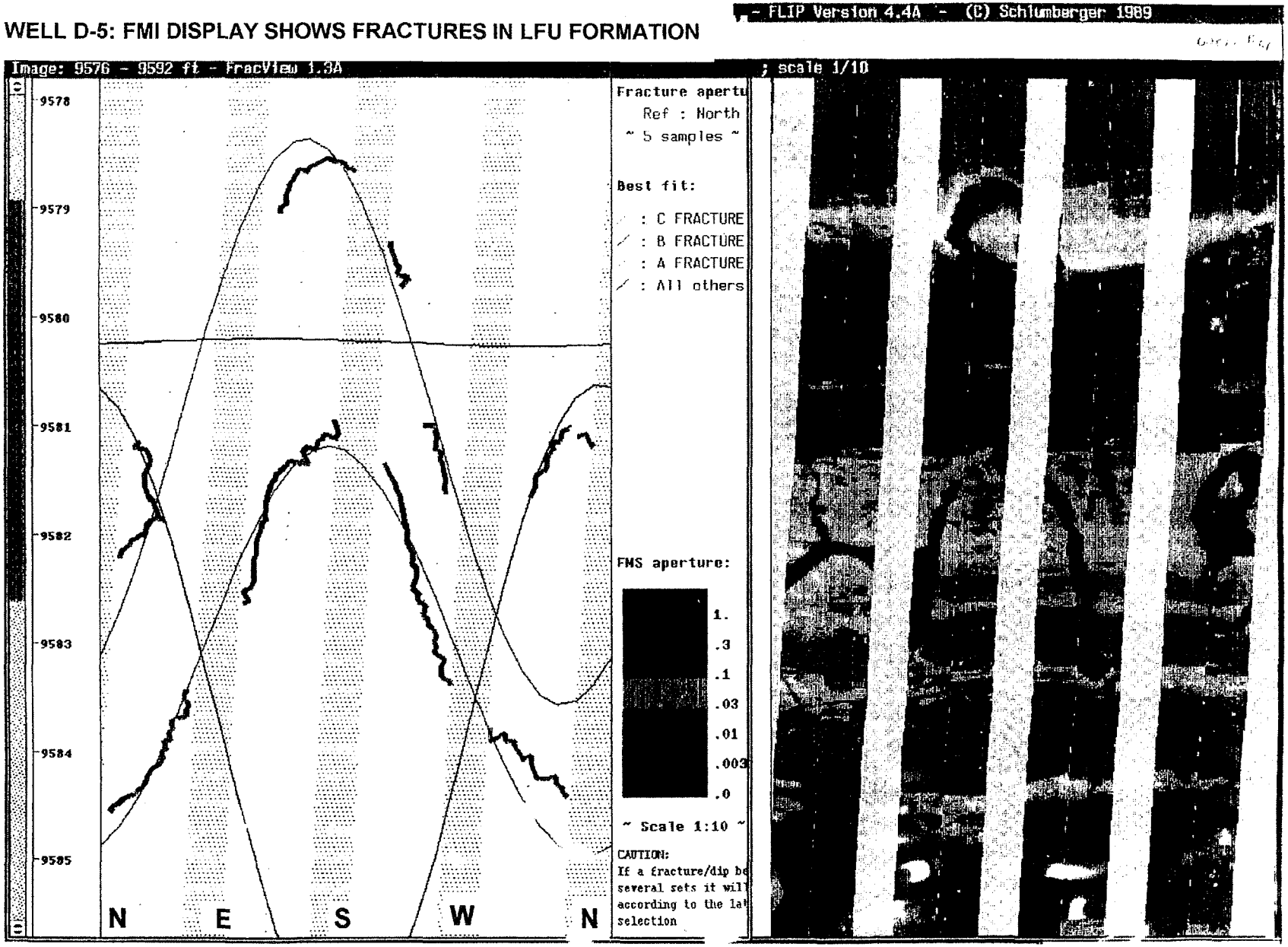

Figure 4-6 **D5 FMI IMAGE (RIGHT) AND INTERPRETATION (LEFT) SHOW TWO FRACTURES.**

THE STEEP SINUSOIDAL FRACTURE TRACES SHOW THAT THE FRACTURES ARE NEAR VERTICAL.

THE APPEARANCE OF THE FRACTURE IMAGES ON ALL FOUR PADS SUGGESTS THAT THE FRACTURES ARE NATURAL, NOT INDUCED

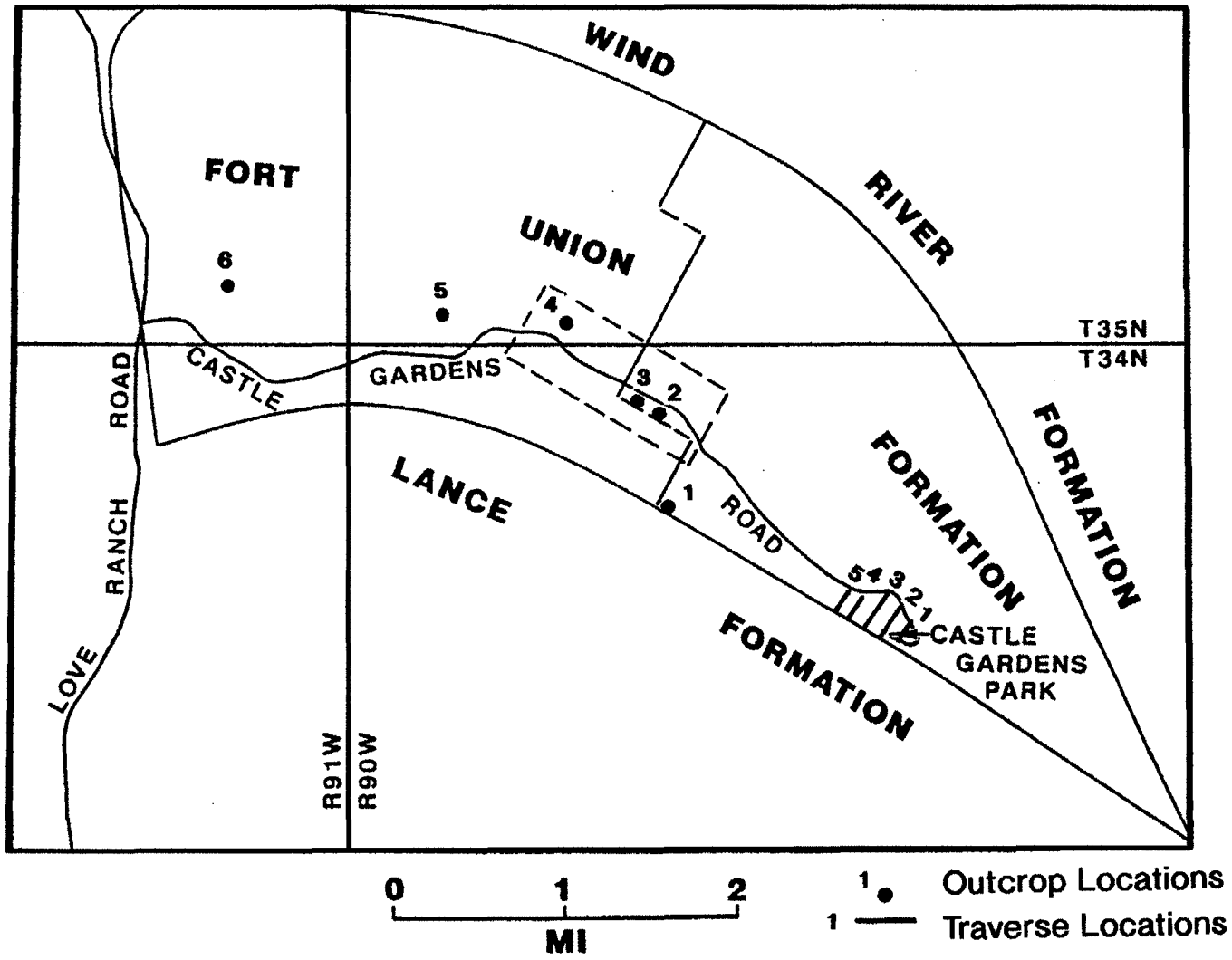

Figure 4-7: Locality Map of Castle Gardens Area

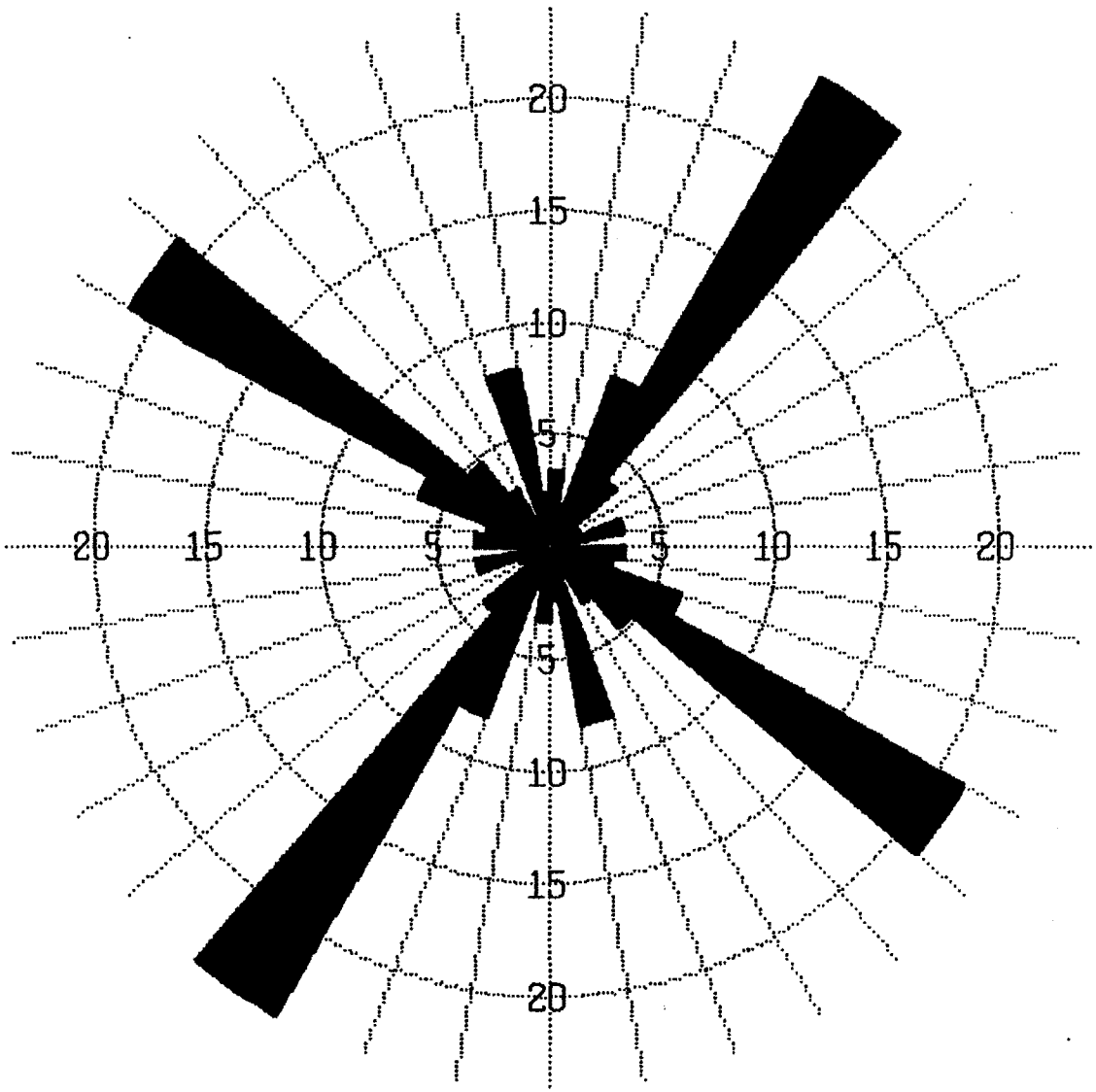

9604LOCA

Calculation Method ...	Frequency
Class Interval	10 Degrees
Filtering	Deactivated
Data Type	Bidirectional
Rotation Amount	0 Degrees
Population	212
Maximum Percentage ...	24.1 Percent
Mean Percentage	5.6 Percent
Standard Deviation ...	6.5 Percent
Vector Mean	351.62 Degrees
Confidence Interval ..	59.27 Degrees
R-mag	0.09

Figure 4-9: Rose Diagram of Fracture Strikes for all Outcrop Locations

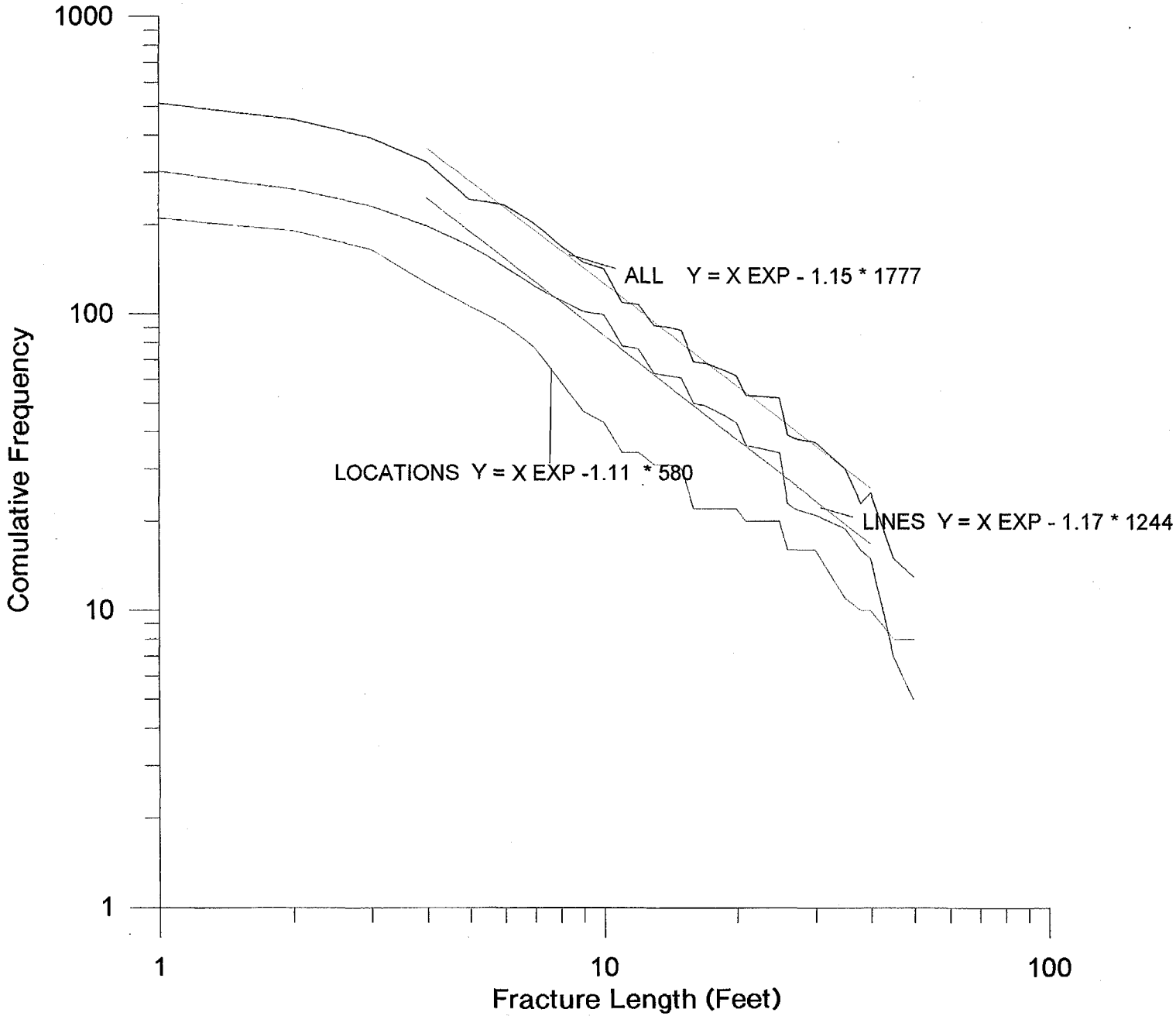

Figure 4-10: Cumulative Frequency Plot of Fracture Lengths

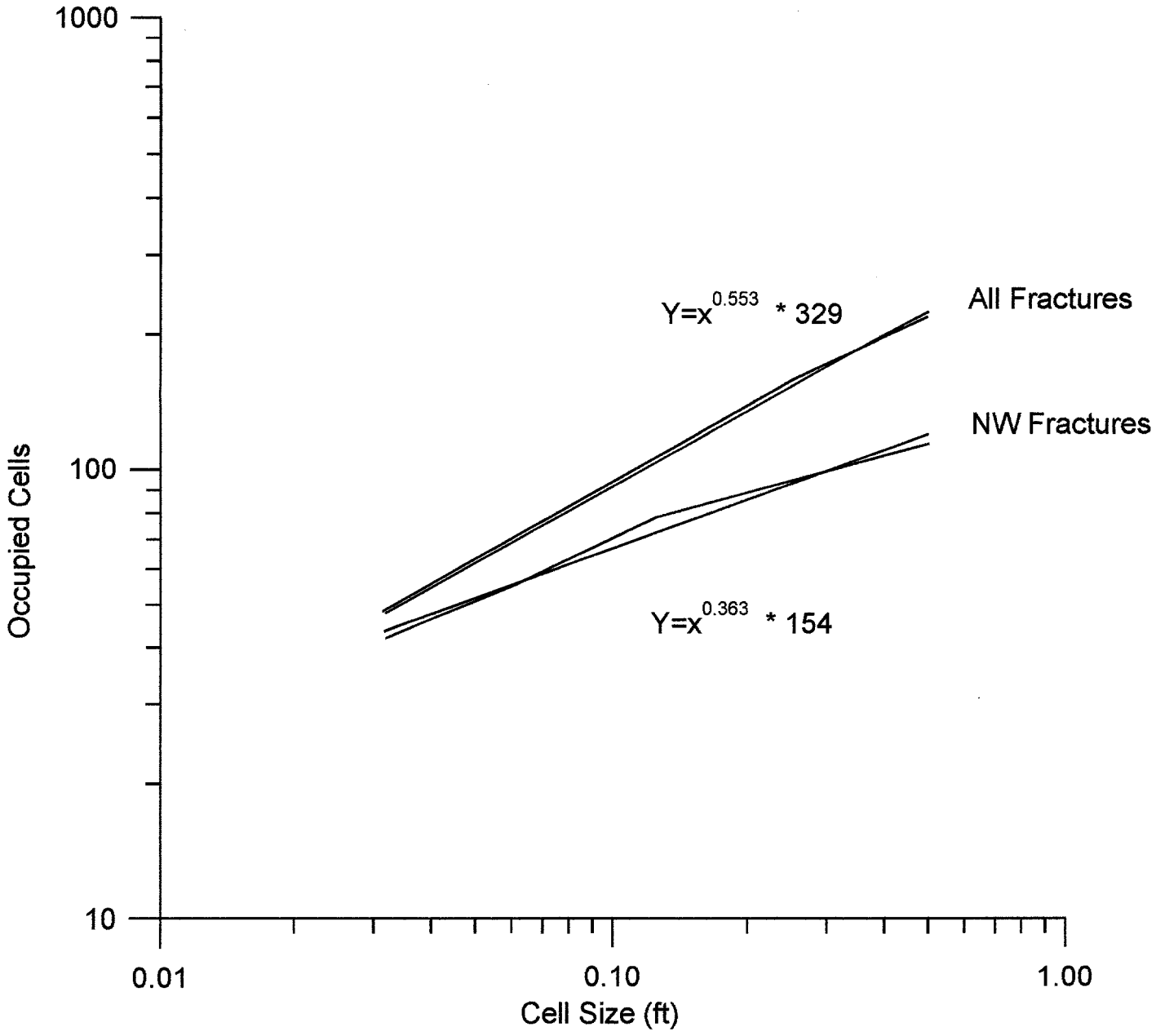

Figure 4-11: Castle Gardens Traverse Lines Total Fracture Data

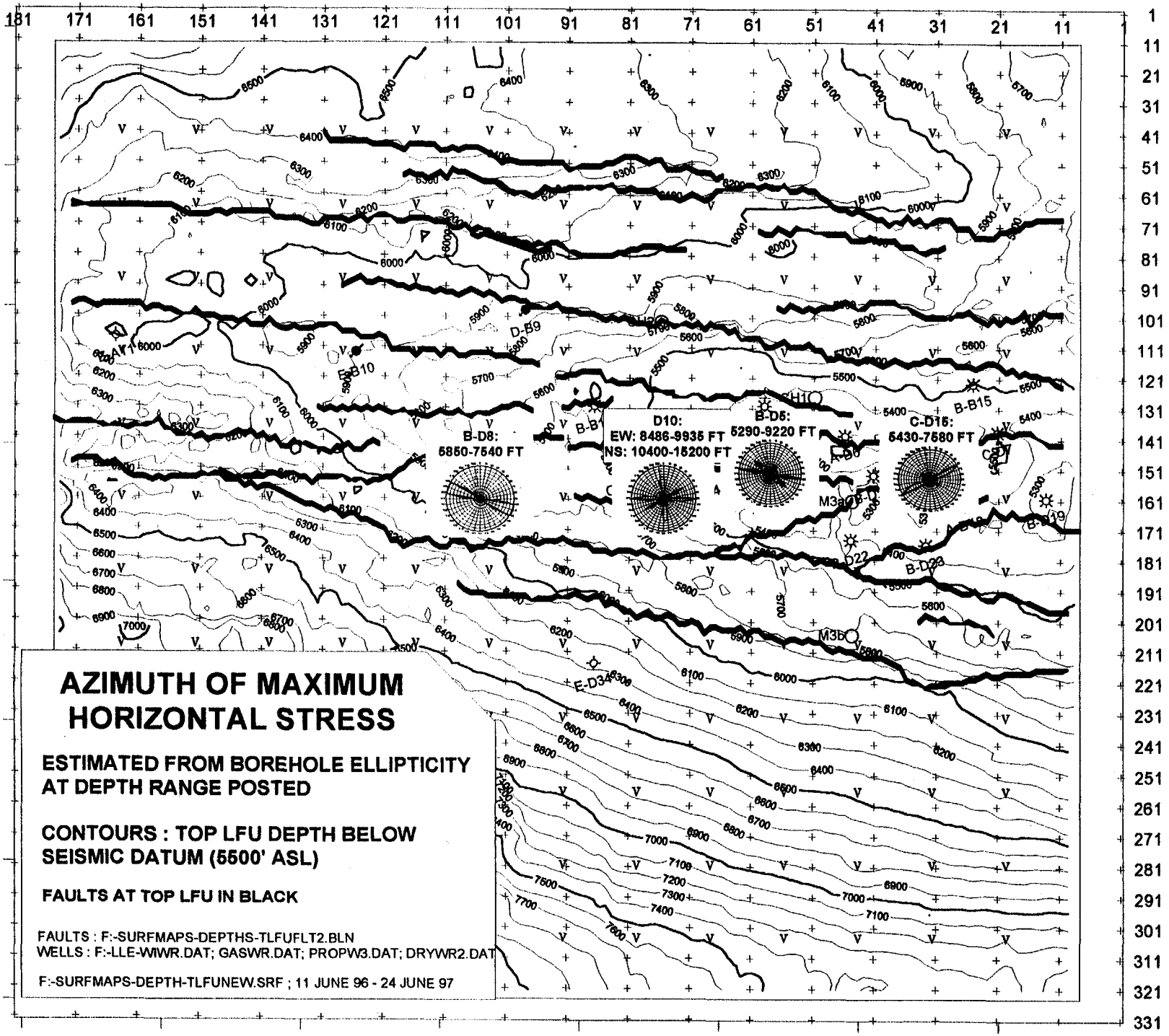
181 171 161 151 141 131 121 111 101 91 81 71 61 51 41 31 21 11
1 11 21 31 41 51 61 71 81 91 101 111 121 131 141 151 161 171 181 191 201 211 221 231 241 251 261 271 281 291 301 311 321 331
N
D10:
EW: 8486-9935 FT
NS: 10400-15200 FT
B-D8:
5850-7540 FT
B-D5:
5290-9220 FT
C-D15:
5430-7580 FT
AZIMUTH OF MAXIMUM HORIZONTAL STRESS
ESTIMATED FROM BOREHOLE ELLIPTICITY AT DEPTH RANGE POSTED
CONTOURS : TOP LFU DEPTH BELOW SEISMIC DATUM (5500' ASL)
FAULTS AT TOP LFU IN BLACK
FAULTS : F:-SURFMAPS-DEPTHS-TLFUFLT2.BLN
WELLS : F:-LLE-WIWR.DAT; GASWR.DAT; PROPW3.DAT; DRYWR2.DAT
F:-SURFMAPS-DEPTH-TLFUNEW.SRF ; 11 JUNE 96 - 24 JUNE 97
0 Ft
5000 Ft
10000 Ft
15000 Ft
20000 Ft

Figure 4-12

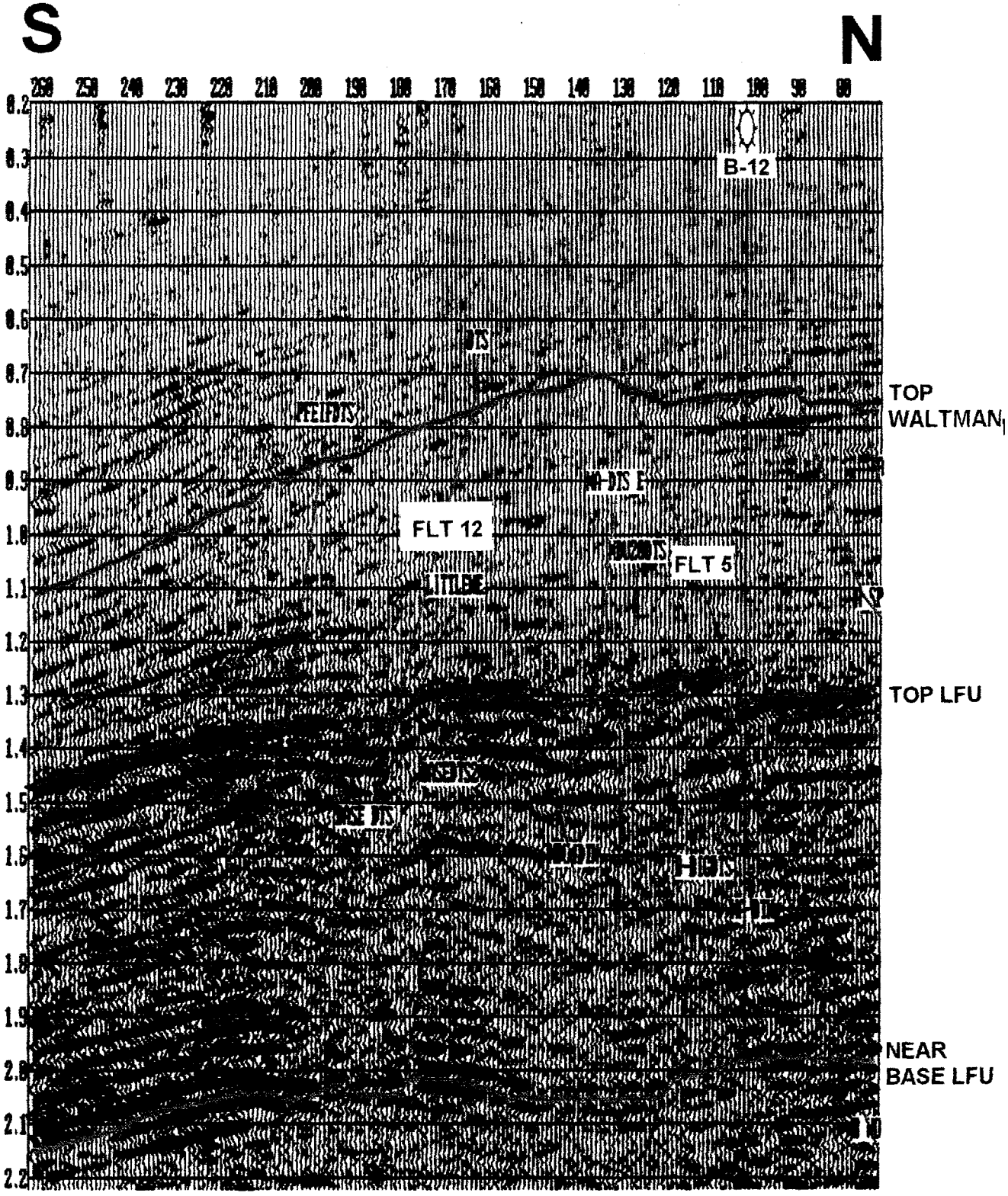

INLINE 64 Figure 4-13

NS SOURCE-RECEIVER AZIMUTHS

0 2K' 4K' 6K' 8K' 10K'

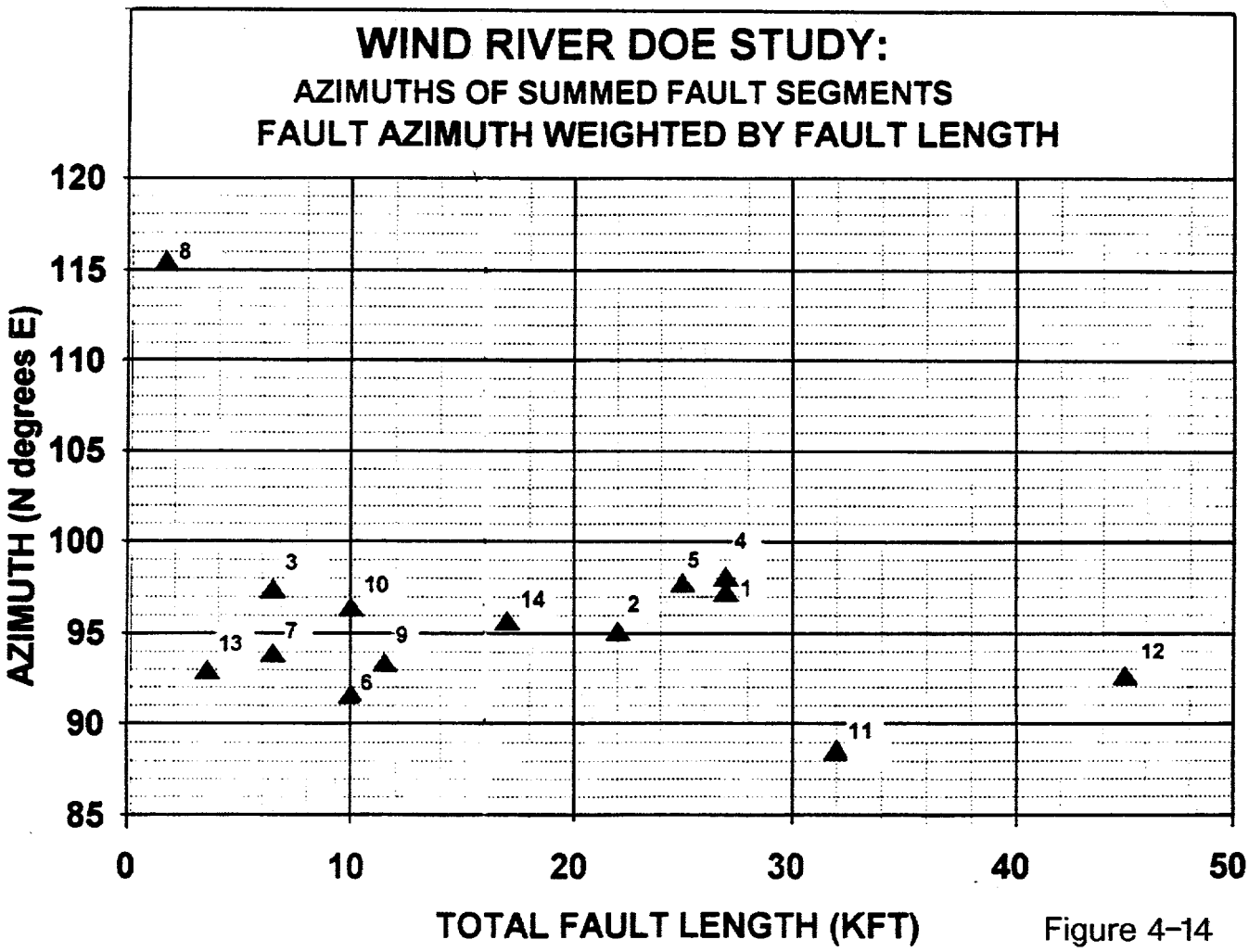
WIND RIVER DOE STUDY:
AZIMUTHS OF SUMMED FAULT SEGMENTS
FAULT AZIMUTH WEIGHTED BY FAULT LENGTH
AZIMUTH (N degrees E)
120
115
110
105
100
95
90
85
0
10
20
30
40
50
TOTAL FAULT LENGTH (KFT)
8
3
10
14
5
4
1
2
13
7
9
12
6
11

Figure 4-14

5. THREE-DIMENSIONAL P-WAVE SEISMIC SURVEY (3D-P)

5.1. Acquisition

The 3D P-wave seismic survey is the principal data set which we analyzed for seismic anisotropy in the Lower Ft. Union formation. The field operator's stated goals of the 3D survey were:

- To seismically image all faults, and in particular the buried thrust fault which limits production of the field to the south;
- To image the deep (approx. 20,000 ft) Madison formation;
- To provide high-resolution seismic imaging of the structure at the LFU, from top to base of the formation.

For the purposes of this DOE fracture-detection project, the additional project-specific goals were set for the 3D data acquisition:

- To obtain data of sufficient distribution of azimuth and offset to perform azimuthal analyses, involving comparisons by azimuth to quantify the azimuthal anisotropy, which is the tool used for detecting the presence of aligned vertical fractures;
- To obtain data of sufficient quality to perform and interpret seismic-amplitude analyses, which could be used to draw conclusions about relative fracture density.

The Field Operator generously altered some acquisition parameters to facilitate this project. These included laying of circular (rather than linear) geophone arrays, absorbing costs involved in planning and executing the wide-azimuth recording necessary for the DOE project goals. A suitable survey was designed by the Field Operator which afforded the maximum number of offsets and azimuths of seismic data, while keeping costs to a minimum.

The 3D P-wave survey was acquired by Capilano, 10-24 August 1994, with the following parameters:

Survey Area:	36.75 square miles
No. Channels:	960 (min. 680), depending on shot location
Source:	20-lb. dynamite (single charges buried 85-95 ft deep). Single shots for each record (point source - azimuthally isotropic); holes backfilled with bentonite; centered on 60-60 split-spread receivers; 1829 sources fired

Receiver Lines:	receiver stations of 12 10-Hz geophones, buried, spaced 220 ft. apart in north-south lines; receiver lines spaced ¼-mile (1320 ft). Receivers laid in 20 ft diameter circles centered on flag (azimuthally isotropic array)
Live Receiver Patch:	120 live channels/receiver; 60+60 channels/receiver line, 8 rcvr lines live
Shot Lines:	shots in brick pattern, 440 ft apart in east-west lines; shot lines spaced ½-mile (2640 ft) apart
Recording Filter:	bandpass 8.7 - 90 Hz, 12 dB/octave roll-off on low side, 72 dB/octave roll-off on high side
Sample Rate:	2 milliseconds
Record Length:	6 seconds
Fold:	30 (nominal fold in central area) to 84 (maximum fold, in eastern area)
Recording System:	I/O System 2 (24-bit recording), 960 channel recording. Nominal CMP fold: N/S az.s, offsets to 10 kft, 22 fold bulk of survey; E/W az.s, offsets to 10 kft, 10 fold in N/S strips along east and west side of survey; E/W az.s, offsets to 5k ft., 5-6 fold bulk of survey. Subsurface bin size:110 ft (north-south) x 220 ft (east-west)

Because this project involves investigation of azimuth-dependent seismic characteristics, every reasonable attempt was made to avoid azimuthal bias at the acquisition stage: single dynamite charges provided powerful, broad-spectrum, and isotropic seismic sources. Receiver stations consisted of strings of 12 geophones in circular arrays of 20-ft diameter, to assure an isotropic recording response. The longer offsets and higher fold in the north-south azimuths did introduce an azimuthal bias in the seismic amplitudes and frequencies (see Section 9.4) that precluded direct comparison of north-south and east-west data for some attributes. The data were of sufficiently high quality, however, that this problem was partially alleviated by limiting the maximum offset to 5000 ft in both north-south and east-west azimuths when comparing the stacked amplitudes and frequency content.

Figure 5.1 shows the north-south receiver lines over the field area surveyed and the recording geometry used for an example shot in the central portion of the survey and example shots near the western and eastern survey edges. Swaths or north-south strips of shots between the receiver lines were recorded in the survey's central portion in patterns of 120 receiver stations in 8 receiver lines (split-spread recording, 60 live receivers both north and south of the shot, 4 live receiver lines both east and west of the shot). Near the western and eastern edges of the survey, the symmetrical shot-receiver pattern was altered as more receivers were live toward the interior of the survey.

The shooting and recording patterns near the survey edges resulted in variations in fold and offset distribution for both north-south source-receiver azimuths (Figs. 5.2 and 5.4) and east-west source-receiver azimuths (Figs. 5.3 and 5.5). As a result, the north-south (±45 degrees) azimuths were recorded with offsets ranging from 12,000 ft to 25,000 ft and fold of 23 to 30 in the survey's central portion, while the east-west (±45 degrees) azimuths were recorded with offsets of typically 5000 ft and variable, low fold of about 8. Despite these differences, the signal-to-noise was excellent in the recorded seismic data of both source-receiver azimuth groups. However, the east-west azimuths have two north-south strips of higher fold and longer maximum offset near the western and eastern edges of the survey (Fig. 5.6). These 15 to 20-fold strips contain offsets of 9000 to 10000 ft, which are comparable with the offsets and fold of the north-south azimuth data. Within the strips, the east-west data could be compared to the north-south data, without limiting the offsets in both data sets to the 5000 ft (east-west) minimum.

Figure 5.1 Geometry for 37-mi^2 3D P-wave seismic acquisition.

Figure 5.2 Fold (number of raypaths per bin) for NS source-receiver azimuths

Figure 5.3 Fold for EW azimuths

Figure 5.4 Maximum source-receiver separation (offset) for NS azimuths

Figure 5.5 Maximum offset for EW azimuths.

Figure 5.6 Locations of all-azimuth equal-offset "supergathers."

5.2. Processing

The investigation of azimuthal anisotropy in the recorded seismic data began by performing azimuthal scans at 10° intervals at selected locations within the survey. Within the north-south strips of high east-west fold, several 1980 ft-square "supergather" areas were defined for preliminary analysis (Fig. 5.6), because the azimuth and offset distribution of source-receiver raypaths was most uniform. The azimuthal scans allowed confirmation of the geologically inferred fast and slow seismic directions and were used to guide the subsequent processing for azimuth-dependent variations in seismic data characteristics.

The azimuth-offset distribution within supergather 2 shows strong effects of anisotropy (Fig. 5.7). The LFU formation is found from approximately 1.3 seconds to 2.0 seconds. The velocity anisotropy in the LFU (actually, the cumulative effect of all overburden) is particularly evident from the variation in normal move-out of the bottom-LFU reflection (about 2.0 s). A single stacking velocity was applied to all the azimuth panels. At an azimuth of 90°, the gather of the bottom-LFU reflection is flat, indicating a proper normal move-out correction.

However, at azimuths of 0° or 180°, the reflection appears to slope downward, indicating that a slower stacking velocity is required (there is also a dip effect, but this is smaller than the anisotropy here). The azimuthal differences can also be seen in the top LFU reflection package (as the single stacking velocity was optimized for the lower reflector, there is a mean uncorrected moveout here). These differences in normal move-out corrections are primary evidence that NS azimuths have slower velocities than EW azimuths at this location. Indeed, the EW direction is generally the fastest in all the supergather velocity scans. In addition to velocity anisotropy, the supergathers also highlight azimuthal differences in frequency and amplitude.

Following this confirmation that the data could be divided into EW and NS raypaths, processing was carried out independently for these two subsets (Fig. 5.8), including dip moveout (DMO) and stacking-velocity analyses at ½-mile spacing. The data processing proceeded through pre-stack time migration using an "extended Stolt" algorithm with a minimum migration function, for both subsets of data, followed by a residual migration post-stack. Final products output for each azimuth data subset, allowing maximum offsets to 10000 ft, were:

- AGC (automatic gain control) seismic data volume with random noise attenuation
- RAP (residual amplitude processing) seismic data volume
- Stacking velocity volume
- Minimum migration function or "Stolt migration" RAP volume
- AVO (azimuthal variation with offset) Gradient volume
- AVO Zero-intercept volume
- Restricted Gradient volume (AVO Gradient multiplied by sign of AVO Intercept)
- 5000 ft offset-limited AGC seismic data volume
- 5000 ft offset-limited RAP seismic data volume

The 5000 ft offset-limited seismic volumes were generated in order to permit direct comparison between the NS and the EW seismic attributes, because the field data were recorded with longer offsets and greater fold in the NS azimuths than in the EW azimuths.

Figure 5.7 Example azimuthal scan in supergather, showing anisotropy. Individual gathers are annotated by azimuth at top. Variations in normal-moveout correction due to anisotropy are especially evident in bottom-LFU reflection at 2 s

Figure 5.8 "Conventional" vs. multiazimuth seismic data processing.

5.3. Results

5.3.1. Structure Maps

The principal use of 3D seismic data is structural and stratigraphic mapping. Interpreters of the 3D P-wave seismic datasets generally concurred that the EW azimuth data volume was better imaged for structural definition and fault placement than the NS data volume, despite the significantly lower fold of the EW-azimuth data (Field Operator, personal communications, 1995-96). We suggest that the EW-azimuth data are better imaged because there is inherently less scattering of the seismic energy in the fracture-parallel direction.

Time-structure maps for the top of the Waltman (Fig. 5.9) and the top of the LFU (Fig. 5.10) were picked from the time-migrated seismic data. Depth-structure maps for the Waltman (Fig. 5.11) and LFU (Fig. 5.12) are expressed relative to a 5000 ft ASL datum. Depth-structure maps were constructed using the "layer-cake" method, where an interval velocity for each layer is used to convert the layers from time intervals (isochrons) to layer thicknesses (isopachs), and the thicknesses are added to yield the depth to the bottom of the lowest layer. In this case there are two layers: seismic datum to top Waltman, and top Waltman to top LFU. The assumption that interval velocities change smoothly between control points (wells) was made to obtain depth maps.

Figure 5.9 Top Waltman time-structure map.

Figure 5.10 Top LFU time-structure map.

Figure 5.11 Top Waltman depth-structure map.

Figure 5.12 Top LFU depth-structure map.

5.3.2. Reflection Attributes

Using the layer boundaries in the time-structure maps, a variety of seismic attributes can be calculated for both NS and EW data volumes; these are described in detail below. The attributes that best demonstrate the seismic response to the fractured LFU reservoir and its gas yield are identified through statistical analysis in Section 5.4 and detailed interpretations follow in Section 5.5.

In reality, all attributes derived from seismic-reflection data are a combination of transmission and reflection effects. However, some local distinctions may be made on the basis of the length of an averaging window compared to the seismic period. As the dominant frequency is about 30 Hz, the dominant period is around 30 ms. Therefore, attributes computed over time-averaging windows less than about 30 ms may be defined as "pure" reflection, whereas those defined over longer times are "interval-average." We adopt windows of 8 ms and 24 ms for "reflection" attributes, and windows of 300 ms and 600 ms for "interval-average" attributes.

5.3.2.1. Reflection Strength

The Reflection Strength of the Top LFU reflector is defined as the average of the absolute values of stacked reflection amplitude, in a 24-ms window centered on the Top LFU seismic pick. This quantity was calculated in the NS (Fig. 5.13) and EW (Fig. 5.14) source-receiver azimuth data volumes with maximum offset limited to 5000 ft. The difference in the two attribute maps (Fig. 5.15) is a measure of reflectivity anisotropy.

Figure 5.13 Reflection Strength Top LFU, 24-ms window, NS±45° azimuths.

Figure 5.14 Reflection Strength Top LFU, 24-ms window, EW± 45° azimuths.

Figure 5.15 Difference between the reflection strength maps (NS minus EW).

5.3.2.2.AVO Intercept and Gradient

AVO Intercepts and Gradients were calculated at every sample in both NS and EW data volumes according to Shuey's (1985) linearization of the Zoeppritz equations for reflectivity with angle of incidence, $R(\theta) = A + B \sin^2 \theta$, where θ is the angle of incidence upon the reflector, A is the AVO Intercept and B is the AVO Gradient. The AVO parameters B and A were output as AVO Gradient and AVO Intercept volumes, for NS and EW azimuth data, as part of the seismic data processing for this project. The AVO Gradient and Intercept computations were performed on the seismic data with offsets allowed up to 10000 ft, as the long offsets were considered necessary for the AVO calculation. The seismic data were acquired with NS offsets >10000 ft and EW offsets to approximately 5000 ft over the bulk of the survey, and the AVO parameters are affected by this disparity in offset for the different azimuths.

The AVO Gradient at the Top LFU reflection was taken as the average value of the processed AVO Gradient volume over an 8 ms window centered at the time of the Top LFU event. The AVO Gradient was averaged over 8 ms rather than 24 ms at the Top LFU, because changes in the waveform of the Top LFU reflection, specifically, a higher-frequency Top LFU response over the northern portion of the survey, adversely affected the AVO Gradient calculation over the longer 24 ms interval that was used for reflection strength. Figures 5.16-5.18 map the AVO Gradient NS, EW, and difference, respectively

The AVO Intercept attribute was extracted in the same way as the AVO Gradient, using the average value in 8 ms centered at the Top LFU event, from the AVO Intercept volumes for NS and EW azimuths generated during processing. Figures 5.19-5.21 map the AVO Intercept NS, EW, and difference, respectively.

Figure 5.16 AVO Intercept Top LFU, 8 ms window, NS±45° azimuths.

Figure 5.17 AVO Intercept Top LFU, 8 ms window, EW±45° azimuths.

Figure 5.18 Difference between AVO Intercept maps (NS minus EW).

Figure 5.19 AVO Gradient Top LFU, 8 ms window, NS±45° azimuths.

Figure 5.20 AVO Gradient Top LFU, 8 ms window, EW±45° azimuths.

Figure 5.21 Difference between AVO Gradient maps (NS minus EW).

5.3.3. Interval-Average Attributes

The combined effects of seismic reflection and transmission through the LFU were characterized by four attributes: the interval velocity, the average reflection strength, the average frequency, and the Amplitude Variation with Offset (AVO Restricted Gradient and AVO Intercept). Azimuthal dependence of these attributes was expressed as ratios or differences of NS and EW attributes. The top 300 ms (approximately 1500 ft) of the LFU was taken to be seismically representative of the entire (~4000 ft thick) LFU formation, as the gas production from the top 1500 ft of the LFU is considered representative of the gas production from the entire formation. Maintaining a standard window length for all interval average calculations avoided the possibility of a window-length bias in the averages. All quantities were computed for the 600-ms window as well but are not reproduced here as the 300-ms window showed a statistically better correlation with well productivity (see below).

5.3.3.1. Interval Velocity

The Interval Velocity was calculated from time maps and stacking velocity slices using the Dix Equation, $V_{int} = [(V_2^2 t_2 - V_1^2 t_1)/(t_2 - t_1)]^{1/2}$, where subscripts 1 and 2 refer to the top and bottom of the layer, respectively, t is the two-way time, and V is the stacking velocity.

Interval velocities were also calculated at seven well locations where fracture direction from FMI log analysis and maximum horizontal stress directions from borehole elongation (BHE) directions were obtained. These are compared with the fast S-wave (S1) direction in Section 7.3 below.

Figure 5.22 Interval Velocity, Top LFU to (Top LFU + 300ms), NS±45° azimuths

Figure 5.23 Interval Velocity, Top LFU to (Top LFU + 300ms), EW±45° azimuths

Figure 5.24 Ratio (NS/EW) of Interval velocities, Top LFU to (Top LFU + 300ms)

5.3.3.2. Interval Average Reflection Strength

The Interval Average Reflection Strength was calculated as the average of absolute values of the amplitude in the 300 ms window starting at the Top LFU event.

Figure 5.25 Interval Average Reflection Strength, Top LFU to (Top LFU + 300ms), NS±45° azimuths;

Figure 5.26 Interval Average Reflection Strength, Top LFU to (Top LFU + 300ms), EW±45° azimuths;

Figure 5.27 Difference in Interval Average Reflection Strength maps (NS minus EW).

5.3.3.3. Interval-Average AVO Attributes

The AVO parameters that were calculated as 300 ms interval averages for NS and EW azimuths were the AVO Restricted Gradient and AVO Intercept.

These interval-average AVO parameters were extracted by taking the average of the appropriate AVO-processed volume over the 300 ms interval starting from the Top LFU. The AVO Restricted Gradient is defined as the AVO Gradient multiplied by the sign of the AVO Intercept. The AVO Restricted Gradient attribute was considered most useful in this study when only the positive values were averaged over the 300 ms interval. The AVO Intercept interval average uses the average of the absolute value of the AVO Intercept.

Figure 5.28 Interval Average AVO Intercept, Top LFU to (Top LFU + 300ms), NS±45°.

Figure 5.29 Interval Average AVO Intercept, Top LFU to (Top LFU + 300ms), EW±45°.

Figure 5.30 Difference of Interval Average Intercept maps, Top LFU to (Top LFU + 300ms).

Figure 5.31 Interval Average Restricted AVO Gradient, Top LFU to (Top LFU + 300ms), positive values averaged, NS±45°.

Figure 5.32 Interval Average Restricted AVO Gradient, Top LFU to (Top LFU + 300ms), positive values averaged, EW±45°.

Figure 5.33 Difference of Interval Restricted AVO Gradient maps, Top LFU to (Top LFU + 300ms).

5.3.3.4. Interval Average Frequency

The Interval Average Frequency is the average value of instantaneous frequency from every sample within the interval from Top LFU to 300 ms below Top LFU.

Figure 5.34 Interval Average Frequency, Top LFU to (Top LFU + 300ms), NS±45° azimuths.

Figure 5.35 Interval Average Frequency, Top LFU to (Top LFU + 300ms), EW±45° azimuths.

Figure 5.36 Difference in Interval Average Frequency maps, Top LFU to (Top LFU + 300ms).

5.4. Statistical Analysis Of Seismic Attributes

In this section, we present several quantitative approaches to using seismic attributes to predict gas yield. Detailed interpretation of the physical meaning of these attributes is given in Section 5.5.

5.4.1. Attribute Correlations With Well Yield

The field operator provided us with estimated ultimate recoveries (EUR) of gas at 19 wells in the 37-mi^2 survey. The wells are assigned a letter designation based on a logarithmic yield scale (Table 5.1). As a rule of thumb, A and B wells are considered commercially viable, whereas C, D, and E wells are non-commercial.

The seismic attributes computed on the 37-mi^2 survey and described above were extracted at the nineteen wells in order to search for correlations with well yield. The attributes appear throughout the text and tables of this section as short acronyms, which are listed in Table 5.2. Because it is thought that most of the yield is in the top part of the LFU (or at least that good production elsewhere in the section is correlated with good production in the upper LFU: Field Operator, personal communication, 1997), attributes were averaged over windows of length 300-ms and 600 ms below the top of the LFU (Table 5.3). In addition to 32 seismic attributes, two geological attributes were also considered (structural altitude and distance to a major fault).

Table 5.1 Well Ranking Scale

Category	EUR (BCF)
A	> 15
B	8-15
C	1-8
D	0-1
E	0

Table 5.2 Attributes And Their Acronyms

Abbrev	Attribute	Abbrev	Attribute	Abbrev	Attribute
VNS	NS interval velocity	BRPNS	NS AVO gradient, sum of positive values	RDIF5	NS-EW reflectivity, 5 kft max offset
VEW	EW interval velocity	BRPEW	EW AVO gradient, sum of positive	AANS	NS AVO intercept, absolute value
VRAT	NS/EW velocity	BRPSUM	NS+EW AVO gradient, sum of positive	AAEW	EW AVO intercept, absolute value
FNS	NS interval frequency	BRPDIF	NS-EW AVO gradient, sum of positive	AASUM	NS+EW AVO intercept, absolute value
FEW	EW interval frequency.	RNS10	NS reflectivity, 10 kft max offset10 kft max offset	AADIF	NS-EW AVO intercept, absolute value
FSUM	NS+EW interval frequency.	REW10	EW reflectivity, 10 kft max offset	BNS	NS AVO gradient
FDIF	NS-EW interval frequency	RSUM10	NS+EW reflectivity, 10 kft max offset	BEW	EW AVO gradient
BRNNS	NS AVO gradient, sum of negative values	RDIF10	NS-EW reflectivity,	BSUM	NS+EW AVO gradient
BRNEW	EW AVO gradient, sum of negative	RNS5	NS reflectivity, 5 kft max offset 5 kft max offset	BDIF	NS-EW AVO gradient
BRNSUM	NS+EW AVO gradient, sum of negative	REW5	EW reflectivity, 5 kft max offset	DEPTH	Depth to top LFU
BRNDIF	NS-EW AVO gradient, sum of negative	RSUM5	NS+EW reflectivity, 5 kft max offset	FDIST	Distance to nearest major fault segment

Table 5.3 Attributes Extracted for 19-Well Control Set

Top LFU + 300 ms Interval-Average Attributes

Well ID	VNS	VEW	FNS	FEW	BRNNS	BRNEW	BRPNS	BRPEW	RNS10	REW10	RNS5	REW5	AANS	AAEW	BNS	BEW	DEPTH	FDIST
A-D4	9800	10800	29	29	-10979	-7044	1585	421	2726	2087	4221	2583	2062	1354	12565	7480	5.405	0.158
A-D6	9800	10450	31	38	-6950	-3493	2806	476	2563	1164	1710	1309	721	490	9791	3970	5.357	0.126
A-D18	11300	12500	27	41	-6975	-4252	467	472	1183	1121	1995	1527	974	730	7604	4676	5.316	0.046
B-B5	9600	10900	29	28	-6858	-8436	1484	204	2160	971	2130	1691	768	770	8343	8641	5.354	0.082
B-B15	9650	10550	27	39	-5121	-2776	1938	2578	1779	2006	2473	1778	990	562	7031	5413	5.521	0.135
B-D23	11300	11300	37	31	-8279	-7414	529	486	1134	1562	2503	2875	1183	1245	8809	7901	5.348	0.12
B-D14	9600	11000	33	34	-8948	-5951	455	229	1659	1429	1943	1739	917	815	9282	6125	5.317	0.037
B-B14	10200	11300	32	30	-5056	-4862	1792	291	1501	1193	1789	1441	932	589	6800	5112	5.515	0.133
B-D22	9800	10700	29	31	-6359	-5982	2269	592	2305	1886	2606	2317	1203	976	8629	6762	5.378	0.394
B-D19	10500	11850	37	37	-6188	-11836	519	1114	885	1048	1464	1125	746	632	6707	13043	5.35	0.016
B-B19	10900	11900	36	35	-6472	-7132	874	1569	1666	1337	2120	1345	1069	670	7347	8613	5.44	1.254
C-D15	10800	11850	41	41	-6730	-3099	3095	613	2048	1176	1540	1674	731	528	9731	3798	5.348	0.652
C-D8	10800	11000	34	27	-4941	-4740	3426	1073	2572	2805	2580	2911	1382	1384	8532	5814	5.739	0.926
C-D7	11000	10800	39	30	-4895	-4209	487	1674	1055	2340	1145	2380	539	898	5278	5884	5.419	0.533
C-D3	10450	9750	35	28	-6459	-9808	1032	1702	1757	2358	2135	2511	912	1287	7571	11817	5.511	0.137
E-A11	11800	11350	32	25	-6491	-8089	3565	3309	3913	3588	4120	3727	1895	1977	10057	11320	6.264	0.63
E-D34	10500	11700	38	29	-8241	-6834	2922	703	4050	3336	4012	3928	2126	1776	11164	7537	6.269	0.965
E-B9	11700	9750	27	28	-11173	-9725	1021	588	2195	3897	4031	4624	2005	1987	12195	10314	5.866	0.139
E-B10	11100	11150	32	28	-6814	-7955	3353	1118	2703	3260	2141	3556	1336	1912	10130	9128	5.927	0.18

Top LFU + 600 ms Interval-Average Attributes

Well ID	VNS	VEW	FNS	FEW	BRNNS	BRNEW	BRPNS	BRPEW	RNS10	REW10	RNS5	REW5	AANS	AAEW	BNS	BEW	DEPTH	FDIST
A-D4	11096	11786	35	35	-7842	-7517	846	362	1198	1108	2812	2161	1291	1153	8689	7908	5.405	0.158
A-D6	11014	12061	33	40	-6367	-6403	2004	477	1977	1234	1593	1396	665	579	8372	6891	5.357	0.126
A-D18	12483	12683	36	41	-4957	-3629	790	265	1883	1745	1689	1608	501	614	5748	3952	5.316	0.046
B-B5	10846	12342	33	34	-6142	-9525	1351	548	1703	1583	1951	1656	683	724	7395	9832	5.354	0.082
B-B15	10668	11106	31	43	-4600	-3195	1369	1536	1382	1333	2171	1662	878	532	5976	4715	5.521	0.135
B-D23	13013	12339	39	33	-6092	-5628	515	229	1816	1725	1985	2318	812	890	6608	5835	5.348	0.12
B-D14	10413	12082	39	42	-6625	-6670	791	849	1350	1111	1714	1561	738	607	7427	7515	5.317	0.037
B-B14	12087	11962	35	35	-5965	-4696	1063	574	1119	1236	1755	1564	858	523	7029	5281	5.515	0.133
B-D22	10239	11371	36	36	-5219	-7016	1227	734	1359	1254	2133	1966	980	749	6448	7746	5.378	0.394
B-D19	11114	11835	40	40	-5101	-12853	389	1950	1626	1354	1386	1256	619	629	5491	14730	5.35	0.016
B-B19	12016	13333	42	37	-5246	-8139	730	1252	2202	2180	1743	1322	772	569	5977	9384	5.44	1.254
C-D15	12783	12812	39	42	-5575	-3172	1461	428	854	1175	1602	1473	713	479	7037	3617	5.348	0.652
C-D8	11442	11412	36	30	-4949	-5619	2176	618	1446	1835	2295	2337	1246	1112	7126	6285	5.739	0.926
C-D7	11617	10819	39	35	-5341	-4161	731	901	1663	963	1289	1869	501	689	6073	5063	5.419	0.533
C-D3	10455	11084	38	32	-6762	-13252	923	1331	1099	1849	1642	1942	713	1046	7685	14627	5.511	0.137
E-A11	11779	11486	34	29	-7291	-9188	1892	2518	1546	2520	3284	3277	1680	1644	9184	11665	6.264	0.63
E-D34	10745	12172	34	29	-9612	-9054	3015	505	2687	2910	4014	3731	2369	1726	12627	9469	6.269	0.965
E-B9	12260	10970	33	34	-8367	-7783	583	417	4058	3030	3017	2882	1377	1369	8951	8201	5.866	0.139
E-B10	11196	12307	36	31	-5873	-7089	2029	685	2122	2293	2011	2657	1043	1287	7903	7775	5.927	0.18

Sum, difference, and ratio attributes not shown here due to space limitations, but can be computed from attributes shown.

The simplest approach to testing for correlation between two variables is to compute the linear, or Pearson, correlation coefficient between EUR and an attribute (due to confidentiality agreements, individual EURs cannot be reproduced here). A significance level alpha, computed from this correlation coefficient and the number of observations, gives the probability of a Type I error (in which a correlation between the variables is inferred when none exists). Because the data studied here are very noisy, linear correlation coefficients are poor (Table 5.4) and hence the probabilities of incorrectly inferring true correlations are large.

In cases where the data set is so small or has correlated noise such that an underlying normal statistical distribution cannot be safely assumed, nonparametric techniques may be more useful. The Spearman rank-correlation coefficient is intuitively similar to the standard linear form, but operates on ordinal data alone: the rank of each datum in a series and not its metric value is the random variable. Furthermore, because the rank of wells by EUR categories alone is likely more reliable than ranking by individual EURs, we assign the same rank to all wells in the same category. The Spearman rank-correlation coefficient proved much better at elucidating and quantifying relationships between the seismic attributes and EUR category (Table 5.4); Type I error probabilities for key attributes are negligible, indicating high confidence that such attributes are correlated with well yield.

Table 5.4 Correlation Coefficients between EUR and Seismic Attributes

	300-ms window			600-ms window		
Property	Pearson R	Spearman R	Spearman Alpha %	Pearson R	Spearman R	Spearman Alpha %
vns	-0.26	-0.49	3.80	0.02	-0.1	67.84
vew	0.09	0.02	92.04	0.15	0.27	25.67
vrat	-0.28	-0.47	4.40	-0.12	-0.26	27
fns	-0.48	-0.35	13.49	-0.30	0.03	88.36
few	0.41	0.60	1.08	0.38	0.63	0.76
fsum	0	0.27	24.43	0.15	0.52	2.79
fdif	-0.64	-0.63	0.75	-0.51	-0.49	3.94
brnns	-0.22	-0.12	62.49	0.04	0.29	22.38
brnew	0.37	0.30	20.93	0.27	0.24	31.48
brnsum	0.15	0.07	75.43	0.23	0.31	18.61
brndif	-0.53	-0.36	12.23	-0.27	-0.06	81.44
brpns	-0.07	-0.43	6.95	-0.05	-0.32	16.86
brpew	-0.28	-0.54	2.21	-0.34	-0.27	25.83
brpsum	-0.20	-0.45	5.43	-0.27	-0.36	12.62
brpdif	-0.41	-0.43	7.07	-0.28	-0.34	15.34
rns10	-0.03	-0.35	13.21	-0.10	-0.18	45.5
rew10	-0.34	-0.74	0.16	-0.33	-0.58	1.45
rsum10	-0.21	-0.64	0.68	-0.22	-0.42	7.45
rdif10	0.38	0.39	9.49	0.28	0.44	6.04
rns5	0.04	-0.27	24.69	-0.09	-0.36	12.23
rew5	-0.33	-0.70	0.30	-0.28	-0.62	0.81
rsum5	-0.16	-0.54	2.19	-0.19	-0.5	3.5
rdif5	0.53	0.70	0.29	0.37	0.48	4.12
aans	0	-0.32	16.98	-0.20	-0.49	3.89
aaew	-0.29	-0.63	0.71	-0.23	-0.55	1.95
aasum	-0.16	-0.50	3.50	-0.22	-0.53	2.45
aadif	0.49	0.56	1.77	-0.01	0.09	68.7
bns	0.18	-0.26	27.69	-0.05	-0.45	5.48
bew	-0.43	-0.41	7.90	-0.31	-0.27	25.99
bsum	-0.24	-0.35	13.72	-0.27	-0.36	12.71
bdif	0.48	0.20	38.73	0.27	0.08	72.19
depth	-0.35	-0.69	0.34	"	"	"
fdist	-0.33	-0.56	1.85	"	"	"

For the 300-ms window, the most highly (Spearman) ranked seismic attributes (alpha < 5%) are, in descending order, REW10, RDIF5, REW5, DEPTH, RSUM10, AAEW, FDIF, FEW, AADIF, FDIST, RSUM5, BRPEW, VNS, VRAT, and AASUM. For the 600-ms window, the order of top attributes is DEPTH, FEW, REW5, REW10, FDIST, AAEW, AASUM, FSUM, RSUM5, AANS, FDIF, RDIF5.

An alternative method of evaluating attribute correlation with pay is based on choosing a single cutoff or threshold of the attribute. The data were divided into commercial and noncommercial categories. For each attribute, a single threshold value was sought so that the product of the correct fraction of commercial and the correct fraction of noncommercial wells was selected. For example, it was shown above that reflection strength is negatively correlated with pay; therefore commercial wells should have low reflectivity and noncommercial wells high reflectivity. A threshold value of 2360 REW5 yields 9 of 11 commercial wells with reflection strength lower than this threshold and 7 of 8 noncommercial wells higher than the threshold (cf Fig. 5.37; threshold in figure was picked by eye and differs slightly).

Moving the threshold up would increase the number of commercial wells that satisfy the criterion but would decrease the number of noncommercial wells that fell above the threshold. Conversely, moving the threshold down would increase the correct fraction of noncommercial wells at the expense of the commercial wells. Thresholds for frequency and velocity are shown in Figures 5.38 and 5.39, respectively.

Figure 5.37 Thresholds for reflectivity attributes.

Figure 5.38 Thresholds for frequency attributes.

Figure 5.39 Thresholds for velocity attributes.

Using all 19 available wells, threshold products for the leading attributes are of order 0.6-0.9, with corresponding correct prediction of commercial vs. noncommercial categories of 80-95%. However, forming the threshold using all the data does not provide any predictive capability for how well the technique will perform for new data. Therefore we computed 10,000 thresholding trials in which 15 wells (~80% of the data) were used to set the threshold (training data) and the remaining 4 wells were used as "new" test data (there are actually 3876 combinations of 19 items taken 15 at a time; as the algorithms were initially set up to select a random sample, it was simpler to oversample the data). Thresholding correctly predicted the commercial vs. noncommercial categorization of the test data for 70-75% of the cases for most of the leading attributes (Table 5.5).

Table 5.5 Threshold-Prediction Ability of Attributes for 300-ms Window

Attribute	Threshold	Std Error	Training Success	Std Error	Test Success	Std Error	Correlation Sign
vns	1.05E+04	1.27E+02	0.79	0.05	0.71	0.21	-1
vew	1.12E+04	4.89E+02	0.62	0.08	0.38	0.23	1
vrat	9.83E-01	7.08E-02	0.84	0.04	0.78	0.20	-1
fns	3.36E+01	1.99E+00	0.72	0.06	0.58	0.22	-1
few	3.06E+01	8.74E-01	0.81	0.05	0.71	0.20	1
fsum	6.59E+01	2.50E+00	0.64	0.07	0.36	0.22	1
fdif	4.54E+00	1.24E+00	0.85	0.05	0.80	0.18	-1
brnns	-6.53E+03	5.10E+02	0.62	0.07	0.35	0.18	1
brnew	-6.69E+03	1.08E+03	0.68	0.06	0.46	0.23	-1
brnsum	-1.26E+04	1.79E+03	0.64	0.07	0.39	0.20	1
brndif	-7.57E+02	9.49E+02	0.65	0.06	0.40	0.22	1
brpns	2.95E+03	1.19E+02	0.84	0.05	0.79	0.20	-1
brpew	6.09E+02	5.58E+01	0.80	0.05	0.72	0.20	-1
brpsum	2.91E+03	6.83E+02	0.78	0.06	0.66	0.21	-1
brpdif	9.49E+03	8.96E+02	0.75	0.06	0.63	0.21	-1
rns10	2.06E+03	2.86E+02	0.72	0.06	0.58	0.21	-1
rew10	2.35E+03	9.95E+01	0.95	0.03	0.92	0.15	-1
rsum10	4.26E+03	1.01E+03	0.84	0.05	0.68	0.20	-1
rdif10	-2.46E+02	1.24E+02	0.79	0.06	0.69	0.21	1
rns5	2.54E+03	6.01E+02	0.70	0.06	0.53	0.22	-1
rew5	2.52E+03	2.72E+02	0.86	0.05	0.76	0.20	-1
rsum5	5.19E+03	5.45E+02	0.79	0.05	0.68	0.21	-1
rdif5	2.11E+02	4.23E+01	0.90	0.04	0.83	0.18	1
aans	1.35E+03	1.11E+02	0.79	0.05	0.73	0.22	-1
aaew	1.21E+03	2.08E+02	0.85	0.05	0.73	0.19	-1
aasum	2.35E+03	2.91E+02	0.80	0.05	0.74	0.20	-1
aadif	1.16E+02	8.27E+01	0.80	0.06	0.67	0.21	1
bns	9.67E+03	3.70E+02	0.74	0.07	0.64	0.24	-1
bew	8.81E+03	1.18E+03	0.73	0.06	0.59	0.24	-1
bsum	1.87E+04	4.10E+02	0.74	0.05	0.67	0.23	-1
bdif	1.56E+03	1.07E+03	0.62	0.06	0.32	0.18	-1
depth	5.57E+00	1.92E-01	0.84	0.05	0.71	0.20	-1
fdist	2.32E-01	1.51E-01	0.81	0.05	0.70	0.21	-1

The Spearman rank-correlation significance level and the threshold-prediction probability are graphically compared in Figure 5.40. The broad inverse correlation is evident: better (lower) significance levels are associated with higher threshold-prediction probabilities. However, the curve is distinctly Z-shaped and hence can be divided into three regions: An upper-left region of attributes poorly correlated with pay, a transition, and a lower-right region of attributes best correlated with pay. Clearly, this last zone is of greatest interest.

Figure 5.40 Threshold-prediction probability vs. Spearman rank-correlation significance level for predicting well yield from seismic attributes. See Table 5.2 for acronym meanings.

Several conclusions can be drawn directly from these analyses:

(i) There is generally good correspondence between 300- and 600-ms windows, but the short window seems to perform somewhat better: more attributes score highly (15 vs 12) and the mean alpha is better (1.6 vs 2.4%).
(ii) Reflectivity and frequency attributes have the strongest correlations with pay (reflectivity negative, frequency positive)
(iii) There are minor differences between 10 kft vs 5 kft offset limitations in reflectivity: the former performs better for individual NS and EW azimuths (with REW10 the single parameter that is best correlated with pay), although the difference attribute is better in for the shorter offset.
(iv) The absolute value of the AVO intercept is (negatively) correlated, which is likely strongly controlled by bulk reflectivity.
(v) Velocity and AVO gradient (actually, sum of positive values of restricted gradient) show weaker correlations and appear in the short window only.
(vi) EW attributes generally have the best correlation probabilities, except velocity in the short window, where the NS value negatively correlates with pay. Sum or difference attributes often degrade the correlation from the EW value because the NS values are poor. Notable exceptions where azimuthal variations improve correlations with pay are frequency, 5-kft offset reflectivity, and velocity: these are all "simple" attributes compared with the wide variety of AVO-derived attributes.
(vii) Geological attributes also have good correlations with pay and should be considered jointly with seismic attributes in assessing prospectivity.

The physical basis for these correlations is discussed in Section 5.5 below. Here, we turn to using these attributes, both singly and in combination, to predict gas yield.

5.4.2. Prediction of Well Yields from Seismic Attributes

The correlations between seismic attributes and well yields discussed may be used as gas predictors in undrilled regions—this is of course a principal goal of seismic exploration. Due to the relatively small number of available classified wells, the letter categories were again simply divided into commercial (AB) vs. noncommercial (CDE) groups.

For further analysis, a "short list" of attributes with the highest correlation coefficients and threshold-prediction probabilities may be selected. As some of the AVO parameters are redundant, only a single reflectivity-based attribute will be chosen. We further restrict the reflectivity data to 5 kft offset, as this characterizes most of the survey area. Lastly, we discard distance to a fault as a geological co-indicator, as this measure is very sensitive to drilling <u>through</u> the fault: experience in this field indicates that it is good to be near, but not on, a fault. Reservoir geologists interpret this to indicate that fracture densities are higher near the fault, but wells drilled into faults have lower production due to clay and gouge accumulation in the fault itself.

Two short lists are possible, consistently using either single-azimuth or difference attributes. Using EW raypaths only, the selected attributes are REW5, FEW, VNS, and DEPTH. Using azimuthal differences, we selected RDIF5, FDIF, VRAT, and DEPTH. We also evaluated separately results using all four attributes and those of the three seismic attributes alone.

The thresholding technique leads to probability-based approaches to predicting well yield using either single or multiple attributes. In the former, the individual threshold values derived above can be used to guide prospectivity, which have confidence levels of order 70-80% of correct classification. A more conservative technique would be to calculate a new threshold using a high confidence level giving, say, a 95% probability of a commercial well. Alternatively, thresholds for individual attributes can be combined using simple probability theory or an empirical weighting scheme. The most general approach may be using neural networks, an emerging set of algorithms that define nonlinear mappings between parameter spaces, here multiple seismic attributes to well classifications. All four methods are presented below.

5.4.2.1. Single-Attribute Prospectivity

Increased confidence for predicting well prospectivity can be attained by specifying a more stringent threshold and consequently reducing and high-grading the prospective area. Revised, single-attribute prospectivity is computed as follows: First, the mean and standard deviation of an attribute for both commercial and non-commercial wells is calculated. Using these parameters in a gaussian probability distribution, the cumulative class-conditional probabilities P_c and P_{nc} can be computed for relative likelihood of membership within the commercial and noncommercial categories, respectively. From Bayes' Theorem, the net probability that a particular attribute value will yield a commercial well is given by $P_c/(P_c+P_{nc})$. In practice, the net commercial-well probability is computed for all attribute values, and the threshold selected at which 95% confidence is attained. Revised threshold attribute values are given for the "short list" in Table 5.6.

A more generalizable measure of the threshold is its percent deviation from the mean, or background attribute value across the survey area. Table 5.6 shows that velocity anomalies (in either a single azimuth or by azimuthal difference) of order 10% are strongly indicative of pay. Frequency and reflectivity variations of order tens of per cent are adequate to indicate a commercial well in a single azimuth, but the variation in azimuthal difference must be several hundred percent.

Table 5.6 95% Confidence Single-Attribute Thresholds For Commercial Well

Attribute	Threshold	% Deviation
vns	< 10080	7
vrat	< 0.86	14
few	> 38	15
fdif	< -2.3	310
rew5	< 1455	41
rdif5	> 673	285
depth	< 5.2	20

5.4.2.2. Binomial Probabilities for Multiple Attributes

A binomial-probability map for commercial wells can be constructed from standard thresholds derived earlier: if the threshold allows correct classification with probability P, then the probability of a commercial well is P when the attribute is positive and 1-P when the attribute is negative. For two attributes with the same P, the probability of a commercial well is $1-(1-P)^2$ for two positive attributes, [1-(1-P)][1-P] for one positive and one negative attribute, and $(1-P)^2$ for two negative attributes. The extension to n attributes is $[1-(1-P_1)(1-P_2)...][...(1-P_{n-1})(1-P_n)]$.

This method assumes that all variables are independent. In reality, the attributes are correlated: because they are correlated with gas they are correlated with each other. The physical response of the rock determines how they behave jointly. This approach rapidly pushes probabilities to very high and very low values, whose absolute values should be discounted. Nonetheless, this method does allow both positive and negative indicators to highlight zones of high vs. low prospectivity, at least in a relative sense.

Two binomial-probability prospectivity maps (Figs. 5.41-42), using the three seismic attributes alone, are given for the EW azimuths and azimuthal differences. For a 50% formal cutoff in testing the prospectivity against the 19 known wells, both maps appear better at screening out poor locations (60-100% ability) than siting good wells (about 40% success).

Figure 5.41 Binomial-probability prospectivity map using three single-azimuth seismic attributes (REW5, FEW, VNS).

Figure 5.42 Binomial-probability prospectivity map using three azimuthal-difference seismic attributes (RDIF5, FDIF, VRAT)

5.4.2.3. Weighted Threshold Stack for Multiple Attributes

As a simpler, perhaps more intuitive, alternative to the binomial-probability method, threshold-based weighted stacks were constructed independently (Figs. 5.43-45), using different combinations of attributes than those adopted elsewhere in this section. This approach uses the threshold values and empirically chosen weight factors: if the attribute value exceeds (or is lower than) a threshold, a number of "points" are given. The stacked point value or "prospectivity index" is formed by summing over several attributes.

Figure 5.43 Threshold-based prospectivity stack using VINT, REW5, and FDIF.

Figure 5.44 Threshold-based prospectivity stack using BRPEW, REW, and VNS.

Figure 5.45 Threshold-based prospectivity stack using VINT, RDIF5, REW, and FDIF.

5.4.2.4. Neural Networks for Multiple Attributes

Because of the intrinsic noise in the seismic data and apparent nonlinear correspondences with gas yield, neural networks were also employed in an attempt to improve classification performance. The term "neural network" arises from the origins of the techniques in artificial-intelligence theory, but these algorithms are now used in many fields. Neural networks are essentially model-free estimators that simply map some arbitrary input space to an output space. A network is typically trained using a number of (noisy) data and then its classification accuracy tested with previously unseen data. Neural networks are used extensively in optical-character recognition (OCR) algorithms, so that scanned or handwritten characters can be classified.

Three neural networks were tested: (1) A feed-forward, multilayer perceptron (MLP), trained using standard backpropagation; (2) a Generalized Regression Neural Network (GRNN), adapted for categorical data; and, (3) a Restricted Coulomb Energy (RCE) System. The MLP is the most widely used neural network and is described in many texts; we used the JETNET code (Peterson et al., 1993). The GRNN and RCE were programmed using algorithms given in Wasserman (1993). The fundamental difference between the MLP and the last two methods is that the MLP attempts to separate the training examples into categories in the output space using decision surfaces or hyperplanes, whereas the GRNN and RCE try to group the examples of a category together. We found that the MLP performed best, followed by the GRNN; RCE results were unsatisfactory in most cases.

For a given set of control parameters, each network was trained similarly to the thresholding algorithm described above, i.e., by randomly selecting 80% of the data for training and using the remaining 20% for testing; this procedure was repeated 100 times. Several variations on each network were performed in search of the optimum control parameters. Once the optimum parameters were selected, the final networks were retrained using all of the data. Neural-network outputs can be interpreted as probabilities under certain conditions (Peterson et al., 1993); although the range is not as extreme as the binomial probabilities, the values of the neural-network map should also be treated as relative prospectivity and not absolute probability.

Four MLP neural-network prospectivity maps are presented in 5.46-5.49, showing differences in EW azimuths vs. azimuthal differences and including or neglecting DEPTH as an additional parameter. In contrast to the binomial-probability approach, the neural networks performed much better at identifying good wells (90-100% success) than bad ones (25-65% success) when requiring an output >50% for commercial classification. As discussed above, prospectivity outputs may not be strictly interpretable as probabilities and there may also be a bias. Using, say, an 80% cutoff as a guide for "true" prospectivity, the neural networks successfully predict 70-90% of the commercial wells (84% average) and 50-90% of the noncommercial wells (63% average).

Figure 5.46 Neural-network prospectivity using three single-azimuth seismic attributes (REW5, FEW, VNS).

Figure 5.47 Neural-network prospectivity using three azimuthal-difference seismic attributes (RDIF5, FDIF, VRAT)

Figure 5.48 Neural-network prospectivity using three single-azimuth seismic attributes, plus DEPTH to top of reservoir.

Figure 5.49 Neural-network prospectivity using three azimuthal-difference seismic attributes, plus DEPTH to top of reservoir.

5.4.2.5. Interpretation of Prospectivity Maps

The generally similar character of all the prospectivity maps indicates that they are robust, i.e., not sensitive to small errors and noise. Several general conclusions can be drawn:

(1) The large-scale (long-wavelength) trends in prospectivity are controlled by the velocity and broadly indicate the inferred correlation of high EW-fracture density with pay (see 5.5 below). Two major high-density fracture zones trend NE from the top of the anticline. Of greater importance to drilling risk reduction is avoidance of the complementary zones of low fracture density.

Although distance to a fault was excluded from the prospectivity studies, the correlation of prospectivity with faults is revealed visually, especially in the neural-network maps. There may also be an increased correlation with changes in fault strike, which could be caused by enhanced local fracturing due to distributed strain accommodation at fault bends.

(2) The small-scale (short-wavelength) variations in prospectivity are controlled by the reflectivity and frequency and likely indicate the variability of individual reservoir units (gas sands; see 5.5 below).

(3) Depth is a simple geological control that helps screen out nonprospective, off-crest sites; its advantage in the neural network is a consistency of approach among geophysical and geological attributes.

(4) The total picture in the prospectivity maps is therefore:
- Overall good prospectivity high on the structure,
- "Dead zones" on the crest of the structure inferred to be lower fracture density,
- Local variations due to quantity and quality of reservoir sand units.

5.4.3. Cost Savings of Multiazimuth Seismic-Attribute Analysis

Drilling decisions are made on the basis of many more geological, geophysical, and reservoir-engineering properties than used here to construct prospectivity maps. Nonetheless, some first-order estimates of the expected improvement in siting of commercial wells by incorporating the techniques described here may be made. Assuming that the nineteen-well sample is representative, only about 60% of the sited wells are considered commercially viable. In contrast, the neural neural networks are at least 85% successful. As commercial well EURs average 12 BCF at this site, whereas noncommercial wells average 1 BCF, the number of wells required to extract the maximum estimated reserves of 2800 BCF would then be reduced from 370 to 270. At approximately $1 M per well, cost savings up to $100 M could be realized.

5.5. Interpretation of Seismic Attributes

5.5.1. Conceptual Framework for Interpretation

The observed seismic velocity, frequency, and amplitude attributes are the result of all of the geological properties along the ray path, including lithology (e.g., sand vs. shale), stress/strain state (e.g., fractures), and pore content (gas vs. water). With the following assumptions, we can, however, attempt to separate some of these effects:

- Fractures are dominantly subvertical and in a single orientation (within, say, a few tens of degrees) along one of the principal azimuths in which the data were separated (here NS and EW). Sections 4.5 and 5.2 documented a variety of geological and geophysical evidence that support this hypothesis at the field site. There are, however, significant variations (see Section 7.3.2 below).

- The effect of fractures on the fracture-parallel (EW) seismic response is minimal, so that the attributes are sensitive mostly to variations in lithology and pore content (frequency variations related to attenuation may be an exception; see below). Fracture-perpendicular attributes (NS) still contain information from both fractures and porosity.

- Azimuthal-difference attributes (NS - EW or NS/EW) remove the background effects of lithology and pore content, and indicate the presence of fractures. There may be differences in the fracture response depending on gas vs. water content (Grimm and Lynn, 1997; Section 9.4) but this is relatively small compared to the content of the primary pores.

In principle, then, single-azimuth (fracture-parallel) attributes should point to prospective regions of gas-in-matrix, and the azimuthal-difference attributes indicate fracture density. The most likely commercial wells in a tight reservoir would be where both gas and fracture indicators were favorable. Although the prospectivity maps reflect favorable combinations of these parameters (Sec. 5.4), it is difficult in reality to sharply separate these effects.

5.5.2. Interval Velocity

Interval velocity is a standardized and robust seismic parameter, and should therefore carry considerable emphasis in seismic-attribute interpretation. Seven well locations where downhole fracture and maximum horizontal stress measurements were available showed dominantly EW directions. At these locations, the EW azimuth was the faster P-wave interval velocity in the top half of the LFU; six out of seven wells have $>5\%$ anisotropy. This is significant evidence that azimuthal variations in the P-wave interval velocity are linked to the dominant fracture/stress orientation. The lack of an EW correlation with gas yield, but the strong correlation of both the NS velocity and NS/EW velocity ratio (Section 5.4), further supports a classical model in which slower P-wave velocities are associated with increased compliance due to greater fracture density.

Strong velocity heterogeneity (nearly a factor of 2) in both NS or EW azimuths is apparent in the LFU (Figs. 5.22 and 5.23, respectively). Because some of these NS and EW variations are correlated, the anisotropy range of 0.7-1.2 (Fig. 5.24) is somewhat smaller than the heterogeneity. Areas where the velocity is significantly slower NS than EW (interval velocity ratio <0.86 or decrease of 14%; Table 5.6) are likely to have commercially pervasive EW fracturing, whereas zones of nearly isotropic interval velocity (ratio closer to unity) are not likely to have dense EW-trending fractures.

Areas where interval velocity is significantly faster NS than EW could contain relatively dense NS-trending fractures. However, available core and borehole image data in the field do not document any NS-trending fractures. These data are on the anticline's crest; more NS fractures may be present on the structure's limbs under either an unloading or flexural origin for extension on the anticline (Sec. 4.3). There is some trend towards higher NS velocities on the south flank, but this is not conclusive. Alternatively, the appearance of high NS velocities may reflect a background NS direction to the most compressive stress σ_{HMAX}. However, the mean interval-velocity ratio over the study area is distinctly EW-fast (0.980 mean and 0.084 standard deviation determined at >130 independent locations implies <0.3% chance using a Z-test that the background is actually NS-fast). Therefore, the effect of EW fracturing must be much greater than NS compression. If the isolated "windows" of NS-fast velocities are representative of the background (mean anisotropy of NS-fast regions is 1.06), then the effects of fracturing on velocity anisotropy must be even greater, i.e, a high-probability commercial well requires a change of -20% instead of -14%. For gas-filled cracks, P-wave anisotropies of order 20% require fracture densities exceeding 10% by volume; greater fracturing may be required for water-filled cracks (Hudson, 1981; Crampin, 1984). These values are minima because the anisotropy measured in the two-azimuth approach is likely a lower bound on the actual anisotropy (see Sec. 7.3)

It should also be noted that the interval-velocity calculations are performed at ½-mile intervals, and so are undersampled with respect to small-scale changes such as faults.

We suggest that a 3D tomographic inversion of the stacking velocities will emerge as the preferred method of anisotropy analysis. The development of industry contractor code for 3D tomography using narrow azimuth P-wave data will permit seismic analysts to separate the effects of heterogeneity from anisotropy.

5.5.3. Reflectivity

The structurally high, central area defined roughly by lines 8 through 87 (EW coordinate) and crosslines 120-180 (NS coordinate) contains most of the best LFU gas-productive wells. Within this area, both the NS reflection strength and the EW reflection strength in both 24-ms (Figs.5.13-14) and 300 ms (Figs. 5.25-26) windows show generally smaller amplitudes than elsewhere in the survey. This is consistent with gas saturation in the upper part of the LFU: the reservoir sands within the LFU are generally of high acoustic impedance (velocity times density), whereas the overlying Waltman shale and any shale units within the LFU have lower acoustic impedance. The increased compliance of gas in the matrix decreases the impedance contrast between shale and reservoir sand, thus dimming the reflection. The patterns of bright and dim amplitudes clearly follow fault boundaries within the LFU. Specific fault blocks showing maximum dimming can be identified, suggesting areas of gas-filled matrix porosity in the uppermost LFU; this is why reflectivity is a leading attribute in the prospectivity analysis above.

The very strong correlation between EW reflectivity in the 300-ms window and gas yield (Section 5.4) supports this inference. The much weaker correlations for the corresponding NS attributes are likely due to significant degradation of amplitude information due to scattering from EW fractures. Therefore the azimuthal-difference attributes still primarily reflect matrix effects with only a small correlated contribution from fractures. These results contrast strongly with the relations for velocity discussed above, in which the travel time across fractures remains robust.

Because the attribute-yield correlations were formulated simply for commercial vs. noncommercial wells, they reflect large-scale trends across the entire area covered by wells, i.e., wells on the crest of the anticline and those on the limbs. As the best commercial wells (categories A and B) are high on the anticline and the worst wells (E) are on the limbs, it is likely that the reflectivity correlation is simply sensing the large-scale distribution of gas (high on structure) vs. water (low on structure). Indeed, as reflectivity and depth are both strongly correlated with yield, reflectivity and depth are strongly correlated with each other: the top of the anticline is dim, as mentioned above. Based on the anomalously large reflection amplitude at well A-D4, the Field Operator (personal communication, 1997) has suggested that high reflectivity may be an indicator of the best wells among those on the anticline crest, due to higher impedance contrasts caused by greater local abundance of reservoir sands. This inference may be supported by a modest correlation between amplitude and mapped sand thickness in a 9-mi^2 area around well A-D4. The Spearman rank-correlation coefficients remain negative, however, regardless of the well-rank groups chosen for analysis (ABCE, ABC, or AB), and discrimination thresholds cannot be found for smaller subsets of the data. The "bright spot" of well A-D4 may indeed indicate more or better local reservoir sands, but the statistics of the spatially distributed nineteen well data set support only the broad "dim spot" concept.

Further artifacts in amplitude interpretation at the LFU may be exist due to fault shadowing from the overlying Waltman shale (Field Operator, personal communication, 1997; see also Section 4.5.5). Amplitude breakup due to faults in the Waltman will result in an apparent decrease in reflectivity below. A related indicator of faults and fractures in the Waltman is the apparent "velocity sag" centered over the crest of the anticline. Therefore some portion of the large, structurally high "dim spot" on the LFU may be correlated with the internal structure of the overlying Waltman. However, the strongest correlations with well yield among all the seismic attributes analyzed occur for azimuthal differences in reflectivity. This indicates that there are indeed small-scale variations of significance, even though artifacts may exist at larger scales.

The strong differences in reflectivity of the LFU as a function of azimuth are evident in the summary statistics: the mean and standard deviation of the 300-ms interval-average, NS data are 2050 and 670, respectively, whereas these values for the EW data are 1300 and 1100, respectively. The EW amplitudes are significantly dimmer and rougher. There could be several potential contributing factors to this result. First, there is larger change in impedance for a fractured reflector looking across the cracks than parallel, causing increased fracture-perpendicular reflectivity (e.g., Grimm and Lynn, 1997; Section 9.4). Alternatively, greater EW dimming could be caused by increased attenuation in the direction of oriented pores (fractures) (Gelensky and Shapiro, 1994; 1996). However, the reflectivity is not well correlated with the most reliable fracture indicator, the interval-velocity ratio. For example, the NS reflectivity shows broad highs to the south and northwest of the crest; this recalls the caveats of fault shadowing above. The EW reflectivity, being less scattered in either the Waltman or the LFU, does not have these long-wavelength patterns. The NS "striping" in the EW data, however, suggests other artifacts. In particular, there may be some signal loss due to the shorter offsets in the EW azimuths; this is also consistent with the higher variance in this direction. As greater variability might be expected for rays going across fractures, this result shows the underlying control of survey geometry.

5.5.4. AVO Intercept

The AVO Intercept represents the true vertical-incidence reflection amplitude and also provides quality control for the AVO Gradient. The AVO Intercept is sensitive to the change in acoustic impedance across the reflecting boundary. With sufficient matrix porosity, the presence of gas in the top of the LFU is indicated by a decreased AVO Intercept value (Section 5.4). In principle, the AVO Intercept, like all normal-incidence attributes, should be insensitive to azimuthal anisotropy, because vertically propagating P-waves do not move across vertical fracture planes. In fact, there are measured azimuthal differences in AVO Intercept (Figs 5.18 and 5.30). There are at least two reasons for these variations. First, the AVO Intercept is not measured solely at vertical incidence, but is calculated from the change in reflector amplitude with offset. Second, the assumption of vertical fractures is undoubtedly oversimplified; non-vertically dipping structures require a nonzero offset for normal incidence, therefore introducing azimuthal variations. The spatial correlation of AVO Intercept with faults is even more pronounced than in reflectivity.

The reduced azimuthal- and offset-dependence of the top-LFU AVO intercept results in a somewhat more spatially coherent map than the raw reflectivity, although the two sets of attribute maps are quite similar (Figs. 5.16-17 and 5.13-14). The same is true of the Interval Average Absolute AVO Intercepts (Figs. 5.28-29) compared to the Interval Average Reflectivity (Figs. 5.25-26). These results attest to the careful, high-quality processing of these data (in that both the stacked amplitudes and the AVO Intercepts are good approximations to the vertical-incidence reflection amplitudes). This also gives credence to the AVO Gradients, since the AVO Intercepts and Gradients are calculated from the same equation.

5.5.5. AVO Gradient

AVO gradients reveal the nature of the contrast in P-to-S velocity ratios (V_p/V_s) ratio, or alternatively, Poisson's ratio at a boundary. Ostrander (1984) showed that decreases in Poisson's ratio are associated with more negative AVO gradients, and vice-versa. The presence of gas beneath a reflector will increase the compliance of the lower unit over its value if brine-filled, decreasing Poisson's ratio and causing a more negative AVO gradient. Conversely, the larger increase in Poisson's ratio going across the bottom of the sand yields a more positive AVO gradient. Sonic logs indicate that the impedances of LFU reservoir sands are usually higher than surrounding shales, leading to positive reflection coefficients (and AVO intercepts) from the tops of the sands and negative reflections at the bases of these units. The Restricted AVO Gradient (sign of AVO intercept multiplied by signed gradient) will therefore be more negative for the top or bottom of a gas sand. By summing only the negative values of this restricted parameter in a windowed interval, the gas signature can be enhanced.

Azimuthal anisotropy strongly affects AVO gradients (e.g., Grimm and Lynn, 1997; Section 9.4). In principle, the presence of water-filled cracks beneath a boundary will increase the Poisson's ratio in the crack-perpendicular direction, thus making the AVO gradient more positive in this direction. Conversely, the AVO gradient should be more negative for gas-filled cracks. In the field, Lynn et al. (1995) found that the azimuthal difference in AVO Gradient at the top of a fractured, gas-saturated interval was proportional to the shear-wave traveltime anisotropy. The AVO Gradient in the fracture-perpendicular direction showed the gas-saturated AVO signature, while the AVO Gradient in the fracture-parallel direction did not.

In the data presented here, the effective sign convention is opposite SEG standard, because interpreters found it more convenient to pick a trough (negative) for the top LFU reflector, in spite of its positive impedance contrast. Therefore AVO gradients as measured here should be more positive for gas sands, and the restricted positive gradient the most robust gas indicator. Similarly, AVO gradients across fractures should be more negative when water-filled and more positive when gas filled.

The statistical analysis (Section 5.4) indeed reveals that the restricted positive EW AVO gradient is the best correlated with gas yield—but negatively. This inverse correlation holds for most of the AVO gradient parameters. We interpret this by considering the low reflectivity and AVO intercepts found for commercial wells. In theory, most low-amplitude reflections do not dim with offset as sharply as high-amplitude reflections. Therefore AVO gradient and intercept are positively correlated. This can be demonstrated in the these data sets as a whole (e.g., linear correlation coefficient of -0.63 between AVO gradient and intercept in the EW top-LFU reflection). Therefore the small AVO gradients observed to correlate with well yield are associated with small AVO intercepts. This in turn implies that the impedance contrast for LFU reservoir sands dominates over changes in Poisson's ratio. The correlations with gas yield do not vary as widely between NS and EW azimuths as for the reflectivity attributes (including AVO intercept), indicating weaker fracture control.

The NS AVO Gradients (Figs. 5.19 and 5.31) show stronger fluctuations than the EW maps (Figs. 5.20 and 5.32). The large-scale anomalies visible in the reflectivity maps are also evident in the NS AVO gradients, whereas small-scale structure (including some NS artifacts) dominates the EW maps. While still evident, the poorer correlation of the azimuthal differences in AVO gradients with major faults (Figs. 5.21 and 5.33) supports the inference of a weaker dependence on fracturing. Structure and faulting can potentially degrade the AVO gradient response, thus contributing to the overall "smearing" (Grimm and Lynn, 1997; Section 9.4).

5.5.6. Frequency

The frequency content of a seismic signal changes throughout its propagation path. One way to express the amplitude of a seismic signal is $A(f) = A_0(f)\exp(-\pi\alpha f t)$, where A(f) is the amplitude as a function of frequency, t is the travel time, and α is the attenuation constant (e.g., Sheriff and Geldart, 1995). It is apparent from this relation that higher frequencies are preferentially lost or attenuated with travel time or distance. The magnitude of high-frequency loss is determined by the attenuation constant, which is a function of rock type and pore content. In general, greater attenuation α occurs for fluids than solids; therefore attenuation usually increases with porosity.

High-frequency loss or attenuation has been used as a gas indicator, but the exact mechanisms are still unclear. Greater attenuation might be expected for gas when the pores and rock frame are treated as a single effective medium ("classical model"). In practice, "low-frequency shadows" below, not at, hydrocarbon accumulations are often seen (Sheriff and Geldart, 1995). These could be due to absorption by the gas or due to gas-induced processing artifacts, for example, improper stacking because of differing velocities or raypaths.

For anisotropic media (e.g., oriented cracks), the detailed attenuation behavior as a function of azimuth and pore fluid depends strongly on the model assumptions. For an effective-medium approach to combined cracks and rock frame, maximum attenuation is expected in the direction perpendicular to cracks. In a more sophisticated treatment, "global flow" can be considered by averaging the relative movement between the solid frame and pore fluid. Gelinsky and Shapiro (1994, 1996) show that maximum attenuation in this model is proportional to permeability in the direction of particle displacement. For P-waves, then, the greatest amplitude loss would be parallel to fractures, in direct contrast to the classical model. However, these workers acknowledge that global flow becomes dominated by local, or "squirt", flow at low permeabilities and seismic frequencies.

Squirt flow predicts a peak in attenuation as a function of the permeability of elongated (cylindrical) pores (Akbar et al., 1993): at large pore radius (permeability) the fluid is relaxed and the shear stresses within the fluid small, resulting in small attenuation. As the pore radius decreases, the shear stresses increase, resulting in high attenuation. At very small pore radii, the fluid is unrelaxed at high pressure—stresses are strongly coupled to the pore walls—leading to a decrease in attenuation. These variations with pore size can also be considered in terms of frequency and fluid vs. gas saturation. At seismic frequencies, attenuation increases with increasing frequency and decreases with increasing permeability (Akbar et al., 1993, Fig. 6). The variation with fluid saturation may provide a gas-discriminant capability: there is a large drop in attenuation for fluid saturations below about 30%, i.e., gas saturation greater than about 30% (Akbar et al., 1993, Fig. 4). Therefore greater attenuation, or high-frequency loss, is expected for water over gas, in contrast to the classical model. This mechanism always yields greater attenuation for rays traveling perpendicular to oriented pores (Akbar et al., 1993; Figs. 2-4), in agreement with an anisotropic effective medium.

The spatial patterns of frequency variations in this survey (Figs. 5.34-36) show some large-scale patterns, but not as closely correlated with position on the anticline as the reflectivity attributes. Locations of major faults are evident as in the reflectivity.

EW frequency is strongly positively correlated with productive wells (Section 5.4). Smaller attenuation is associated with gas, in agreement with the squirt-flow model of Akbar and co-workers. The NS frequencies have a weaker negative correlation with well yield. The azimuthal difference NS minus EW therefore also has a negative correlation that is slightly improved over EW alone. As with the reflectivity data, these results indicate that the gas-correlated seismic response is dominated by matrix porosity, with some contribution from fractures.

There are, however, additional complexities when the data are examined more closely. A plot of azimuthal frequency difference versus interval velocity ratio (Fig. 5.50) reveals two distinct groups. Group I may be defined as those points that collectively show a positive correlation between frequency difference and velocity ratio. Productive wells are generally associated with negative NS minus EW frequencies and NS/EW interval-interval velocity ratios less than unity, and unproductive wells with the converse. The productive wells in Group I may be interpreted as a combination of gas-in-matrix and EW fractures. It follows that the nonproductive subset of Group I is due to NS fractures and/or water-in-matrix (recall, however, that there is little field evidence for NS-striking fractures).

Group II may be defined as those wells showing little azimuthal difference in frequency but strong velocity anisotropy. It contains both commercial and noncommercial wells, mostly of intermediate rank. If the lack of frequency anisotropy is due to the absence of fractures, the presence of velocity anisotropy alone could be attributed to a regional stress anisotropy, i.e., the seismically fast direction along NS-oriented greatest compressive stress. However, there is no spatial pattern in the map locations of Group II and it is unlikely that the background velocity is strongly NS-fast (see Section 5.5.2 above). If the velocity anisotropy is due to EW fracturing, the lack of frequency anisotropy may instead be related to gas-water partitioning in intermediate-ranking wells. If gas is in the matrix but the fractures have been invaded by water, the azimuthal variation in attenuation will be minimal (Akbar et al., 1993; Fig. 4) but the high-frequency signature of gas-in-matrix can be preserved. This model does not explain the NS-fast, high NS-frequency Group I wells, as any NS cracks would likely be water-filled for these poorly producing wells and hence display little azimuthal anisotropy in frequency.

Figure 5.50 Interval-velocity ratio versus azimuthal differences in frequency and reflection strength. Note two distinct groups for frequency: Group I shows positive slope between attributes; Group II has strong negative velocity anisotropy but small azimuthal differences in reflectivity and frequency.

5.5.7. Conclusions: Seismic-Attribute Interpretation

The statistical analysis and map patterns of the multiazimuth seismic attributes demonstrate that these methods are useful in identifying fractured zones and their relation to gas production. Seismic-velocity anisotropy is the most robust attribute and may be interpreted as broad regions of varying fracture density across the producing structure. The good correlation of velocity anisotropy with well yield supports the hypothesis that fractures are important in providing high-permeability pathways. However, strong correlations of EW reflectivity and frequency with commercial wells indicate that these attributes are responding directly to gas-in-matrix. Therefore the local distribution of suitable reservoir units controlling gas availability can also be determined. Scattering from EW fractures is likely the origin of poor correlation of NS reflectivity and frequency with gas production. However, the improvement of correlations for both reflectivity and frequency in the NS minus EW azimuthal differences implies that fractures do play a role in the response of these attributes as well.

The anticorrelation of reflection amplitude (or AVO intercept) with pay may be interpreted as a "dim spot" in which gas-charged sands have a lower, but still positive, impedance contrast with surrounding shales than do water-filled sands. AVO-Gradient attributes are derivatives that could potentially provide greater information about reflectivity, but in this study were overwhelmed by the dim-spot effect and also possibly by degradation due to survey geometry and scattering. The correlation of pay with an increase in frequency is puzzling at first glance, as decreases in frequency are often associated with gas accumulations. This result is, however, consistent with squirt-flow theory for partially water-saturated pores (Akbar et al., 1993).

The generally brighter reflection amplitudes in the NS direction is consistent with a greater impedance contrast due to EW fractures; however, the greater deviations in EW azimuths are likely due to survey constraints, particularly the shorter offsets available in this direction. The same can be said for frequency: slightly lower NS values are likely due to attenuation in water-filled fractures and/or scattering, but the higher variance EW may be attributable to survey geometry.

In summary, seismic attributes selected for matrix response yield results consistent with increased porosity and gas saturation over the crest of the structure where the best LFU gas production is found. Attributes selected for fracture response emphasize the role of azimuthal anisotropy, but do not match a single physical model. Reflectivity variations agree with classical equivalent-medium anisotropy theory where greater impedance contrasts, and hence reflection strengths, occur in the NS, fracture-normal direction. Alternatively, this effect could also be due to greater attenuation in the fracture-parallel direction as predicted by the Gelinsky-Shapiro global-flow model. However, greater high-frequency loss in the fracture-normal direction is also a manifestation of attenuation, and is consistent with either an equivalent medium or the more sophisticated squirt-flow model of Akbar and colleagues.

We emphasize that the statistical interpretation was obtained based on the correlation of numerical ranking of the Estimated Ultimate Recovery of nineteen wells over the entire LFU interval with seismic attributes averaged over the upper 1500 ft of the LFU. A more rigorous analysis would break out the EUR in just the upper 1500 ft and analyze both gas yield and seismic attributes in three dimensions rather than as two-dimensional, vertically averaged maps. Such detail was not available for this study, and would likely require a much larger number of control wells also. Because the top-LFU reflection attributes are sensitive to a much smaller vertical interval, our evaluation of these attributes was entirely qualitative.

We anticipate as more theoretical, modeling, and field studies are done to explain the effects of azimuthal anisotropy on P-wave amplitudes at seismic frequencies, a more complete interpretation of the response of these attributes will become clearer.

5.6. Conclusions: 3D-P

The 3D, 37-mi^2 P-wave survey was divided into two volumes, with raypaths parallel and perpendicular ($\pm 45°$) to the dominant EW fracture direction, in order to construct azimuthal differences in seismic attributes that highlight the fracture response. The EW, fracture-parallel data volumes were judged superior for structural and stratigraphic interpretation; poorer imaging in the NS direction is likely due to scattering by EW fractures.

The seismic attributes were correlated with well rank using two different statistical methods, with comparable results. Window length is an important consideration. The stacked EW amplitude is the best-correlated seismic attribute to gas pay in the survey area, based on the 19-well control set. The decreased amplitudes may be physically interpreted as the response from lowered impedance in gas-charged sands. AVO responses are correlated with simple reflectivity and support this interpretation. EW frequency also shows a positive correlation with gas yield, in agreement with the attenuation predicted by squirt-flow theory. Reflectivity and frequency in the NS, fracture-perpendicular direction shows poor correlations with well yields, likely due to scattering by fractures; however, azimuthal differences in these attributes represent a combined matrix/fracture response. The azimuthal ratio of interval velocity is likely the best direct fracture indicator (Figs. 1.1, 5.24). The role of both matrix and fractures in controlling seismic attributes shows the dual-porosity nature of the LFU reservoir.

The statistically best-correlated seismic attributes were used to make maps showing relative likelihood of commercial gas pay using several methods. The neural-network prospectivity map using azimuthal differences in velocity, reflectivity, and frequency, as well as structural altitude, is >80% accurate in selecting commercial wells (Figs. 1.2, 5.49). These attributes combine both matrix and fracture controls on well yield. Large-scale variations in the prospectivity maps are likely due to broad variations in fracture density: areas of lower prospectivity high on the structure are inferred to be zones of low fracture density. Small-scale variations in prospectivity are due to changes in reflectivity and frequency that can be related to the quantity and/or quality of local reservoir units.

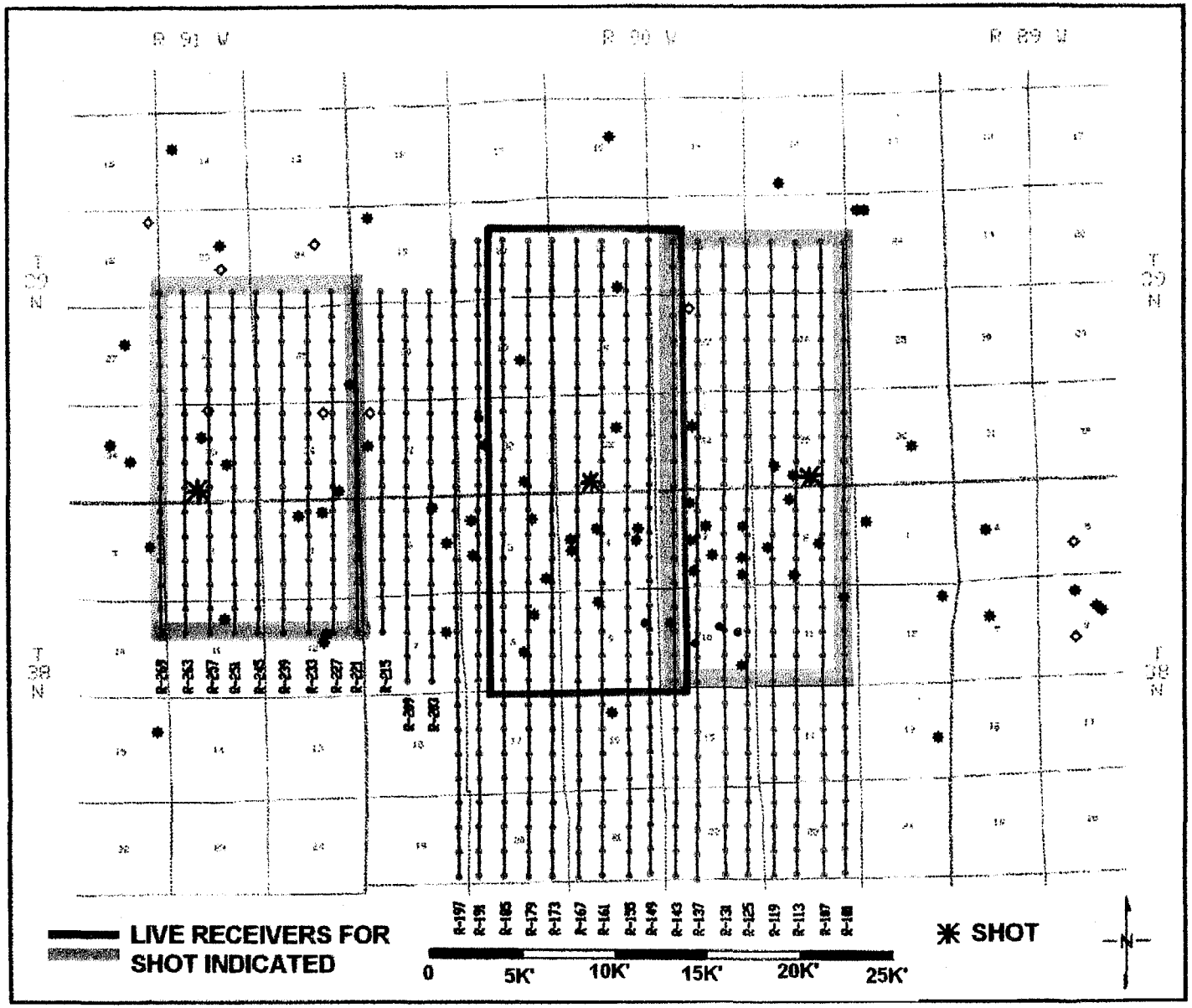

RECEIVER LINES R-101 THROUGH R-269 FOR 3D P-WAVE SEISMIC ACQUISITION. Figure 5-1

HIGHLIGHTED RECEIVER STATIONS WERE LIVE FOR SHOT LOCATIONS INDICATED.

THIS SHOOTING GEOMETRY RESULTED IN "HIGH EW-FOLD STRIPS" NEAR SURVEY EDGES, DISCUSSED IN TEXT.

WESTERN GEOPHYSICAL
NORTH/SOUTH FOLD
LINE RANGE (SECONDARY ORDINA
SHOTPOINT RANGE (PRIMARY ORDINATE)
GRID CORNER CELL CENTER
NORTH
LOWER LEFT
X COORDINATE 759029.4
Y COORDINATE 975679.4
CDP NUMBER 59401
LINE NUMBER 181.0
SHOTPOINT NUMBER 1.0
LOWER RIGHT
X COORDINATE 759930.0
Y COORDINATE 939989.4
CDP NUMBER 59730
LINE NUMBER 181.0
SHOTPOINT NUMBER 330.0
UPPER RIGHT
X COORDINATE 809429.9
Y COORDINATE 939989.9
CDP NUMBER 330
LINE NUMBER 1.0
UNDER 1
1 TO 3
3 TO 5
5 TO 7
7 TO 9
9 TO 11
11 TO 13
13 TO 15
15 TO 17
17 TO 19
19 TO 21
21 TO 23
23 TO 25
25 TO 27
27 TO 29
29 TO 31
AND OVER

Figure 5-2

FROM WESTERN GEOPHYSICAL

EAST/WEST FOLD

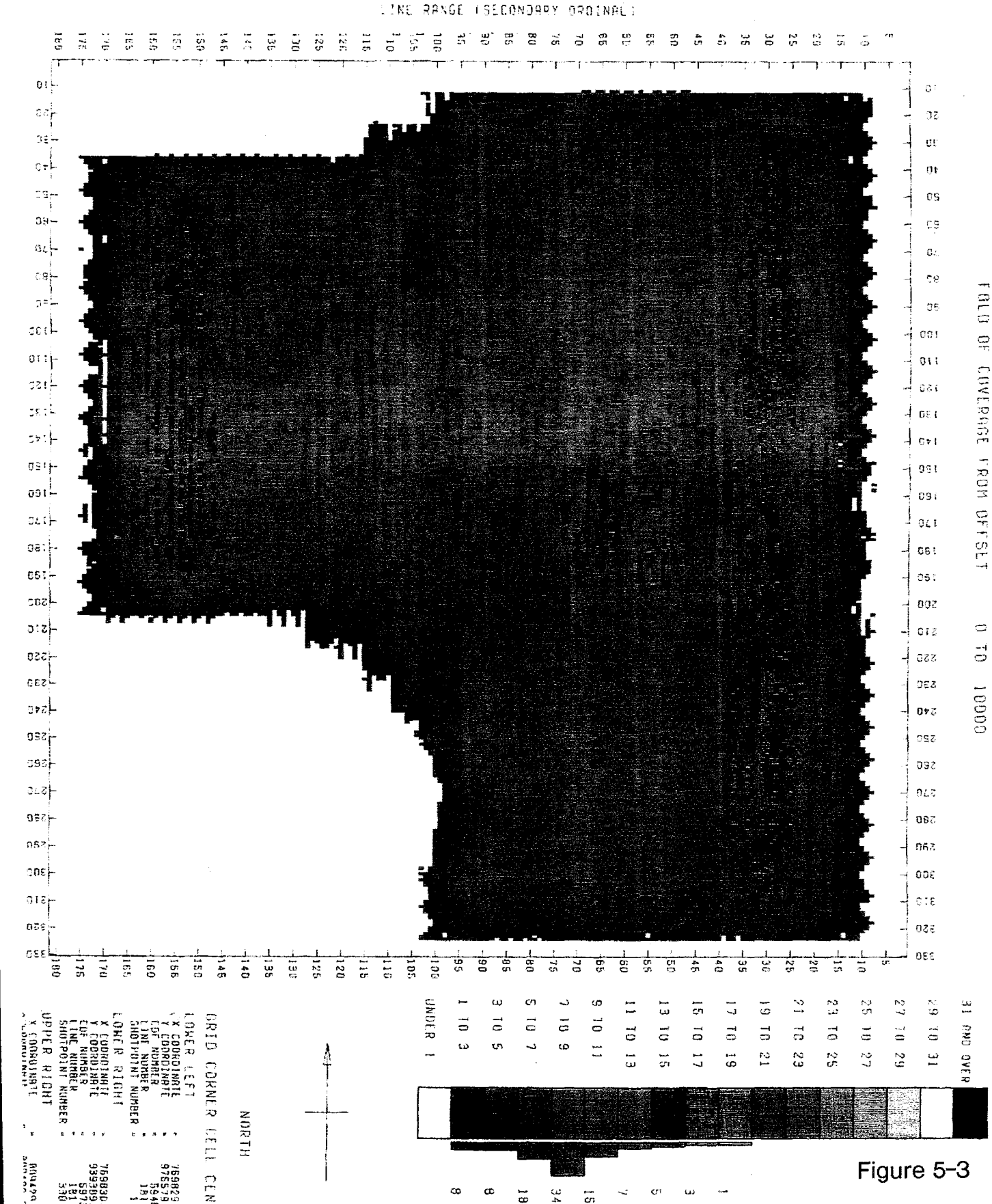

Figure 5-3

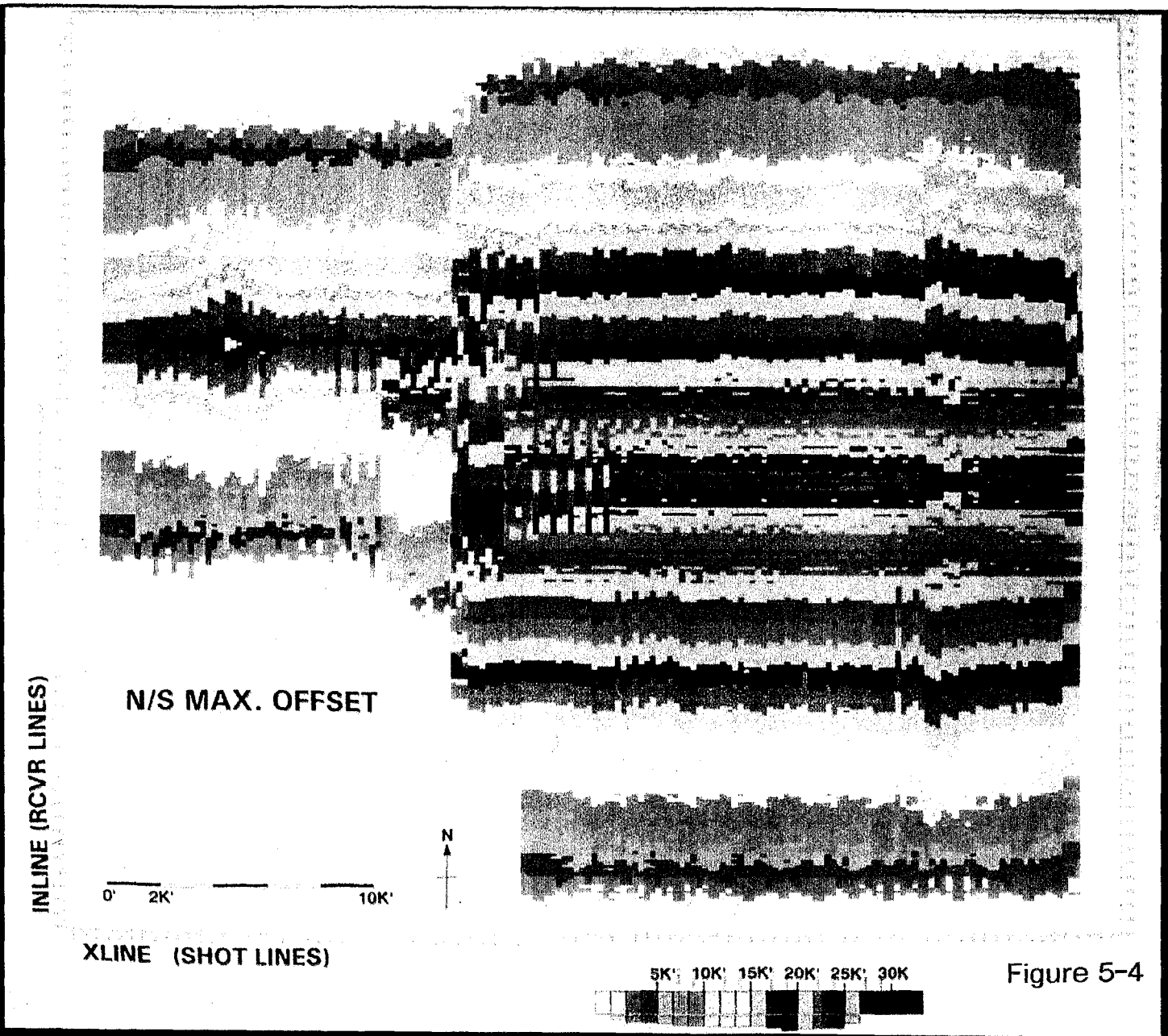
N/S MAX. OFFSET
INLINE (RCVR LINES)
XLINE (SHOT LINES)
0'
2K'
10K'
N
5K'
10K'
15K'
20K'
25K'
30K

Figure 5-4

MAXIMUM EAST/WEST OFFSET IN A CELL (110'X220')
3D SURVEY

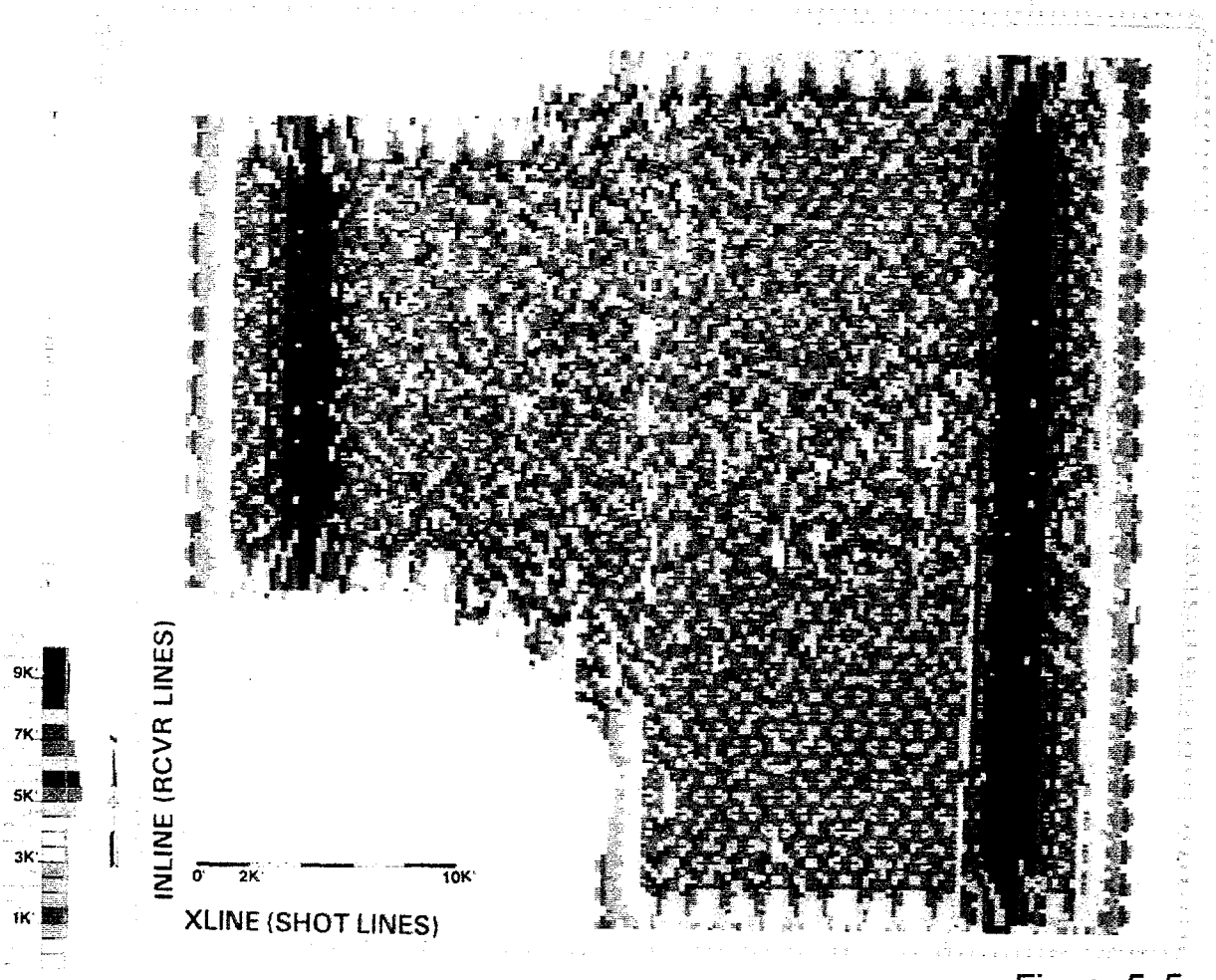

Figure 5-5

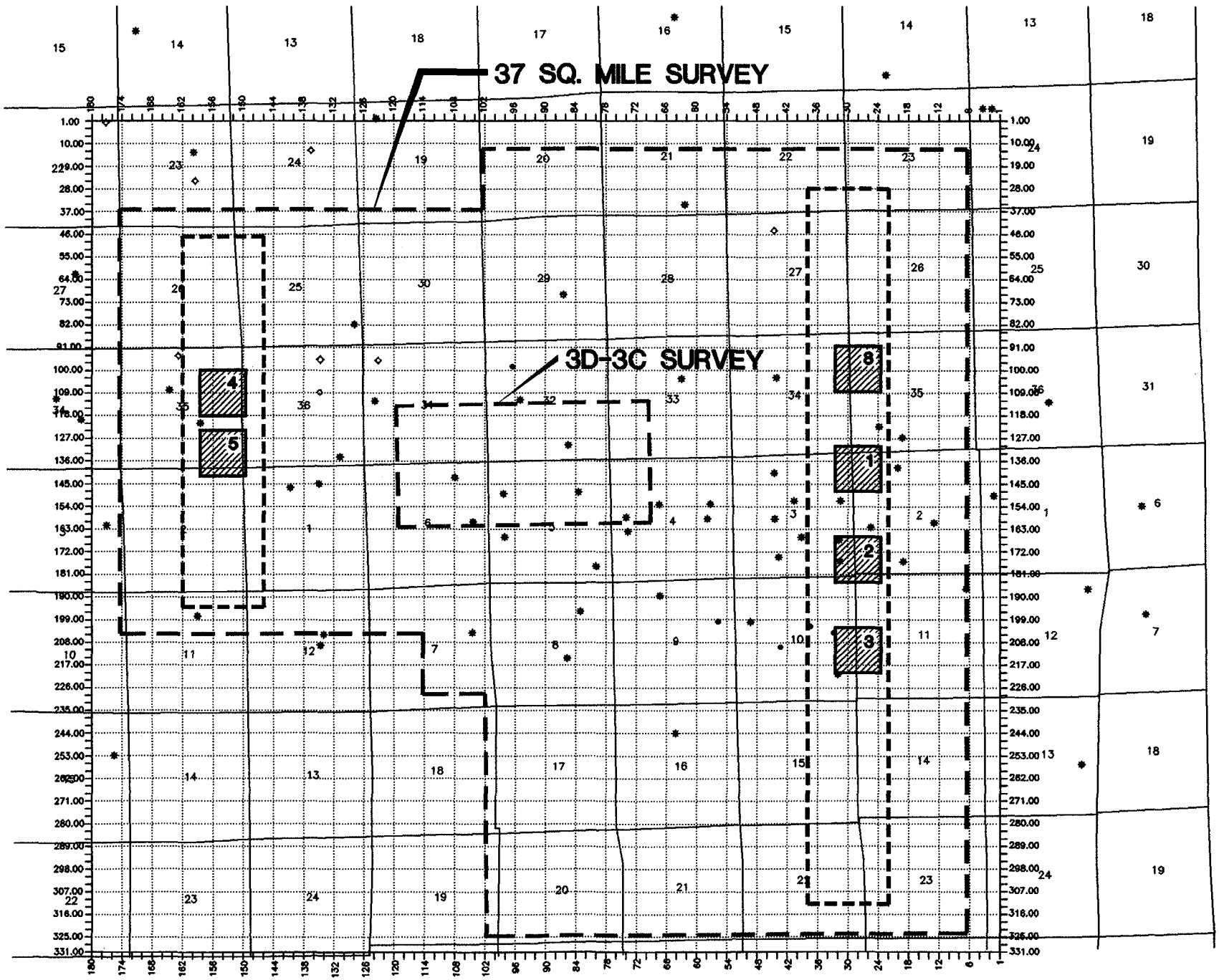

Location of Super Gathers for Azimuthal Analysis

Figure 5-6

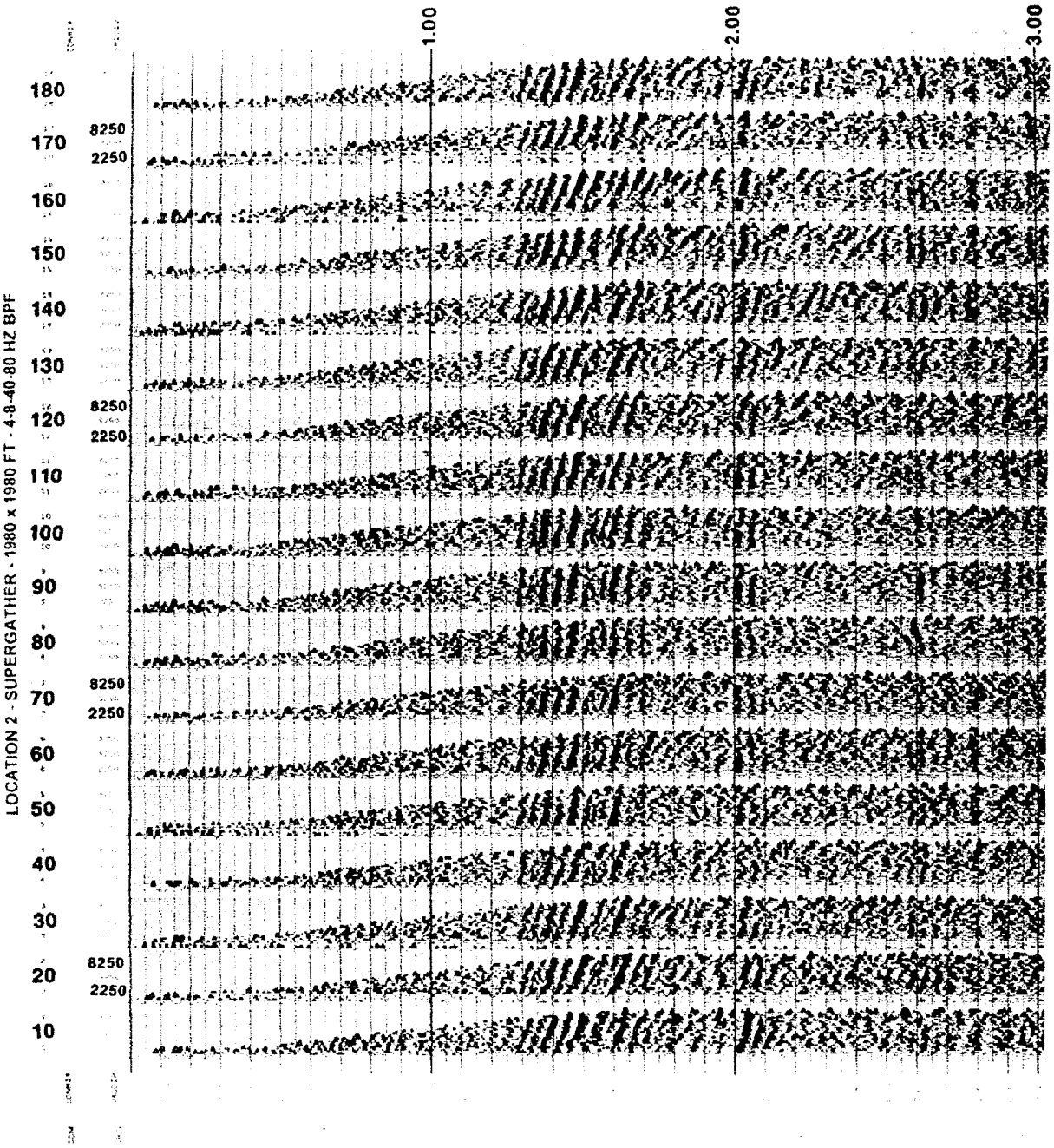
LOCATION 2 - SUPERGATHER - 1980 x 1980 FT - 4-8-40-80 HZ BPF
1.00
2.00
3.00
180
170
160
150
140
130
120
110
100
90
80
70
60
50
40
30
20
10
8250
2250
8250
2250
8250
2250
8250
2250

Figure 5-7

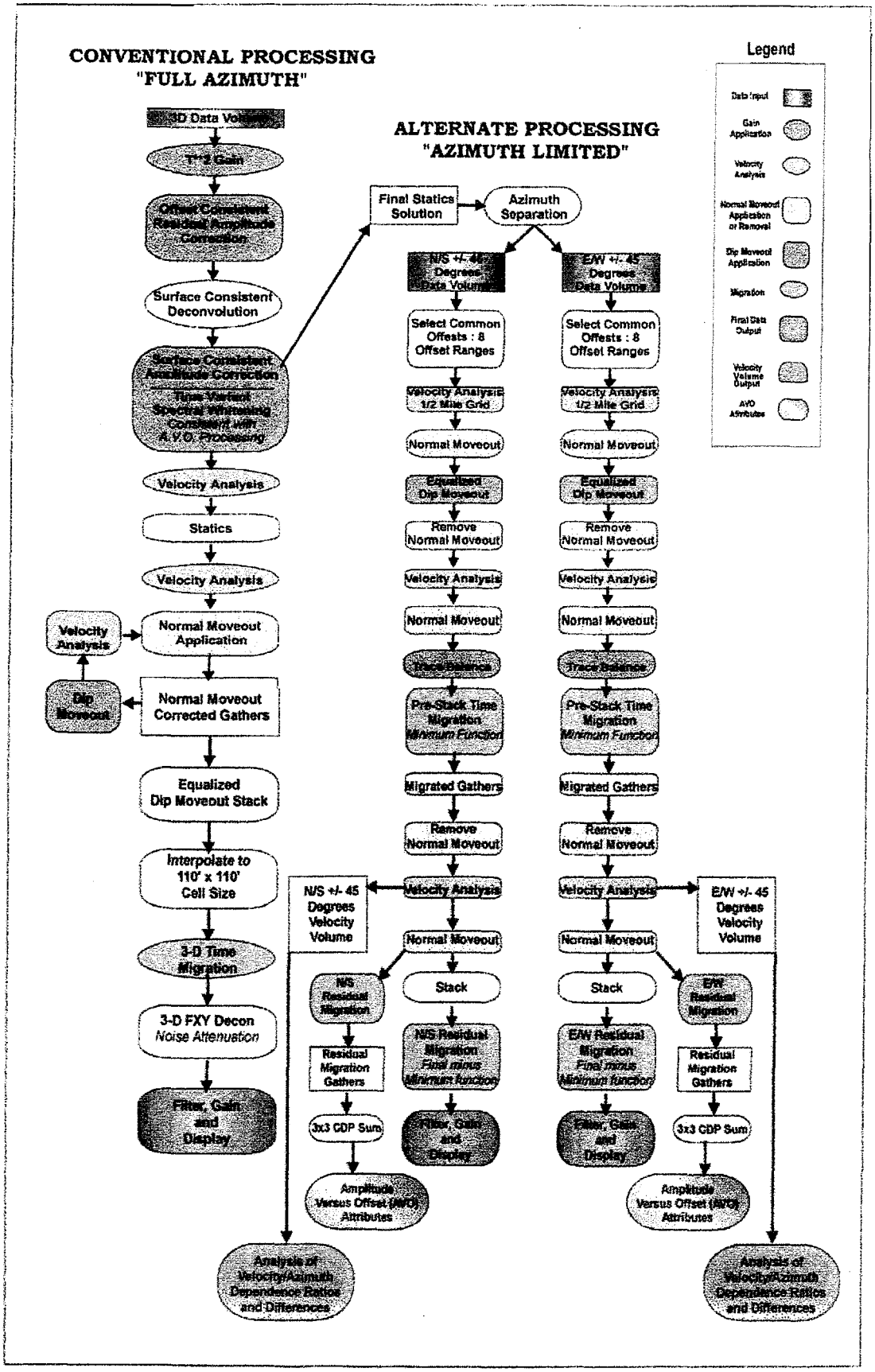

Seismic processing flow for two-azimuths or "Azimuth Limited" processing, compared to conventional ("Full Azimuth") processing flow.

Figure 5-8

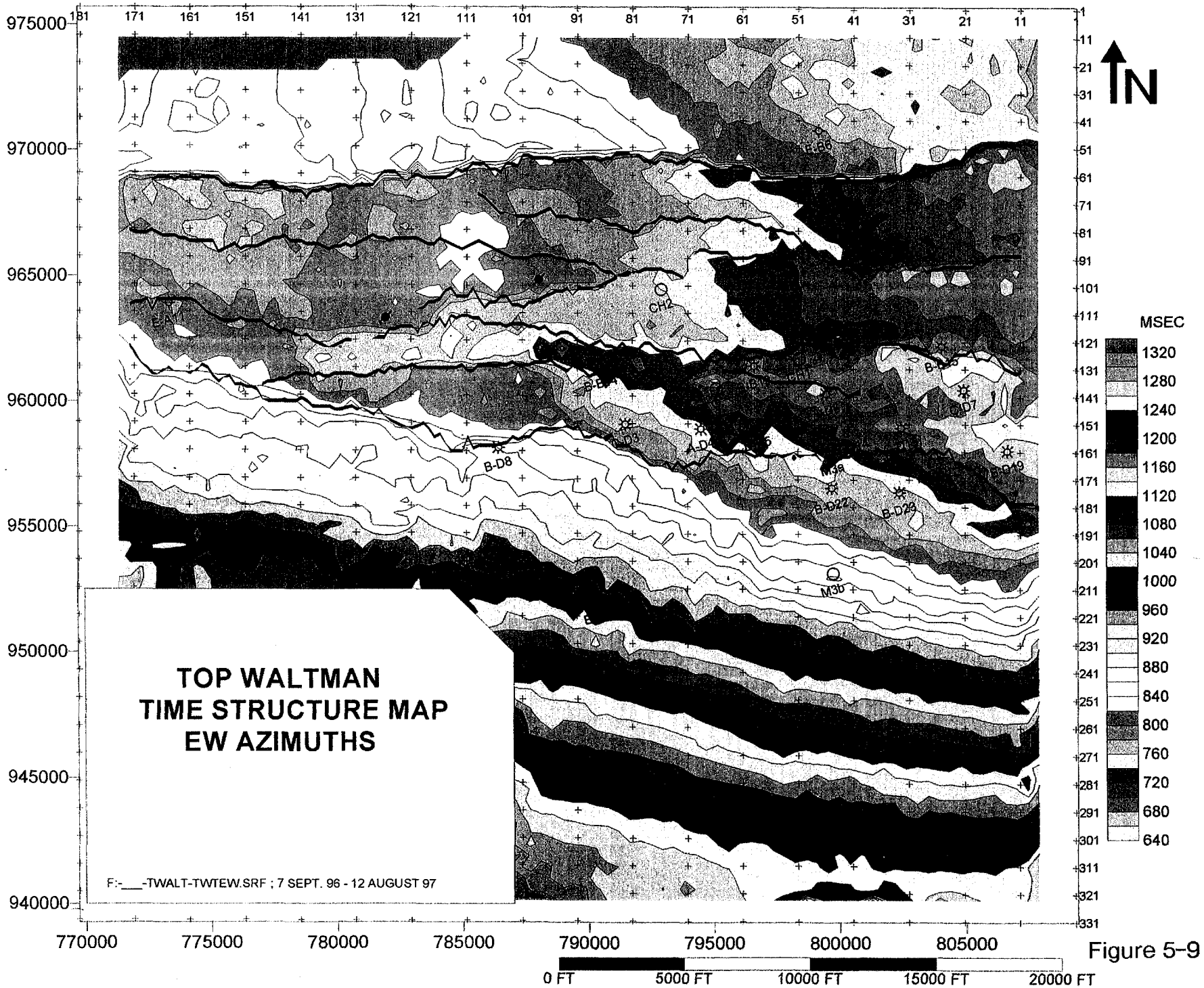
TOP WALTMAN
TIME STRUCTURE MAP
EW AZIMUTHS
F:-___-TWALT-TWTEW.SRF ; 7 SEPT. 96 - 12 AUGUST 97
N
MSEC
1320
1280
1240
1200
1160
1120
1080
1040
1000
960
920
880
840
800
760
720
680
640
975000
970000
965000
960000
955000
950000
945000
940000
770000
775000
780000
785000
790000
795000
800000
805000
0 FT
5000 FT
10000 FT
15000 FT
20000 FT

Figure 5-9

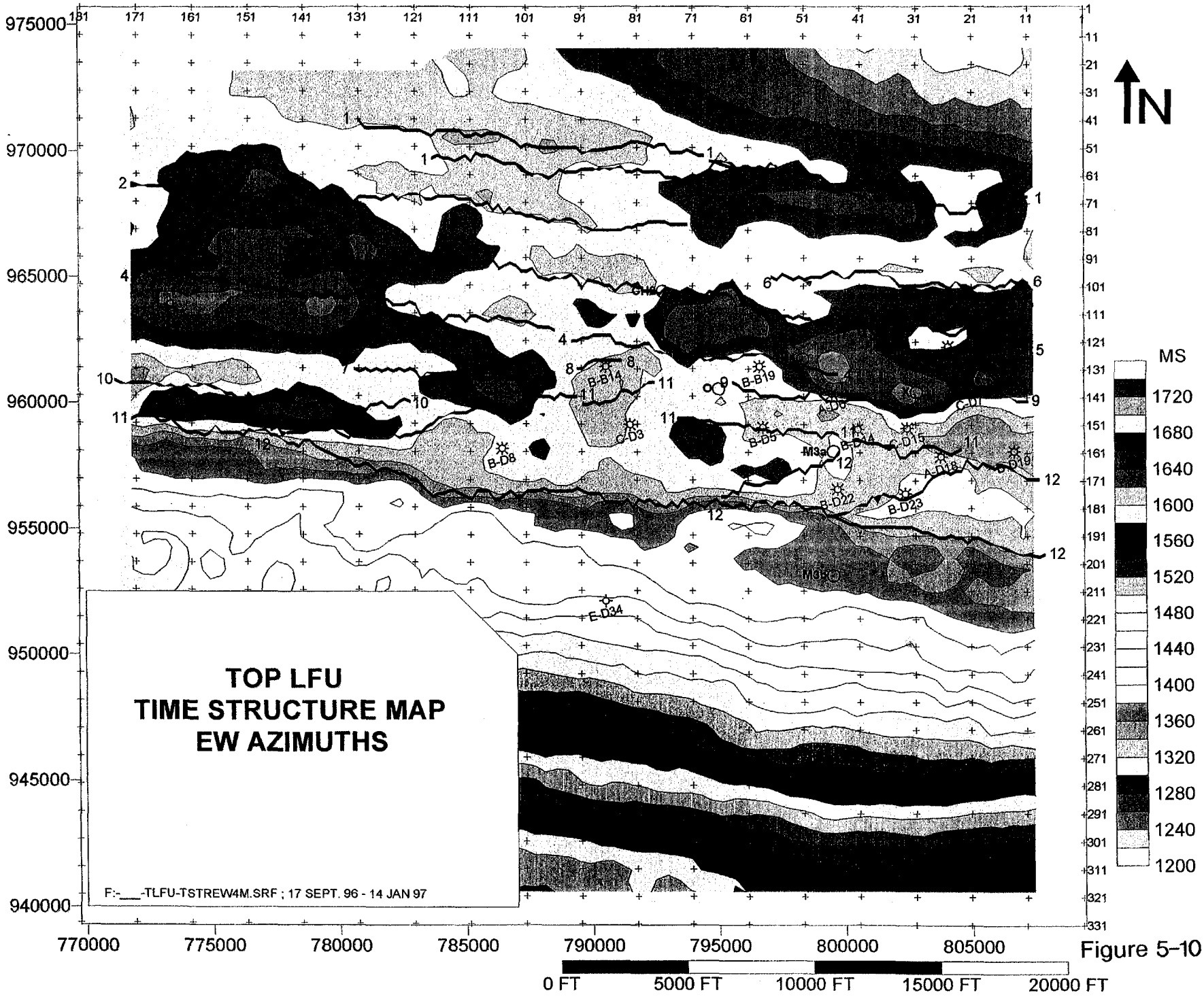
TOP LFU
TIME STRUCTURE MAP
EW AZIMUTHS
F:-___-TLFU-TSTREW4M.SRF ; 17 SEPT. 96 - 14 JAN 97
N
MS
1720
1680
1640
1600
1560
1520
1480
1440
1400
1360
1320
1280
1240
1200
975000
970000
965000
960000
955000
950000
945000
940000
770000
775000
780000
785000
790000
795000
800000
805000
0 FT
5000 FT
10000 FT
15000 FT
20000 FT

Figure 5-10

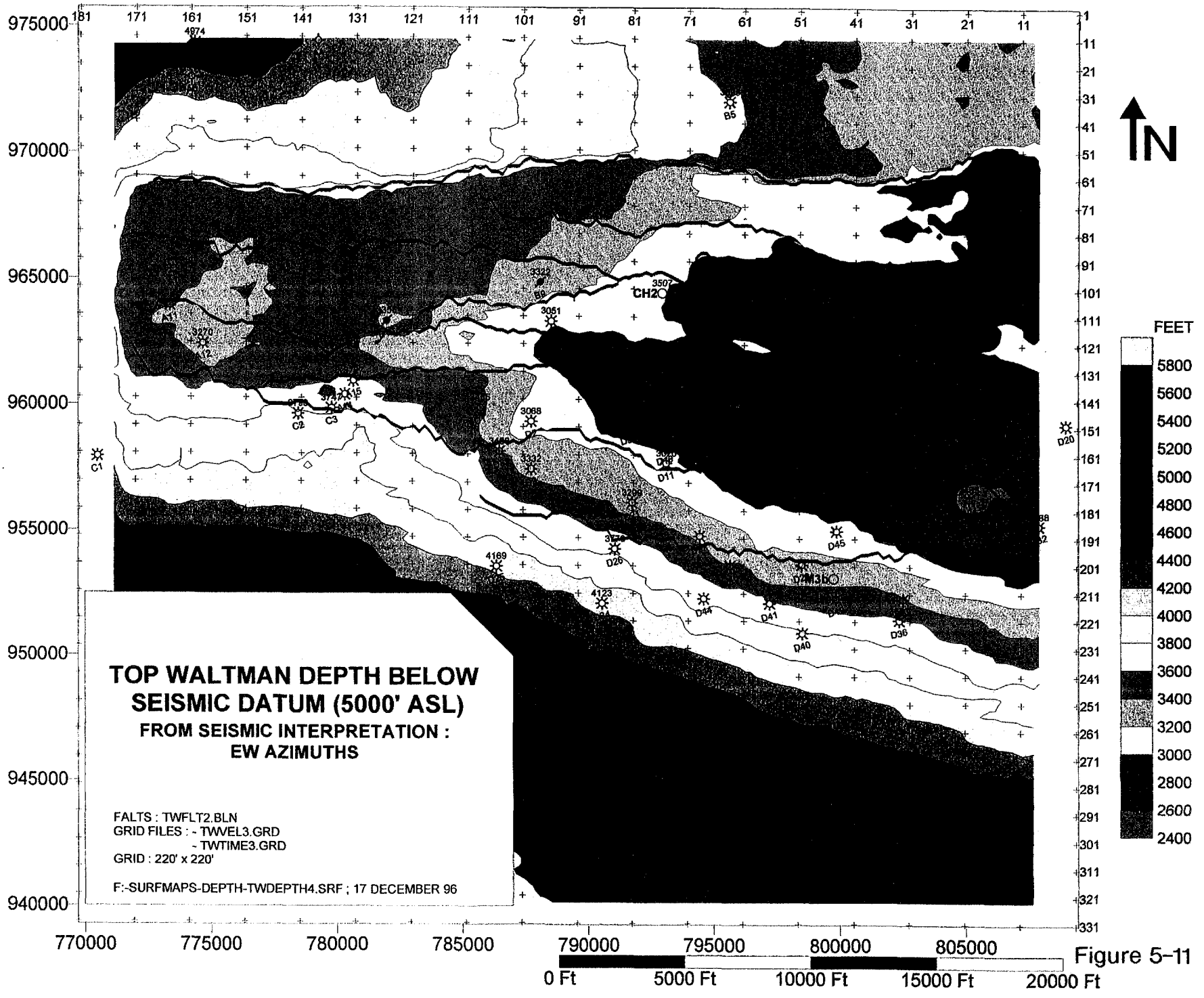
TOP WALTMAN DEPTH BELOW SEISMIC DATUM (5000' ASL)
FROM SEISMIC INTERPRETATION : EW AZIMUTHS
FALTS : TWFLT2.BLN
GRID FILES : - TWVEL3.GRD
- TWTIME3.GRD
GRID : 220' x 220'
F:-SURFMAPS-DEPTH-TWDEPTH4.SRF ; 17 DECEMBER 96
N
FEET
5800
5600
5400
5200
5000
4800
4600
4400
4200
4000
3800
3600
3400
3200
3000
2800
2600
2400
0 Ft
5000 Ft
10000 Ft
15000 Ft
20000 Ft

Figure 5-11

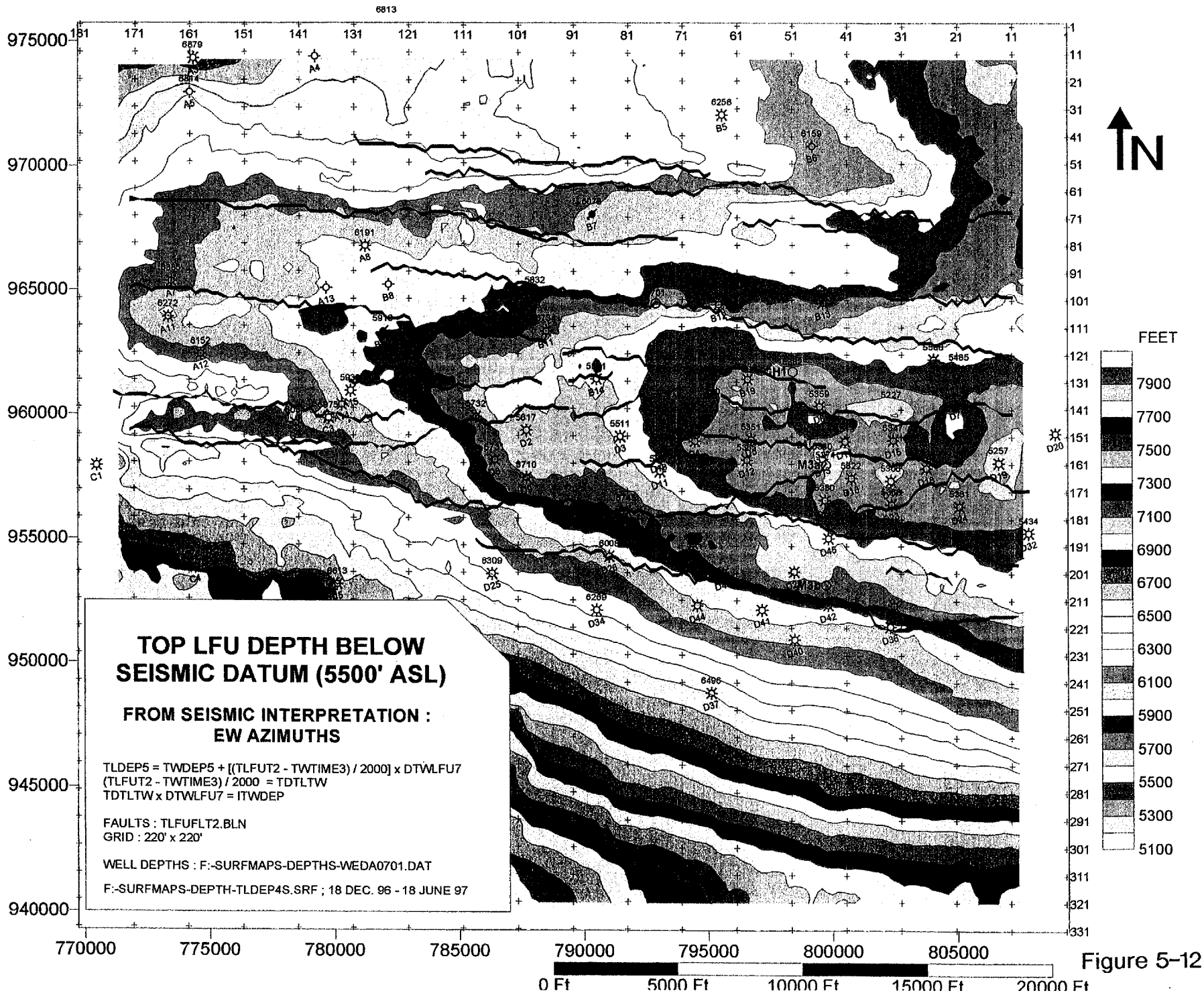
TOP LFU DEPTH BELOW
SEISMIC DATUM (5500' ASL)
FROM SEISMIC INTERPRETATION :
EW AZIMUTHS
TLDEP5 = TWDEP5 + [(TLFUT2 - TWTIME3) / 2000] x DTWLFU7
(TLFUT2 - TWTIME3) / 2000 = TDTLTW
TDTLTW x DTWLFU7 = ITWDEP
FAULTS : TLFUFLT2.BLN
GRID : 220' x 220'
WELL DEPTHS : F:-SURFMAPS-DEPTHS-WEDA0701.DAT
F:-SURFMAPS-DEPTH-TLDEP4S.SRF ; 18 DEC. 96 - 18 JUNE 97
N
FEET
7900
7700
7500
7300
7100
6900
6700
6500
6300
6100
5900
5700
5500
5300
5100
975000
970000
965000
960000
955000
950000
945000
940000
770000
775000
780000
785000
790000
795000
800000
805000
0 Ft
5000 Ft
10000 Ft
15000 Ft
20000 Ft

Figure 5-12

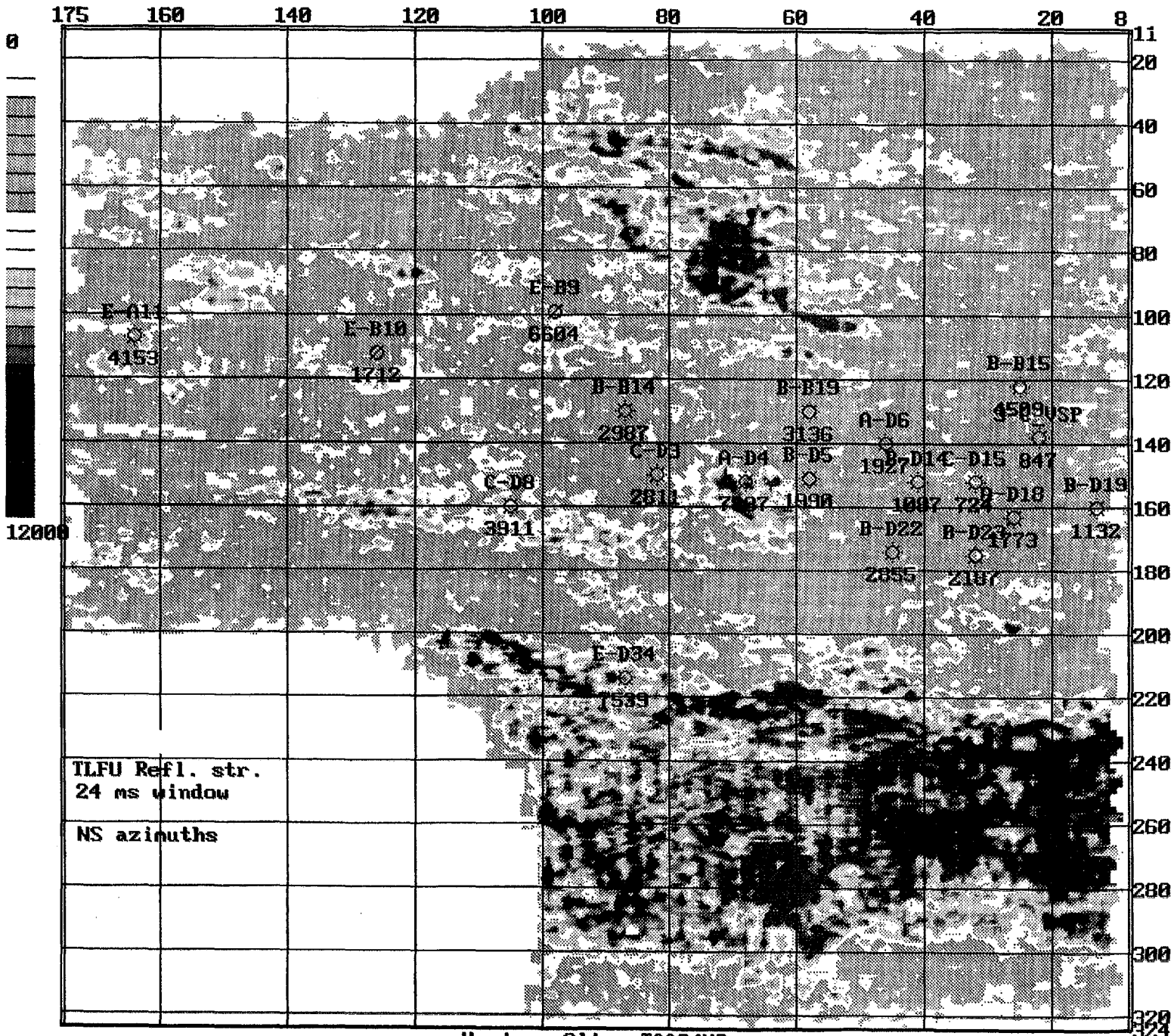
175
160
140
120
100
80
60
40
20
8
0
12000
E-A11
4153
E-B10
1712
E-B9
6604
B-B14
2987
B-B15
4509
B-B19
3136
A-D6
1927
USP
C-D3
2818
A-D4
B-D5
1990
C-D8
3911
C-D15
847
B-D18
724
B-D19
1132
B-D22
2855
B-D23
1773
2187
E-D34
7539
TLFU Refl. str.
24 ms window
NS azimuths
Horizon Slice TAA24NS
Project 5kmewrap

Figure 5-13

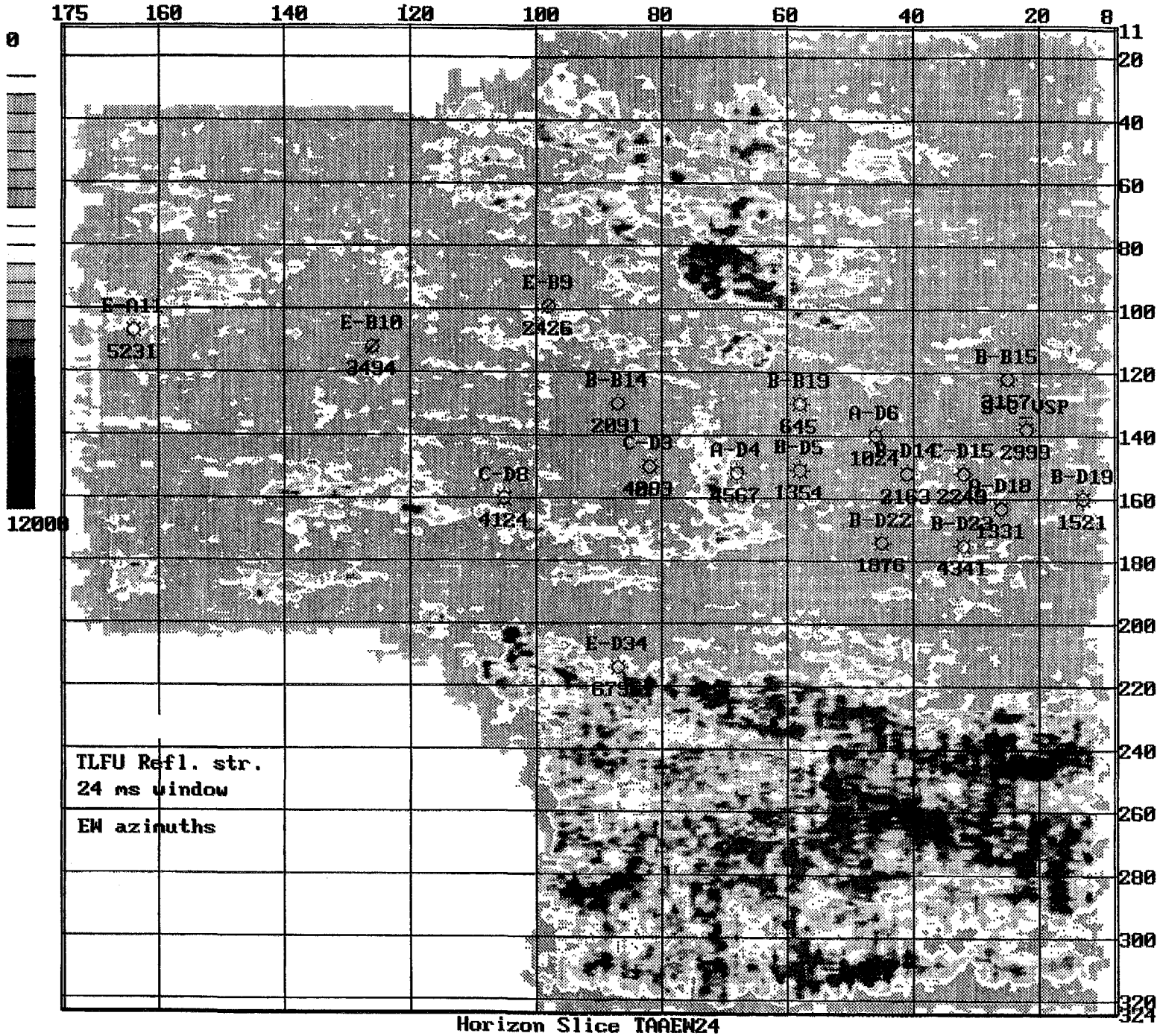
175
160
140
120
100
80
60
40
20
8
0
12000
11
20
40
60
80
100
120
140
160
180
200
220
240
260
280
300
320
324
E-A11
5231
E-B10
3494
E-B9
2426
B-B14
2091
B-B15
B-B19
645
A-D6
9167USP
C-D3
A-D4
B-D5
1024
C-D15 2999
C-D8
4124
4083
R567
1354
2103 2249
B-D18
B-D19
B-D22
B-D23
1331
1521
1876
4341
E-D34
TLFU Refl. str.
24 ms window
EW azimuths
Horizon Slice TAAEW24
Project 5kmewrap

Figure 5-14

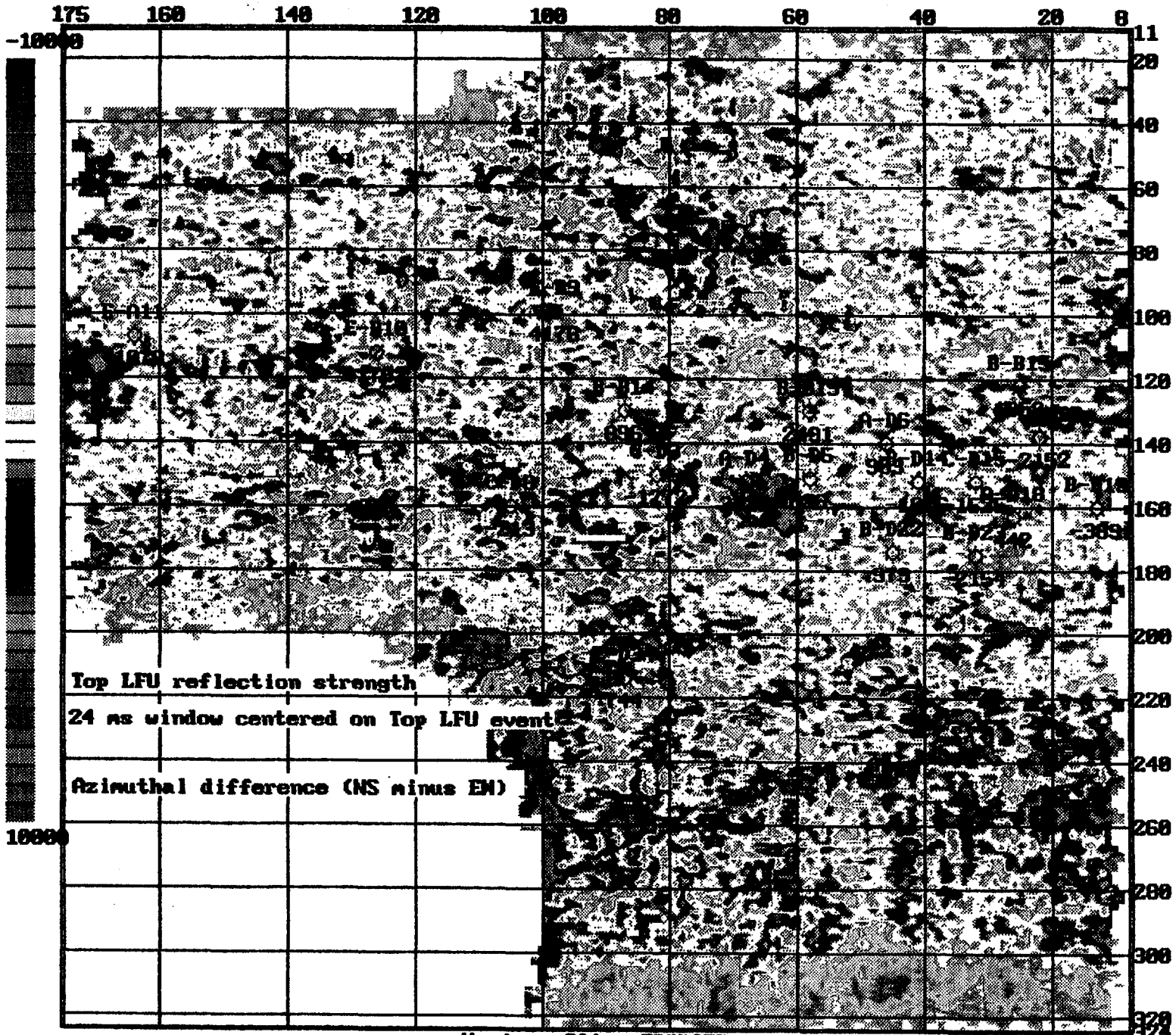
175
160
140
120
100
80
60
40
20
0
11
20
40
60
80
100
120
140
160
180
200
220
240
260
280
300
320
324
Top LFU reflection strength
24 ms window centered on Top LFU event
Azimuthal difference (NS minus EW)
Horizon Slice TRSDIFF
Project Skmeurap

Figure 5-15

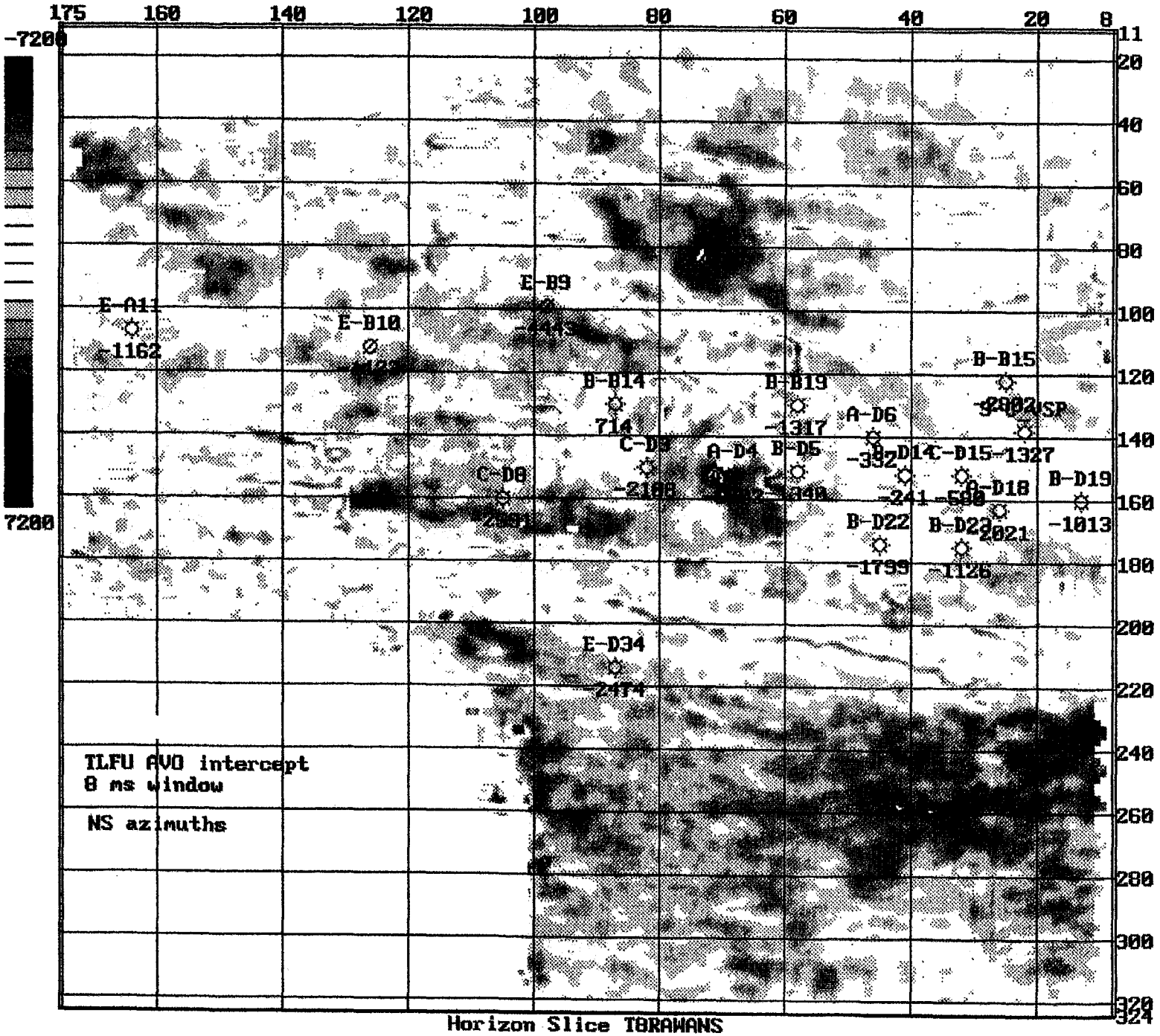
175
160
140
120
100
80
60
40
20
8
-7200
7200
11
20
40
60
80
100
120
140
160
180
200
220
240
260
280
300
320
324
E-A11
-1162
E-B10
E-B9
B-B14
714
B-B19
-1317
B-B15
A-D6
C-D3
A-D4
B-D5
C-D8
-2108
-332
D14
C-D15
-1327
B-D18
B-D19
-241
-1013
B-D22
B-D23
2021
-1799
-1126
E-D34
2474
TLFU AVO intercept
8 ms window
NS azimuths
Horizon Slice TBRAWANS
Project yintew

Figure 5-16

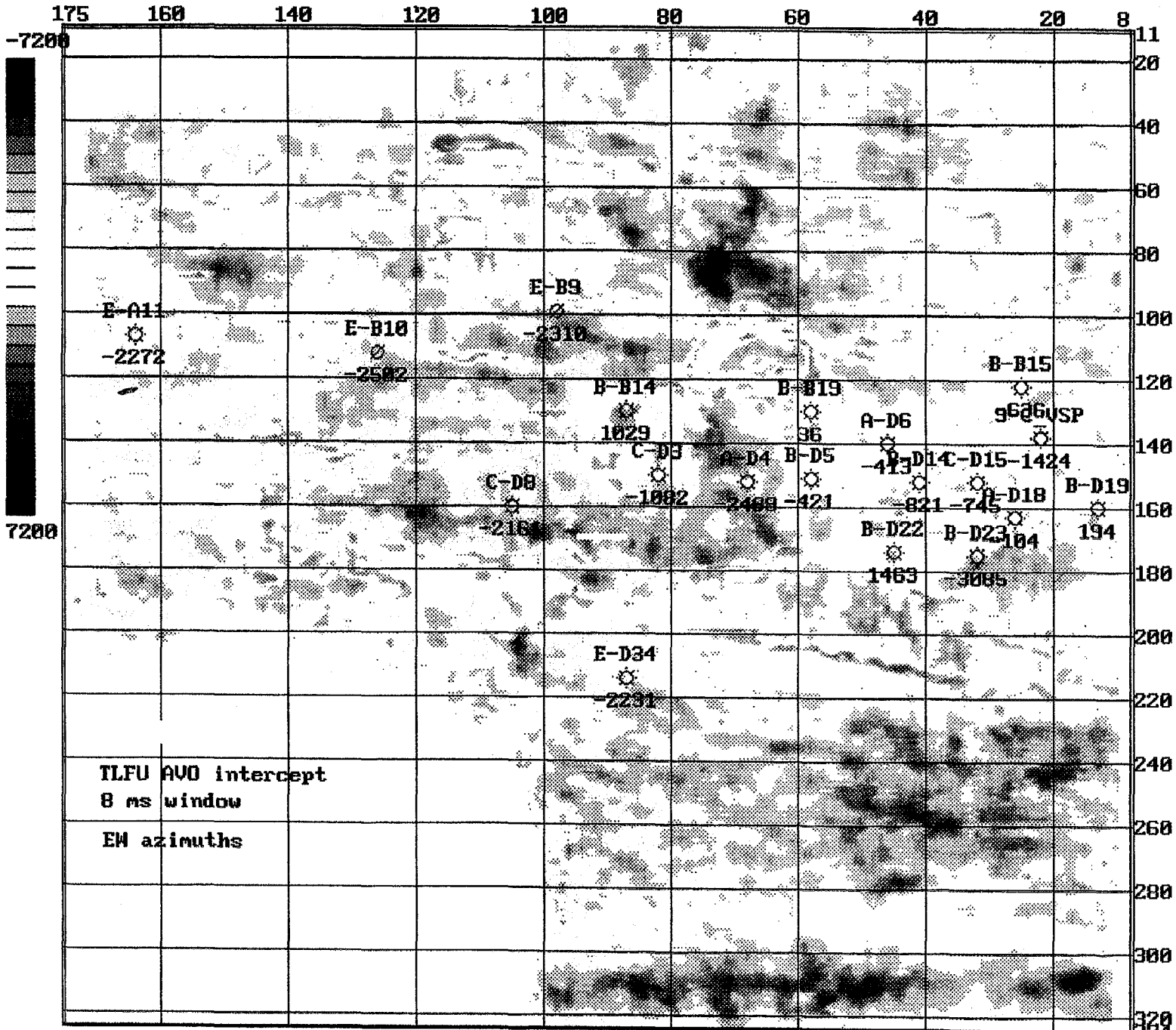
175
160
140
120
100
80
60
40
20
8
-7200
7200
11
20
40
60
80
100
120
140
160
180
200
220
240
260
280
300
320
324
E-A11
-2272
E-B10
-2502
E-B9
-2310
B-B14
1029
C-D3
-1002
C-D8
-2164
A-D4
2409
B-B19
36
B-D5
-421
A-D6
-413
B-B15
9636
USP
B-D14
-821
C-D15
-745
-1424
B-D18
104
B-D19
194
B-D22
1463
B-D23
-3085
E-D34
-2231
TLFU AVO intercept
8 ms window
EW azimuths
Horizon Slice T8RAWAEW
Project yintew

Figure 5-17

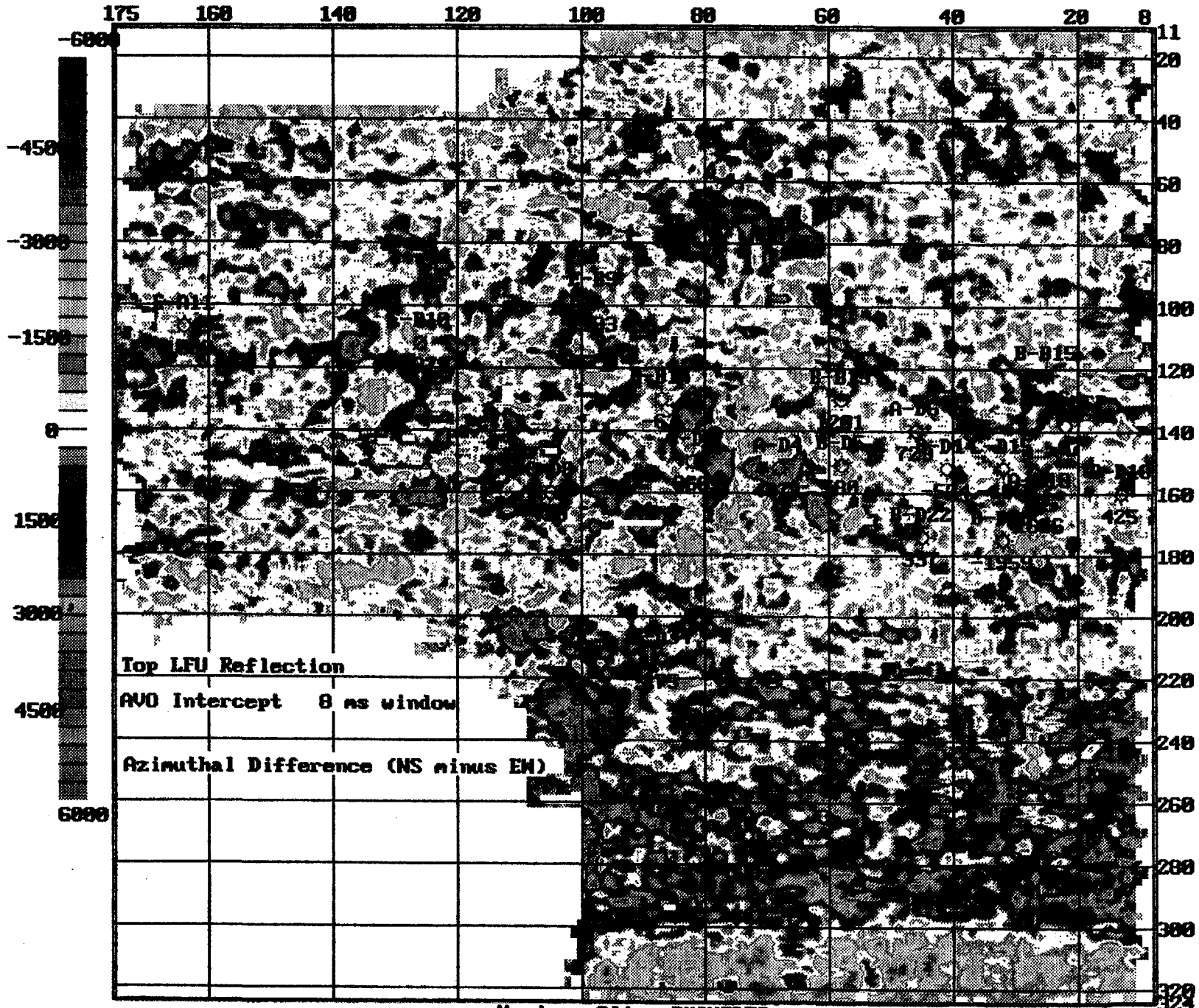
175
160
140
120
100
80
60
40
20
8
11
20
40
60
80
100
120
140
160
180
200
220
240
260
280
300
320
324
-6000
-4500
-3000
-1500
0
1500
3000
4500
6000
Top LFU Reflection
AVO Intercept 8 ms window
Azimuthal Difference (NS minus EW)
Horizon Slice TYINTDF8
Project yintew

Figure 5-18

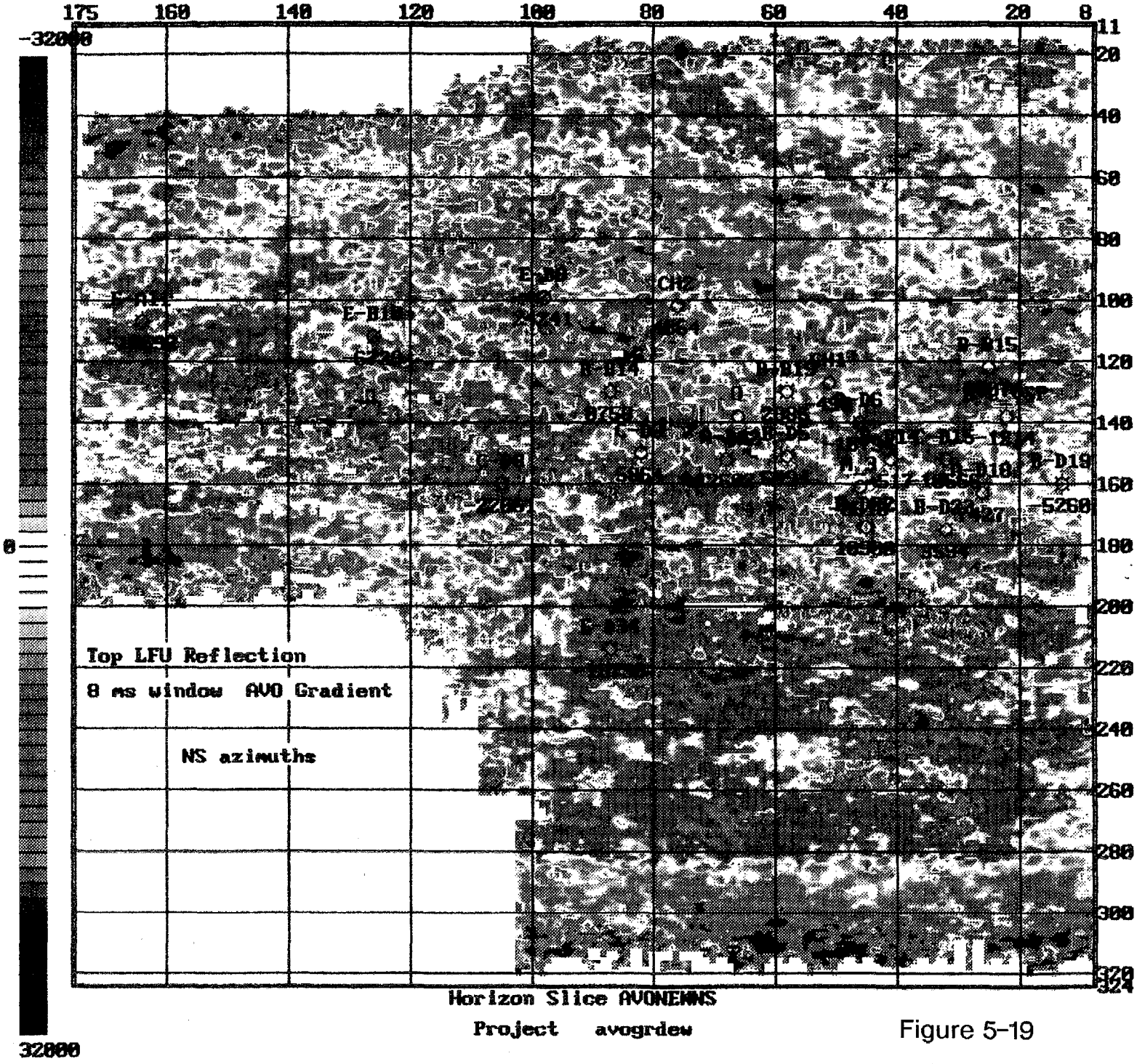
175
160
140
120
100
80
60
40
20
8
-32000
11
20
40
60
80
100
120
140
160
180
200
220
240
260
280
300
320
324
0
32000
Top LFU Reflection
8 ms window AVO Gradient
NS azimuths
Horizon Slice AVONEWNS
Project avogridw

Figure 5-19

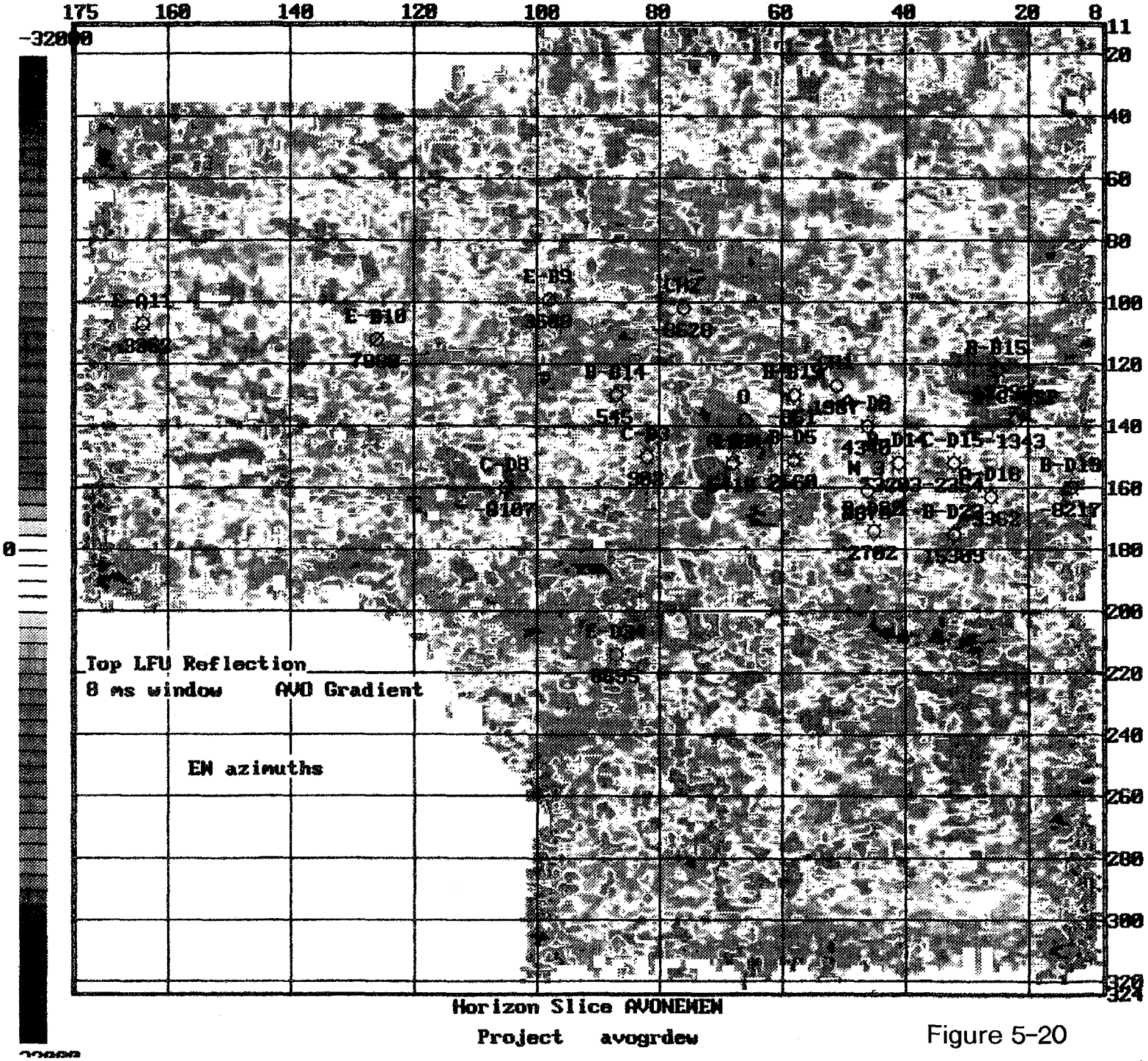
175
160
140
120
100
80
60
40
20
0
-32000
0
11
20
40
60
80
100
120
140
160
180
200
220
240
260
280
300
320
324
E-09
E-011
E-010
D-014
D-015
C-08
C-07
D-05
D-D8
D14
D-D19
Top LFU Reflection
8 ms window
AVO Gradient
EN azimuths
Horizon Slice AVONEMEN
Project avogrdew

Figure 5-20

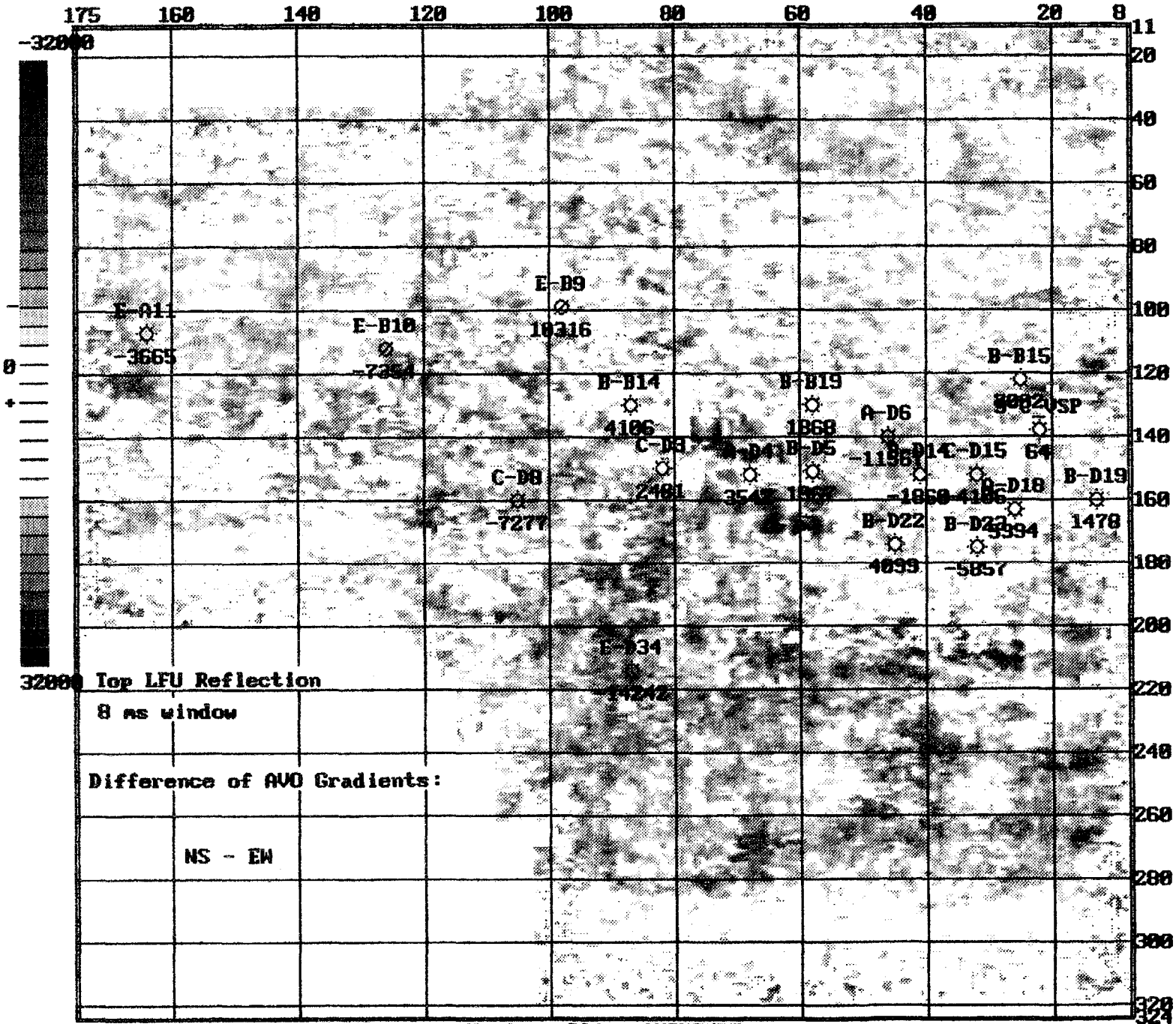

Horizon Slice AVONENDF

Project avogrdew

Figure 5-21

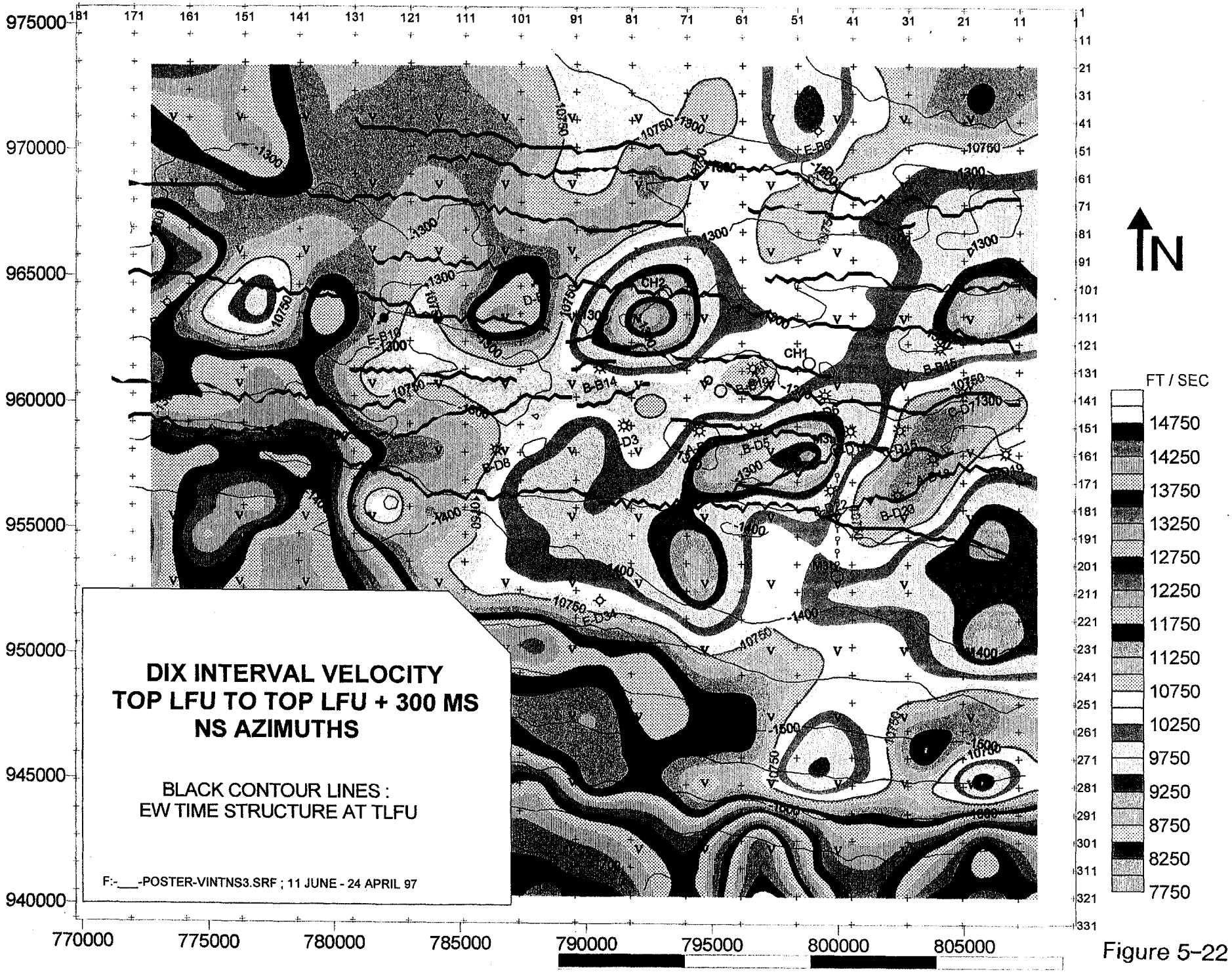
DIX INTERVAL VELOCITY
TOP LFU TO TOP LFU + 300 MS
NS AZIMUTHS
BLACK CONTOUR LINES :
EW TIME STRUCTURE AT TLFU
F:-___-POSTER-VINTNS3.SRF ; 11 JUNE - 24 APRIL 97
FT / SEC
14750
14250
13750
13250
12750
12250
11750
11250
10750
10250
9750
9250
8750
8250
7750
N
975000
970000
965000
960000
955000
950000
945000
940000
770000
775000
780000
785000
790000
795000
800000
805000

Figure 5-22

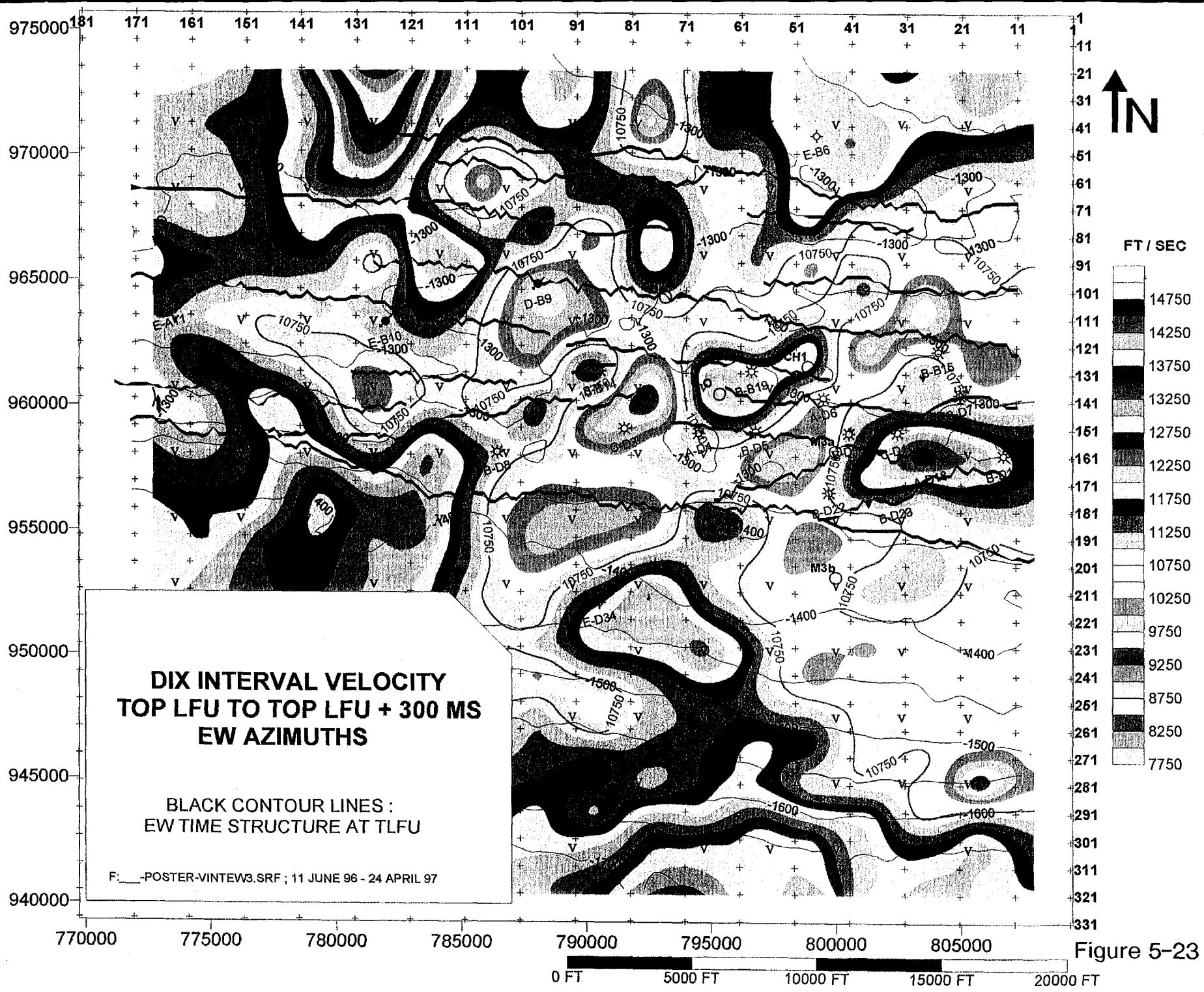
DIX INTERVAL VELOCITY
TOP LFU TO TOP LFU + 300 MS
EW AZIMUTHS
BLACK CONTOUR LINES :
EW TIME STRUCTURE AT TLFU
F:___-POSTER-VINTEW3.SRF ; 11 JUNE 96 - 24 APRIL 97
N
FT / SEC
14750
14250
13750
13250
12750
12250
11750
11250
10750
10250
9750
9250
8750
8250
7750
0 FT
5000 FT
10000 FT
15000 FT
20000 FT

Figure 5-23

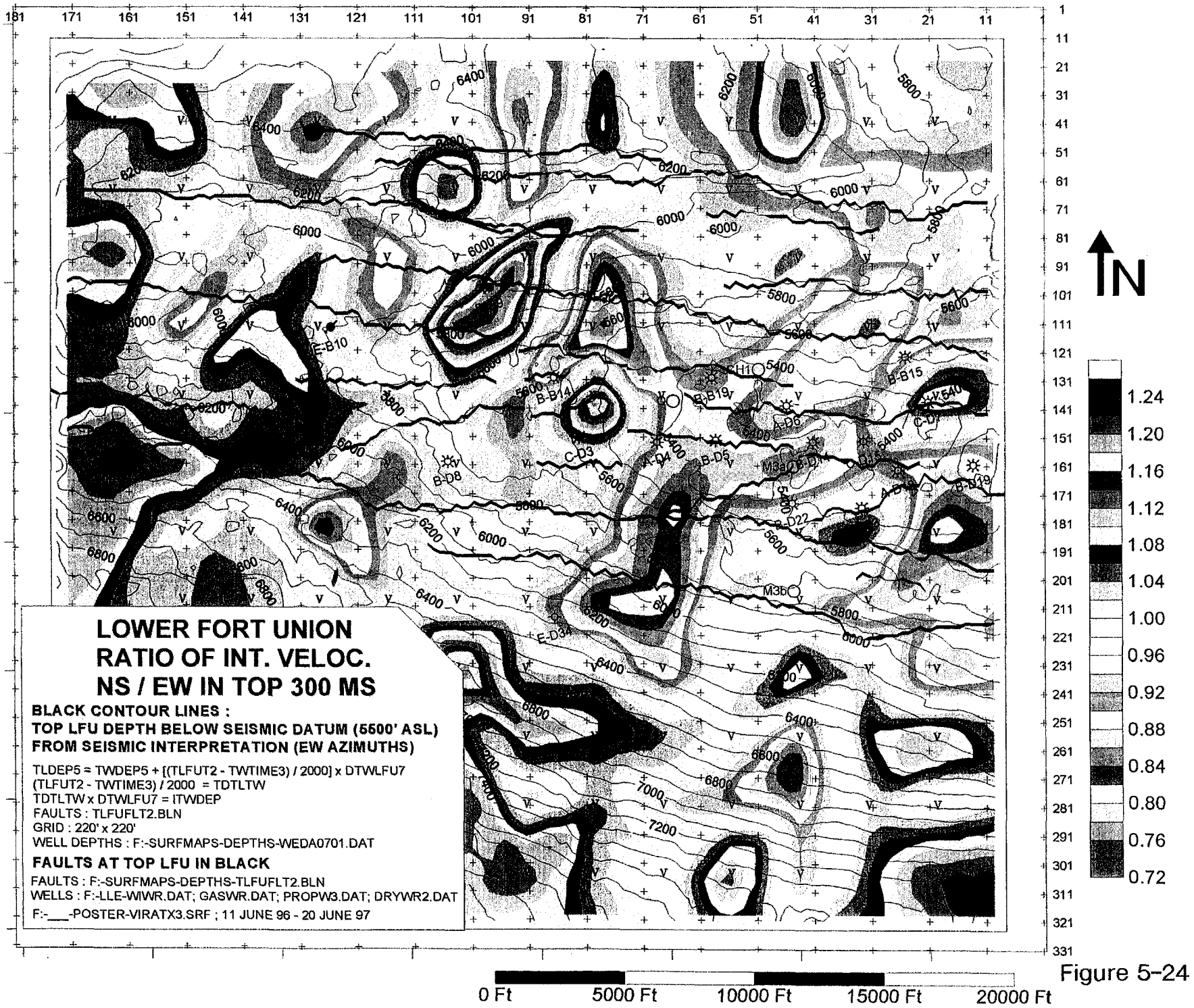
LOWER FORT UNION
RATIO OF INT. VELOC.
NS / EW IN TOP 300 MS
BLACK CONTOUR LINES :
TOP LFU DEPTH BELOW SEISMIC DATUM (5500' ASL)
FROM SEISMIC INTERPRETATION (EW AZIMUTHS)
TLDEP5 = TWDEP5 + [(TLFUT2 - TWTIME3) / 2000] x DTWLFU7
(TLFUT2 - TWTIME3) / 2000 = TDTLTW
TDTLTW x DTWLFU7 = ITWDEP
FAULTS : TLFUFLT2.BLN
GRID : 220' x 220'
WELL DEPTHS : F:-SURFMAPS-DEPTHS-WEDA0701.DAT
FAULTS AT TOP LFU IN BLACK
FAULTS : F:-SURFMAPS-DEPTHS-TLFUFLT2.BLN
WELLS : F:-LLE-WIWR.DAT; GASWR.DAT; PROPW3.DAT; DRYWR2.DAT
F:-___-POSTER-VIRATX3.SRF ; 11 JUNE 96 - 20 JUNE 97
N
1.24
1.20
1.16
1.12
1.08
1.04
1.00
0.96
0.92
0.88
0.84
0.80
0.76
0.72
0 Ft
5000 Ft
10000 Ft
15000 Ft
20000 Ft

Figure 5-24

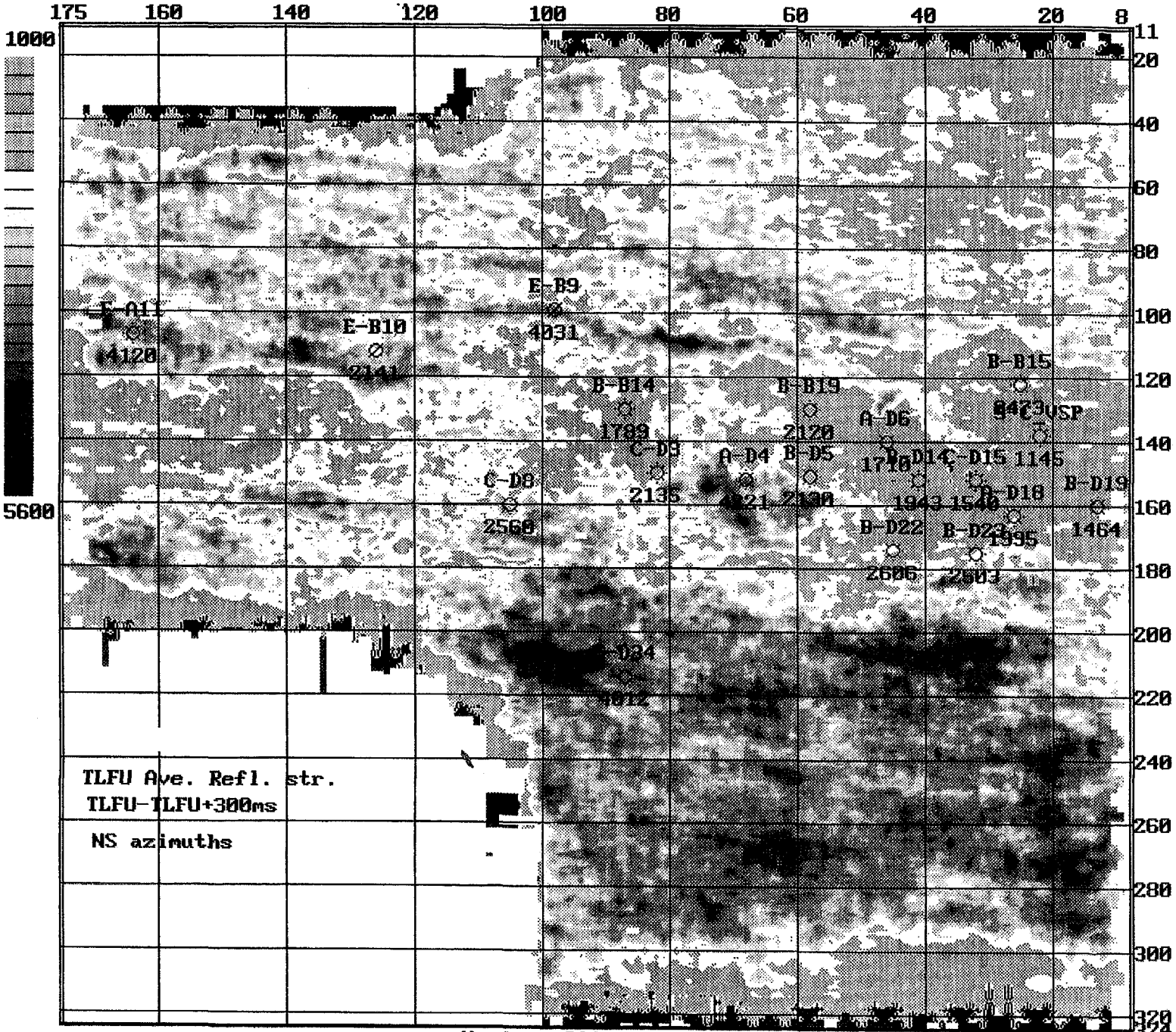
175
160
140
120
100
80
60
40
20
8
1000
5600
11
20
40
60
80
100
120
140
160
180
200
220
240
260
280
300
320
324
E-B9
4031
E-A11
4120
E-B10
2141
B-B14
1789
B-B19
2120
B-B15
A-D6
C-D9
A-D4
B-D5
C-D8
2135
2560
C-D15
1145
B-D19
B-D18
1943
1540
1464
B-D22
B-D23
1995
2606
2603
TLFU Ave. Refl. str.
TLFU-TLFU+300ms
NS azimuths
Horizon Slice 3RSNS5K
Project 5kmewrap

Figure 5-25

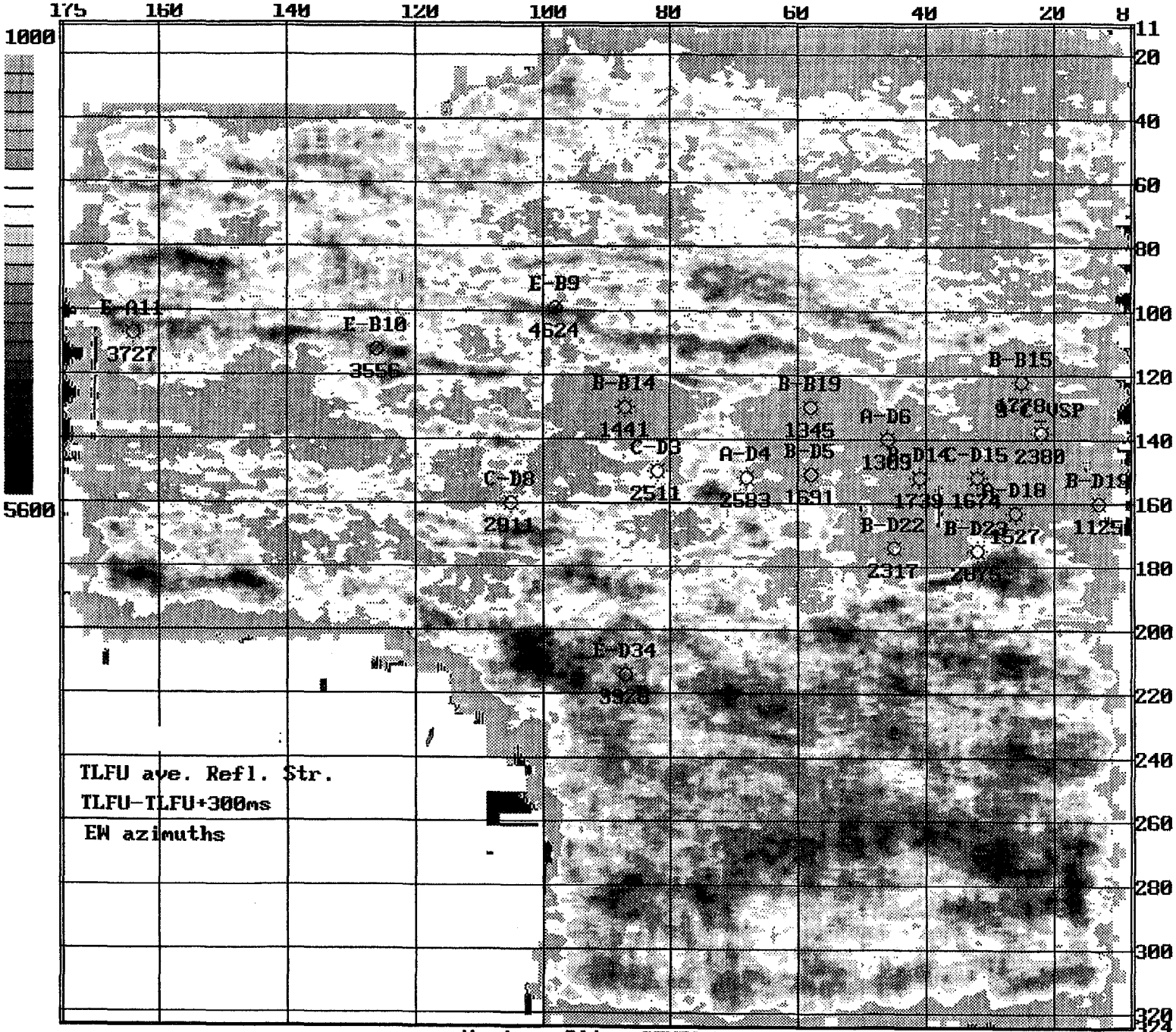

Horizon Slice 3EWRS5K

Project 5knewrap

Figure 5-26

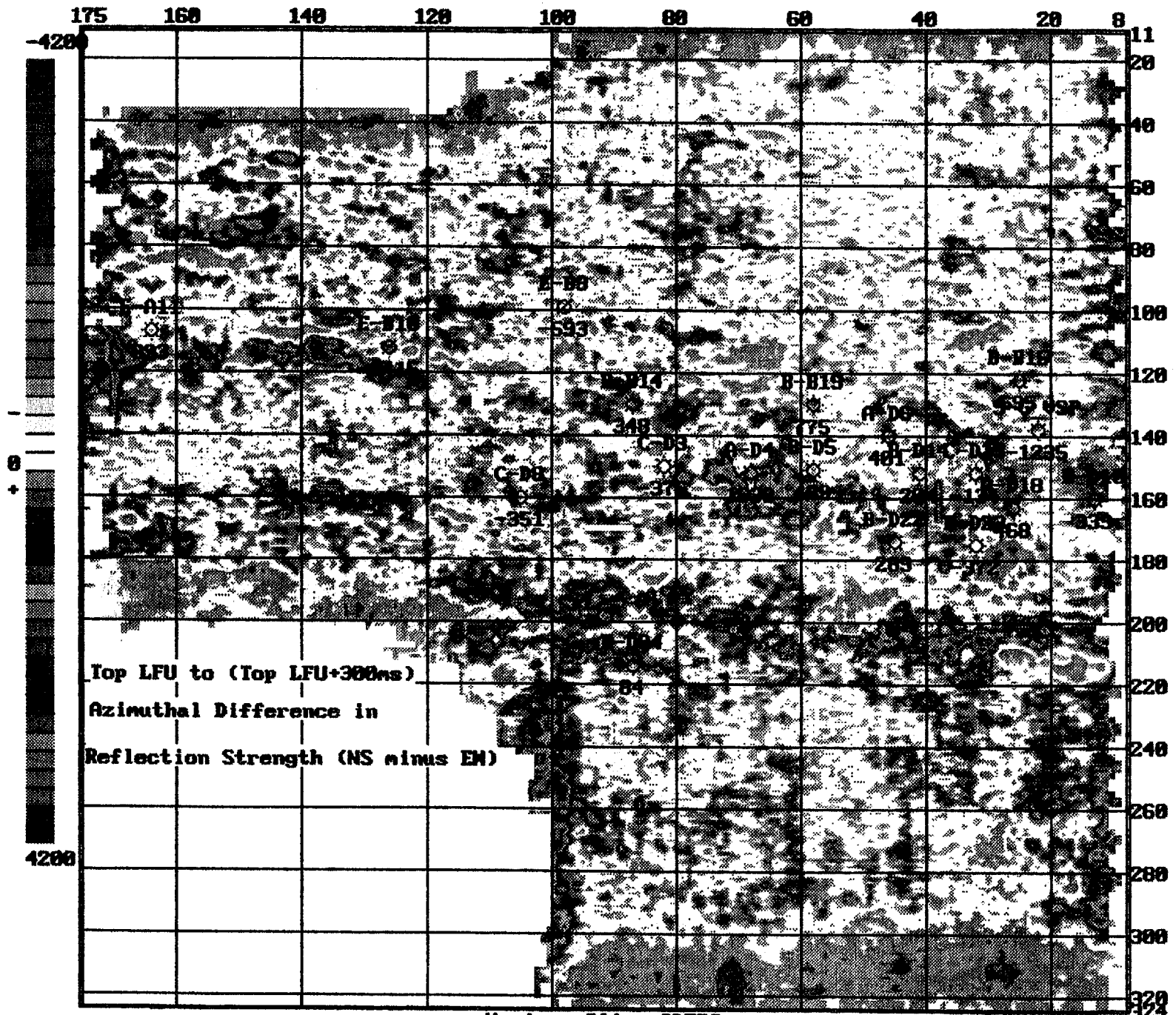
175
160
140
120
100
80
60
40
20
8
-4200
4200
0
Top LFU to (Top LFU+300ms)
Azimuthal Difference in
Reflection Strength (NS minus EM)
Horizon Slice 3DFRS
Project 5kneurap

Figure 5-27

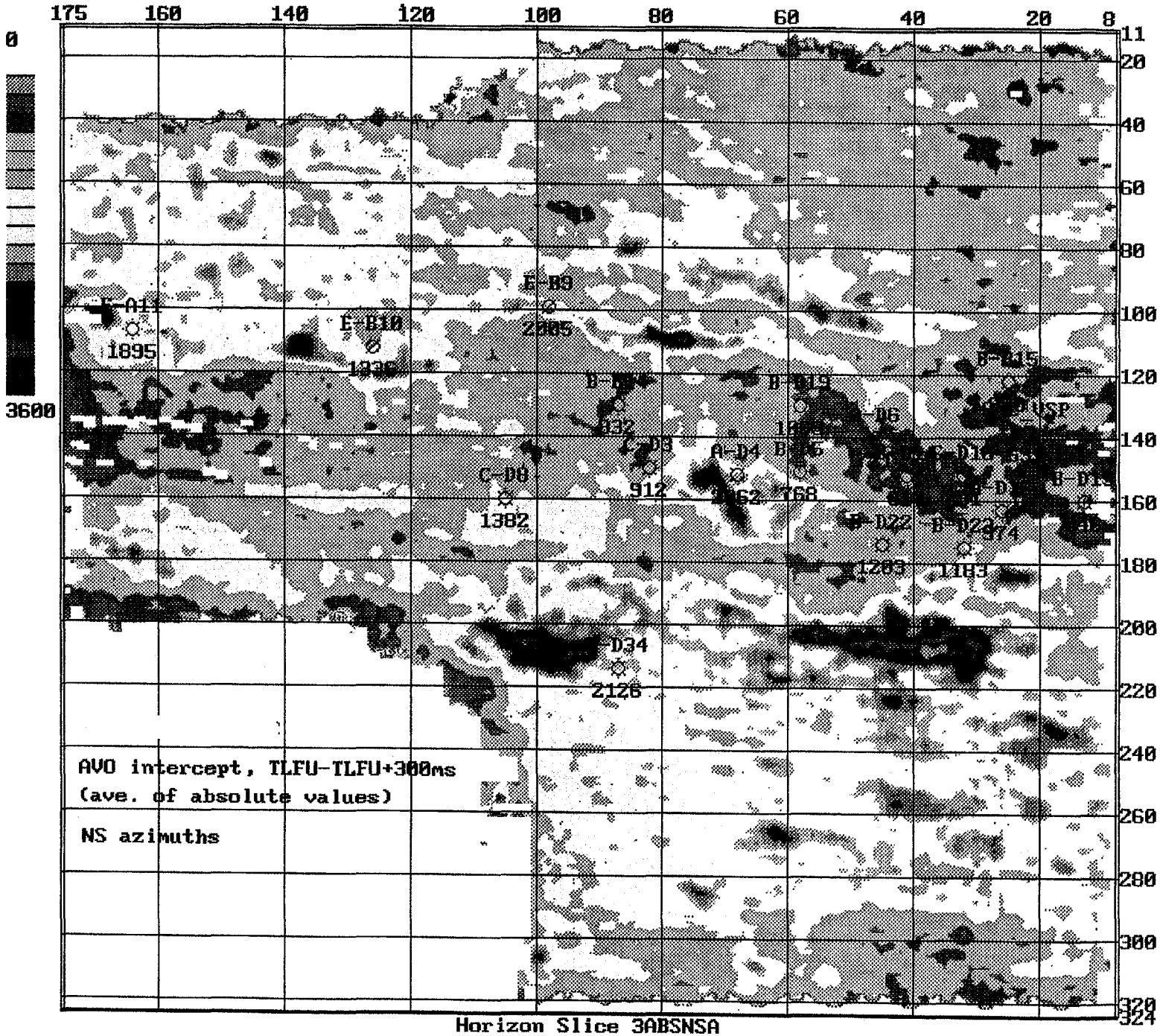
175
160
140
120
100
80
60
40
20
8
11
20
40
60
80
100
120
140
160
180
200
220
240
260
280
300
320
324
0
3600
E-A11
1895
E-B10
E-B9
2305
C-D8
1382
912
A-D4
D6
D34
2126
1203
1183
AVO intercept, TLFU-TLFU+300ms
(ave. of absolute values)
NS azimuths
Horizon Slice 3ABSNSA
Project yintew

Figure 5-28

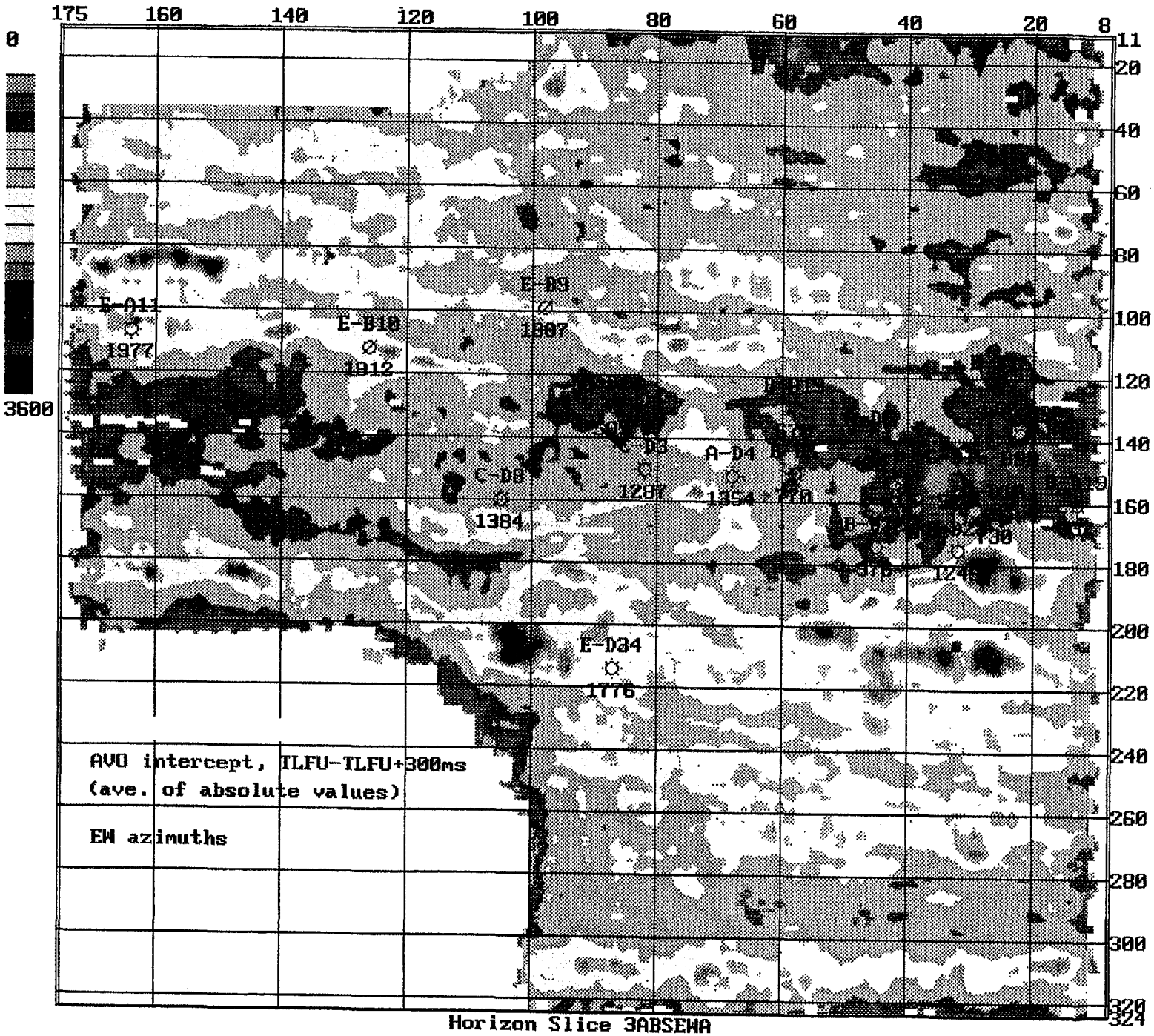
175
160
140
120
100
80
60
40
20
8
0
3600
11
20
40
60
80
100
120
140
160
180
200
220
240
260
280
300
320
324
E-A11
1977
E-B10
1912
E-B9
1907
C-D8
1384
A-D4
1354
E-D34
1776
AVO intercept, TLFU-TLFU+300ms
(ave. of absolute values)
EW azimuths
Horizon Slice 3ABSEWA
Project yintew

Figure 5-29

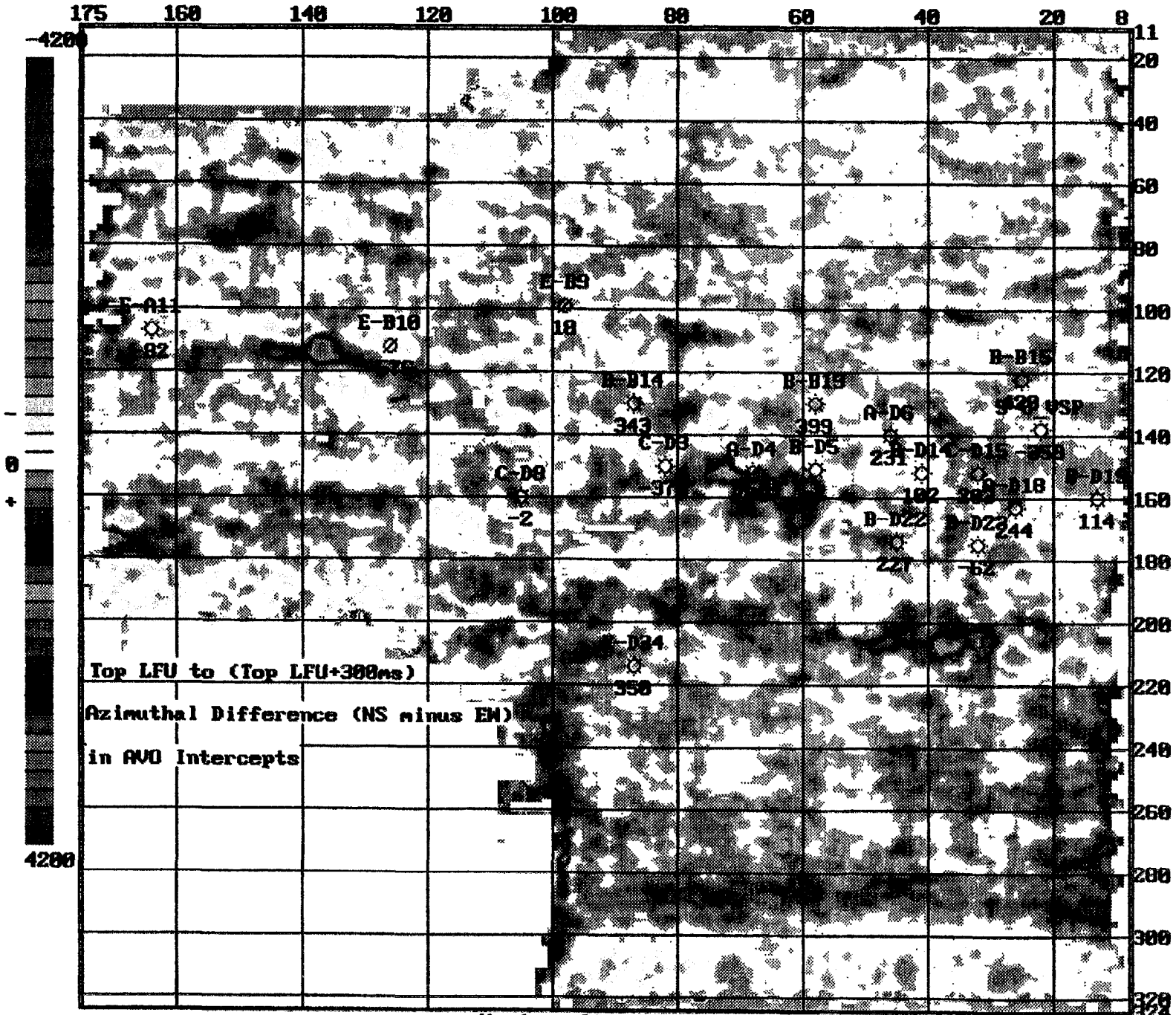
175
160
140
120
100
80
60
40
20
8
11
20
40
60
80
100
120
140
160
180
200
220
240
260
280
300
320
324
-4200
4200
0
+
E-A11
82
E-B10
Ø
E-B9
18
B-B14
343
B-B15
299
A-D6
231
C-D3
C-D8
-2
B-D14
102
B-D18
B-D22
221
244
114
B-D24
350
Top LFU to (Top LFU+300ms)
Azimuthal Difference (NS minus EW)
in AVO Intercepts
Horizon Slice 3DIFFA
Project yintew

Figure 5-30

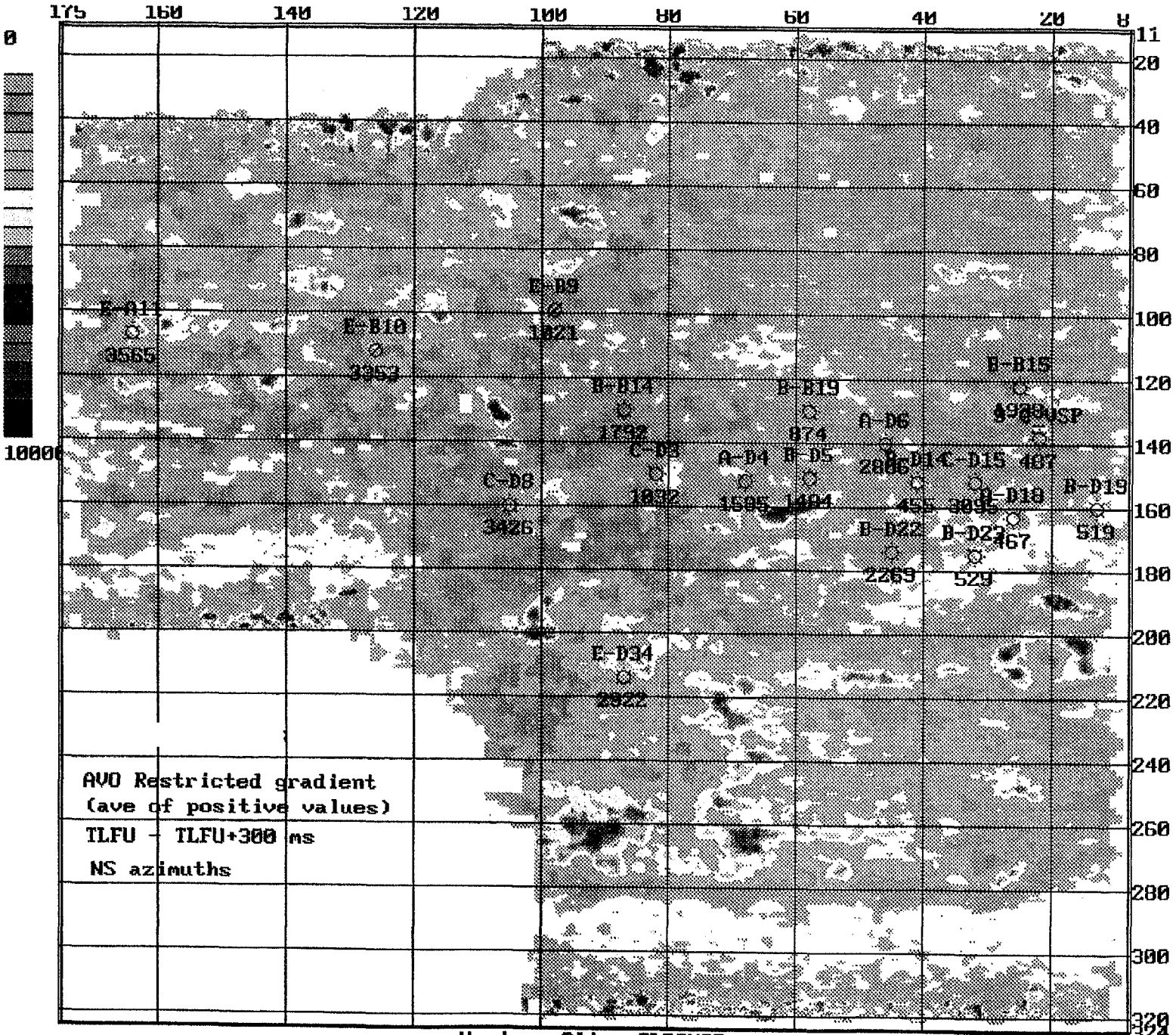
175
160
140
120
100
80
60
40
20
8
0
1000
11
20
40
60
80
100
120
140
160
180
200
220
240
260
280
300
320
324
E-B11
9565
E-B10
3353
E-B9
1821
B-B14
1792
B-B19
874
A-D6
2806
B-B15
C-D3
1032
A-D4
1595
B-D5
1484
C-D14
C-D15
407
C-D8
3426
B-D18
B-D19
519
B-D22
2269
467
529
E-D34
2522
AVO Restricted gradient
(ave of positive values)
TLFU - TLFU+300 ms
NS azimuths
Horizon Slice TLRGN3P
Project avogrdew

Figure 5-31

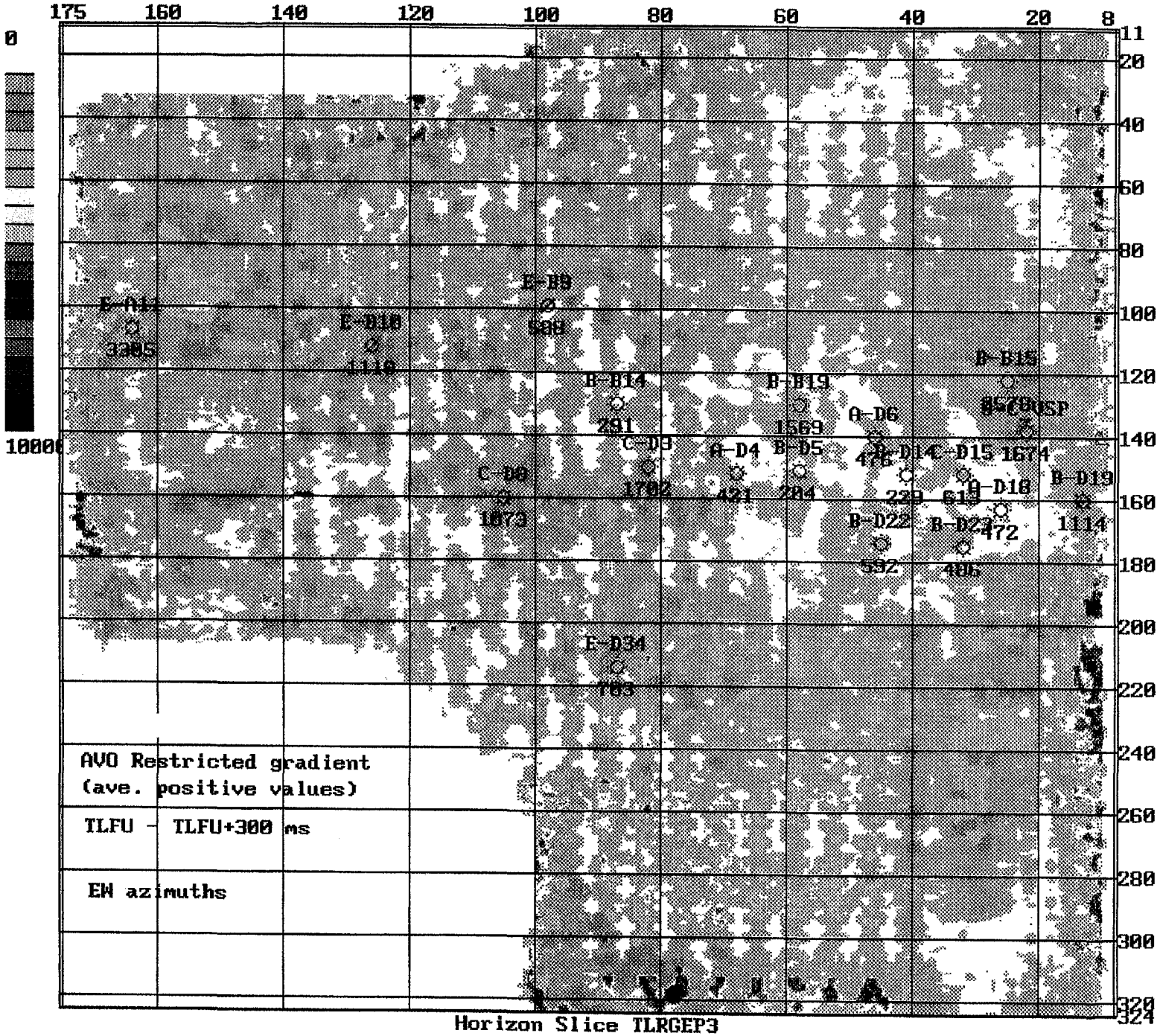
175
160
140
120
100
80
60
40
20
8
11
20
40
60
80
100
120
140
160
180
200
220
240
260
280
300
320
324
0
10000
E-A11
3285
E-B9
588
E-B10
1110
B-B14
291
B-B15
B-B19
1569
A-D6
C-D9
A-D4
B-D5
C-D8
1702
421
204
B-D14
C-D15
1674
B-D19
B-D10
B-D22
B-D23
472
1114
592
406
E-D34
703
AVO Restricted gradient
(ave. positive values)
TLFU - TLFU+300 ms
EW azimuths
Horizon Slice TLRGEP3
Project avogrdew

Figure 5-32

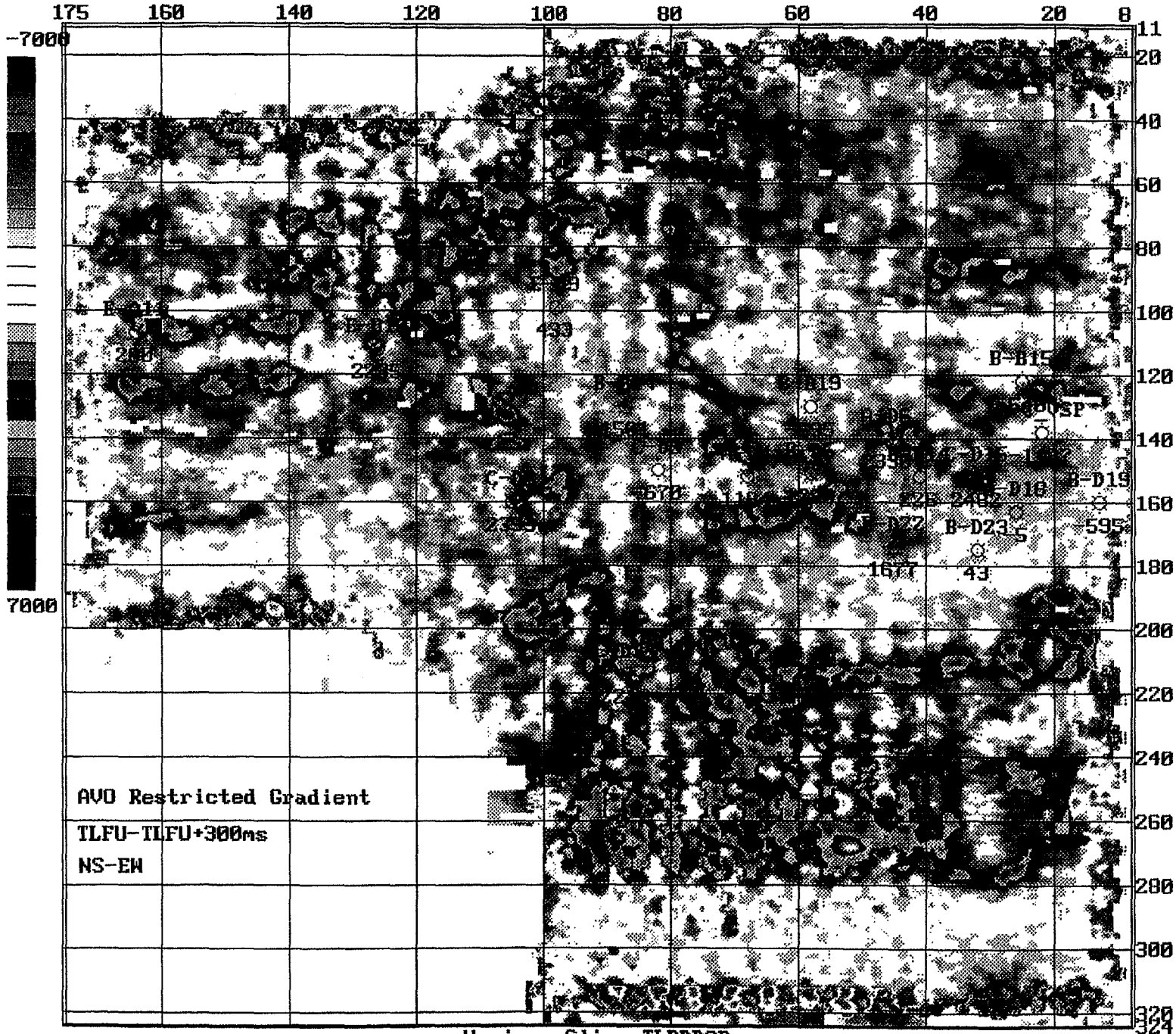
175
160
140
120
100
80
60
40
20
8
11
20
40
60
80
100
120
140
160
180
200
220
240
260
280
300
320
324
-7000
7000
B-B15
B-D19
B-D18
B-D19
B-D23
AVO Restricted Gradient
TLFU-TLFU+300ms
NS-EW
Horizon Slice TLRDD3P
Project avogrdew

Figure 5-33

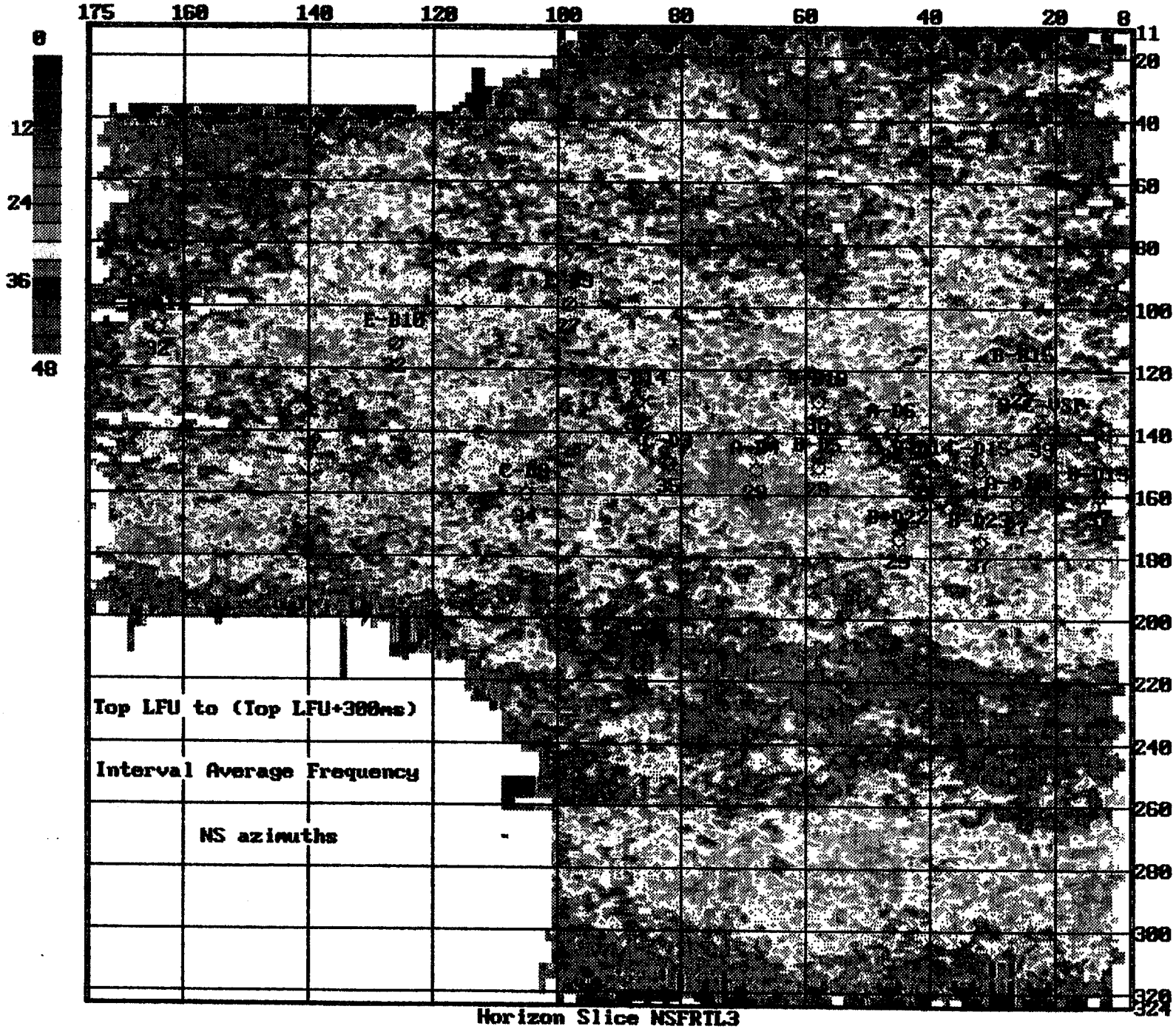
175
160
140
120
100
80
60
40
20
0
0
12
24
36
48
11
20
40
60
80
100
120
140
160
180
200
220
240
260
280
300
320
324
Top LFU to (Top LFU+300ms)
Interval Average Frequency
NS azimuths
Horizon Slice NSFRTL3
Project 5kneurap

Figure 5-34

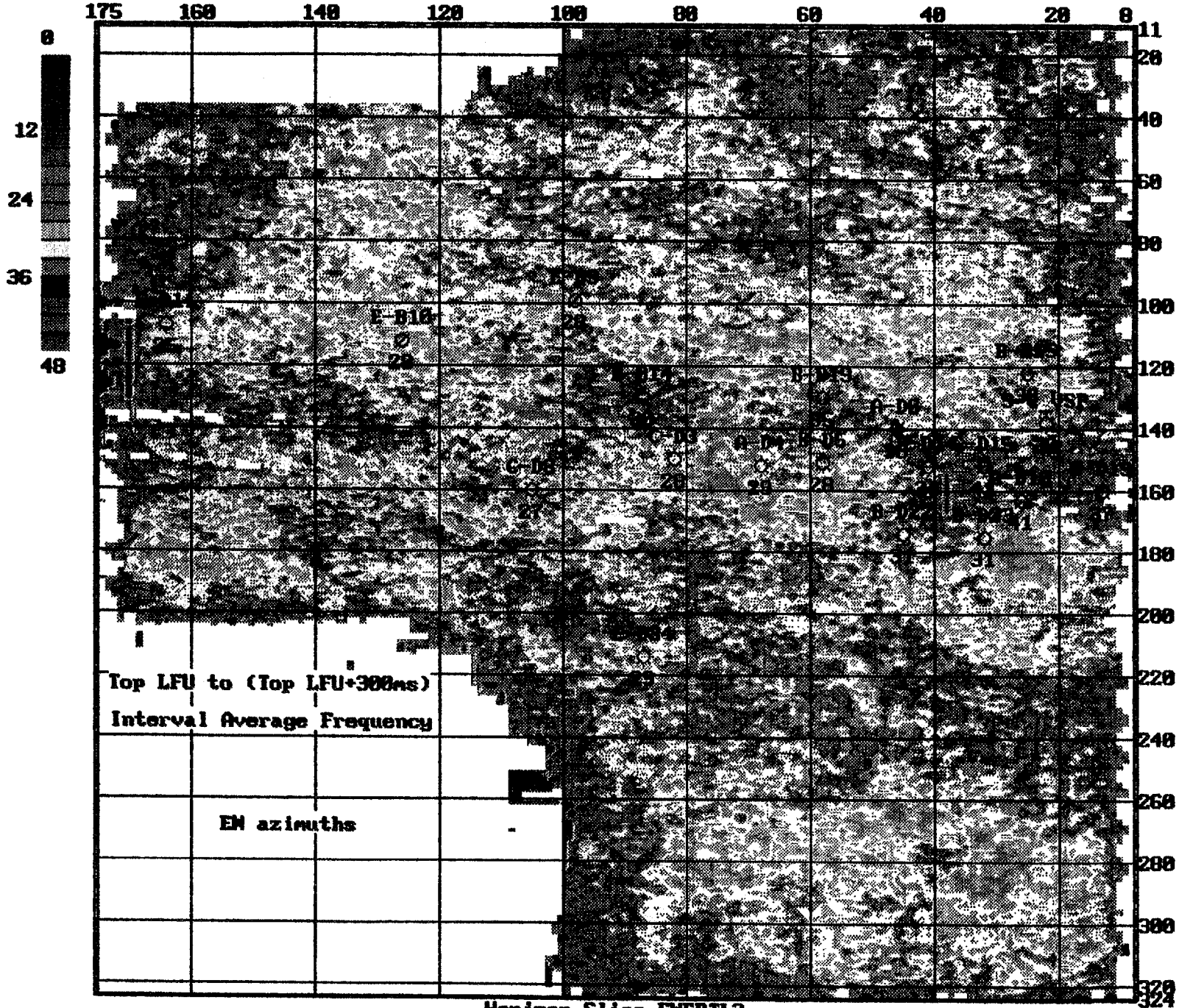

Horizon Slice EMFRTL3

Project Skneurap

Figure 5-35

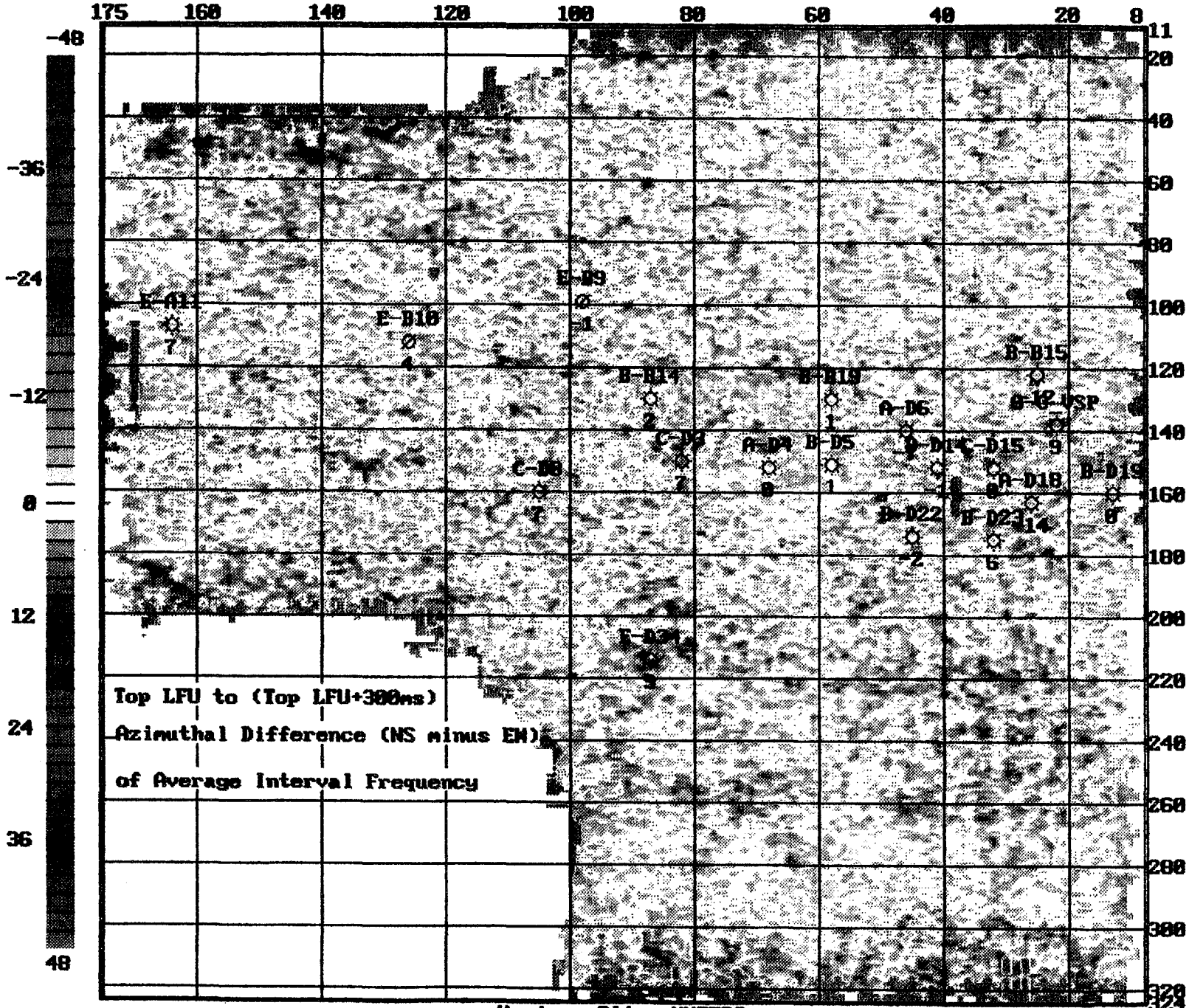

Horizon Slice NMEFR3

Project 5knewrap

Figure 5-36

Top LFU to (Top LFU+300 ms)

Interval Average Reflection Strength

(offsets to 5000 ft)

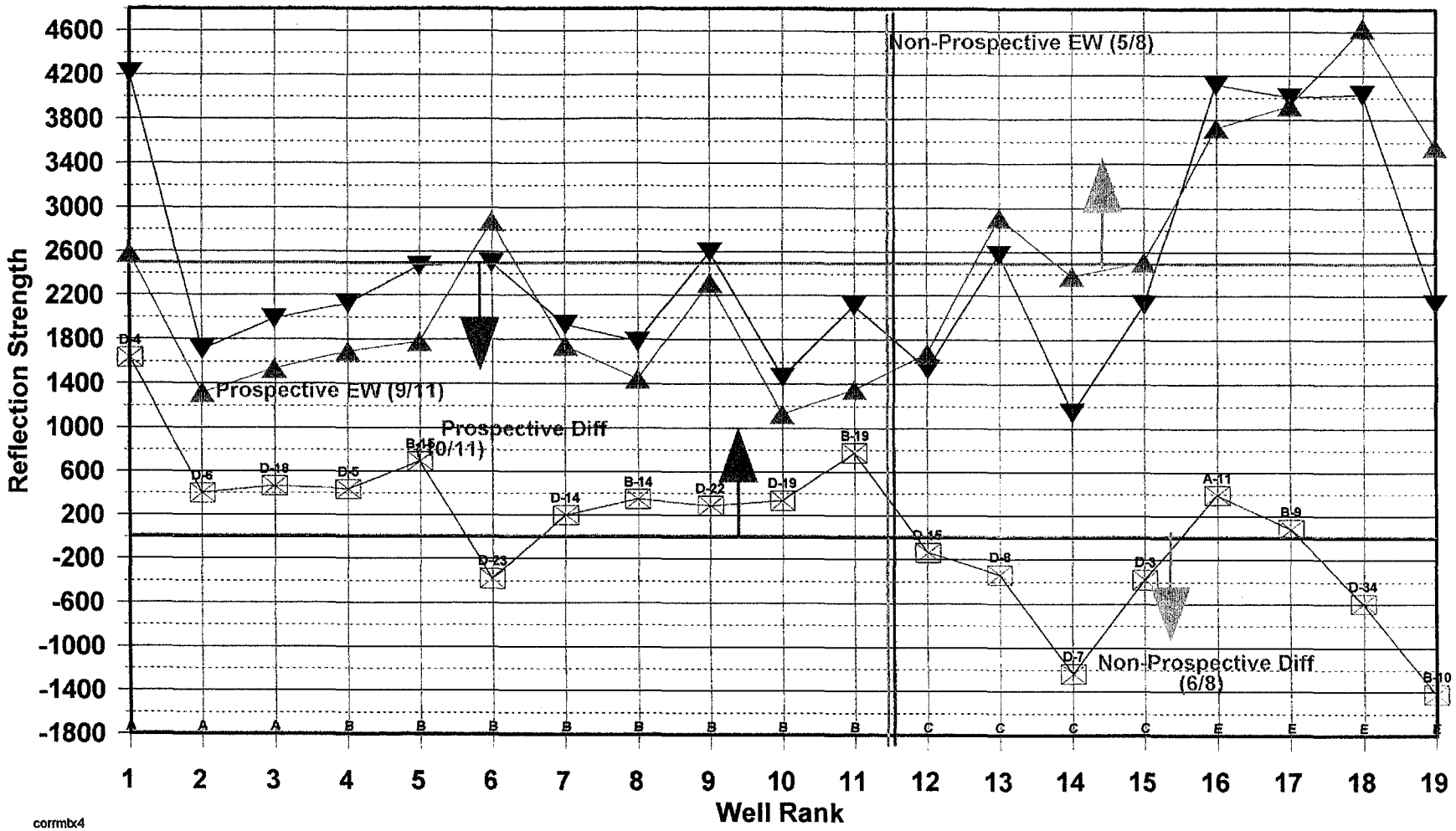

corrmbx4
22 May 1997

Figure 5-37

NS Refl. Str. (5K') EW Refl.Str. (5K') Difference (NS-EW): 5K'

Threshold for EW Refl. Str.

Threshold for Refl. Str. Diff.

Top LFU to (Top LFU+300ms)

Average Interval Frequency

0 to 5000 ft offsets

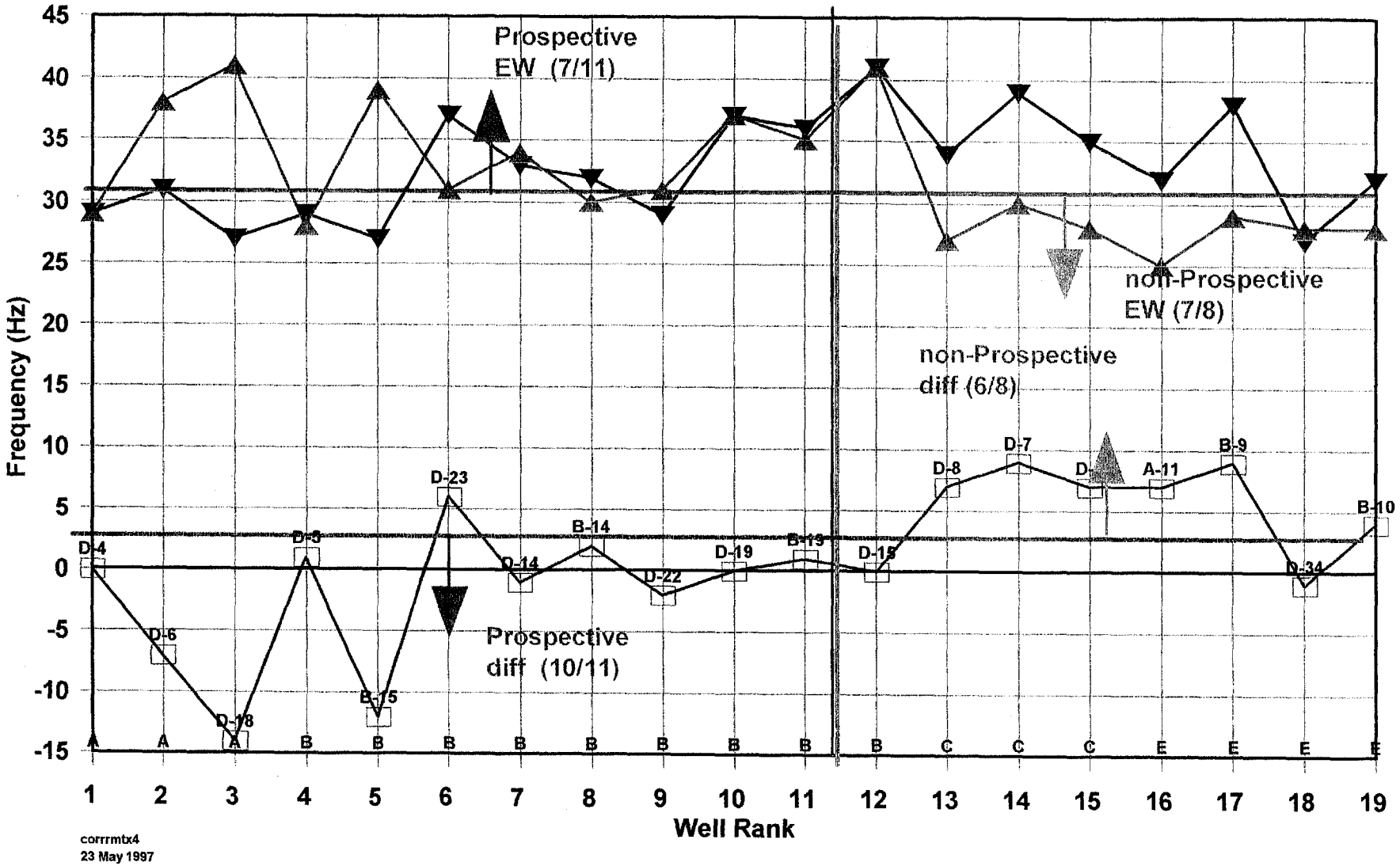

NS EW Difference (NS-EW)

Threshold for EW avg. frequency Threshold for avg. frequency difference

Figure 5-38

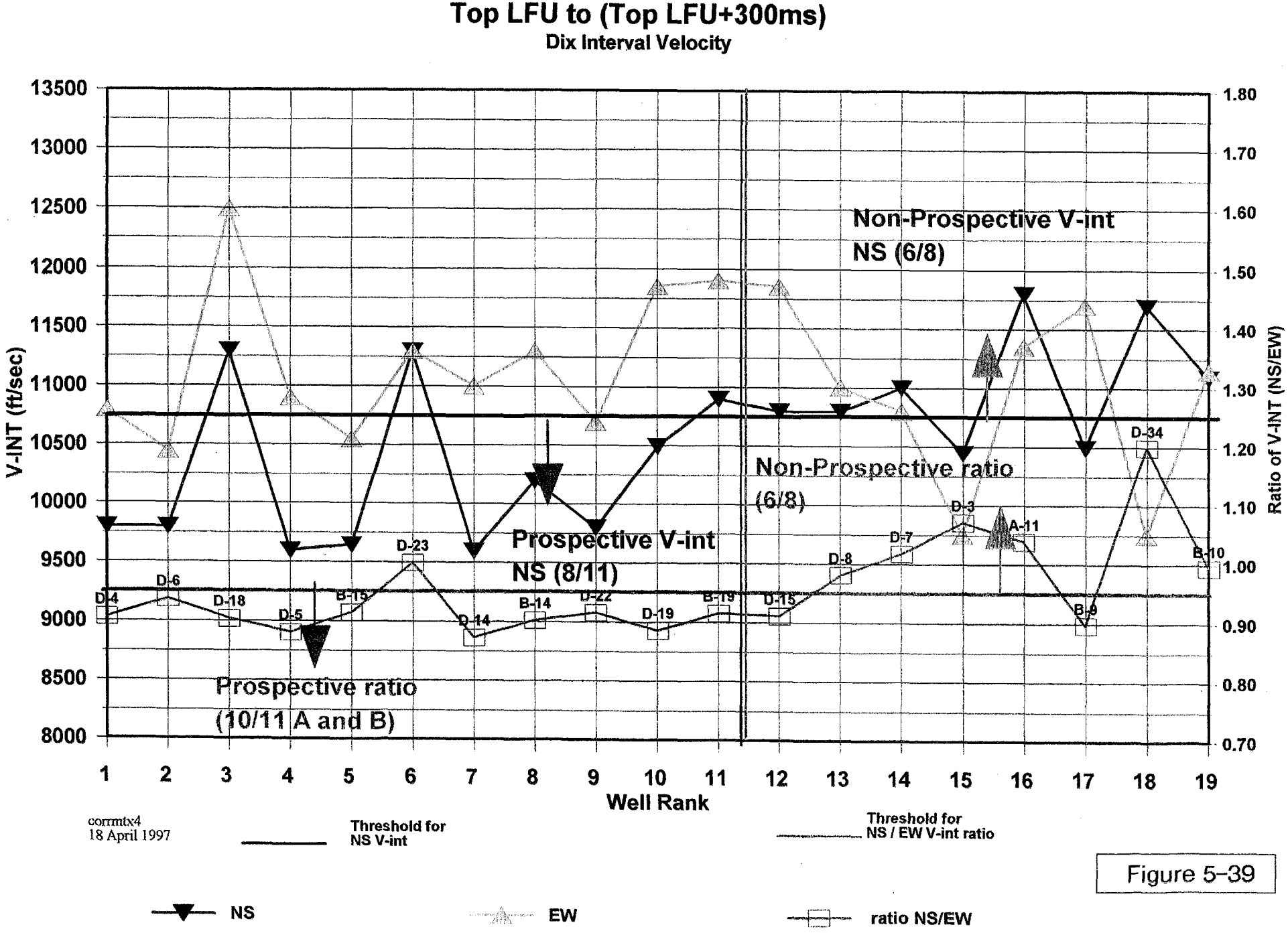
Top LFU to (Top LFU+300ms)
Dix Interval Velocity
V-INT (ft/sec)
Ratio of V-INT (NS/EW)
Well Rank
Non-Prospective V-int
NS (6/8)
Non-Prospective ratio
(6/8)
Prospective V-int
NS (8/11)
Prospective ratio
(10/11 A and B)
D-4
D-6
D-18
D-5
B-15
D-23
D-14
B-14
D-22
D-19
B-19
D-15
D-8
D-7
D-3
A-11
B-9
D-34
B-10
corrmtx4
18 April 1997
Threshold for
NS V-int
Threshold for
NS / EW V-int ratio
NS
EW
ratio NS/EW

Figure 5-39

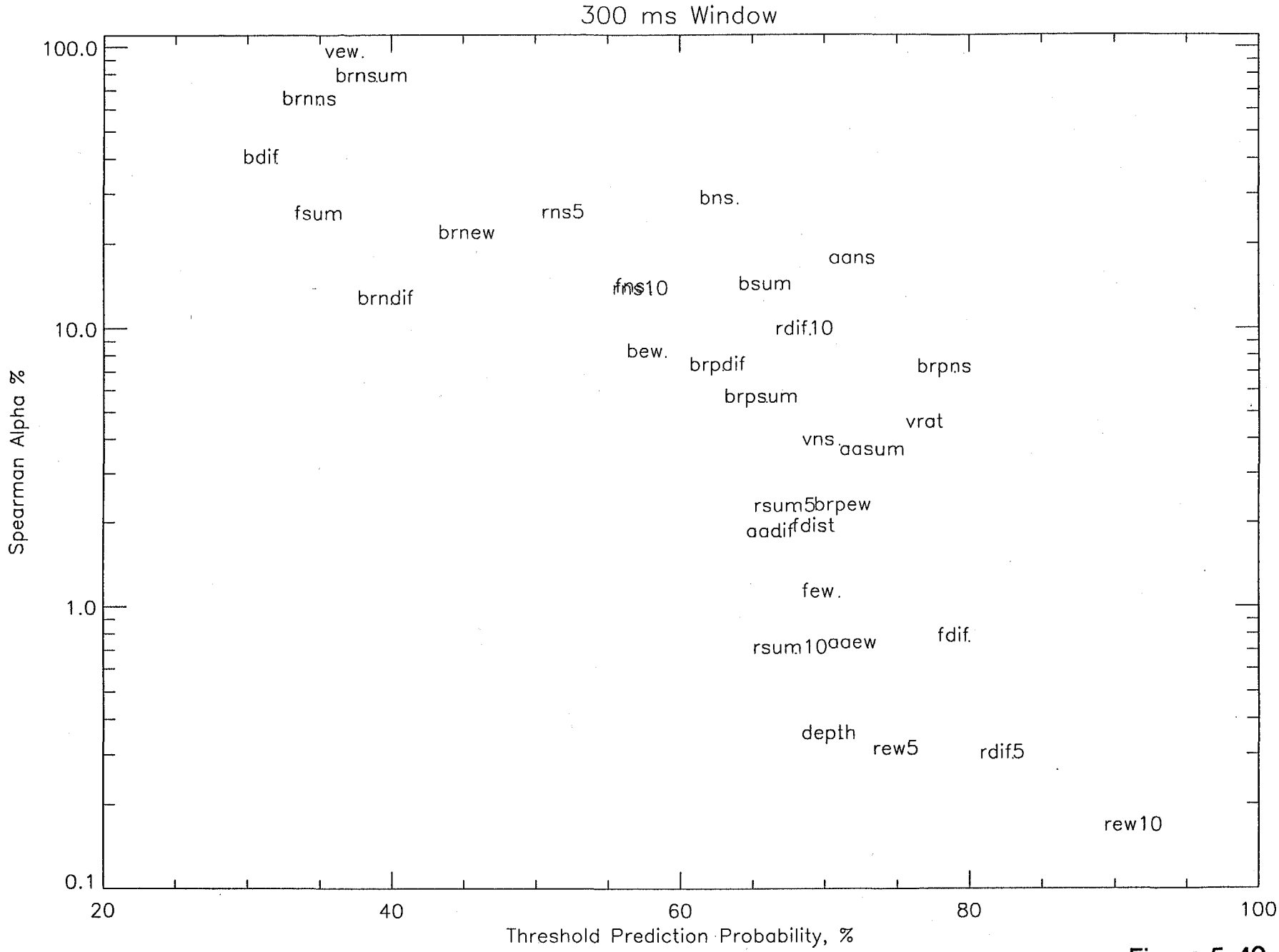
300 ms Window
100.0
10.0
1.0
0.1
Spearman Alpha %
20
40
60
80
100
Threshold Prediction Probability, %
vew.
brnsum
brnns
bdif
fsum
brnew
rns5
bns.
aans
fns10
bsum
brndif
rdif10
bew.
brpdif
brpns
brpsum
vrat
vns
aasum
rsum5
brpew
aadif
fdist
few.
fdif
rsum10
aaew
depth
rew5
rdif5
rew10

Figure 5-40

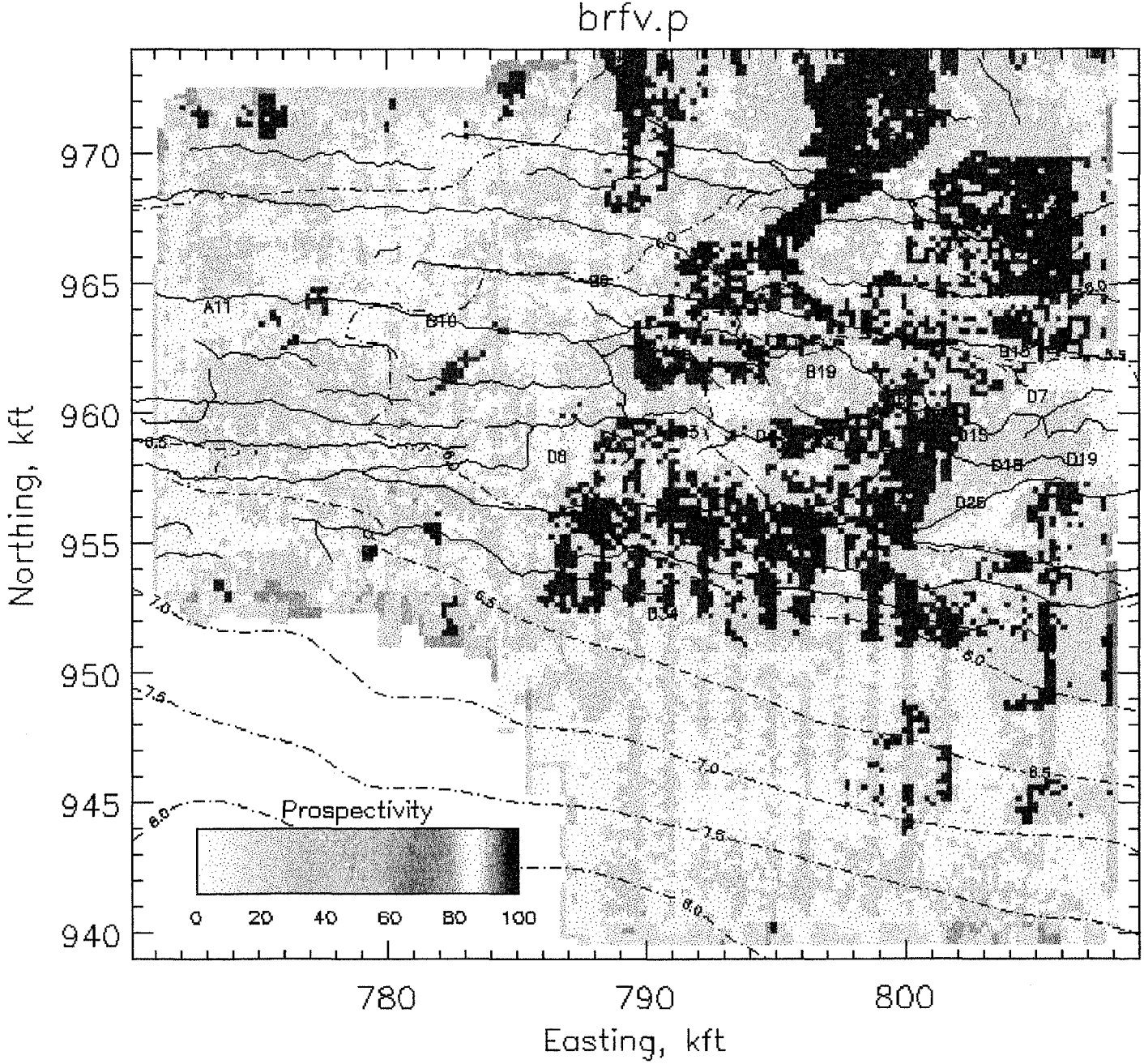

Fig. 5.41: Binomial Prospectivity using REW5,FEW,VNS

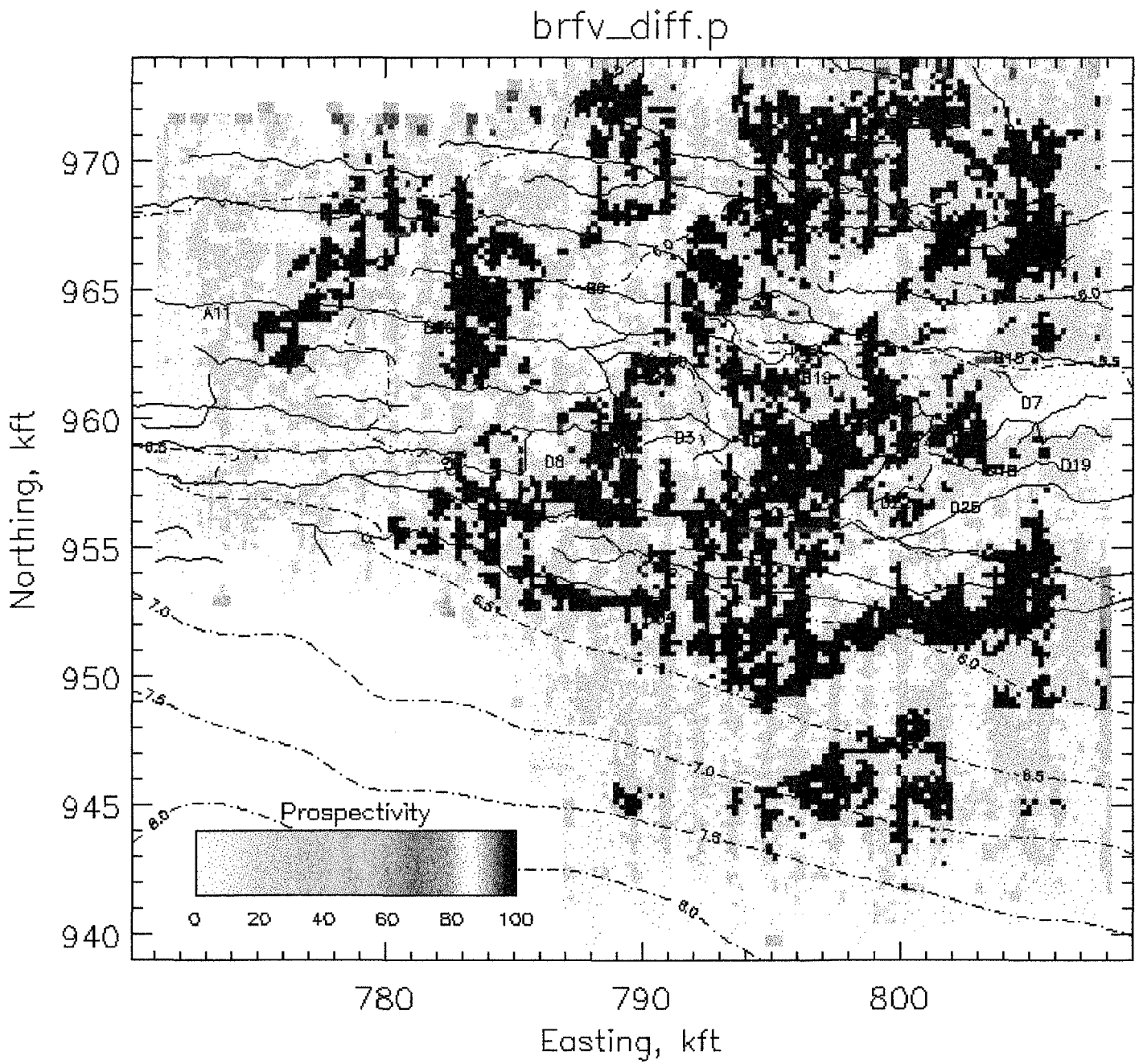

Fig. 5.42: Binomial Prospectivity using RDIF5,FDIF,VRAT

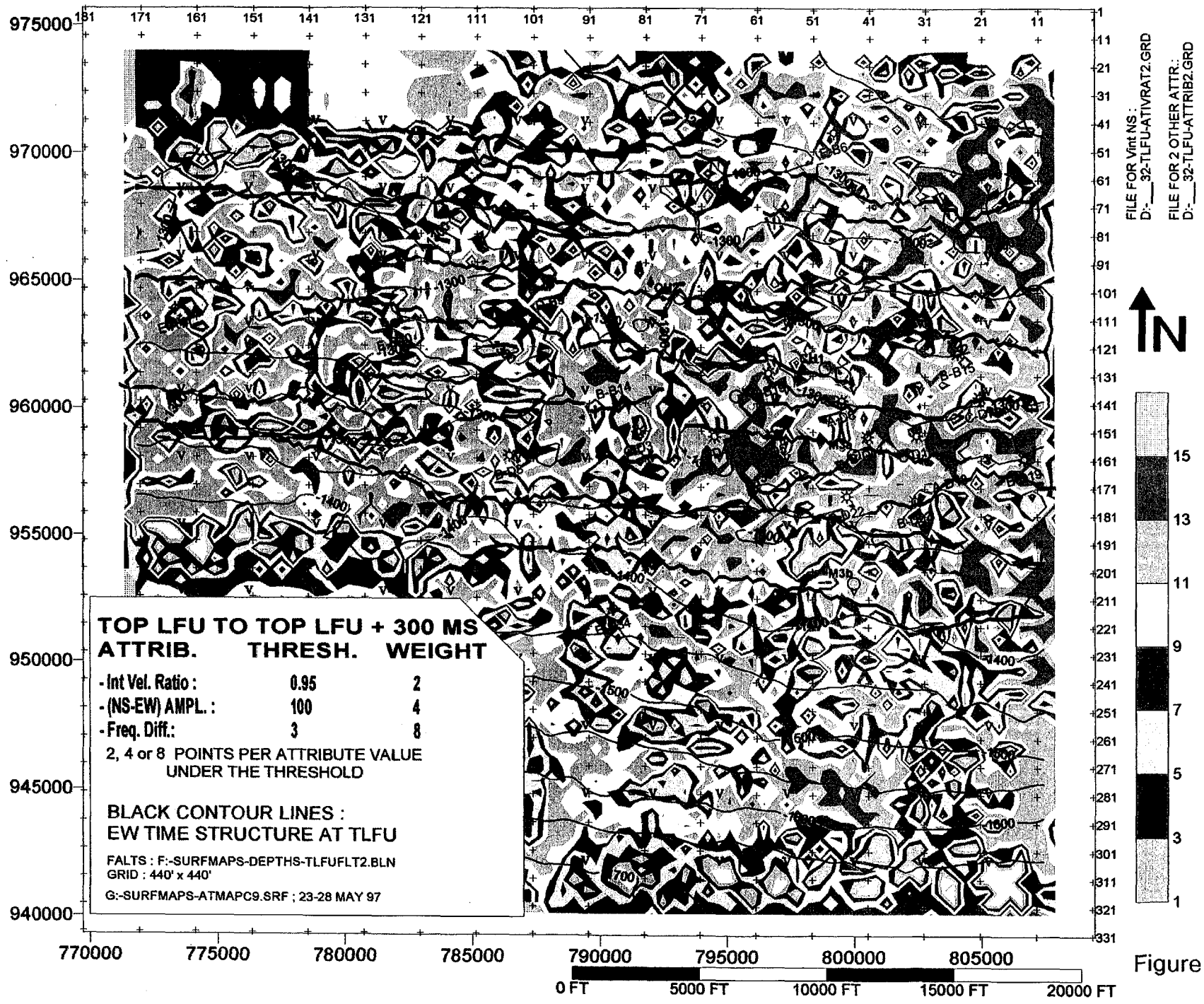
TOP LFU TO TOP LFU + 300 MS
ATTRIB. THRESH. WEIGHT
- Int Vel. Ratio : 0.95 2
- (NS-EW) AMPL. : 100 4
- Freq. Diff.: 3 8
2, 4 or 8 POINTS PER ATTRIBUTE VALUE UNDER THE THRESHOLD
BLACK CONTOUR LINES :
EW TIME STRUCTURE AT TLFU
FALTS : F:-SURFMAPS-DEPTHS-TLFUFLT2.BLN
GRID : 440' x 440'
G:-SURFMAPS-ATMAPC9.SRF ; 23-28 MAY 97
FILE FOR Vint NS :
D:-__32-TLFU-ATIVRAT2.GRD
FILE FOR 2 OTHER ATTR.:
D:-__32-TLFU-ATTRIB2.GRD
N
15
13
11
9
7
5
3
1
0 FT
5000 FT
10000 FT
15000 FT
20000 FT

Figure 5-43

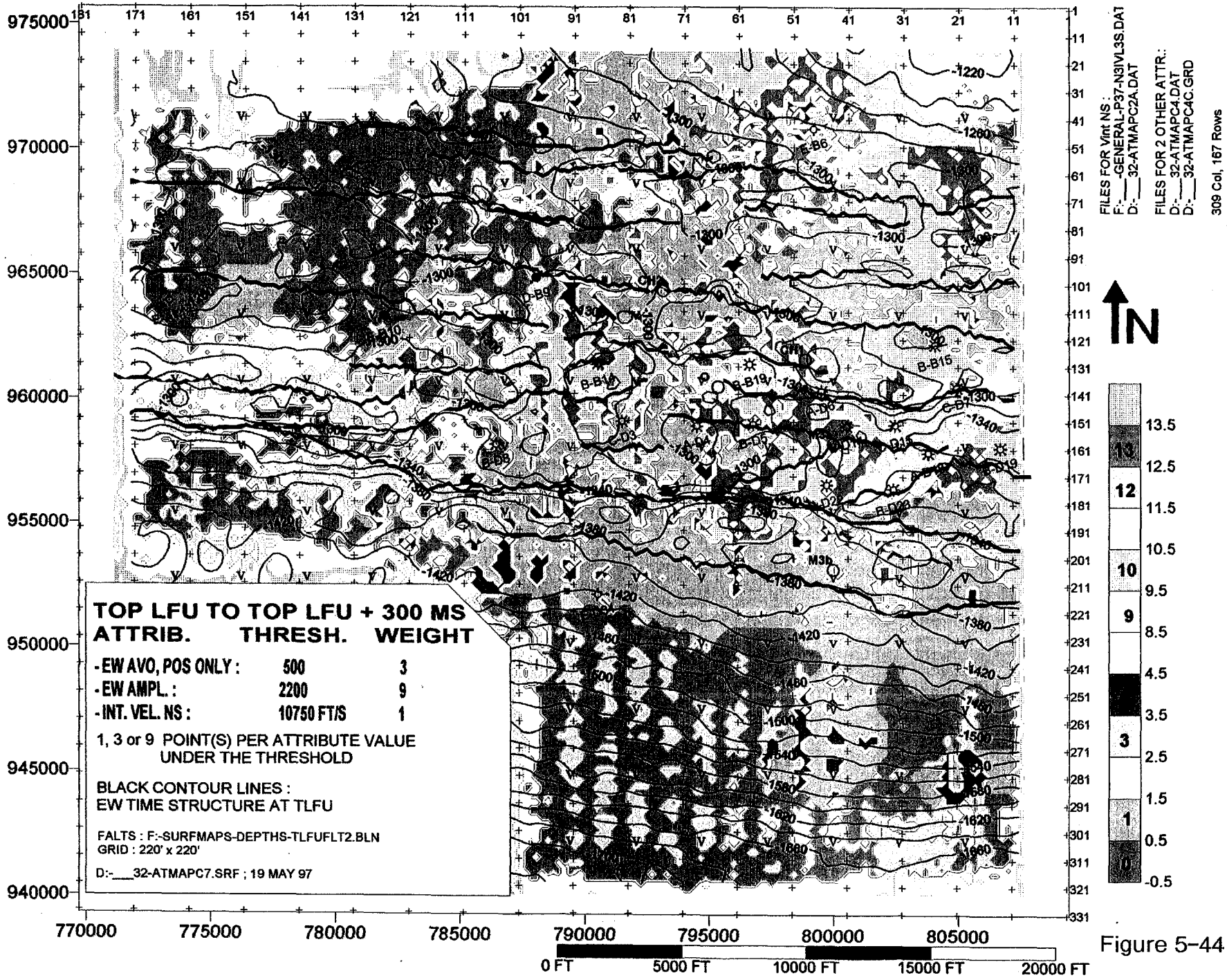
TOP LFU TO TOP LFU + 300 MS
ATTRIB. THRESH. WEIGHT
- EW AVO, POS ONLY : 500 3
- EW AMPL. : 2200 9
- INT. VEL. NS : 10750 FT/S 1
1, 3 or 9 POINT(S) PER ATTRIBUTE VALUE UNDER THE THRESHOLD
BLACK CONTOUR LINES :
EW TIME STRUCTURE AT TLFU
FALTS : F:-SURFMAPS-DEPTHS-TLFUFLT2.BLN
GRID : 220' x 220'
D:-___32-ATMAPC7.SRF ; 19 MAY 97
FILES FOR Vint NS :
F:-___-GENERAL-P37-N3IVL3S.DAT
D:-___32-ATMAPC2A.DAT
FILES FOR 2 OTHER ATTR.:
D:-___32-ATMAPC4.DAT
D:-___32-ATMAPC4C.GRD
309 Col, 167 Rows
N
0 FT
5000 FT
10000 FT
15000 FT
20000 FT

Figure 5-44

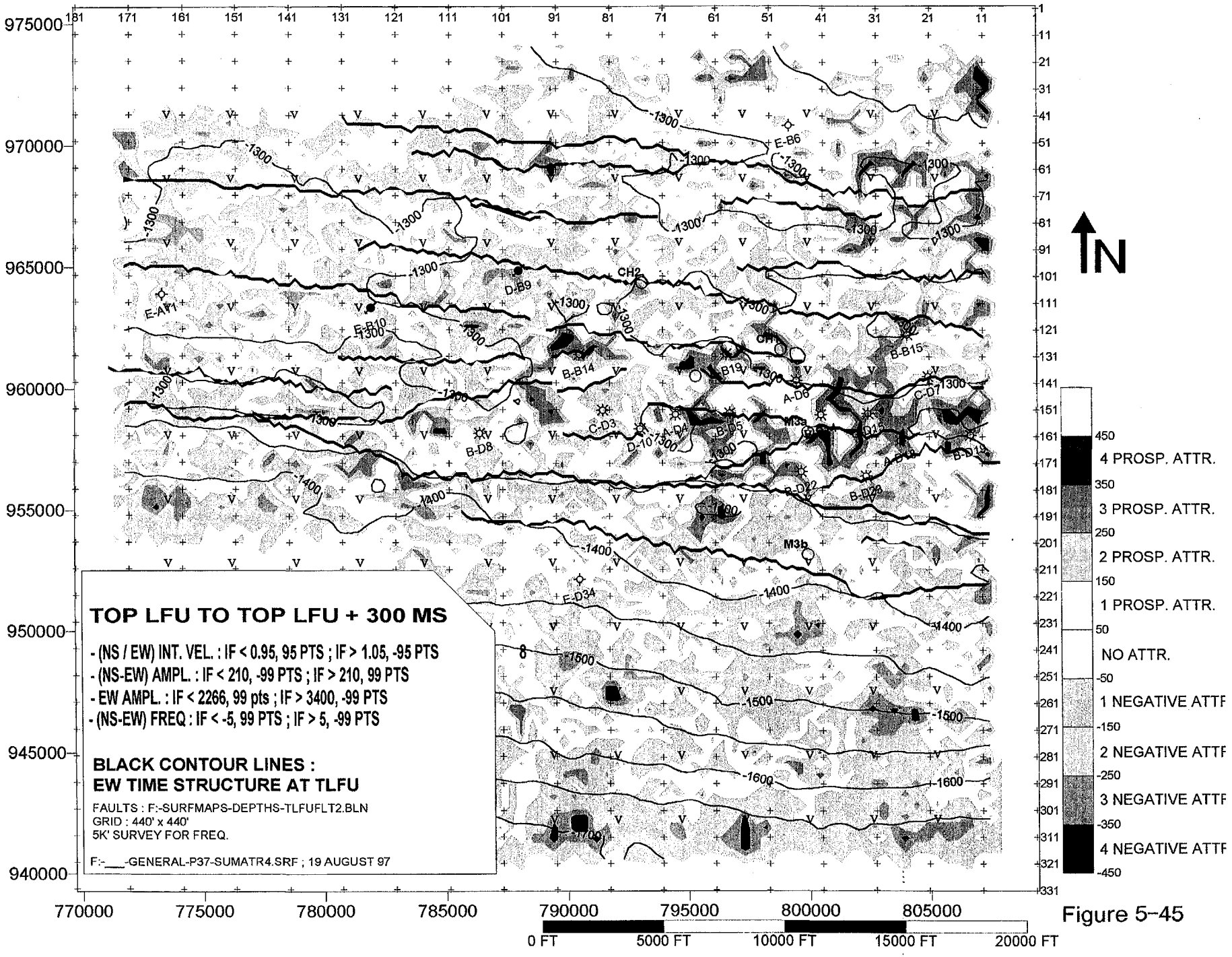
TOP LFU TO TOP LFU + 300 MS
- (NS / EW) INT. VEL. : IF < 0.95, 95 PTS ; IF > 1.05, -95 PTS
- (NS-EW) AMPL. : IF < 210, -99 PTS ; IF > 210, 99 PTS
- EW AMPL. : IF < 2266, 99 pts ; IF > 3400, -99 PTS
- (NS-EW) FREQ : IF < -5, 99 PTS ; IF > 5, -99 PTS
BLACK CONTOUR LINES :
EW TIME STRUCTURE AT TLFU
FAULTS : F:-SURFMAPS-DEPTHS-TLFUFLT2.BLN
GRID : 440' x 440'
5K' SURVEY FOR FREQ.
F:-___-GENERAL-P37-SUMATR4.SRF ; 19 AUGUST 97
N
450
4 PROSP. ATTR.
350
3 PROSP. ATTR.
250
2 PROSP. ATTR.
150
1 PROSP. ATTR.
50
NO ATTR.
-50
1 NEGATIVE ATTF
-150
2 NEGATIVE ATTF
-250
3 NEGATIVE ATTF
-350
4 NEGATIVE ATTF
-450
0 FT
5000 FT
10000 FT
15000 FT
20000 FT

Figure 5-45

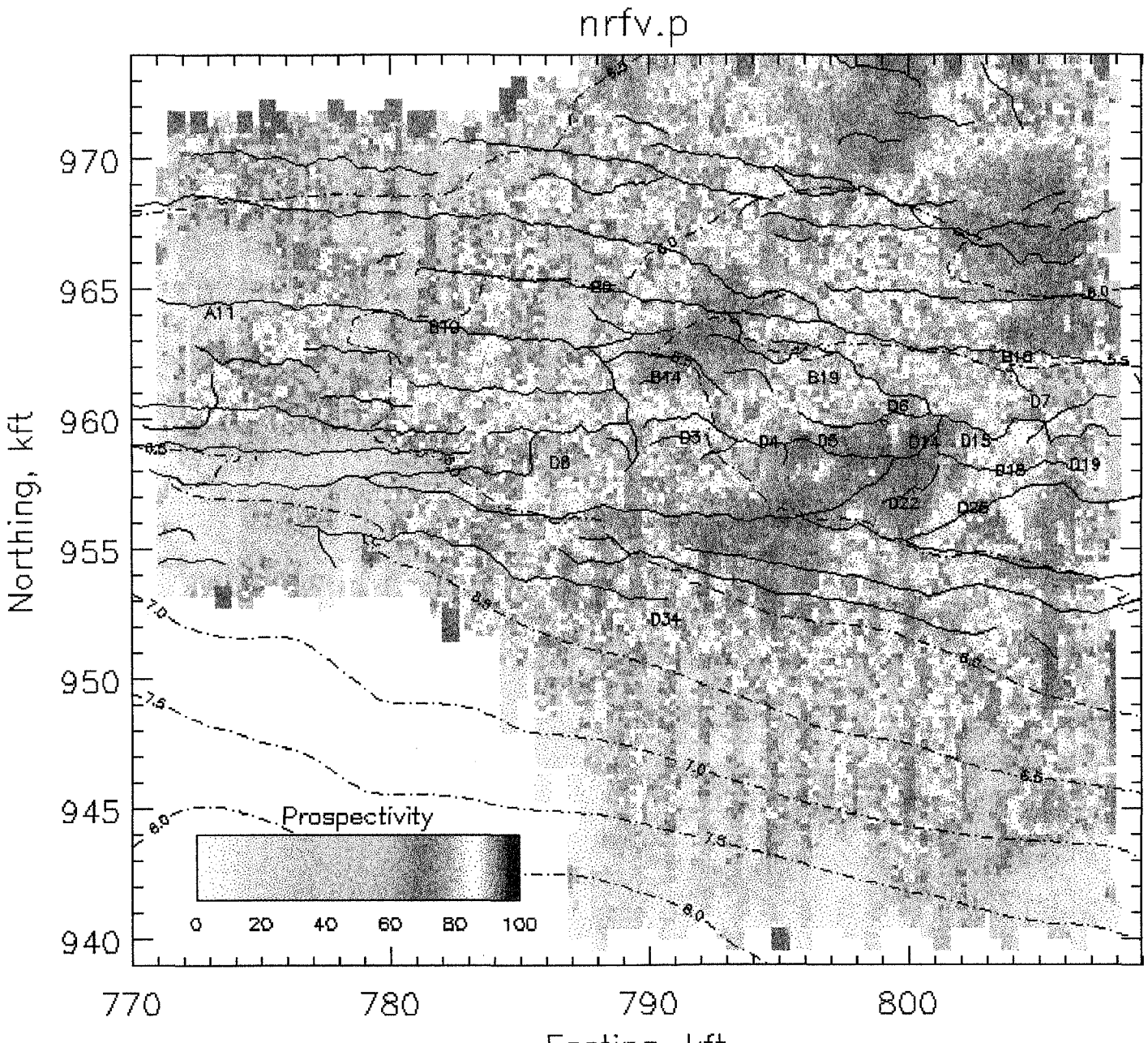

Fig. 5.46: NN Prospectivity using REW5,FEW,VNS

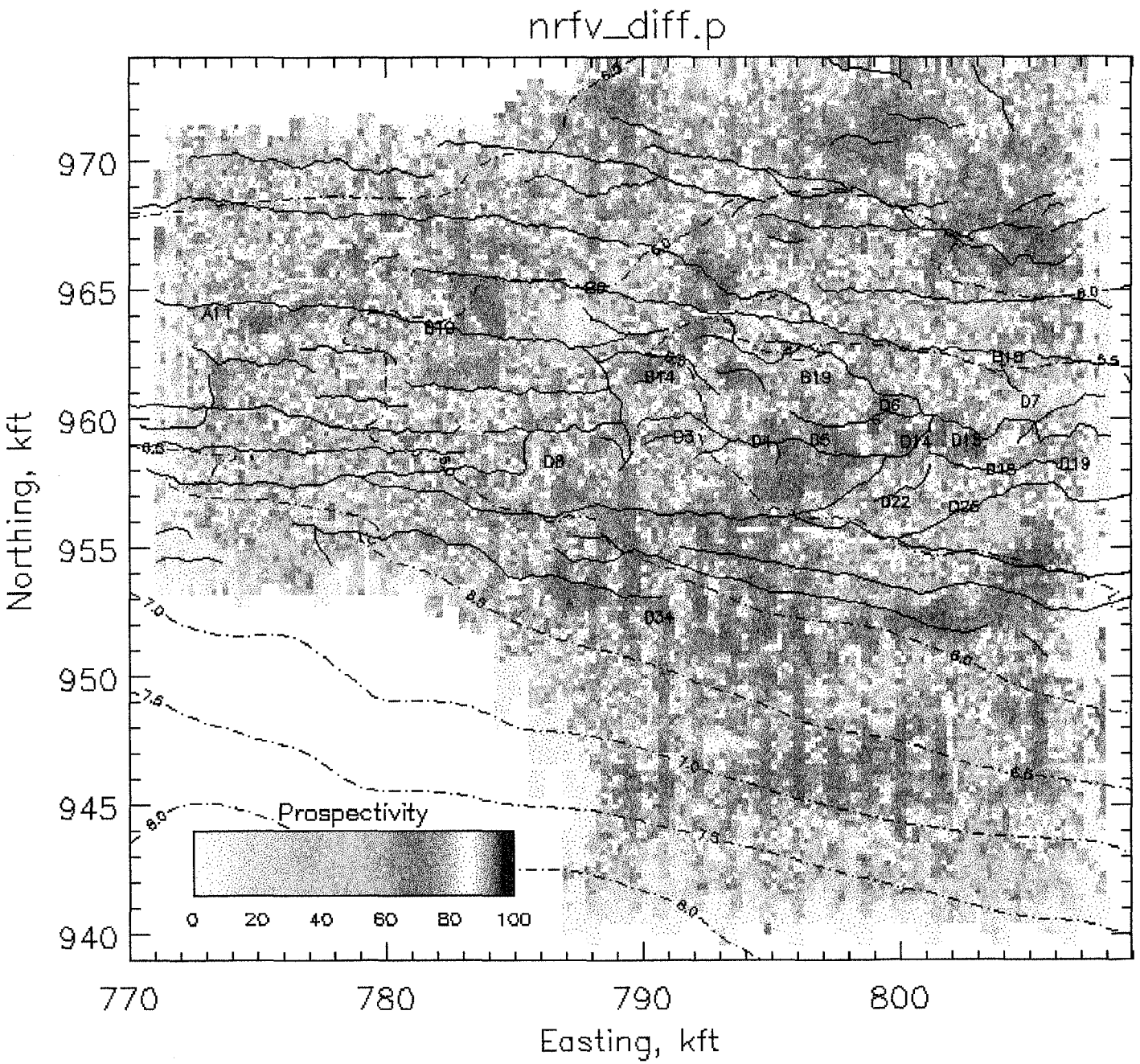

Fig. 5.47: NN Prospectivity using RDIF5,FDIF,VRAT

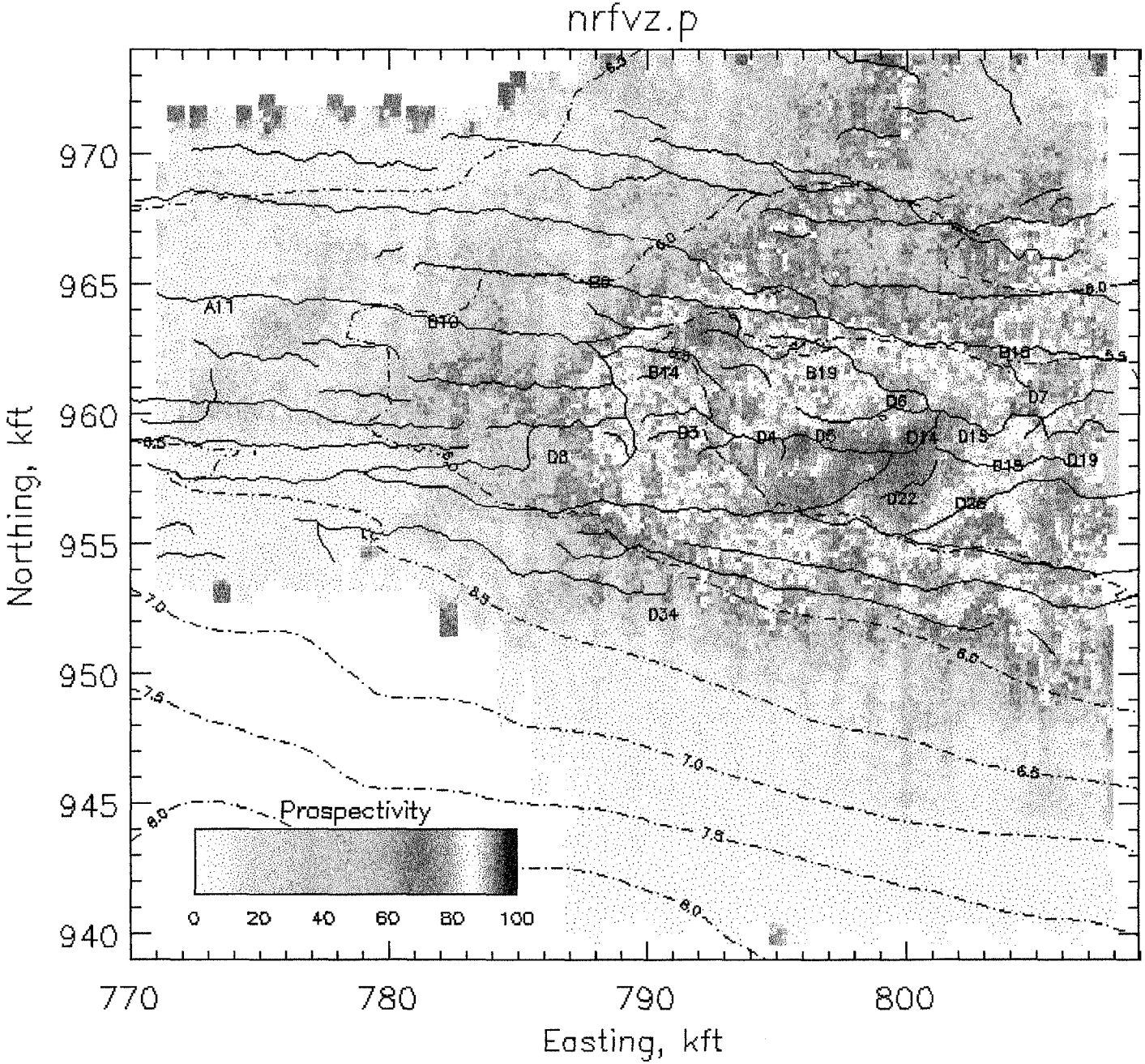

Fig. 5.48: NN Prospectivity using REW5,FEW,VNS,DEPTH

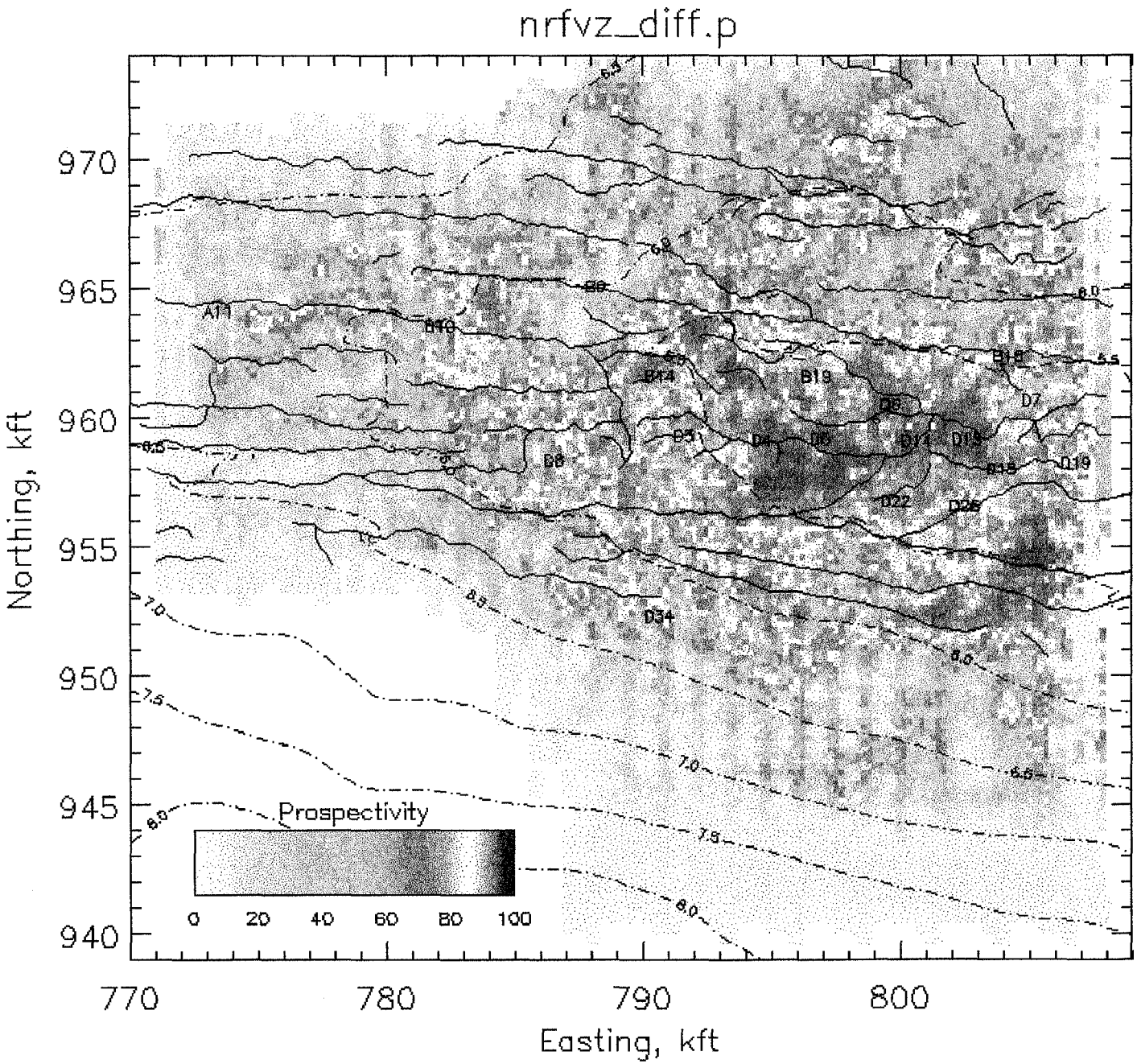

Fig. 5.49: NN Prospectivity using RDIF5,FDIF,VRAT,DEPTH

D.O.E. Wind River Basin Study

P-wave anisotropy indicators-300 ms

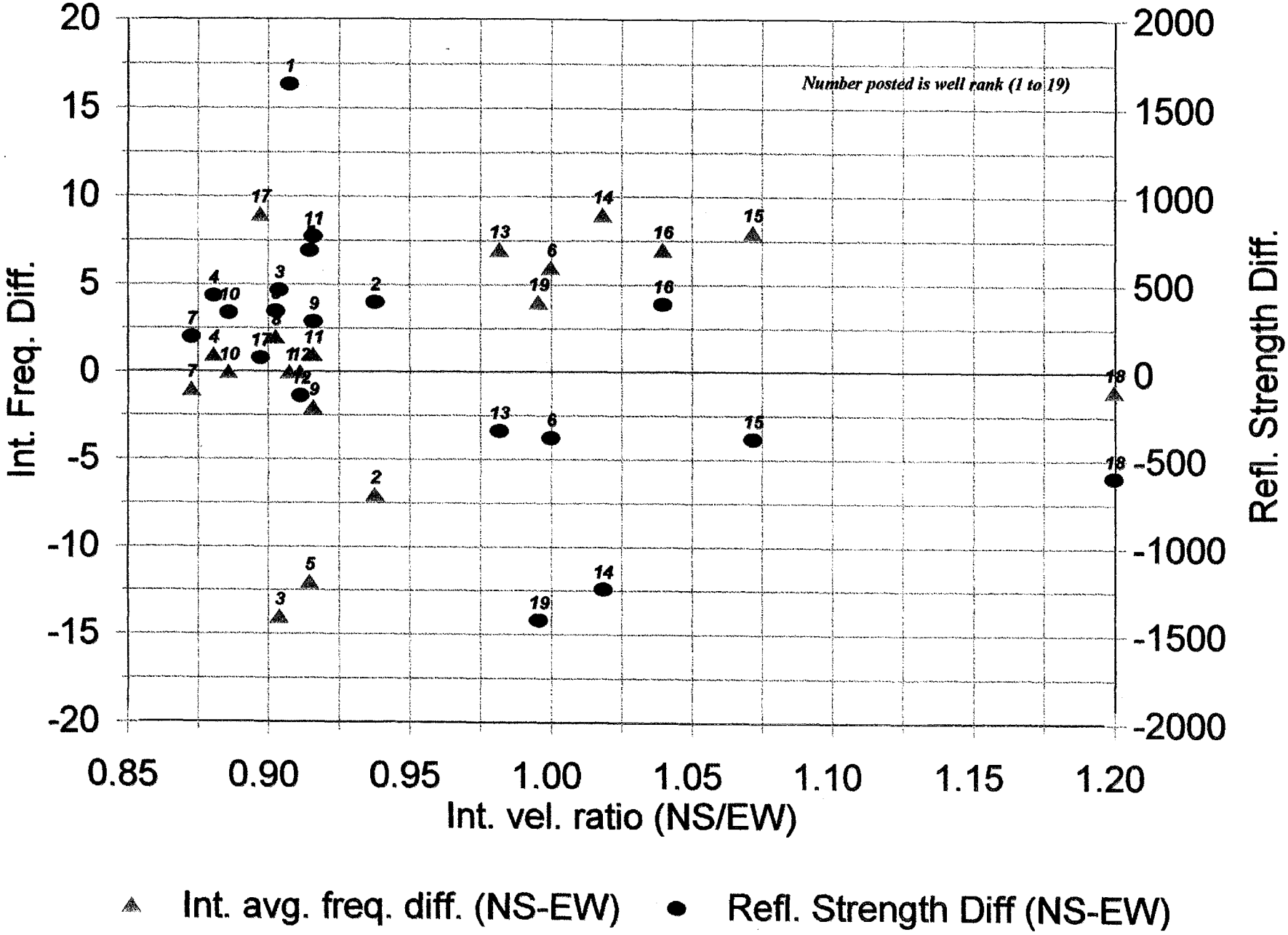

Figure 5-50

6. NINE-COMPONENT VERTICAL SEISMIC PROFILE (9C-VSP)

6.1. Acquisition

At well C-D7, a 9C-VSP was acquired 17-18 Sept. 1994, by Schlumberger Canada, with the following parameters

Tool:	Schlumberger 5-level, 3-component, clamping geophone
Vertical Interval:	9390 ft to 2000 ft TD. Levels 3470-5150 missing.
Vertical Spacing:	50 ft
Sources:	P- and S-wave vibrators
Offsets:	Near: 1090 ft due south from hole. P- and S-waves recorded; SH waves polarized both NE (Y) and NW (X) particle motion. Far: P waves only. 3200 ft due south from hole. At level 3240, an orientation checkshot was acquired at 1700 ft, due west.
Sweep:	6-16 Hz, 15 s for S waves; 10-60 Hz, 15 s for P-waves
Notes:	Southerly offsets were selected for the VSP in order to maximize sensitivity to EW fractures. Far-offset P-waves were recorded for tool-spin corrections. Levels 8190-8390 were recorded twice as S-wave vibrators were moved, having dug themselves into a hole and having become improperly coupled.

At depths of 2290-2090 ft, a 9-component walkaway VSP was acquired, with 150-ft surface-station spacing on a southerly azimuth offset 360 ft due west of the hole.

6.2. Processing

6.2.1. P-wave

Schlumberger Canada processed the P-P near offset VSP data as follows:

- Trace edit (reject noisy traces)
- Stack multiple source initiations for tool locked at same level.
- Filter 8-64 Hz, 13-36 dB/octave rolloff,
- Amplitude normalization (in 160-ms window starting 40 msec before P-arrival).
- Gain function: time to the 1.7 power.
- Wavefield separation
  - (1) Downgoing P-wave subtracted using median filter
  - (2) Enhance upgoing P-wave using median filter
  - (3) Wiener filtering
- Corridor stack (100-ms and 50-ms windows)

6.2.2. S-wave

S-wave processing generally resembled the pre-stacked P-waves, with the following additions:

- Tool-spin correction using far-offset P-wave, horizontal channels.
- Shear-wave source-static calculated and applied to each common-source dataset to match the lower part of the hole to the upper part of the hole, since the bulk of the data was acquired with the second shear-wave source location.
- Determination of the orthogonal fast (S1) and slow (S2) shear-wave directions using (1) Hodogram analysis, and (2) two- and four-component rotations. The two-component method was favored over the four-component (Alford) rotation because of the inequality of the cross traces (X-component of Y-source and vice-versa; Lavely and Bates, 1996).

6.3. Results

6.3.1. P-wave

The 9C-VSP well (C-D7) ties line 22 at crossline 138 in the 37-mi^2, 3D P-wave survey (Fig. 6.1). The well was drilled close to a large fault (crossline 143 at top LFU, ~1.3 sec); significant disruptions to travel-time and character are evident in the footwall (southern side, higher crossline numbers) as expected for fault shadowing (see above). The VSP raypaths cross this fault (the near-offset VSP source location is approximately at crossline 148, the far-offset at crossline 167). Therefore the VSPs have likely been affected by the fault (see below). The first-arrival time-lagged VSP (Fig. 6.2) aligns upgoing waves, which are summed to provide a single composite VSP trace showing the location of reflections. This trace is repeated for clarity in a corridor stack (Fig. 6.3). The corridor stack shows good agreement with LFU reflectors derived from the surface 3D P-wave survey.

Figure 6.1 Stacked sections (NS and EW azimuths) of 3D P-wave survey at location of 9C-VSP well.

Figure 6.2 Filtered, time-shifted VSP compared to part of 3D survey.

Figure 6.3 Corridor-stacked VSP at tie point to 3D survey.

6.3.2. S-wave

The apparent S1 direction varied strongly with the source azimuth, the analysis method, and depth. The hodograms yield S1 directions at N110±15 (approximately E-striking fractures) from 2 to 5 or 7 kft depths (Fig. 6.4). Below 5-7 kft the azimuth appears to rotate with depth toward the NE; the NE-motion (Y) polarizations are more southerly than the NW-motion (X) data. The hodogram results are complete only for the X-component because this orientation displayed better-quality data. The two-component rotations (Fig. 6.5) generally indicate easterly cracks above about 5 kft (the top of the LFU is at 5540 ft) and NE cracks rotating back to E between 5 and 8 kft. However, the X- and Y-rotations often sharply diverge strongly due to the disagreement between the "mismatched" traces XY and YX. The discrepancy is severe enough (90°) that the data are not useful below about 8.5 kft.

Figure 6.4 Hodogram results for fast shear-wave direction (S1), which may be interpreted as parallel to cracks or greatest compressive stress. (NW motion = X-direction, NE = Y-direction).

Figure 6.5 Two-component rotation results for fast shear-wave direction (S1).

The Vp/Vs ratio in the LFU is relatively constant, between 1.5 and 2.5 (about 1.8 average). The ratio appears to be somewhat higher in the overlying Waltman, 1.8-2.7 (about 2.2 average).

6.4. Interpretation

The S1 directions suggest easterly cracks in the Waltman and E to NE cracks in the LFU. The latter result is in direct disagreement with the prediction from the 3D P-wave interval-velocity ratio map in the top 300 ms (1.5 kft) of the LFU (Fig. 5.24), which shows velocity anisotropy of 0-10% fast NS. There are three possibilities for this discrepancy: errors in determination of the S1 directions in the VSP, errors in the velocity analysis from the surface seismic survey, or incorrect physical assumptions about the P- and S-wave responses to the same geological medium.

Multicomponent VSP analysis is fraught with subtle difficulties (Lavely and Bates, 1996). The four-component (Alford) rotation is preferred because it uses all of the data simultaneously, but is extremely sensitive to model assumptions and noise. The two-component technique is simpler, but additional variance is introduced because the two independent rotations may not agree. Because no "layer-stripping" methods were applied, the S1 directions in the LFU could be affected by anisotropy in shallower layers (particularly the Waltman), thus biasing deeper results. Shear-wave splitting is cumulative along a ray path: S1 and S2 wavelets encountering a medium with different anisotropy will each split into S1' and S2' wavelets, where the primes denote the new condition. It is assumed that S1' and S2' develop on time scales on the order a wavelet period or less and that the original S1 and S2 wavelets are sufficiently separated in time so that S1' and S2' can be derived from S1 alone.

However, Winterstein and Meadows (1991) have shown that shear-wave splitting analyses can be strongly biased by overlying anisotropic layers. In their data, errors in the S1-direction of up to 30° were removed by layer stripping, that is, eliminating the anisotropic time lag of an overburden layer, thus effectively positioning the source anew at the bottom of this layer. Before layer stripping, S1-azimuths in the lower layer appeared to increase monotonically away from the S1-direction in the overburden toward the "true" direction in the lower layer. In our case, this could correspond to the gradual apparent rotation in the hodogram results (Fig. 6.4) from E (the direction of Waltman anisotropy) toward N (the direction of LFU anisotropy). We also note the orientations of the geophones derived from P-wave toolspin analysis may be in error by up to 15° (D. Winterstein, personal communication, 1995).

As a velocity-analysis (velscan) location was quite nearby to the VSP (several hundred feet), any errors in the interval-velocity map must be due to an error in that particular velscan and not in gridding or interpolation. The location of the velscan is line 20, crossline 135. The NS- and EW-azimuth prestack time-migrated gathers near this position (Figs. 6.6 and 6.7, respectively) show the large fault just a few CMP bins away (crosslines 137-141). Some far offsets of the NS data show high-amplitude, low-frequency energy that is incorrectly moved out; i.e., the pulses are not all shifted to the same arrival time. The increasing time delays associated with greater offsets indicate that more moveout, or slower velocity, would be needed in order to align the arrivals. However, most of these anomalies lie in the fault footwall, where shadowing effects (e.g., delays, non-hyperbolic moveouts) are expected to be worst. In particular, the velscan gather (on the hanging wall) appears to be affected only in the first few tens of milliseconds below the top LFU. The apparent lack of EW cracks from the interval-velocity ratio map is consistent with the comparatively poor production at this well (C rating). While we cannot rule out inconsistencies in the velocity analysis, these errors appear less likely than those associated with the VSP.

Figure 6.6 NS prestack time-migrated CMP (common-midpoint) gathers for Line 20. Velscan location is crossline 135; projected position of VSP is crossline 138. Note fault near crossline (CMP) 137.

Figure 6.7 EW prestack time-migrated CMP gathers for Line 20. Note fault near crossline 141.

Finally, we must consider whether the physical assumptions involved in the VSP analysis, and its comparison to the surface seismic survey, are valid. Winterstein and Meadows (1991) showed that introduction of modest, dipping, bedding-plane anisotropy causes strong variations in the S1 direction as a function of azimuth. Furthermore, the near-source sediments of the LFU are very heterogeneous: when raypaths are not orthogonal to bedding, due to VSP source offset or geological dip, changes in lithology could cause apparent changes in anisotropy.

6.5. Conclusions: 9C-VSP

The P-wave VSP was successful in providing depth ties to reflector sequences in the heterogeneous LFU. However, the S-wave results are ambiguous. Moving the S-wave source even a small distance can completely change the signal character and is not recommended unless absolutely necessary. Source directions at 45° to the expected principal directions were used to maximize the signal-to-noise of the analytical rotations, but resulted in poorer signal-to-noise of the propagating S-waves themselves. The inferred EW-fast shear-wave (S1) direction in the Waltman is consistent with the surface-seismic P-wave velocity anisotropy, but the computed E-NE S1-directions in the LFU differ significantly from the expected fast azimuth (NS) from the surface survey. Although this discrepancy could be due to errors in the velocity analysis of the surface survey, incomplete reduction of the VSP data and/or incorrect processing assumptions are likely significant contributors. Layer-stripping of the VSP could alleviate the former problem, but the locally complex geology may not simplify the latter.

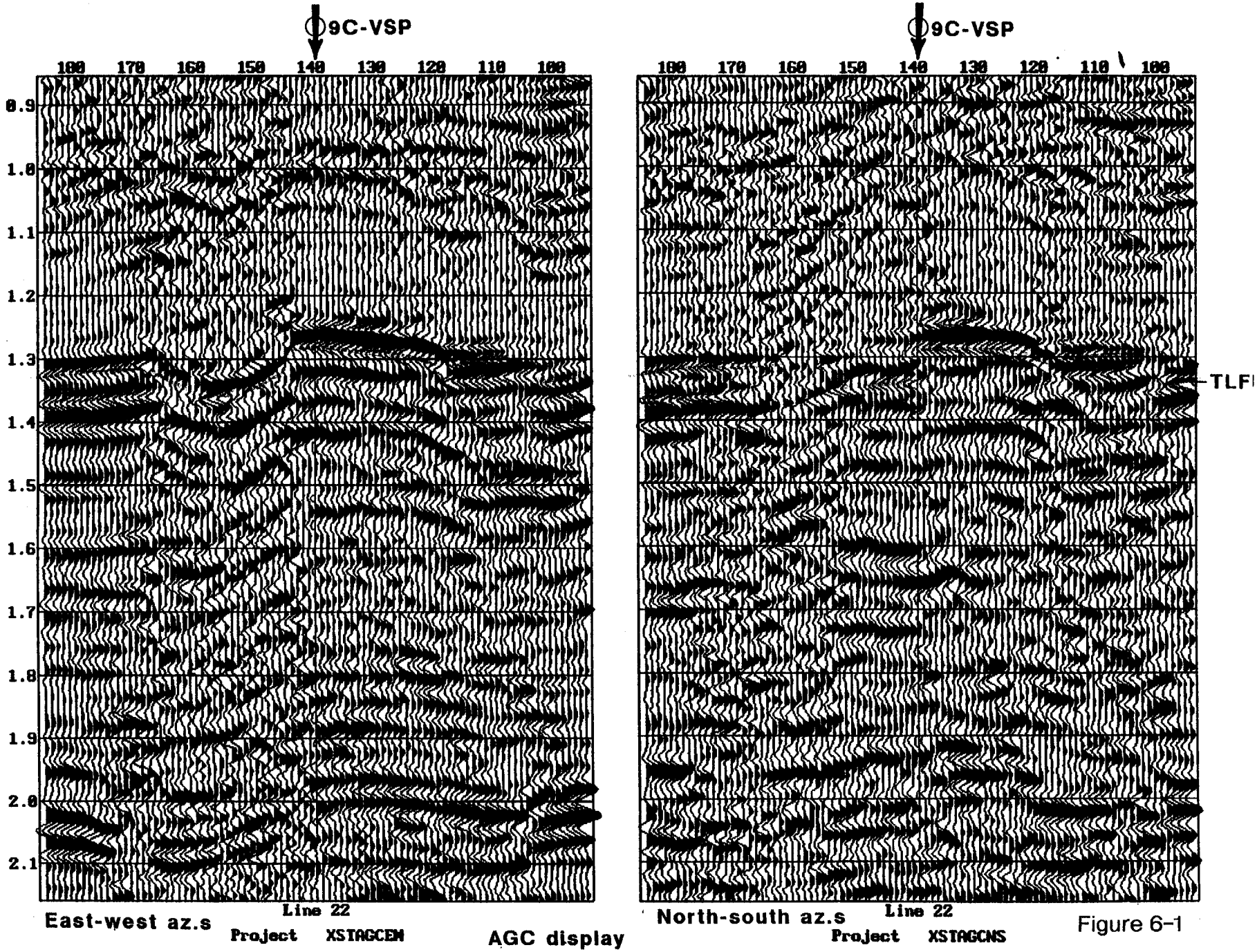
9C-VSP
190 170 160 150 140 130 120 110 100
0.9
1.0
1.1
1.2
1.3
1.4
1.5
1.6
1.7
1.8
1.9
2.0
2.1
East-west az.s
Line 22
Project XSTAGCEM
AGC display
9C-VSP
190 170 160 150 140 130 120 110 100
TLF
North-south az.s
Line 22
Project XSTAGCNS

Figure 6-1

RAW DEPTF

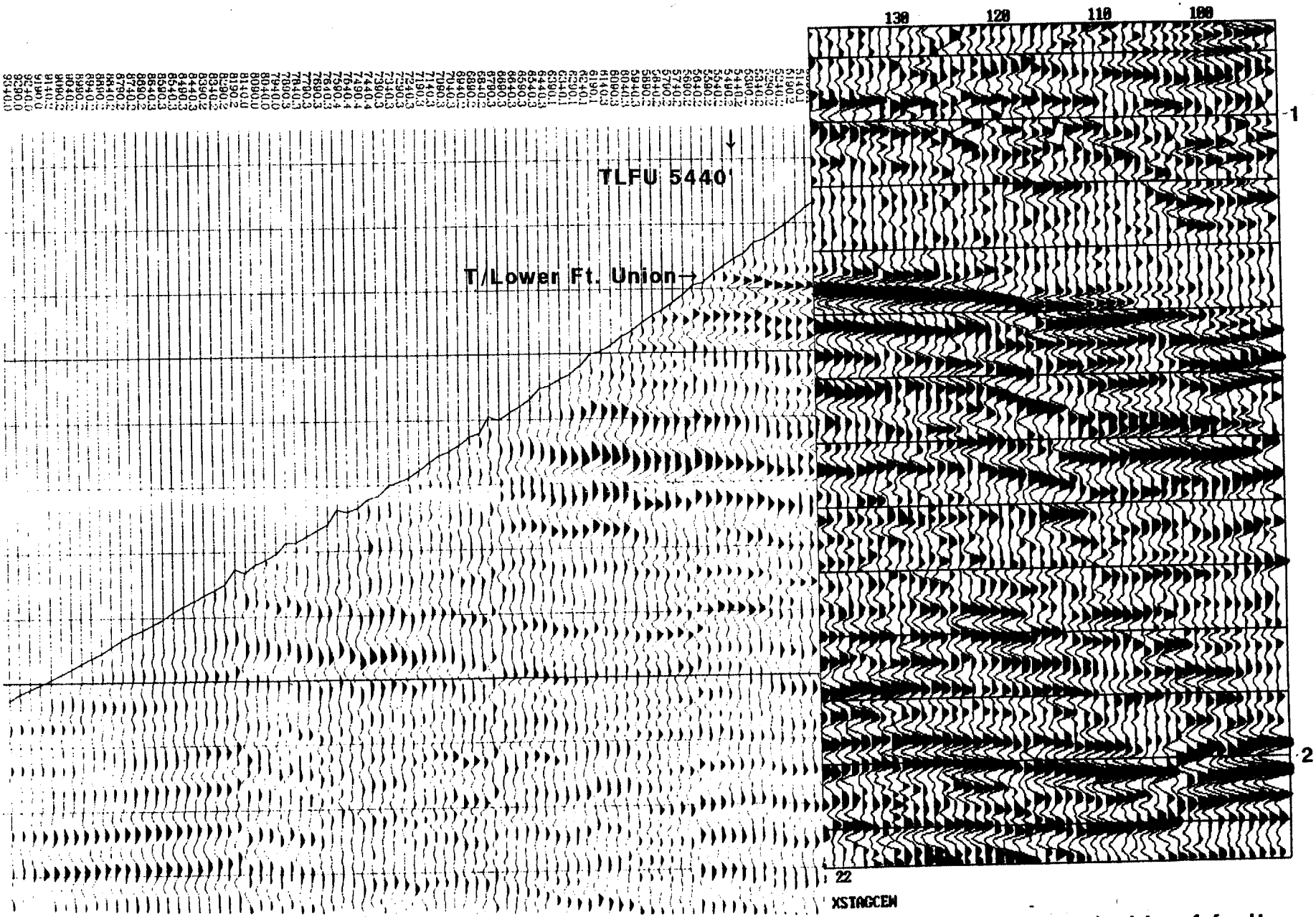

Proj. onto high (no.) side of fault

Figure 6-2

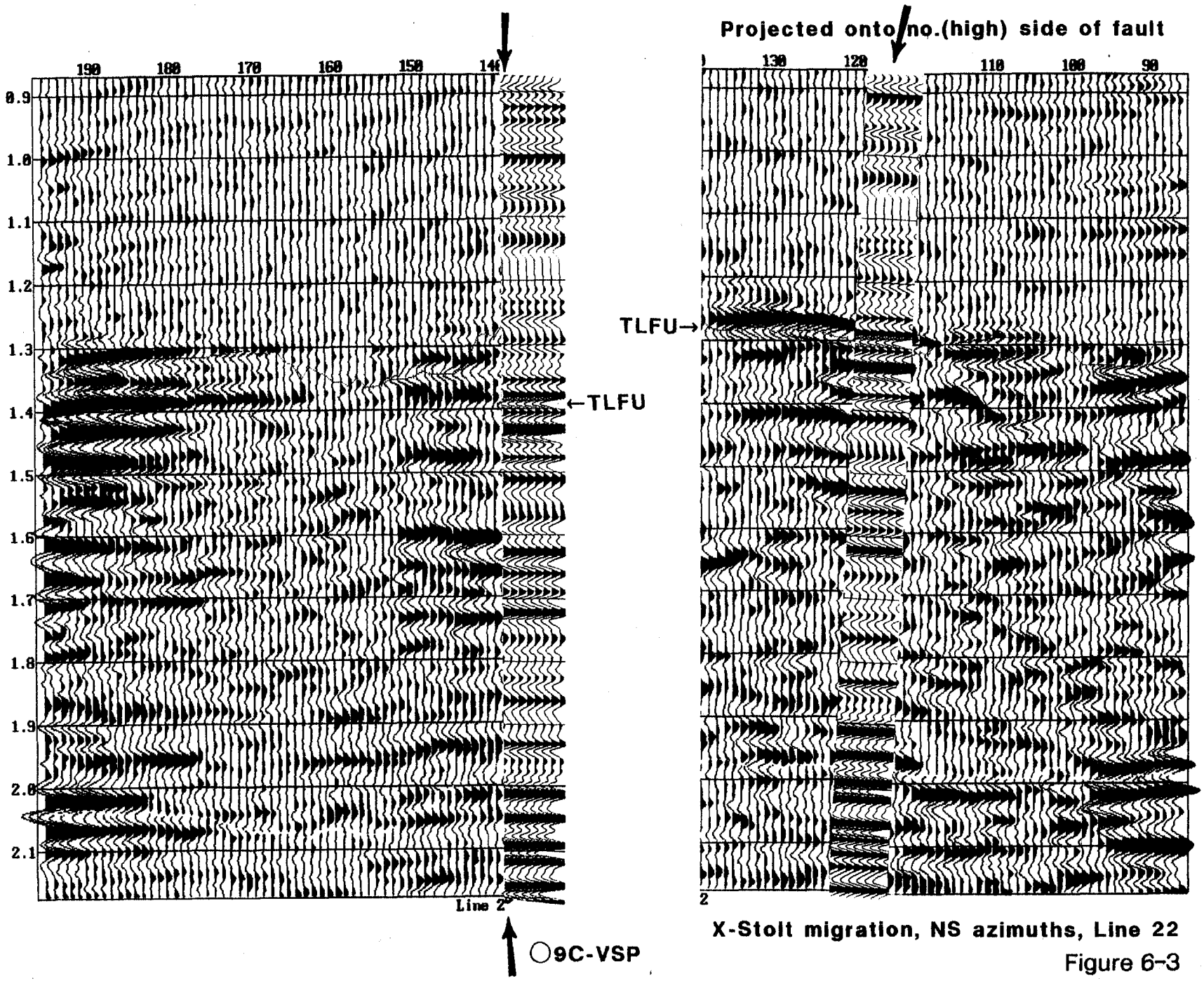

X-Stolt migration, NS azimuths, Line 22

Figure 6-3

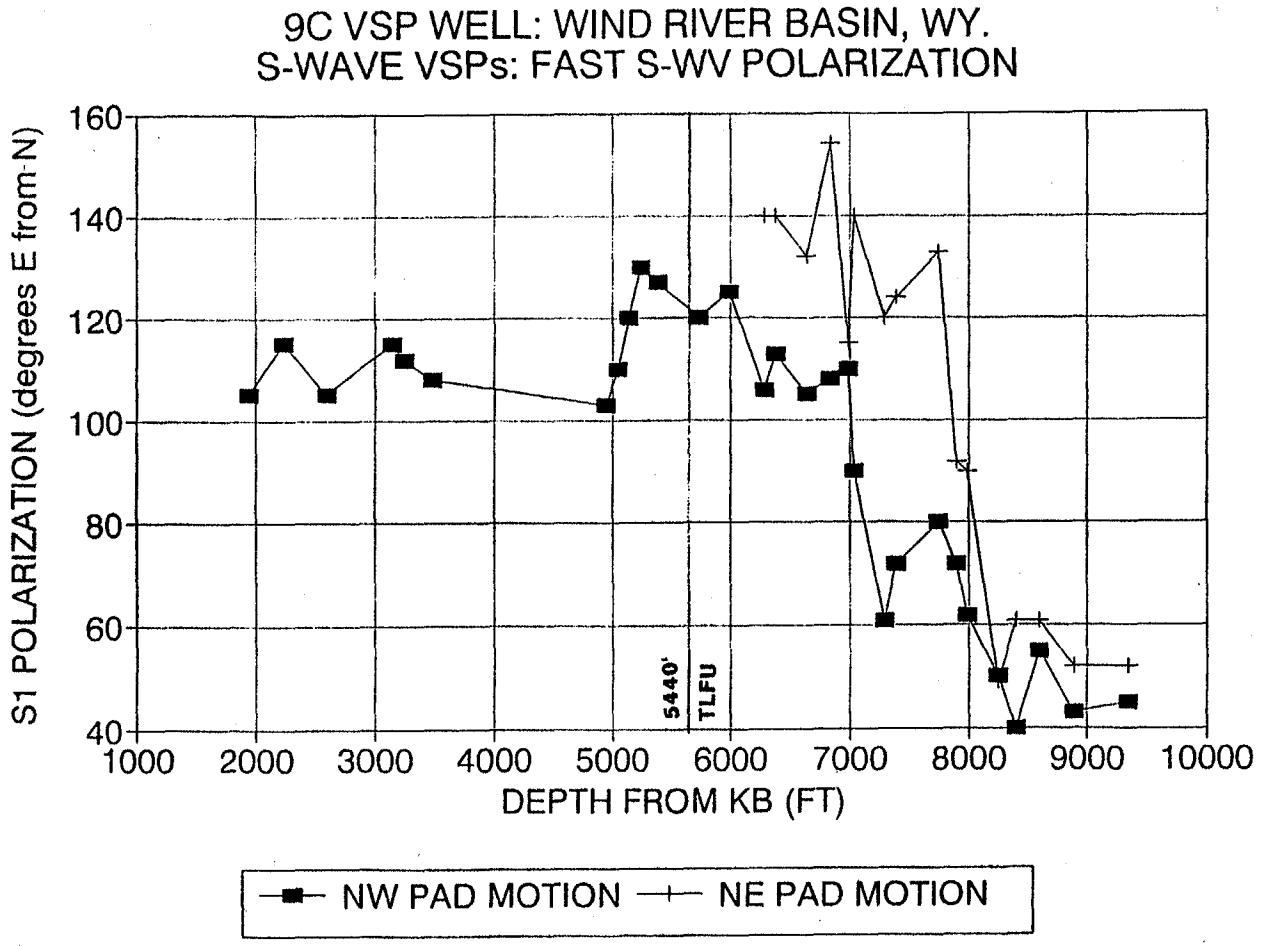

A) Interpreted S1 azimuth vs. depth
B) The interval velocities and the percent anisotropy vs. depth

Figure 6-4

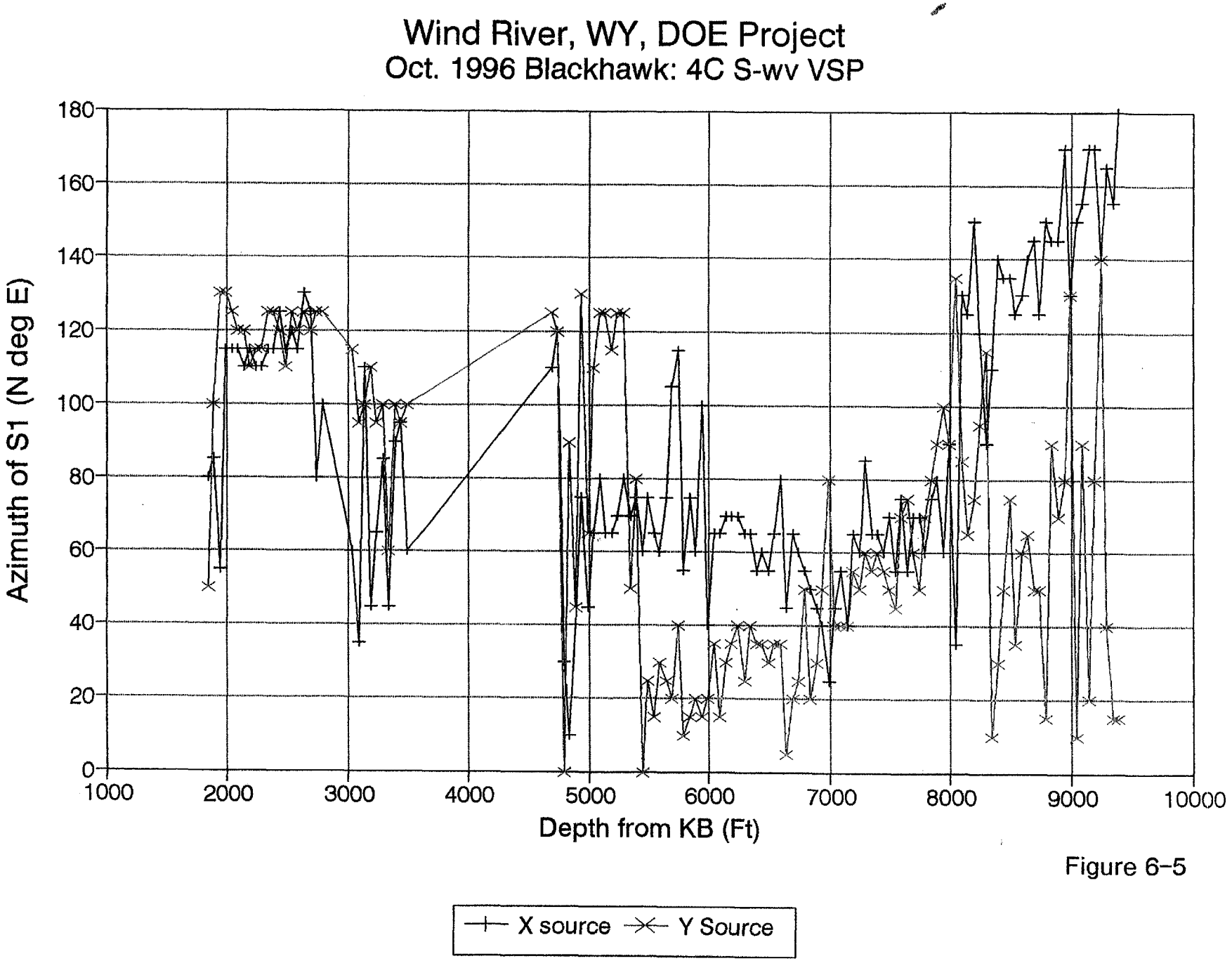
Wind River, WY, DOE Project
Oct. 1996 Blackhawk: 4C S-wv VSP
Azimuth of S1 (N deg E)
180
160
140
120
100
80
60
40
20
0
1000
2000
3000
4000
5000
6000
7000
8000
9000
10000
Depth from KB (Ft)
X source
Y Source

Figure 6-5

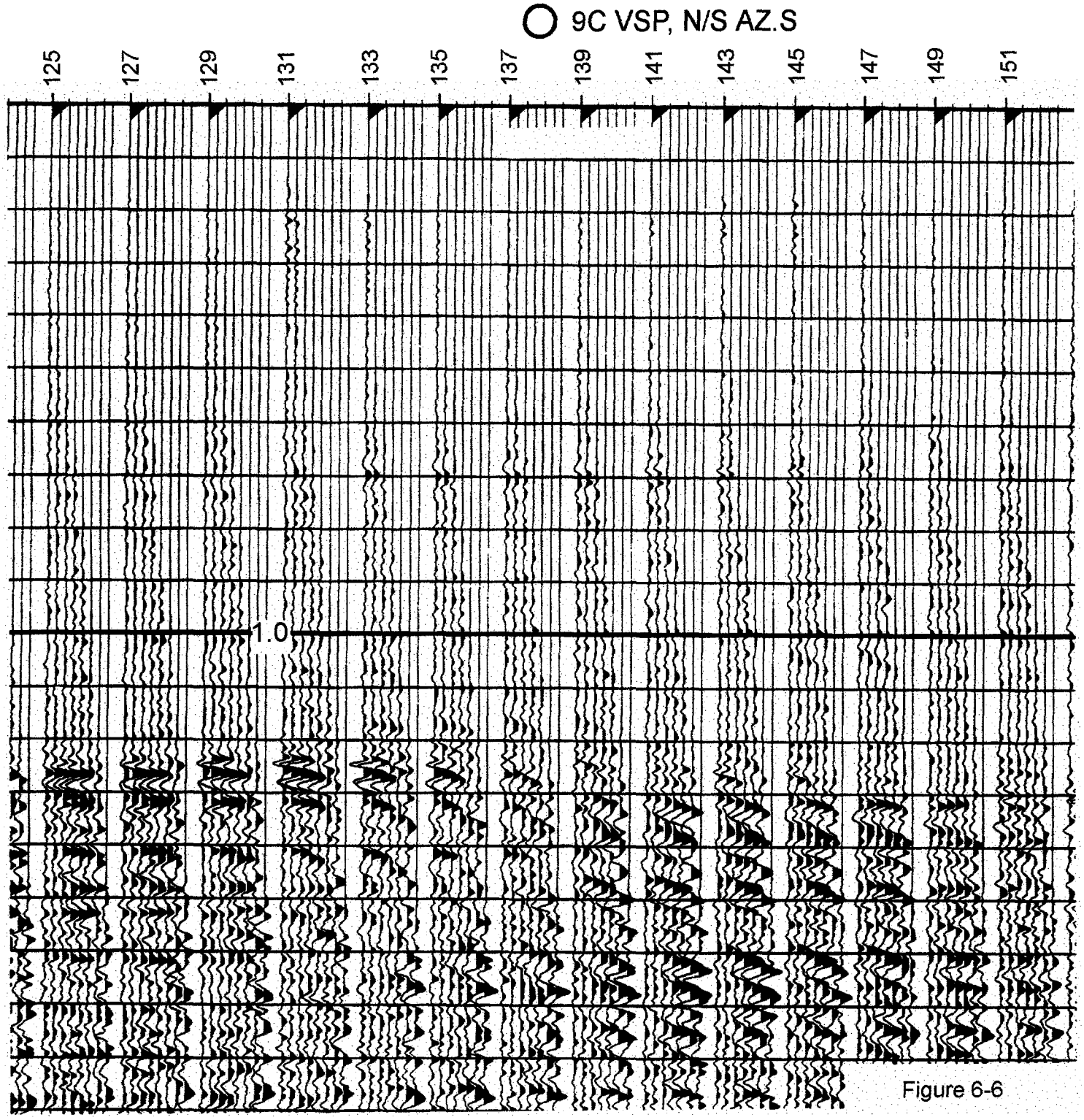
9C VSP, N/S AZ.S
125
127
129
131
133
135
137
139
141
143
145
147
149
151
1.0

Figure 6-6

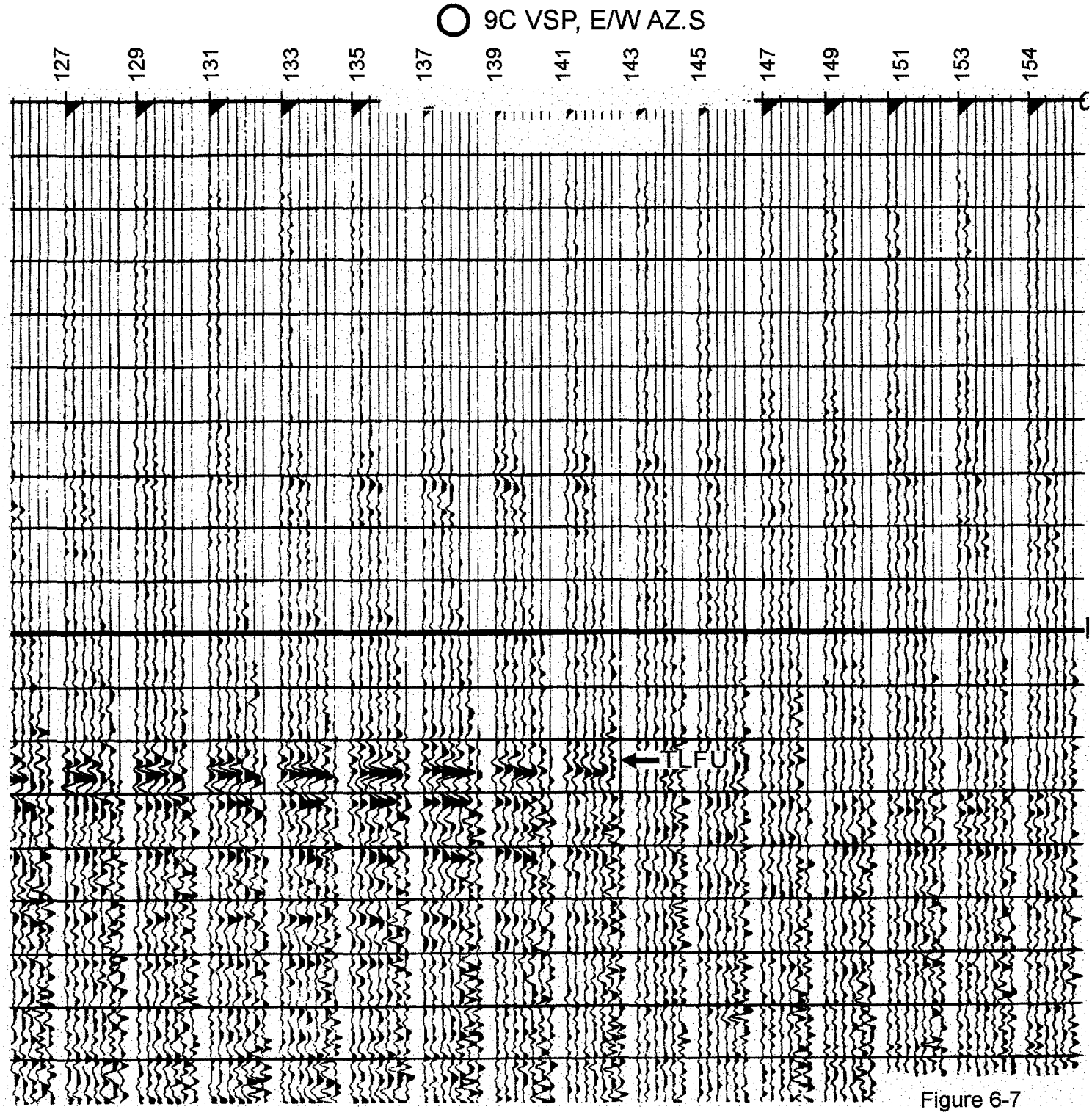
9C VSP, E/W AZ.S
127
129
131
133
135
137
139
141
143
145
147
149
151
153
154
TLFU

Figure 6-7

7. THREE-COMPONENT, THREE-DIMENSIONAL, P-TO-S CONVERTED WAVE SEISMIC SURVEY (3D-3C)

The main purpose of the 3D-3C experiment was to establish relationships between P-wave and S-wave azimuthal velocity anisotropy in the same survey, in order to verify that cheaper, P-wave surveys can be used to characterize fractures similarly to either full-source or converted P-to-S shear-wave surveys.

7.1. Acquisition

The 3D-3C seismic data set was acquired in an area covering approximately two square miles, in the center of the 37-square mile P-wave multi-azimuth survey; lines 40-150, crosslines 60-120 (Fig. 7.1). The 3D-3C survey was acquired between 13-17 October 1995, by Western Geophysical. The acquisition was designed to produce equal maximum offsets in both the NS and EW azimuthal volumes. The final acquisition parameters are given in the table below.

Table 7.1 3D-3C Acquisition Parameters	
Recording System	I/O System 2
Sample Rate	2 ms
Record Length	10 s
Recording Filters	3-207 Hz bandpass Antialias @ 3/4 Nyquist
Pre-amplifier Gain	48 dB
Tape Format	SEG-D 8048/6250 BPI 9 track
Spread Type	Multi-line layout
Channel Distribution	Static patch
Receiver Lines	9 (EW orientation)
Receiver Line Spacing	660 ft
Receiver Station (Group) Spacing	220 ft
Receiver Total Stations	458
Receiver Group Size	12
Receiver Layout within Group	20-30 ft diameter circle about survey stn., bury phones, lay cable flat to reduce wind vibration.
Receiver Leakage Specification	500 kΩ [I/O internal "common-mode" test at -65 dB range]
Receiver String Resistance	OYO-Geospace GS-20DX or SMT-70 3-component elements per case, 10 Hz, 70% damping, wired 12 in series R(tot) =~850Ω; 5% acceptance tolerance
Source Type	Explosive: 20 lbs. Vibrogel (non-cast exp.)
Source Deployment	Single shot, double cap/51-ft top depth (9-ft charge)
Source Lines	37
Source Spacing	Variable 220-ft inside spread, 440 ft outside
Source Total Shots	872
Survey X (EW) Extent	25648.12 ft
Survey Y (NS) Extent	18215.00 ft
Common-Midpoint Bin Width	110 ft
Common-Midpoint Bin Height	110 ft
Inline Bins	167
Crossline Bins	234
Total Bins	39078
Total Traces	399376
Nominal Fold	10
Maximum Fold	110
Minimum Offset	76 ft
Maximum Offset	21453 ft

The 3C geophones at each receiver location consisted of 12 buried phones arranged in a 6-9 m circular array. The geophones were oriented such that one of the horizontal phones was exactly east-west (H1), and the other north-south (H2).

Prior to the acquisition of the 3D-3C data, thirty three-component geophones with dynamite charges were deployed at a depth of 60 ft. P- and S- traveltime measurements were made to document the magnitude, orientation and variability of the near-surface anisotropy. The results are documented in a SEG paper (Bates et al., 1996) and appended here as Section 9.5.

Figure 7.1 Geometry for 2-mi^2, 3D-3C seismic survey, approximately centered within 37-mi^2, 3D-P survey. Shots, red; receiver groups, blue; wells, green.

7.2. Processing

All processing was performed by Western Geophysical.

7.2.1. P-P Processing

7.2.1.1. Two-Azimuth Processing

The basic processing flow for the P-P portion of the 3-D 3-C dataset was modeled closely after the processing sequence performed on the 37-square mile 3-D data. A major exception is that instead of pre-stack time migration of the NS and EW data volumes, the P-P data from the two principal azimuths of the 3D-3C survey were pre-stack corrected for DMO and post-stack time migrated. Also, velocity analyses were performed at ¼-mile spacing rather than the ½-mile spacing used for the larger P-wave survey. The processing flow for the P-wave component of the 3D-3C survey is outlined below.

- Azimuth Separation (NS $\pm$ 45°, EW $\pm$ 45°)
- Amplitude Recovery Using $t^{1.5}$ Gain Function
- Residual Amplitude Analysis and Compensation (time and offset-variant scalar)
- Surface-Consistent Deconvolution
- Refraction Statics
- Surface-Consistent Statics
- Velocity Analysis
- Iterate Previous Two Steps Until Convergence
- DMO
- Stack
- Time-Migrate

7.2.1.2. Fractogram

A new methodology was developed by Western Geophysical to allow the azimuthal variations in P-wave anisotropy to be more finely delineated than ± 45° (Mallick et al., 1996; Craft et al., 1997). The "Fractogram" accomplishes this by fitting interval velocities measured in four azimuths to a smooth sinusoid: the amplitude and phase of this function give the magnitude and azimuth of velocity anisotropy. The following modifications are made to the standard processing flow:

- Azimuth Separation into 4 Volumes at ±22.5°
- DMO Velocity Analysis on 1/4-mi spacing.
- Stacking Velocity Volumes
- Interval Velocity Volumes Calculated in 300-ms Time Window Near Top LFU
- Fit Velocity Variation with Azimuth θ in Each Bin to $\cos 2\theta$ Function.
- Compute Azimuth and Magnitude of Velocity Anisotropy (2 Output Volumes).

7.2.2. P-S Processing

The principal goals of the P-S processing are to extract S-waves produced by mode conversions of P-waves incident upon reflectors, and then to analyze the S-wave data for splitting or birefringence that is the main indicator of anisotropy:

- Azimuth Limitation [(separation into 4 volumes; each azimuth has two horizontal components of motion: H1 (EW motion) and H2 (NS motion). The eight volumes are labeled S0H1,S0H2 (azimuth 0), S45H1,S45H2 (azimuth 45), S90H1,S90H2 (azimuth 90), and S135H1,S135H2 (azimuth 135)].
- Common Conversion-Point Binning (assuming constant Vp/Vs)
- Geometrical Spreading Correction
- Surface-Consistent Amplitude Balance
- Automatic Trace Edit
- Adaptive F-X Ground-Roll Filtering
- Surface-Consistent Deconvolution
- Refraction Statics
- Surface-Consistent Statics
- Velocity Analysis
- Common-Conversion Point Binning (using constant Vp/Vs)
- Iterate Previous Three Steps Until Convergence (equivalent to DMO)
- Stack
- Time Migration
- Alford Rotation Incorporating Layer Stripping (convert H1 and H2 components to S1 and S2 as functions of depth)
- Principal Directions and Magnitude of S-Wave Velocity Anisotropy in Waltman and LFU.

The biggest technical challenges in P-S experiments are (1) maintenance of sufficiently high signal-to-noise in all channels during acquisition, (2) correct positioning of reflection points (exacerbated because angle of incidence does not equal angle of reflection for mode conversions), and (3) accurate recovery of principal shear-wave directions (S1 and S2). All three factors affected this survey.

The highest amplitudes and coherence occur for the H1 volumes, particularly S90H1. This is broadly consistent with S-waves scattering and/or attenuating on EW cracks. The S45 data are generally higher quality that the S135 data, which is inconsistent with simple vertical cracks alone; more complex anisotropy symmetry and/or heterogeneity is required to explain these differences (see Section 6). All of the data exhibit severe dip toward the ends of the lines, which is not structurally consistent with the P-P data. This may be the result of a 3D migration-aperture problem, in which additional uncertainty is introduced by the necessity of computing common conversion points.

The four components necessary for the layer-stripping and Alford rotation to the principal shear-wave directions are provided in P-S data by the two receiver components of two orthogonal azimuth volumes (Van Dok et al., 1997). The azimuthal volumes S45 and S135 were used for the analysis because of the more comparable signal-to-noise than between S0 and S90 volumes. More stable results were obtained for larger windows (intervals). The magnitude and direction of anisotropy was mapped over two windows: an upper window 1.1-2.1 sec (P-S two-way travel time is 50-100% longer than P-P) which roughly corresponds to the Waltman shale, and a lower interval 2.1-3.6 sec, which includes the upper LFU. It should be noted that both the S1 and Fractogram are based on time intervals and not reflector boundaries as is the two-azimuth interval velocity anisotropy.

7.3. Results and Interpretation

7.3.1. Two-Azimuth P-Waves

7.3.1.1. Structure

Time horizons corresponding to Top Waltman and Top LFU were interpreted on the NS (± 22.5°) and EW (± 22.5°) P-wave data and compared to the corresponding 3D-P maps (Figs. 7.2-7.5). There are some discrepancies in event-picking due to the higher frequencies (noise) on the 3D-P and migration differences that cause variations in amplitude and timing of events (Fig. 7.6).

Figure 7.2 Comparison of top of Waltman time-structure, NS azimuths, from 3D-3C (top) and 3D-P (bottom).

Figure 7.3 Comparison of top of Waltman time-structure, EW azimuths, from 3D-3C (top) and 3D-P (bottom).

Figure 7.4 Comparison of top of LFU time-structure, NS azimuths, from 3D-3C (top) and 3D-P (bottom).

Figure 7.5 Comparison of top of LFU time-structure, EW azimuths, from 3D-3C (top) and 3D-P (bottom).

Figure 7.6 Comparison of record sections from 3D-3C (left) and 3D-P (right).

7.3.1.2. Interval Velocity

There are profound differences in the computed velocity anisotropies between the 3D-3C and the 3D-P surveys. In the 3D-3C, both the Waltman (Fig. 7.7) and the top LFU + 300 ms (Fig. 7.9) are dominantly NS-fast, whereas the same regions extracted from the 3D-P survey (Figs. 7.8 and 7.10) are dominantly EW fast. There appears to be a bias in V_{NS}/V_{EW} of a few tens of percent between the two surveys, such that this ratio is greater than unity in the 3D-3C and less than unity in the 3D-P. Furthermore, the 3D-3C map is rougher, with smaller spatial scale, larger-amplitude anomalies than in the 3D-P. The relative fast-slow structure can be crudely correlated between the surveys in parts of the LFU, but the spatial correspondence is poorer for the Waltman.

These discrepancies are likely due to the different processing applied to the different surveys. The 3D-3C used DMO, whereas the 3D-P was prestack time-migrated; the latter approach more accurately repositions reflecting elements. In particular, migration will move reflecting elements farther updip than does DMO, resulting in earlier arrivals and hence higher interval velocities. The 3D-3C survey is on the crest of the anticline and the dips are generally in the plunge direction, toward the west. Hence the EW velocities will appear slower in the 3D-3C than in the 3D-P, i.e., V_{NS}/V_{EW} is biased NS-fast. Interpolation scales also differed: velocities for the 3D-3C were constructed on ¼-mi spacings, whereas the 3D-P used ½-mi intervals. Therefore the smaller-scale structure in the 3D-3C is likely partly real, although the magnitudes are probably incorrect due to the lack of prestack time migration.

Figure 7.7 Waltman NS/EW Interval-Velocity Ratio, 3D-3C survey.

Figure 7.8 Waltman NS/EW Interval-Velocity Ratio, 3D-P survey.

Figure 7.9 Top LFU + 300 ms NS/EW Interval-Velocity Ratio, 3D-3C survey.

Figure 7.10 Top LFU + 300 ms NS/EW Interval-Velocity Ratio, 3D-P survey.

7.3.1.3. Stacked Amplitudes

The LFU reflectivity trends in the 3D-3C data correspond well with the 3D-P survey, but are stronger (Figs. 7.11-7.14).

Figure 7.11 NS Reflection Strength, top LFU + 24 ms, 3D-3C survey.

Figure 7.12 NS Reflection Strength, top LFU + 24 ms, 3D-P survey.

Figure 7.13 EW Reflection Strength, top LFU + 24 ms, 3D-3C survey.

Figure 7.14 EW Reflection Strength, top LFU + 24 ms, 3D-P survey.

7.3.1.4.Interval Average Frequency

The recovered bandwidth of the 3D-3C data is only 10-30 Hz; in contrast, frequencies up to 60 Hz were extracted from the 3D-P. Although azimuthal variations in frequency of 5 Hz were often observed in the 3D-3C, the differences in acquisition preclude a meaningful comparison between the two surveys.

7.3.2. Four-Azimuth P- and S-Waves

In this section we compare the results of the anisotropy analysis from the P-wave Fractogram, P-to-S converted-wave analysis (S1 direction), and P-wave interval velocity from the 3D-P survey. Note that the S1 direction need not be aligned with the fast P-wave direction, although they can and are often assumed to do so.

As the data from which the P-wave Fractogram were unmigrated (see above), we also use unmigrated data for P-S converted-wave analysis, to facilitate direct comparison of the methods. The P-S results on migrated data do show more spatial heterogeneity than the unmigrated results, possibly due to better focusing of events achieved by migration.

As a whole, the two-azimuth and four-azimuth methods gave comparable results. The mean directions and magnitudes for the two four-azimuth methods over the Waltman and LFU intervals are summarized in Table 7.2. The mean azimuth from S1 is in excellent agreement with ancillary data on fracture directions (Section 4.5). The Fractogram appears to have a northerly bias. Both the direction and relative magnitudes of the two-azimuth results compare well to the four-azimuth methods. There are substantial differences in the details, however, as outlined below.

Table 7.2 Summary of 2- and 4-Azimuth Anisotropy Tests in 3D-3C Area

Interval	Two-Azimuth	Four-Azimuth		
	NS/EW P-wave Velocity	Method	Mean Fast Azimuth	Mean Anisotropy, %
Waltman	0.985 (=1.5% anisotropy)	P-wave Fractogram	76	17
Waltman		S-wave (S1)	93	3
LFU	0.967 (=3.3% anisotropy)	P-wave Fractogram	75	22
LFU		S-wave (S1)	106	4

7.3.2.1.Waltman Interval

The P-wave Fractogram anisotropy shows alternating zones with varying direction, but anisotropy is typically 5%-15% NE, N, or NW (Fig. 7.15). The variations in the Fractogram are relatively smooth because the function is constructed only at 1/4-mile velscan locations and interpolated in between. A zone of anomalously large (>30%), NE oriented anisotropy occurs in the southwest corner of the study area. This region has the highest dips of the rock units in the 3D-3C area, which suggests that artifacts may be introduced in the Fractogram due to the lack of prestack time migration (see above). Other regions show smaller, but discernible, correlations of structure with the Fractogram.

The S1 direction is dominantly easterly with magnitudes around 2%-5% (Fig. 7.16). The S1 map is more heterogeneous than the Fractogram; this is in part due to construction of S1 at every bin (110 ft) rather than at velscans only (1320 ft). Correlations with geological structure are not as apparent. There are only a few well-defined regions of relatively strong S1 anisotropy (mostly NE or NW) and there are two disorganized zones.

The magnitude of P-wave anisotropy can be either greater or less than S-wave anisotropy, depending on crack contents (Hudson, 1981; Crampin, 1984). As the Fractogram and converted-wave methods compute velocity anisotropies for P- and S-waves, respectively, direct comparison of anisotropies requires that some normalization is used. For both the Waltman and LFU intervals, dividing the Fractogram magnitudes by 2.6 brings the anisotropy-magnitude histograms into approximate agreement (Fig. 7.17).

The vector differences between the normalized Fractogram and S1 are dominantly NW, N, and NE (Fig. 7.18). This is consistent with the general NE- and NW-directions in the Fractogram compared to the E-orientations in S1. Quantitatively, mean difference vector is 1.6% anisotropy at azimuth 50.

Figure 7.15 P-wave Fractogram principal (fast) anisotropy direction and magnitude for Waltman from 3D-3C survey (vectors). NS/EW interval velocity from 3D-P survey (contoured)

Figure 7.16 S-wave principal (fast or S1) anisotropy direction and magnitude for Waltman) from 3D-3C survey (vectors. NS/EW interval velocity from 3D-P survey contoured.

Figure 7.17 Anisotropy histograms for Waltman (top) and LFU (bottom). P-wave Fractogram anisotropy has been approximately normalized to S-wave anisotropy by dividing Fractogram by 2.6.

Figure 7.18 Difference in anisotropy in LFU between normalized P-wave Fractogram and S1.

7.3.2.2. Lower Ft. Union Interval

The P-wave fractogram for the LFU is dominated by N-to-NW fast directions in the central and western portion of the survey, with mixed orientations elsewhere (Fig. 7.19). The largest amplitudes (again around 30%) occur toward the southwest, also NE-directed as in the Waltman.

S1 for the LFU is the most heterogeneous of the anisotropy maps (Fig. 7.20), although much of the survey can be characterized to have NE-to-SE directions. The east is highly disorganized.

The difference between the Fractogram and S1 (again with the Fractogram magnitudes divided by 2.6) is more strongly northerly (mean difference vector 1.9% anisotropy at azimuth 20), as expected for differences up to 45° between easterly S1 azimuths and NW-SE Fractogram azimuths.

Figure 7.19 P-wave Fractogram principal anisotropy direction and magnitude for LFU.

Figure 7.20 S-wave principal anisotropy direction and magnitude for LFU.

Figure 7.21 Difference in anisotropy in LFU between normalized P-wave Fractogram and S1.

7.3.2.3. Comparison With 2-Azimuth Results

Each of the four main 3D-3C anisotropy vector plots (7.15,7.16,7.19,7.20) is superimposed on an interval-velocity azimuthal ratio map from the larger 3D-P survey, allowing a visual comparison between the different methods. We can quantitatively rank the directional agreement by computing the number of bins in which the 3D-3C methods yield an azimuth of NW-to-NE where $V_{NS}/V_{EW} > 1$ in the 3D-P, and also where 3D-3C azimuths of NE-to-SE occur where 3D-P $V_{NS}/V_{EW} < 1$.

The two-azimuth method is "blind" to anisotropy at 45° to the selected principal directions, i.e., NW- or NE-fast zones will appear to be isotropic (V_{NS}/V_{EW} ~1). Compensation for such blind zones can be achieved by discounting two-azimuth measurements where the anisotropy is within some fraction χ of unity: $1-\chi < V_{NS}/V_{EW} < 1+\chi$ are not used in computing the fraction of locations in agreement. As χ is increased, regions of stronger NS or EW anisotropy are selected, which in principle should have the best correlations with NS or EW directions from S1 or the Fractogram. Note, however, that as regions of higher anisotropy are selected, the sample size decreases, and so the error on the estimate of the fraction in agreement will increase. In practice, we assume there are at most 100 independent samples corresponding to the entire 3D-3C map area; this is approximately the number of velscan locations in the 3D-3C survey. This effective

sample size is decreased in proportion to the fraction of the survey area surviving the anisotropy cutoff. The standard errors are then estimated assuming the samples are drawn from a binomial distribution. Computing the agreement between the two- and four-azimuth methods over all the interpolated map points is effectively a smoothing filter, but the errors are calculated assuming a sample size more representative of the original data.

With no two-azimuth anisotropy cutoff, the detailed agreement with the four-azimuth methods (Fig. 7.22) is little better than that expected by chance (although the mean directions are comparable; see Table 7.2 above). Indeed, the Fractogram for the LFU agrees with the two-azimuth results at less than 50% of the test locations, which suggests some systematic error is present. As the S1 correlation with the two-azimuth result (and geological data) is better, the systematic error is likely in the Fractogram method.

Within the Waltman, S1 correlates better with the two-azimuth anisotropy than does the Fractogram. Where the two-azimuth anisotropy exceeds about 7% however, significant improvement in the correlations with both S1 and the Fractogram begin. In other words, the fast direction in the Waltman inferred from the two-azimuth method is likely robust when the two-azimuth anisotropy exceeds about 7%.

Within the LFU, the S1 and Fractogram techniques give divergent results. The match between the fast P-wave direction as measured by the two-azimuth and four-azimuth (Fractogram) methods steadily increases with increasing anisotropy magnitude. The improvement begins at 5% two-azimuth anisotropy and levels off above 12%; in broad agreement with the cutoff level of 7% seen for the Waltman. However, the S1 match with the two-azimuth directions is not monotonic; the best agreement is found at about 8% two-azimuth anisotropy, with poorer correlations at higher anisotropy magnitudes. This could be an unrepresentative result, as the regions of highest two-azimuth anisotropy are near edges of the 3D-3C survey, where the S1 directions appear to become disorganized (Fig. 7.20).

Figure 7.22 Comparison of 2-azimuth and 4-azimuth methods. For Waltman, agreement increases dramatically for both Fractogram and S1 once 2-azimuth anisotropy exceeds about 6-8%. Methods diverge for LFU: 2-azimuth match with Fractogram steadily increases, whereas S1 has best match at about 8% 2-azimuth anisotropy. Note LFU Fractogram agreement is less than 50% at small 2-azimuth anisotropy, suggesting some systematic error. Bottom panel is identical to top, but superimposes estimated errors.

7.4. Conclusions: 3D-3C

There is mixed similarity of the principal directions and magnitudes of anisotropy derived from the two-azimuth P-wave interval velocities and the four-azimuth P-wave Fractogram and P-to-S converted-wave analysis (S1). While the average values over the survey area are in general agreement, there are many small-scale discrepancies. The two kinds of maps for the Waltman derived from four-azimuth data have somewhat better agreement than for the LFU interval. At low anisotropy magnitudes (as measured by two-azimuth interval-velocity ratio), the S1 azimuth generally better matches the two-azimuth anisotropy direction than does the Fractogram; this could be due to systematic errors in the latter. At two-azimuth anisotropies above about 8-10%, however, the Fractogram is the better match. Both four-azimuth methods in the Waltman correlate significantly better with the two-azimuth results for two-azimuth anisotropies above 6-8%. The LFU Fractogram correlation improves rapidly between 5 and 12%, but the LFU S1 correspondence decreases above 8%. This last behavior may be an artifact due to the location of strong anomalies on the periphery of the survey area. Other factors that could account for discrepancies between the four-azimuth methods include non-hyperbolic moveouts, errors in layer-stripping, misalignment of the normal-moveout ellipse and S1 azimuth, presence of multiple fracture sets, and effects of structural complexity. The last may be particularly important because the 3D-3C data were prestack processed through dip-moveout (DMO) only and not migrated. Incomplete repositioning of reflectors may have introduced noticeable biases into both the two-azimuth 3D-3C P-wave interval velocities and the Fractogram.

Mean S-wave anisotropy of 3-4% (Table 7.2) implies comparable fracture porosities, and the greater P- over S-wave anisotropy suggests that these fractures are largely gas-filled (Hudson, 1981; Crampin, 1984). The mean P-wave anisotropies derived by the Fractogram are unreasonably large, especially relative to the S-wave anisotropies; a factor of two in P-to-S anisotropy would be realistic (Hudson, 1981; Crampin, 1984). Comparison of the two-azimuth and four-azimuth methods indicates that the former approach is robust for apparent anisotropies above about 8%.

FINAL 3D-3C SHOT-RECEIVER LOCATION MAP

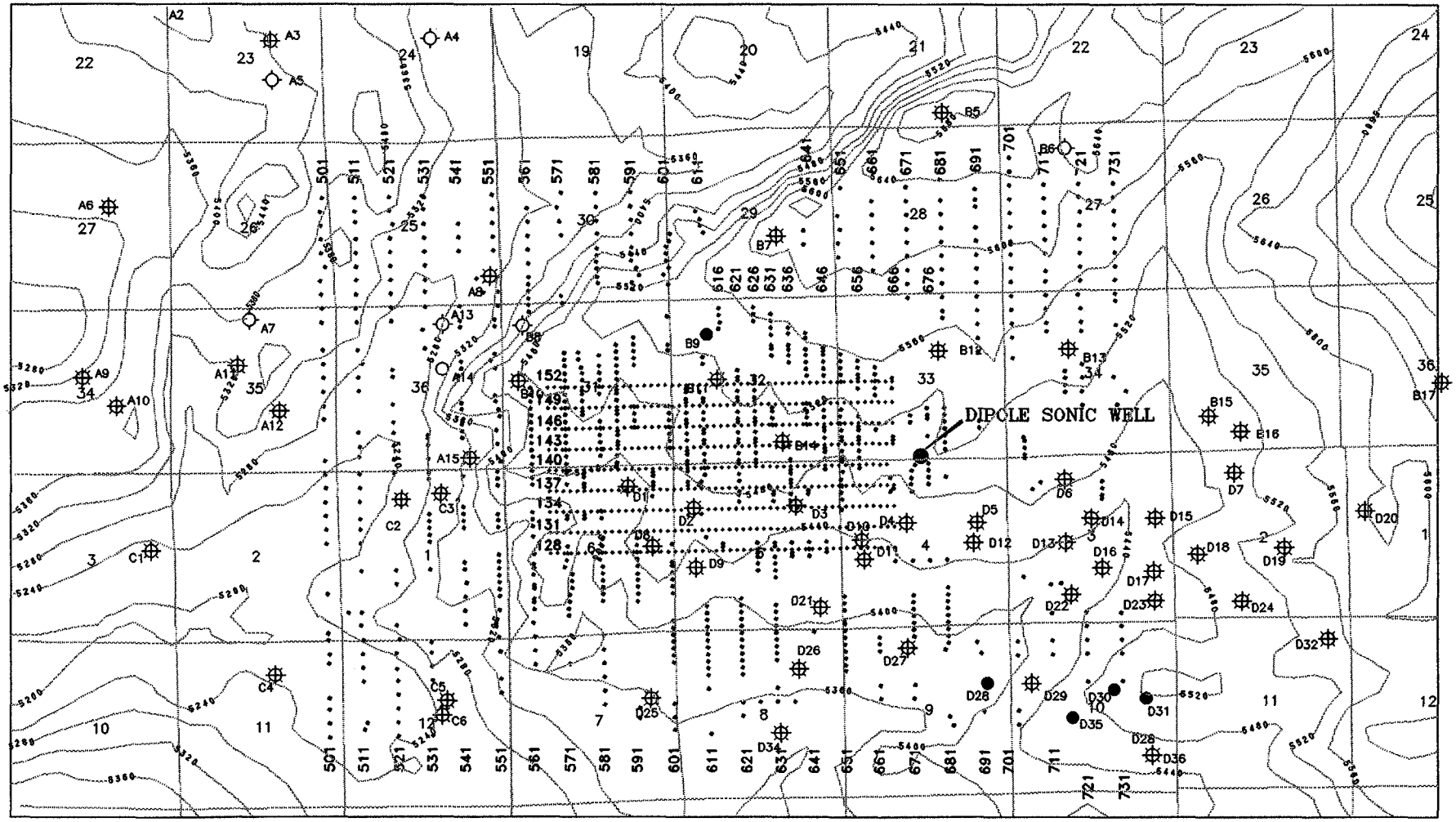

LEGEND
SHOTS = RED CROSSES
RECEIVERS = BLUE CIRCLES

SCALE IN FEET
2000 0 2000 4000 6000 8000 10,000 12,000

Figure 7–1

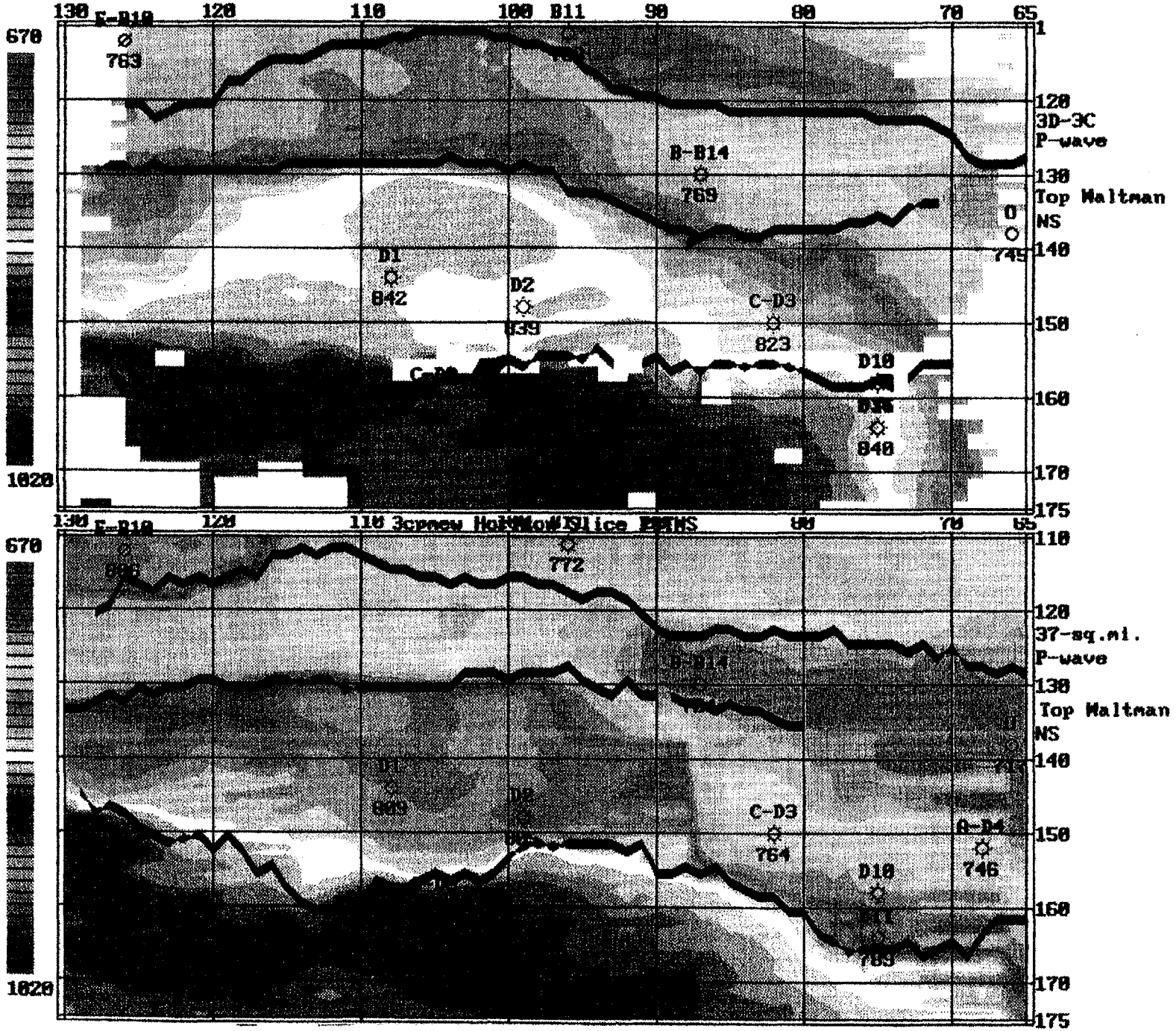

TOP WALTMAN TIME STRUCTURE NS

Figure 7-2

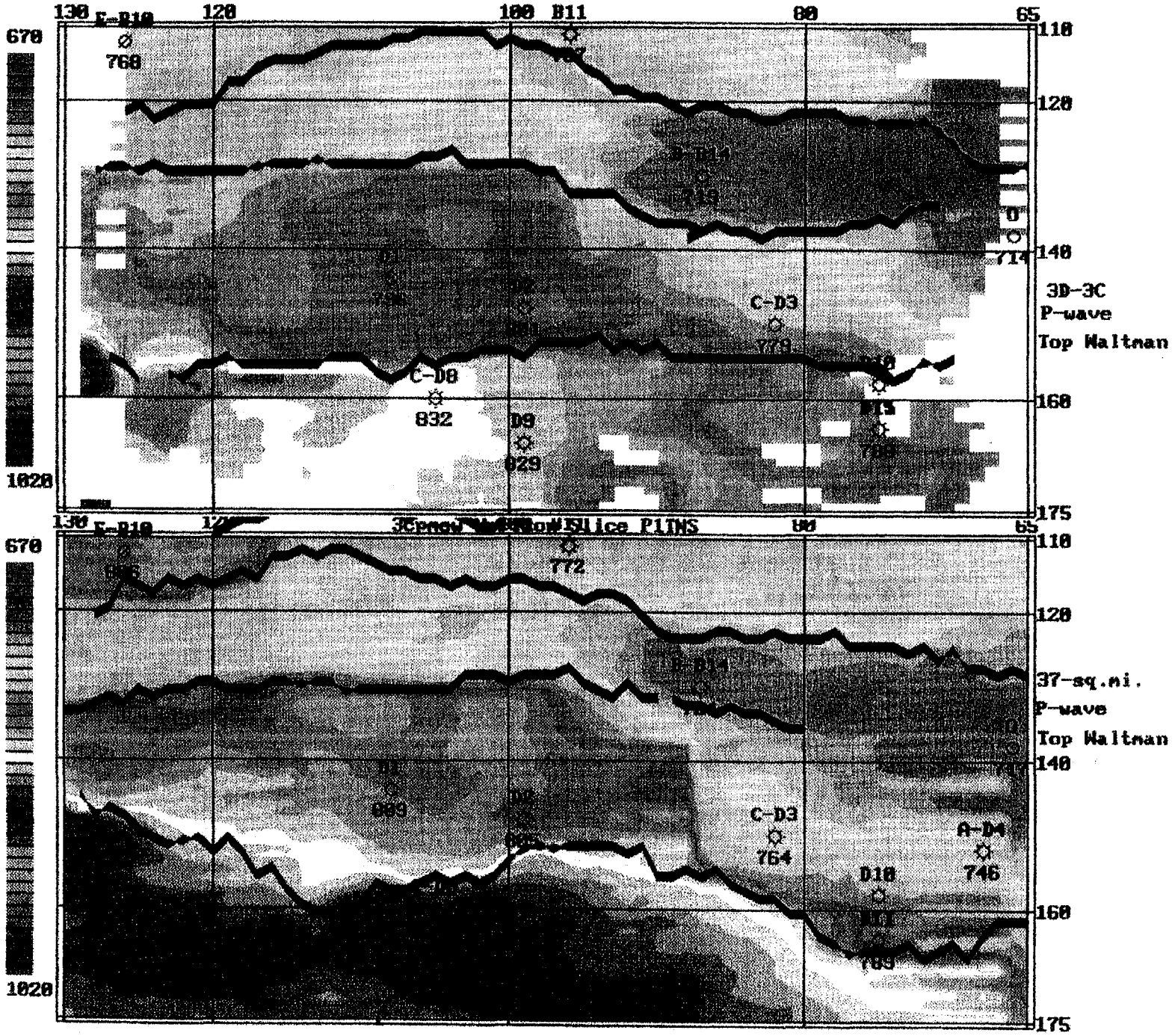

TOP WALTMAN TIME STRUCTURE EW

Figure 7-3

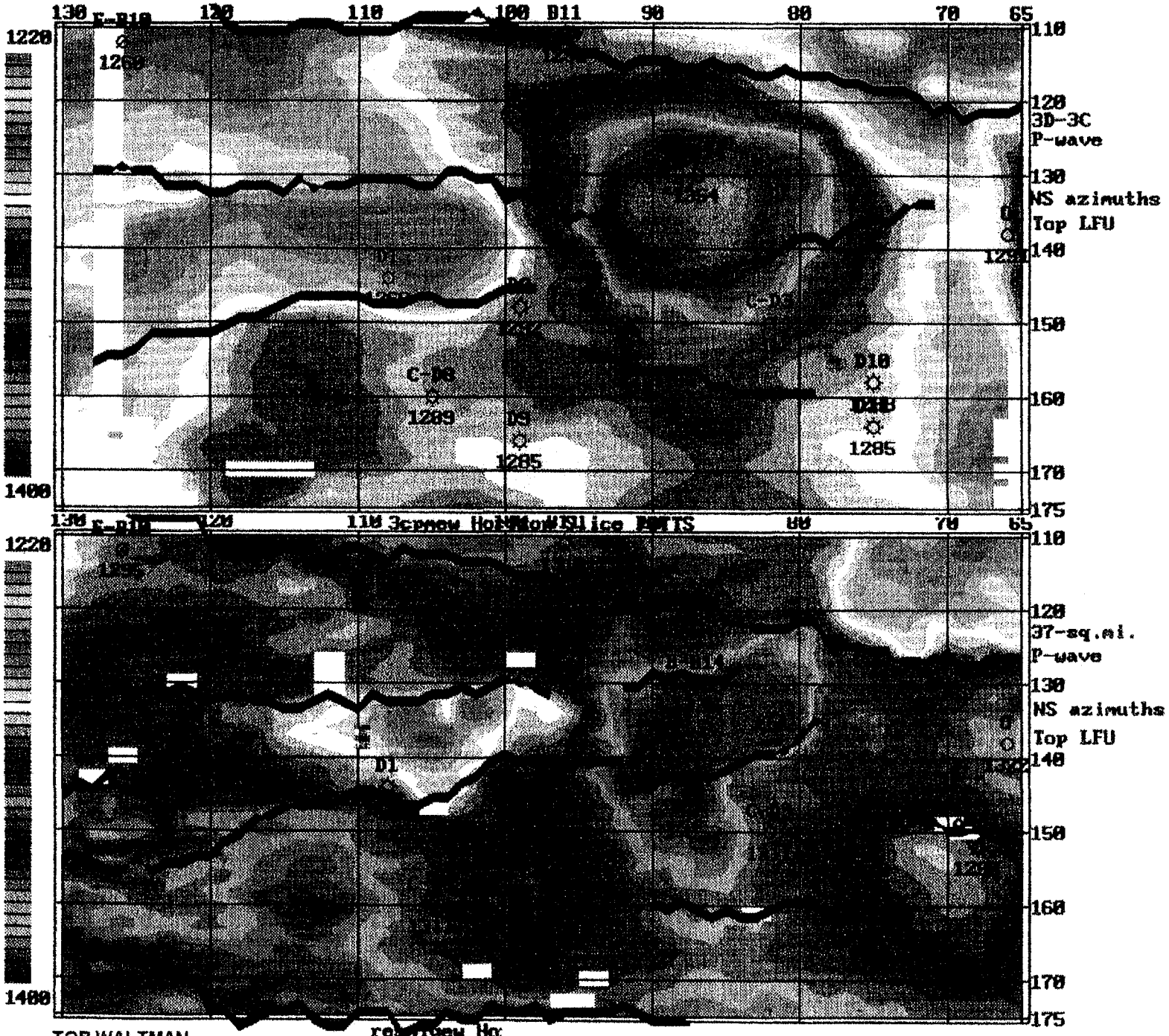
130
120
110
100
D11
90
80
70
65
1220
1400
110
120
3D-3C
P-wave
130
NS azimuths
Top LFU
140
150
160
170
175
1289
1285
1220
1400
37-sq.mi.
P-wave
NS azimuths
Top LFU
TOP WALTMAN
TIME STRUCTURE TLFU NS

Figure 7-4

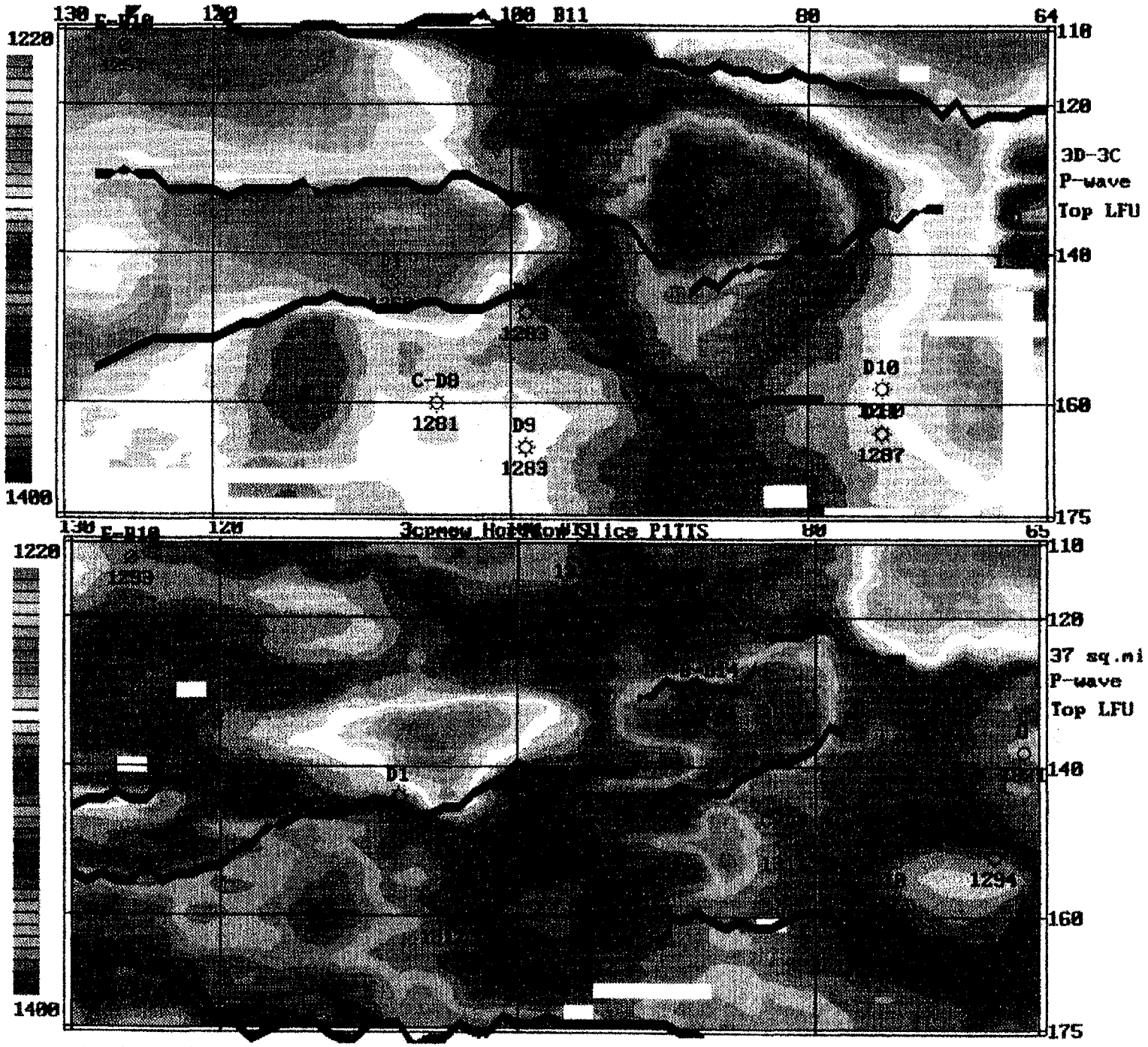

TOP WALTMAN

TIME STRUCTURE TLFU EW

Figure 7-5

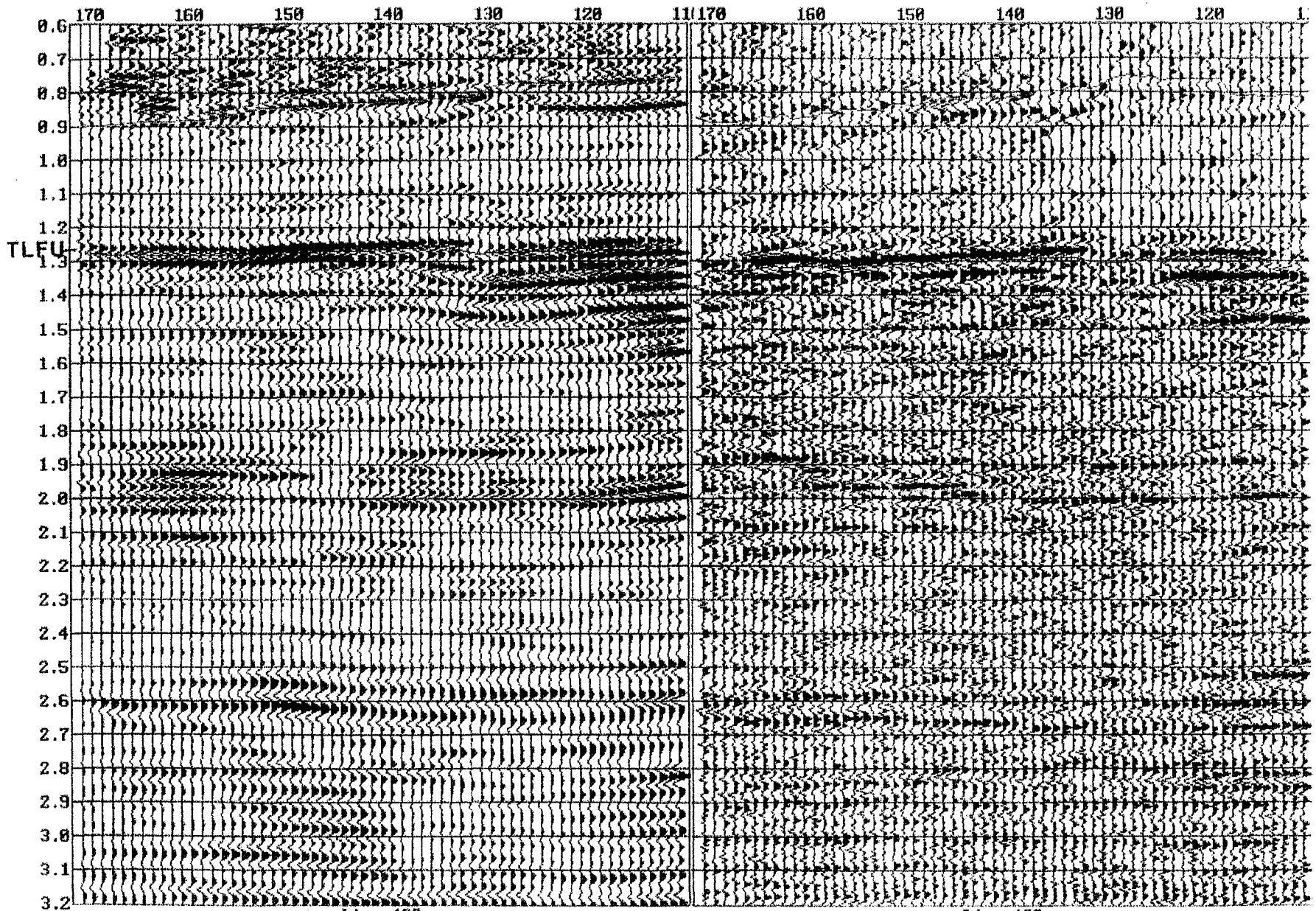

EW azimuths
3D-3C

37 sq. mile P-P

Figure 7-6

DIX INTERVAL VELOCITY ; TOP WALTMAN TO TOP LFU ; RATIO NS / EW
3-C SURVEY ; P-WAVES

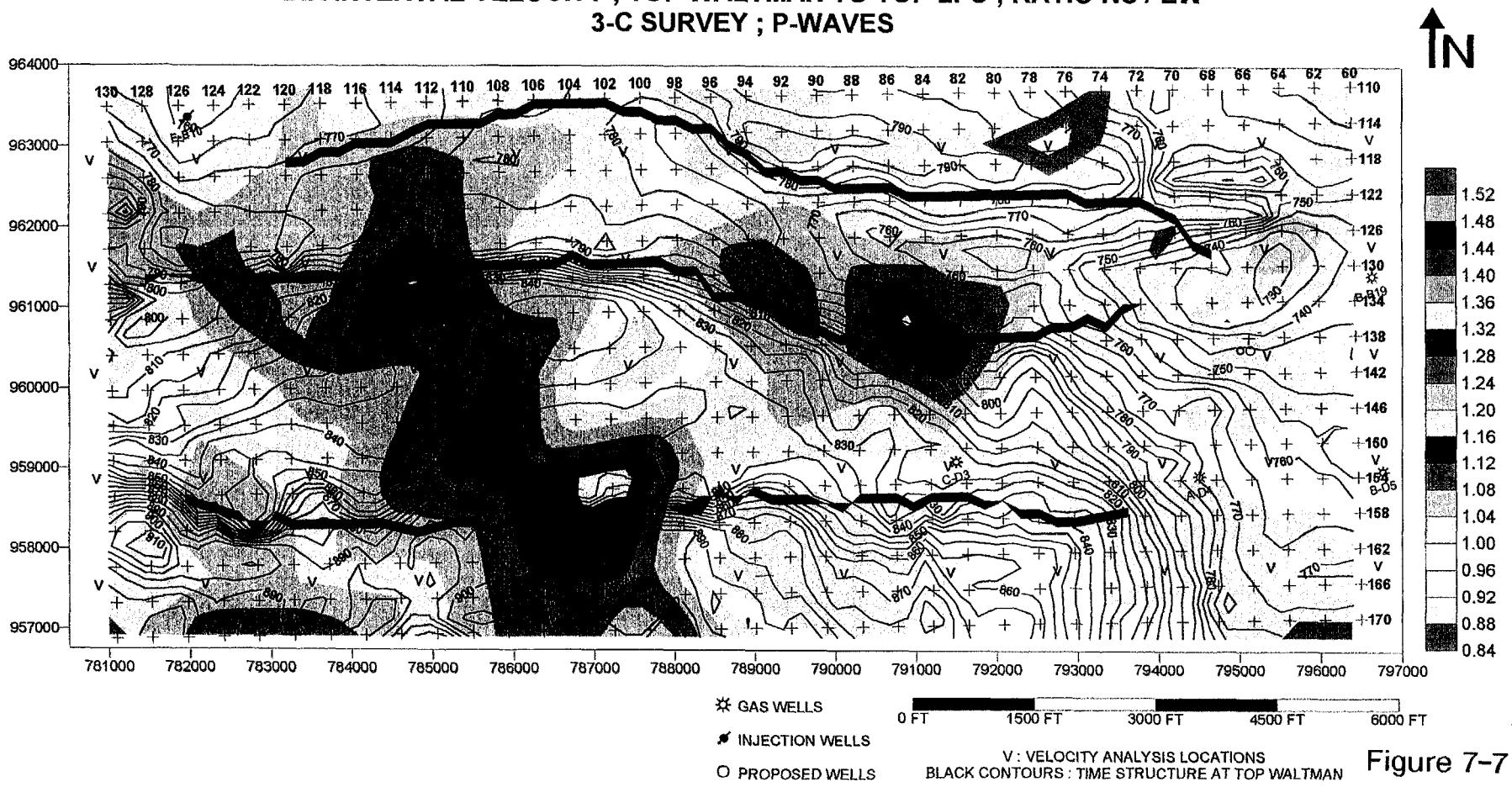

Figure 7-7

DIX INTERVAL VELOCITY ; TOP WALTMAN TO TOP LFU ; NS / EW
37 SQ. MILES SURVEY

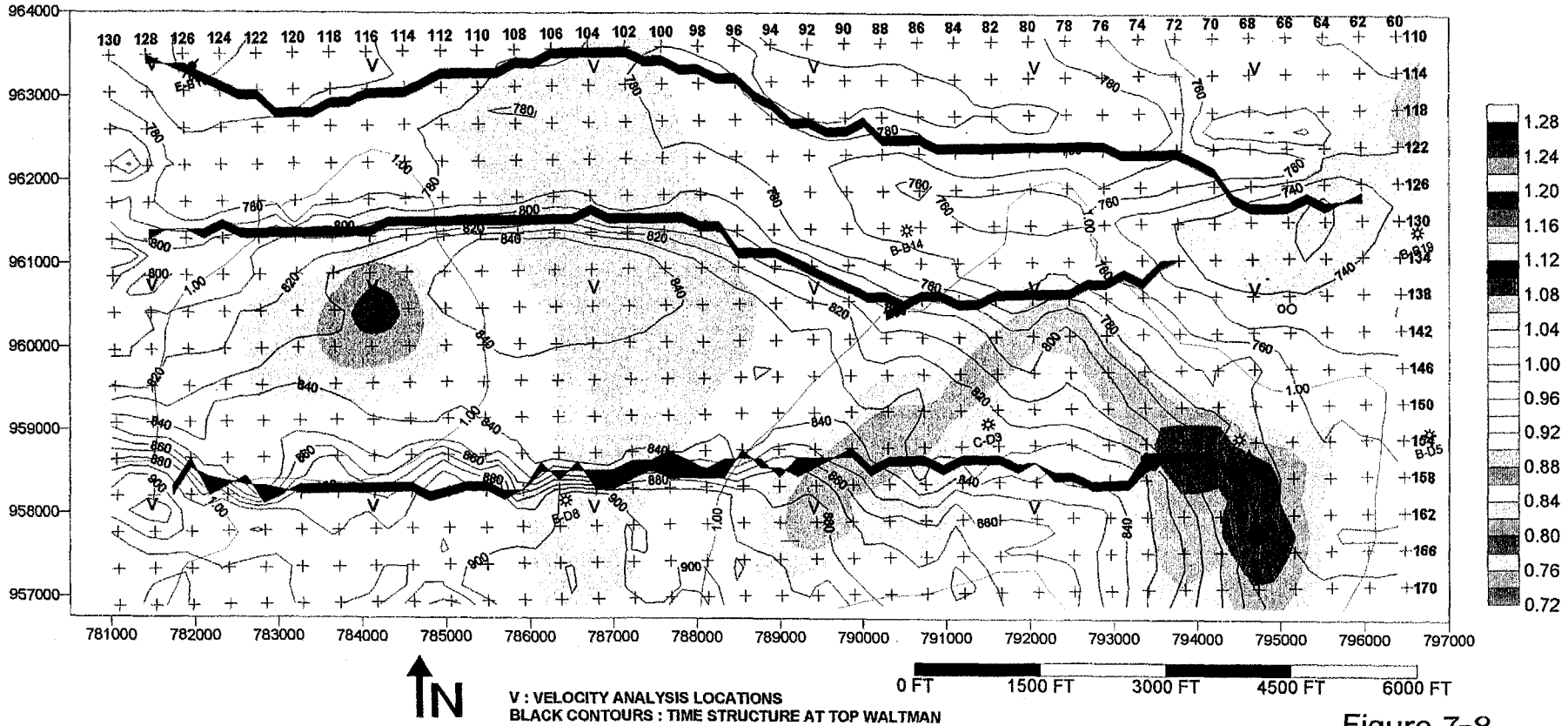

V : VELOCITY ANALYSIS LOCATIONS
BLACK CONTOURS : TIME STRUCTURE AT TOP WALTMAN

Figure 7-8

DIX INTERVAL VELOCITY ; TOP LFU TO TOP LFU + 300 ; RATIO NS / EW
3-C SURVEY ; P-WAVES

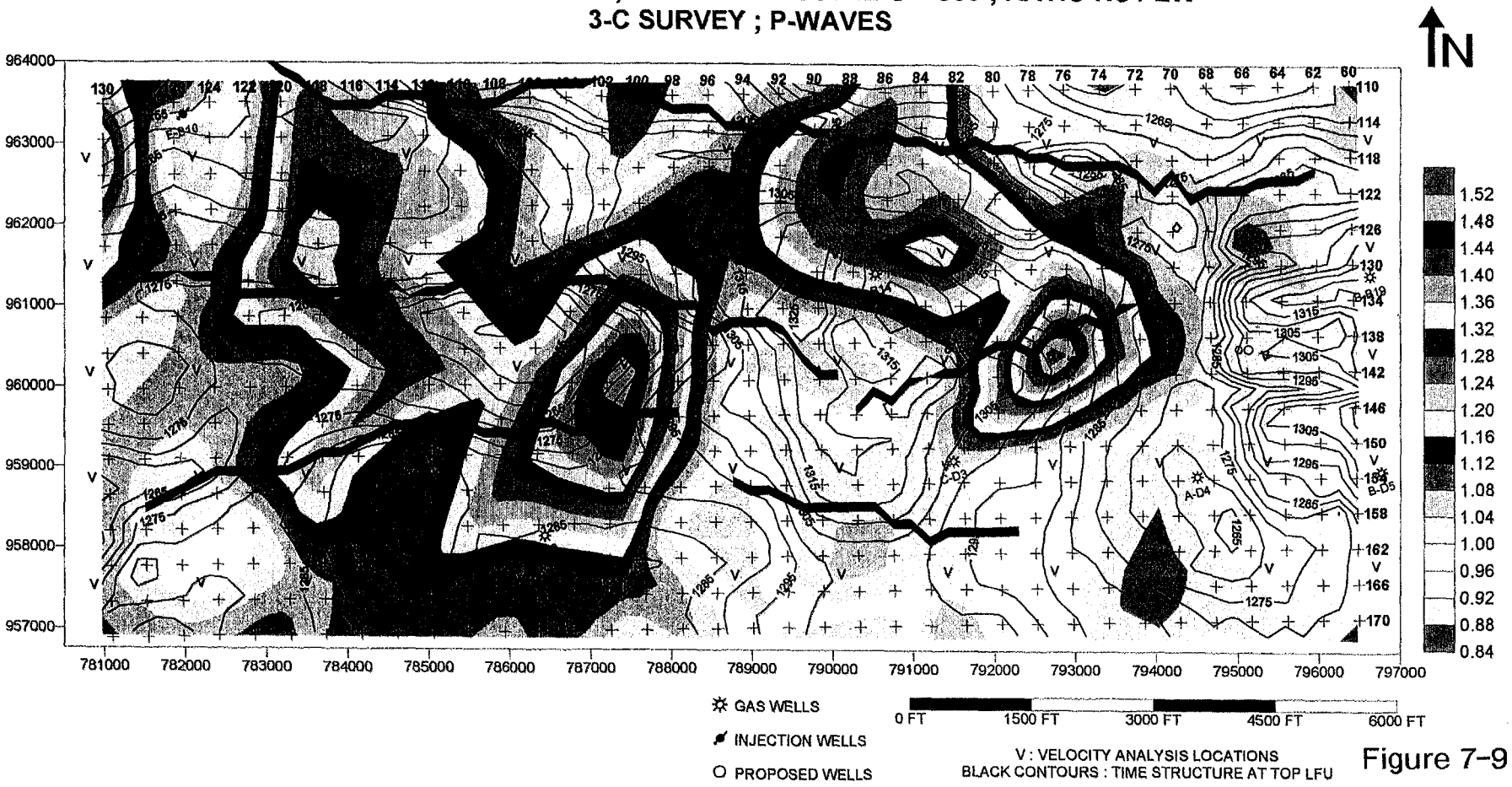

Figure 7-9

DIX INTERVAL VELOCITY ; TOP LFU TO TOP LFU + 300 MS ; NS / EW
37 SQ. MILES SURVEY

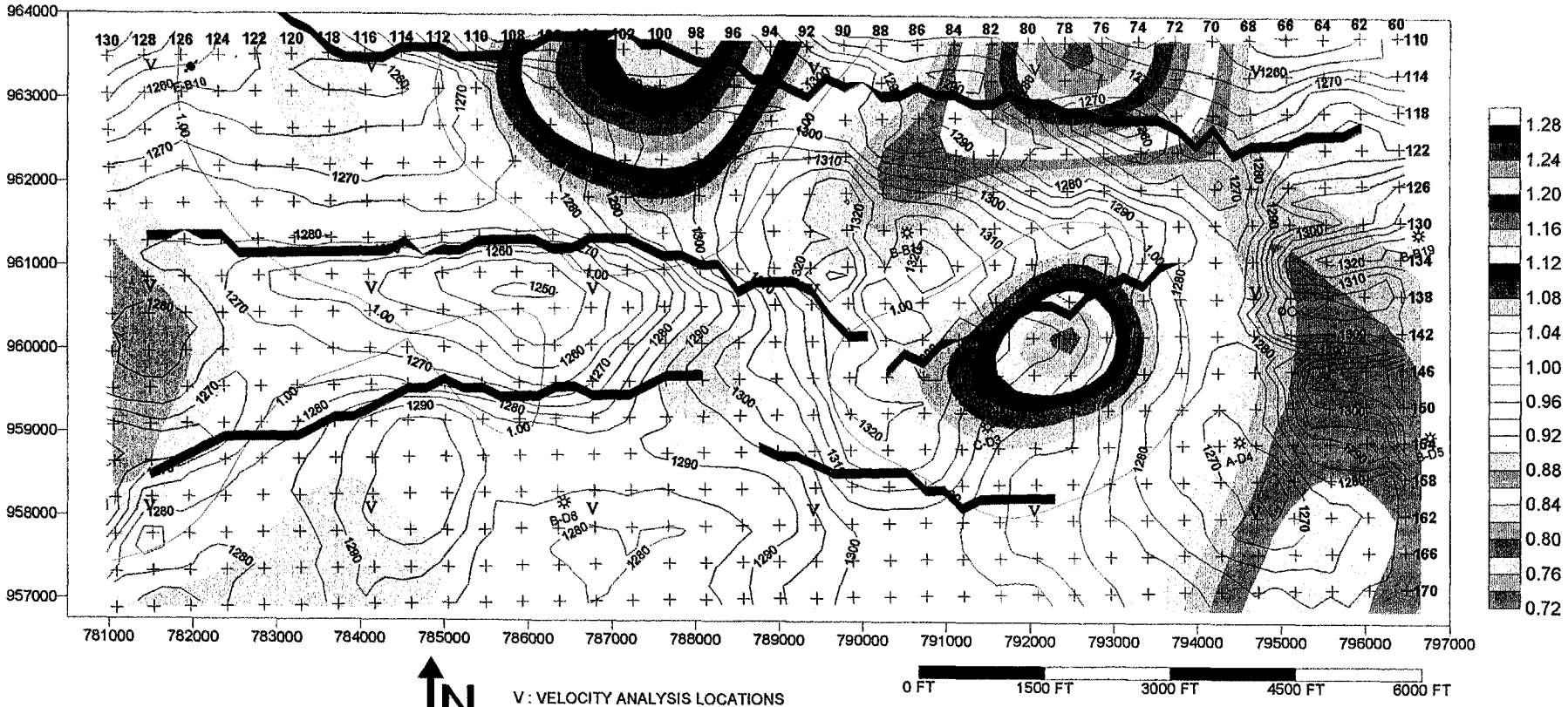

Figure 7-10

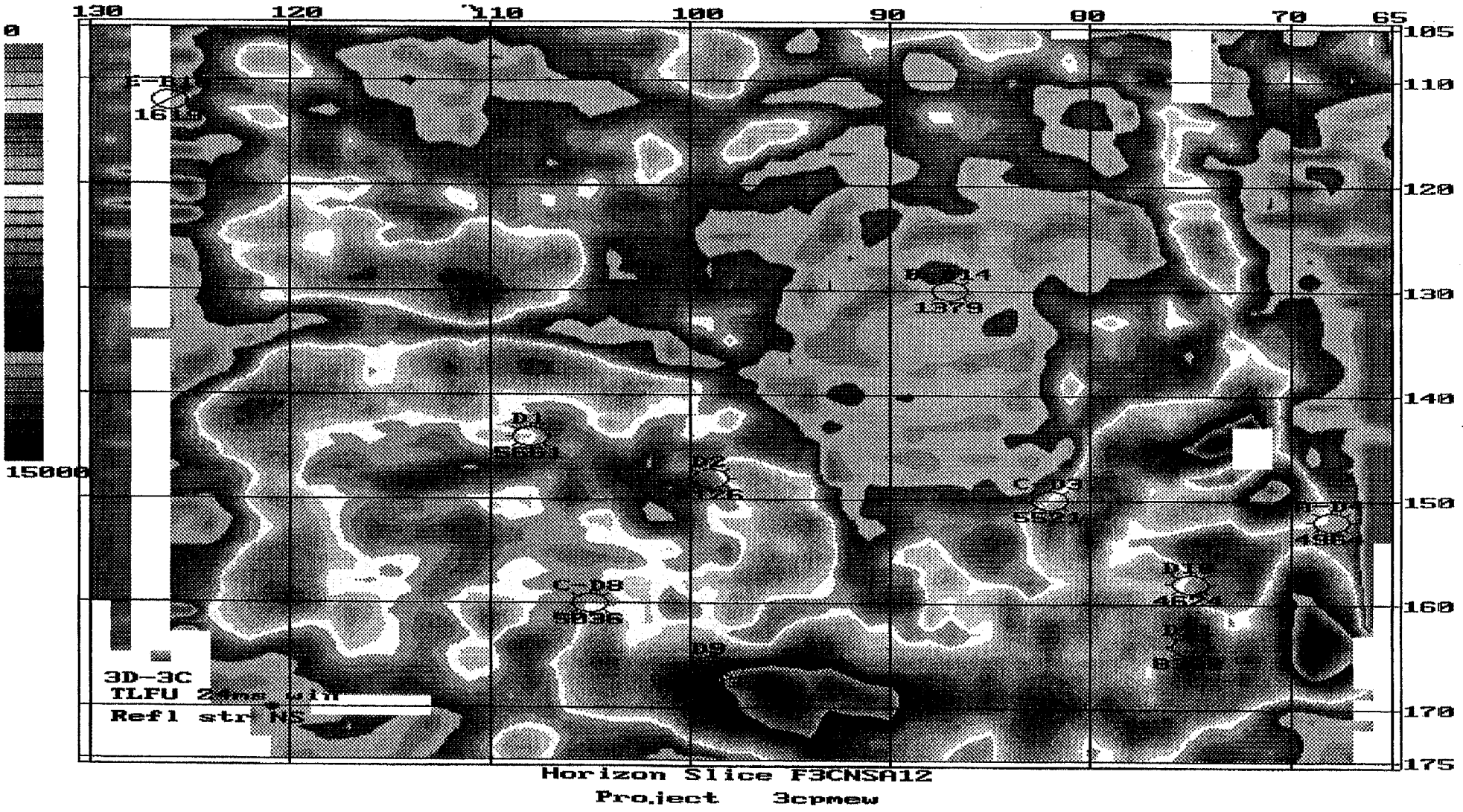
130
120
110
100
90
80
70
65
105
110
120
130
140
150
160
170
175
0
15000
1379
3D-3C
TLFU 24ms win
Refl str NS
Horizon Slice F3CNSA12
Project 3cpnew

Figure 7-11

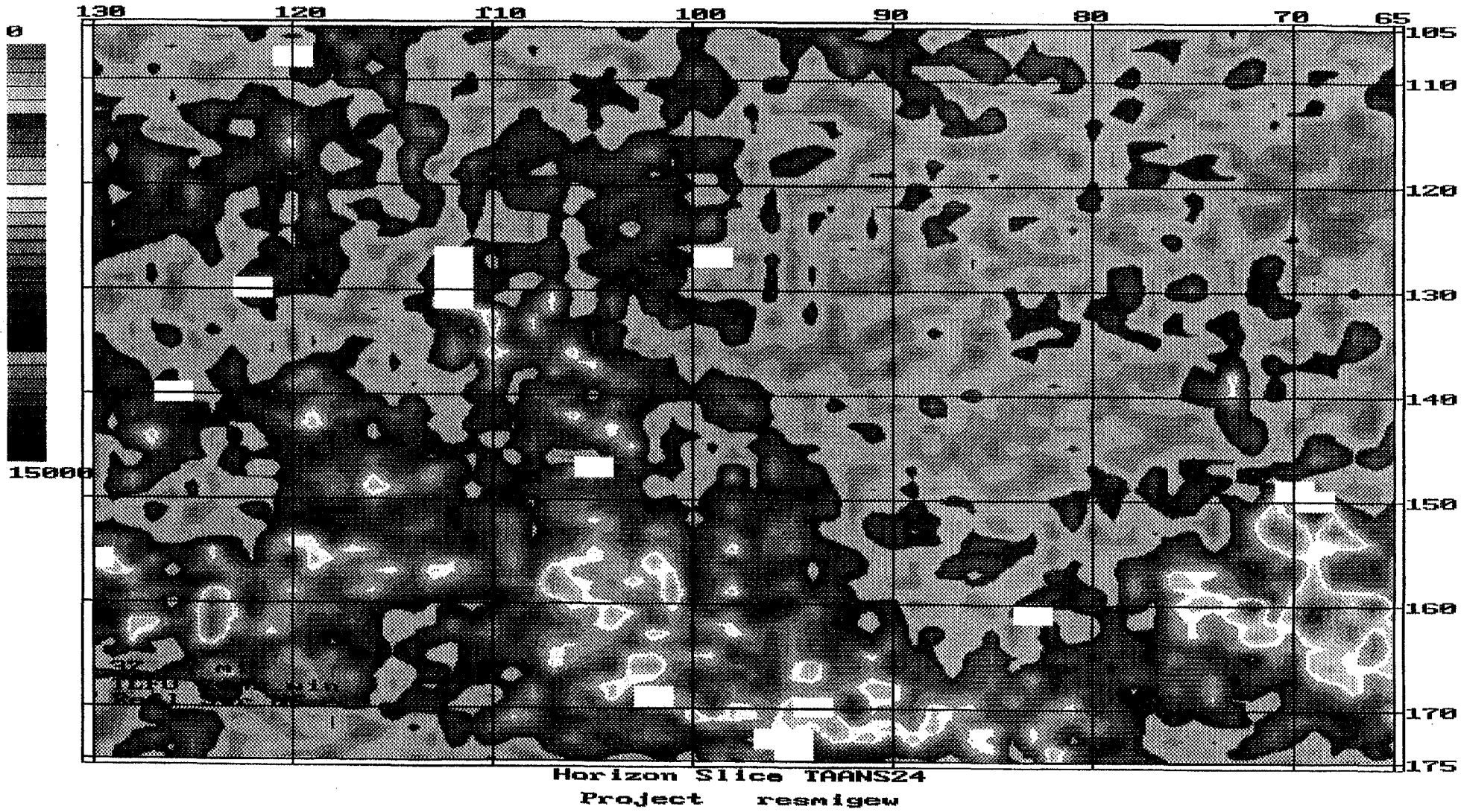
130
120
110
100
90
80
70
65
0
15000
105
110
120
130
140
150
160
170
175
Horizon Slice TAANS24
Project resmigew

Figure 7-12

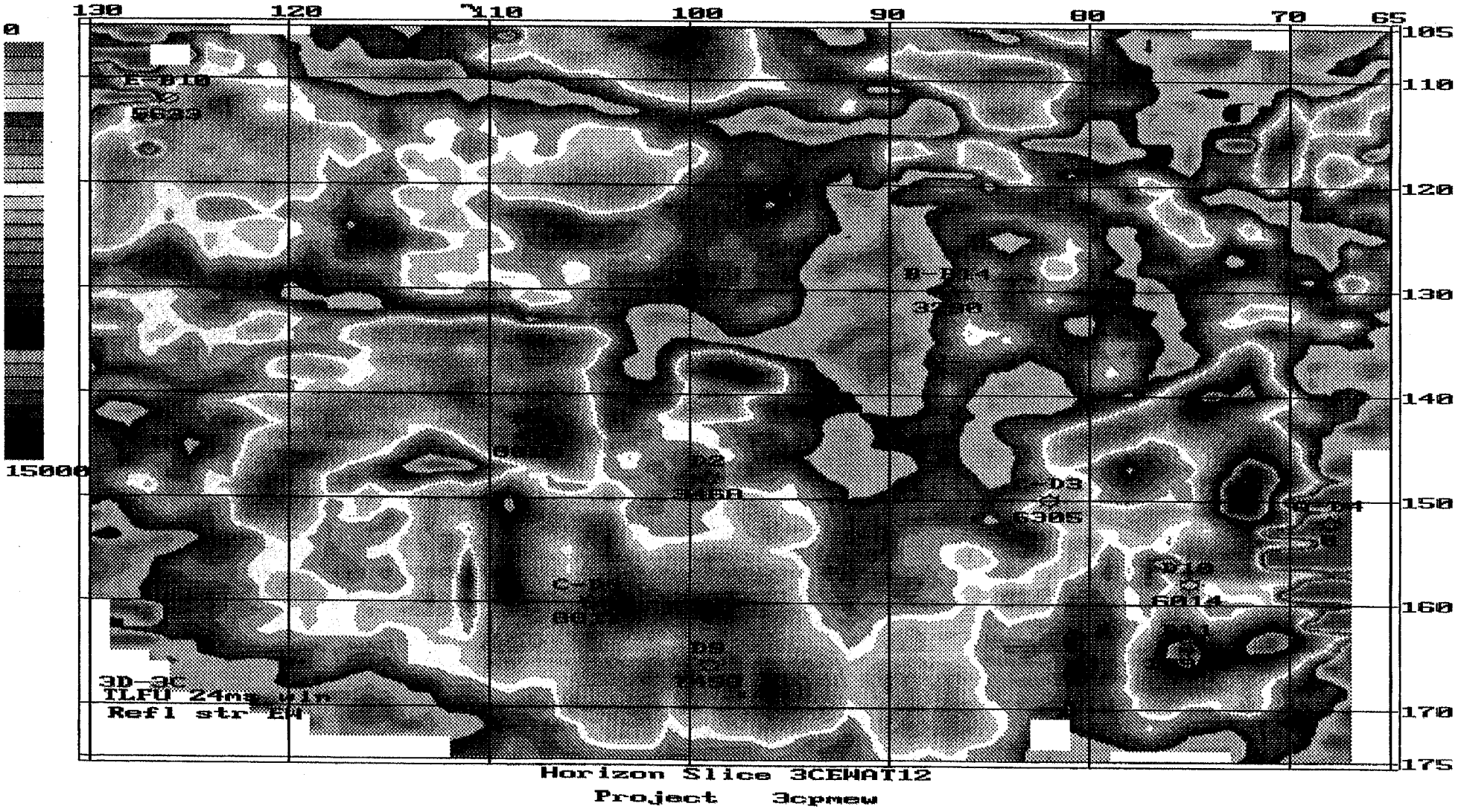
130
120
110
100
90
80
70
65
105
110
120
130
140
150
160
170
175
0
15000
E-B10
5633
C-D9
5305
D-D4
5014
3D-3C
ILFU 24ms win
Refl str EW
Horizon Slice 3CEWAT12
Project 3cpmew

Figure 7-13

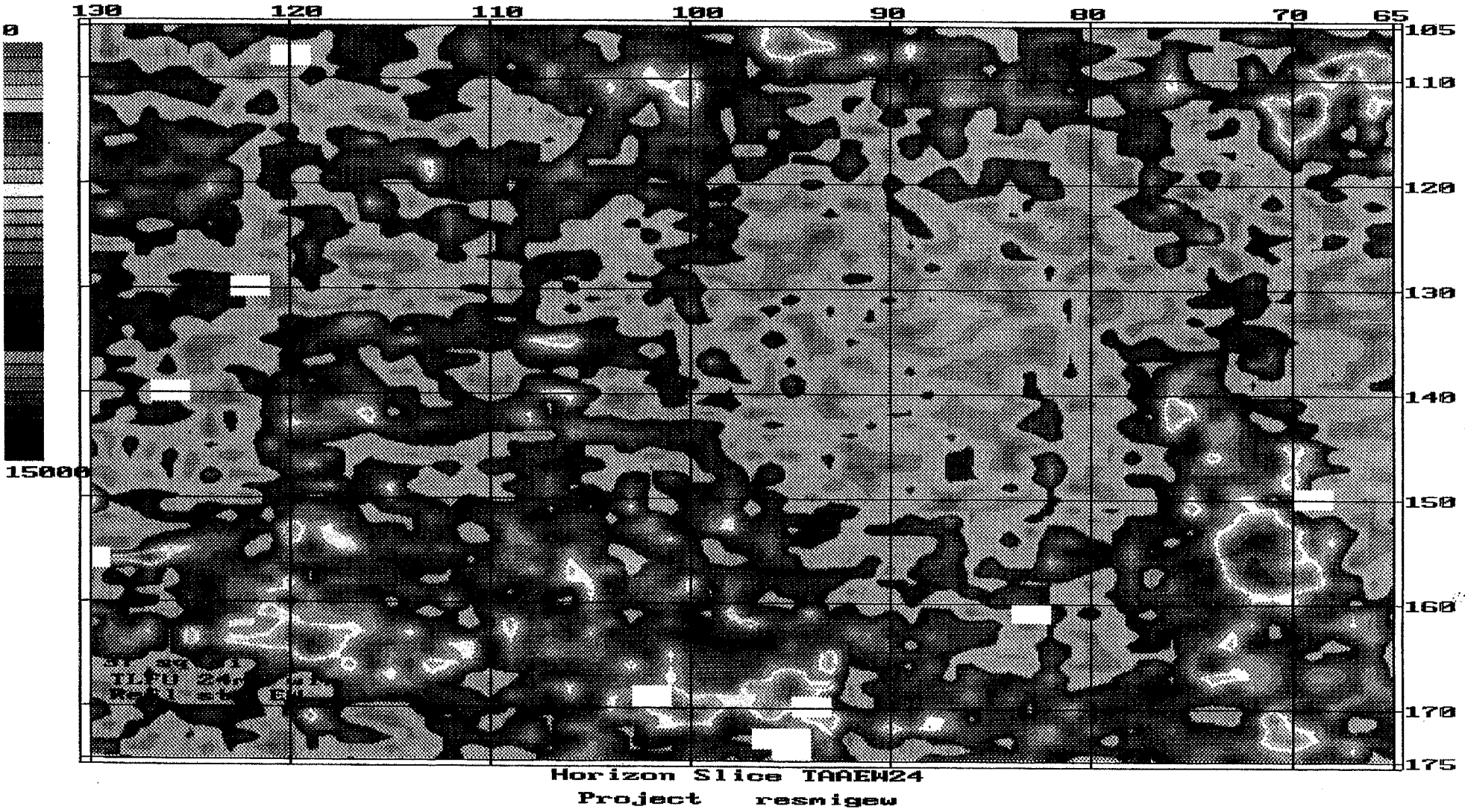
130
120
110
100
90
80
70
65
105
110
120
130
140
150
160
170
175
0
15000
Horizon Slice TAAEW24
Project resmigew

Figure 7-14

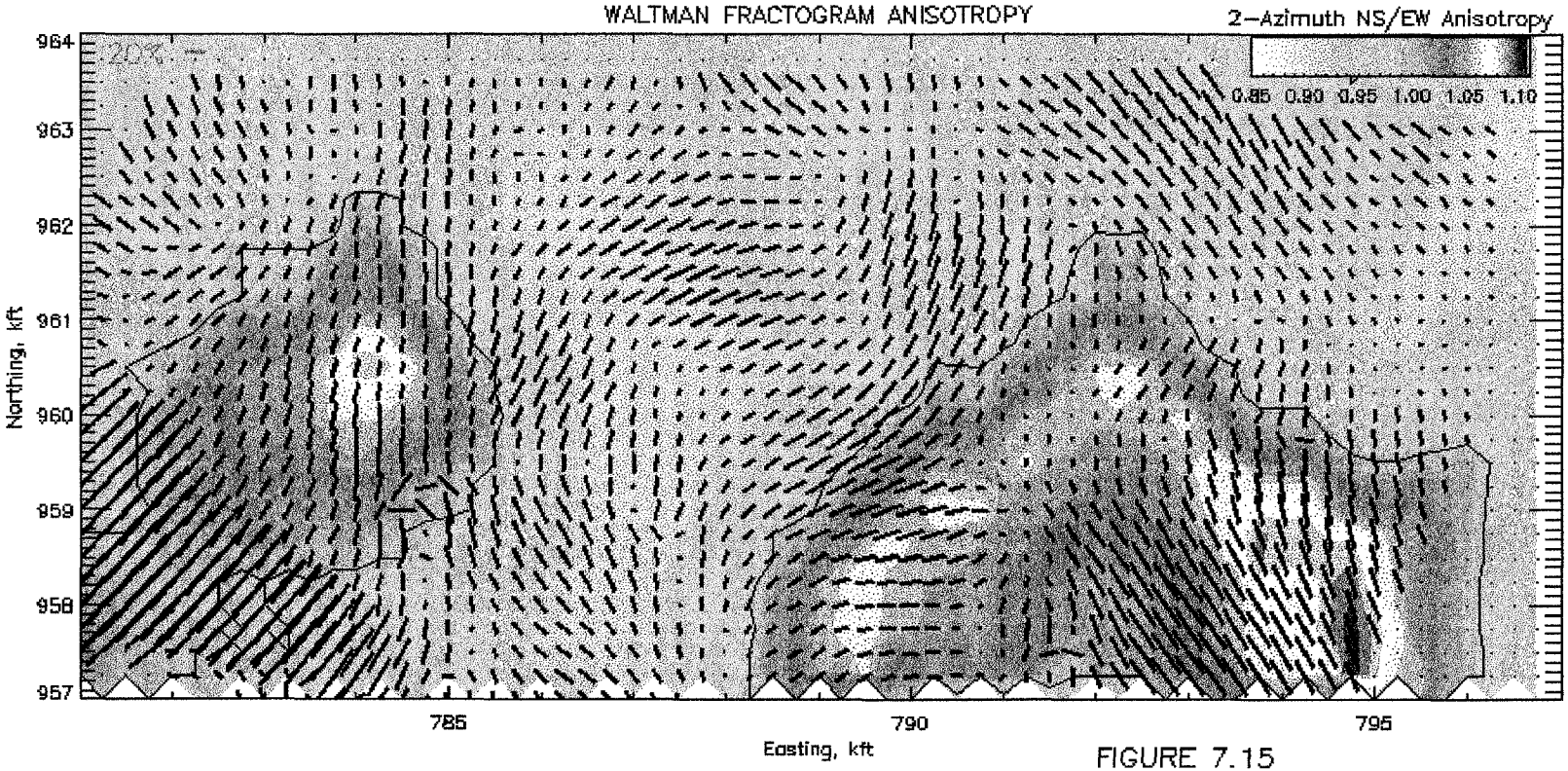
WALTMAN FRACTOGRAM ANISOTROPY
2-Azimuth NS/EW Anisotropy
0.85 0.90 0.95 1.00 1.05 1.10
964
963
962
961
960
959
958
957
Northing, kft
785
790
795
Easting, kft

FIGURE 7.15

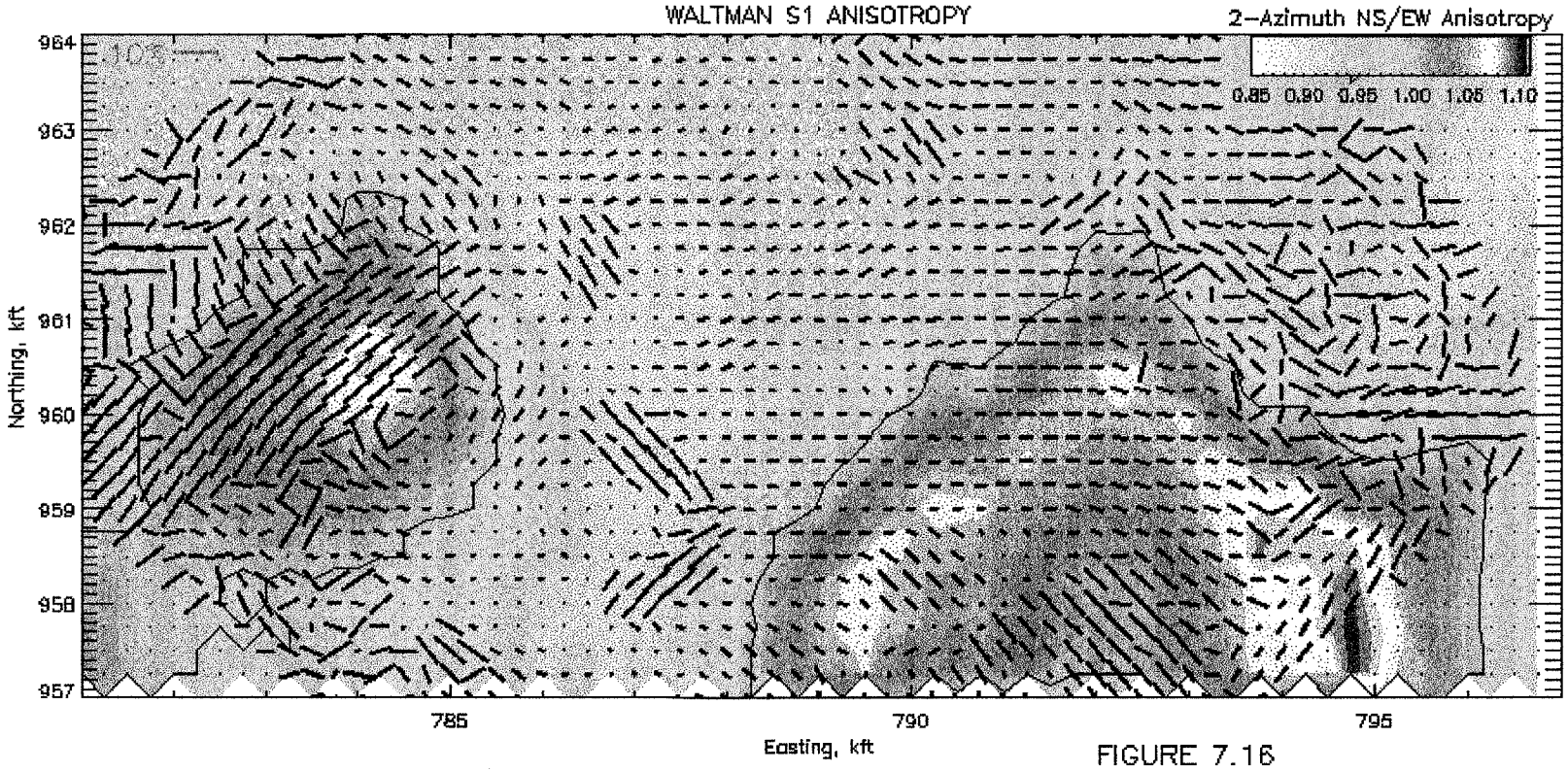
WALTMAN S1 ANISOTROPY
2-Azimuth NS/EW Anisotropy
0.85 0.90 0.95 1.00 1.05 1.10
964
963
962
961
960
959
958
957
Northing, kft
785
790
795
Easting, kft

FIGURE 7.16

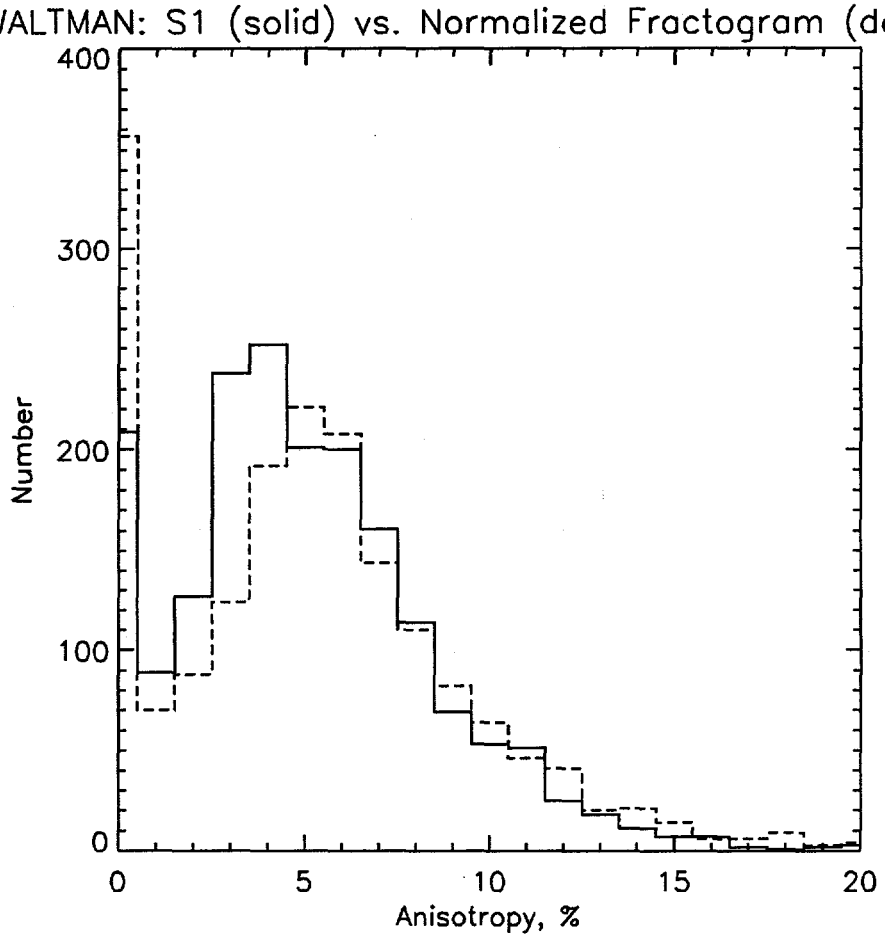
WALTMAN: S1 (solid) vs. Normalized Fractogram (dashed)
400
300
200
100
0
Number
0
5
10
15
20
Anisotropy, %

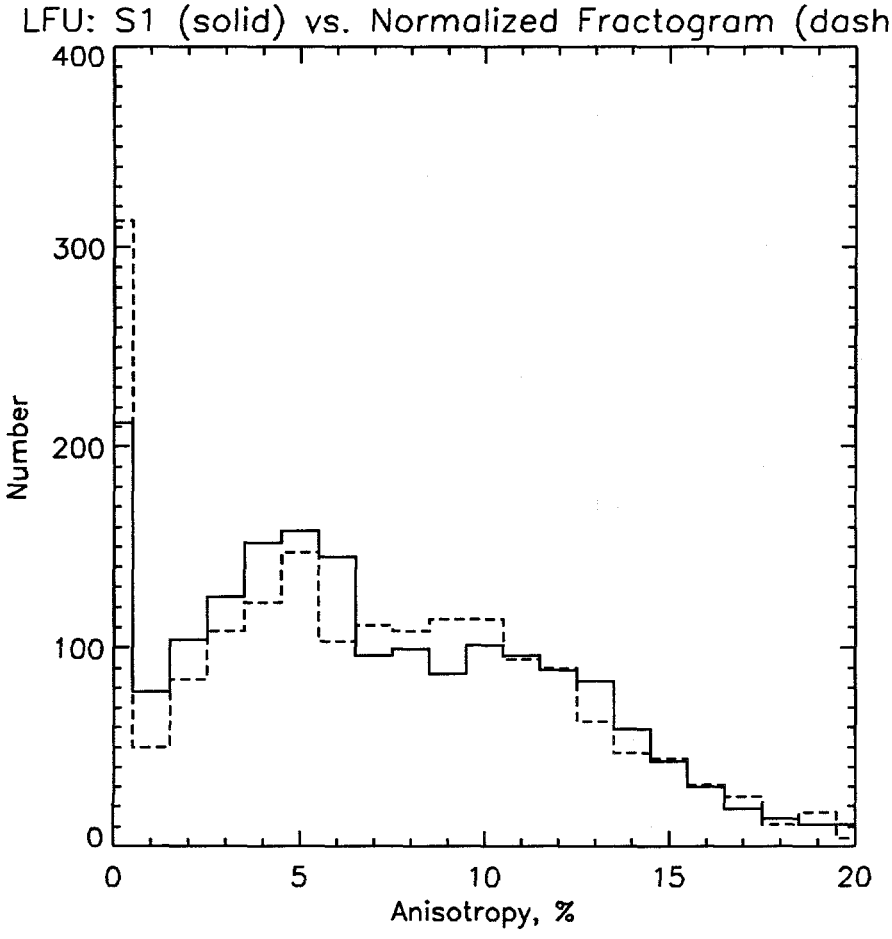
LFU: S1 (solid) vs. Normalized Fractogram (dashed)
400
300
200
100
0
Number
0
5
10
15
20
Anisotropy, %

Figure 7-17

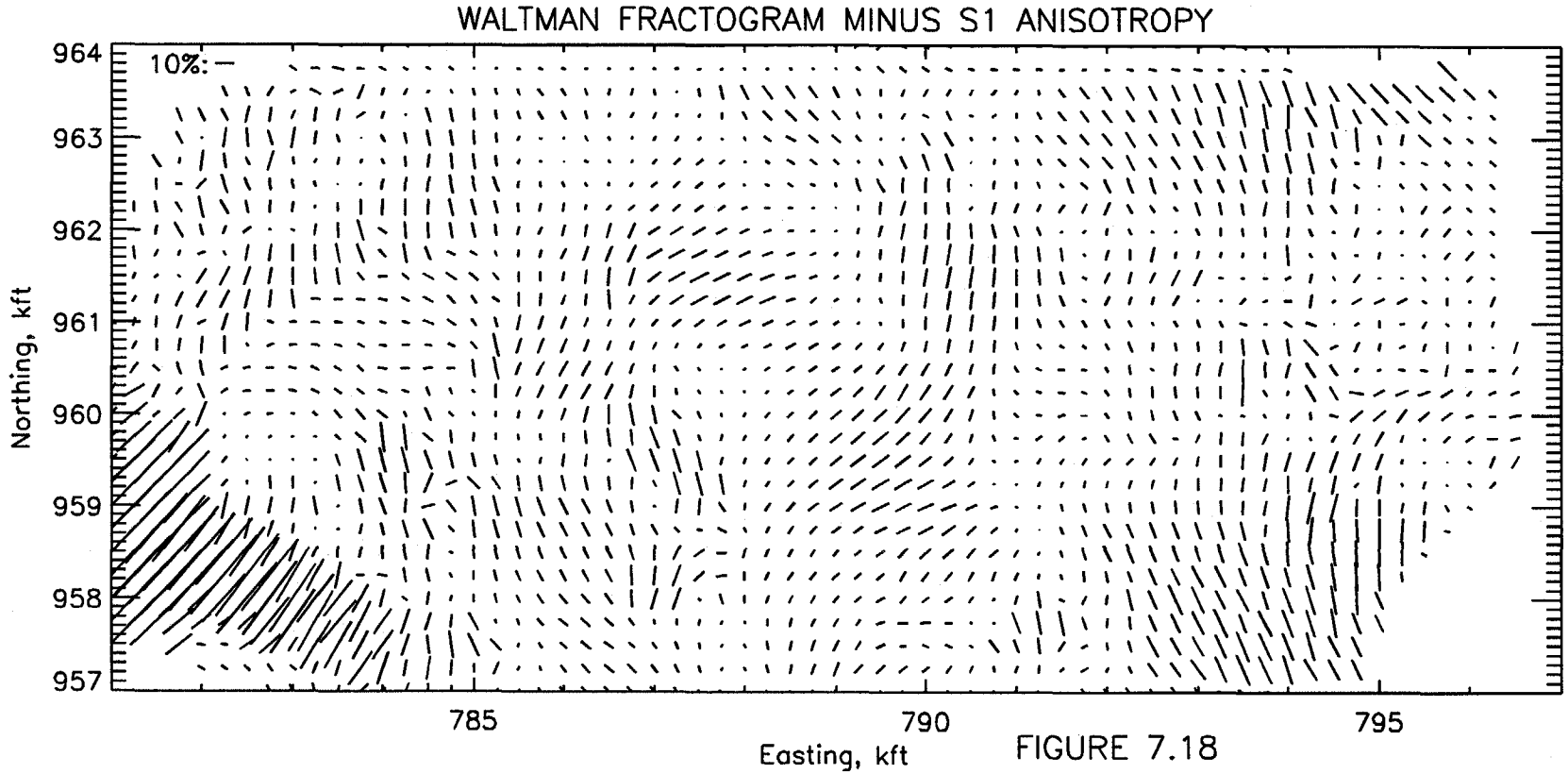
WALTMAN FRACTOGRAM MINUS S1 ANISOTROPY
10%:
964
963
962
961
960
959
958
957
Northing, kft
785
790
795
Easting, kft

FIGURE 7.18

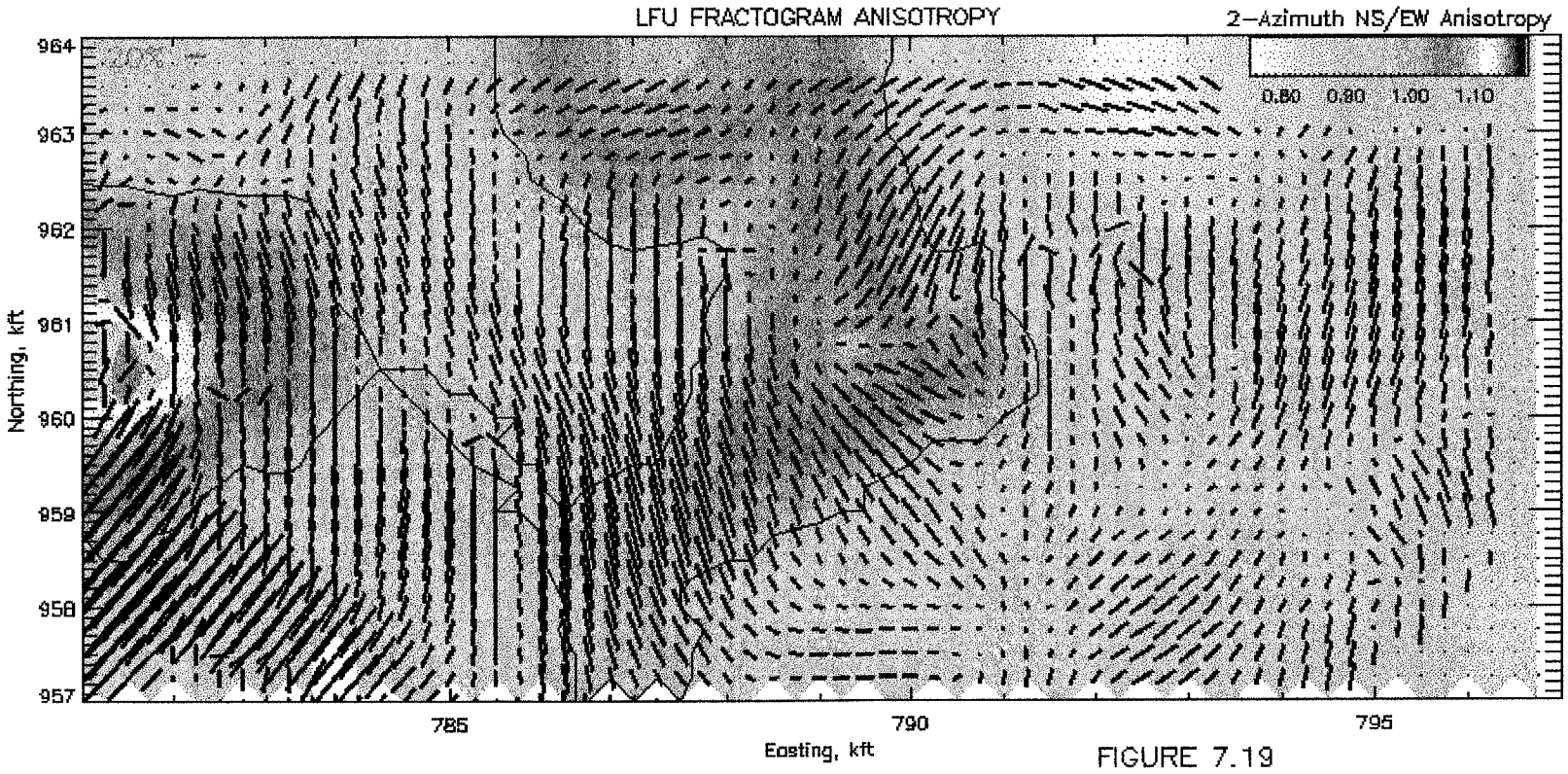
LFU FRACTOGRAM ANISOTROPY
2-Azimuth NS/EW Anisotropy
0.80
0.90
1.00
1.10
964
963
962
961
960
959
958
957
Northing, kft
785
790
795
Easting, kft

FIGURE 7.19

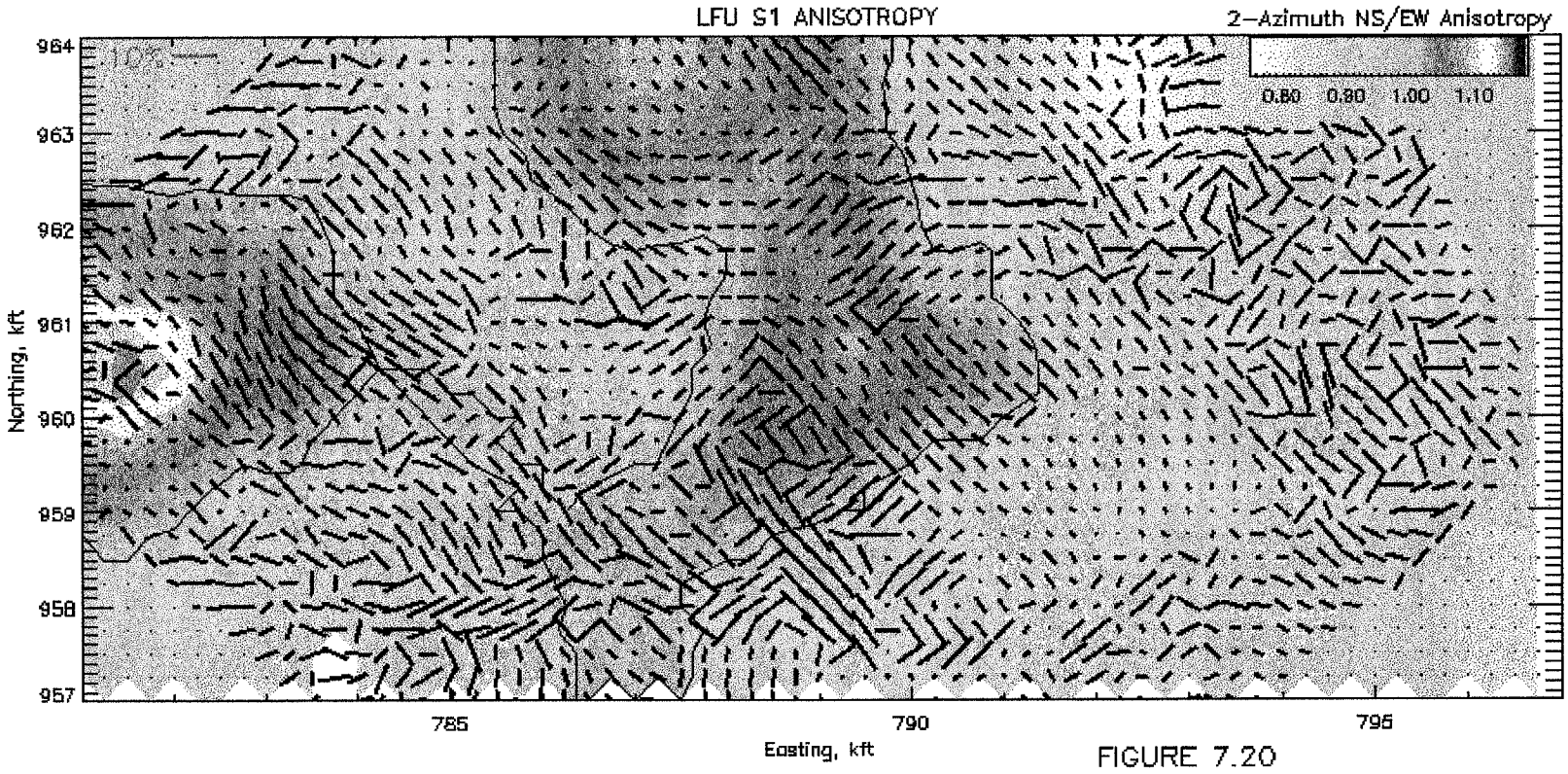
LFU S1 ANISOTROPY
2-Azimuth NS/EW Anisotropy
0.80
0.90
1.00
1.10
964
963
962
961
960
959
958
957
Northing, kft
785
790
795
Easting, kft

FIGURE 7.20

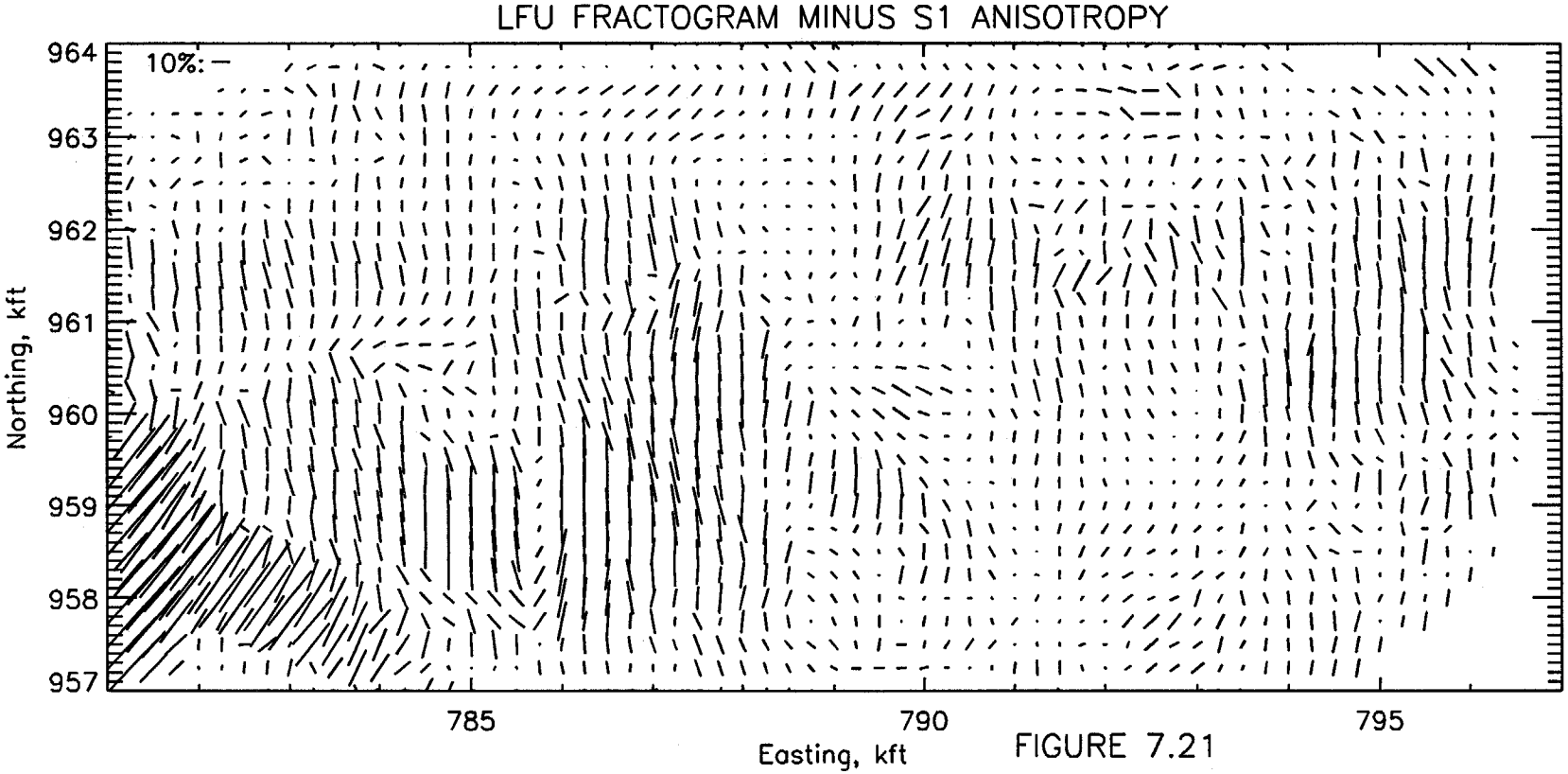
LFU FRACTOGRAM MINUS S1 ANISOTROPY
10%
964
963
962
961
960
959
958
957
Northing, kft
785
790
795
Easting, kft

FIGURE 7.21

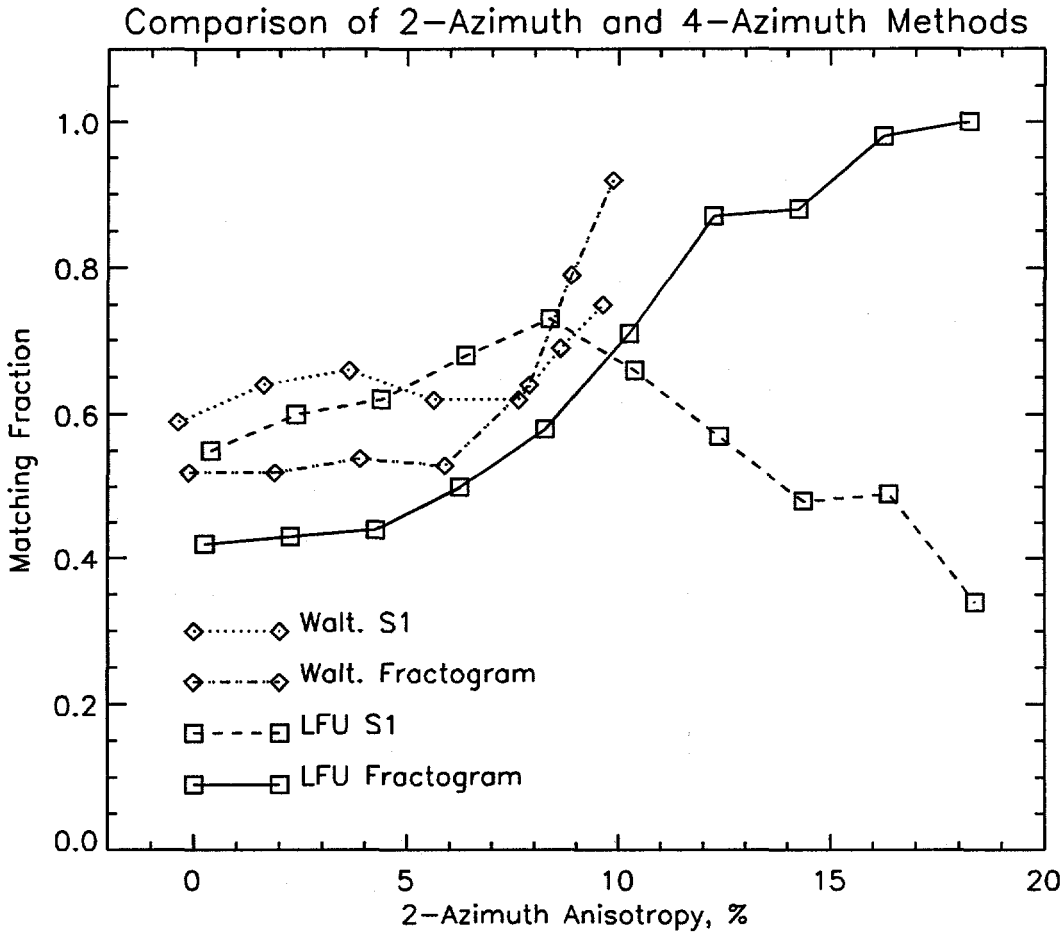
Comparison of 2–Azimuth and 4–Azimuth Methods
Matching Fraction
1.0
0.8
0.6
0.4
0.2
0.0
0
5
10
15
20
2–Azimuth Anisotropy, %
Walt. S1
Walt. Fractogram
LFU S1
LFU Fractogram

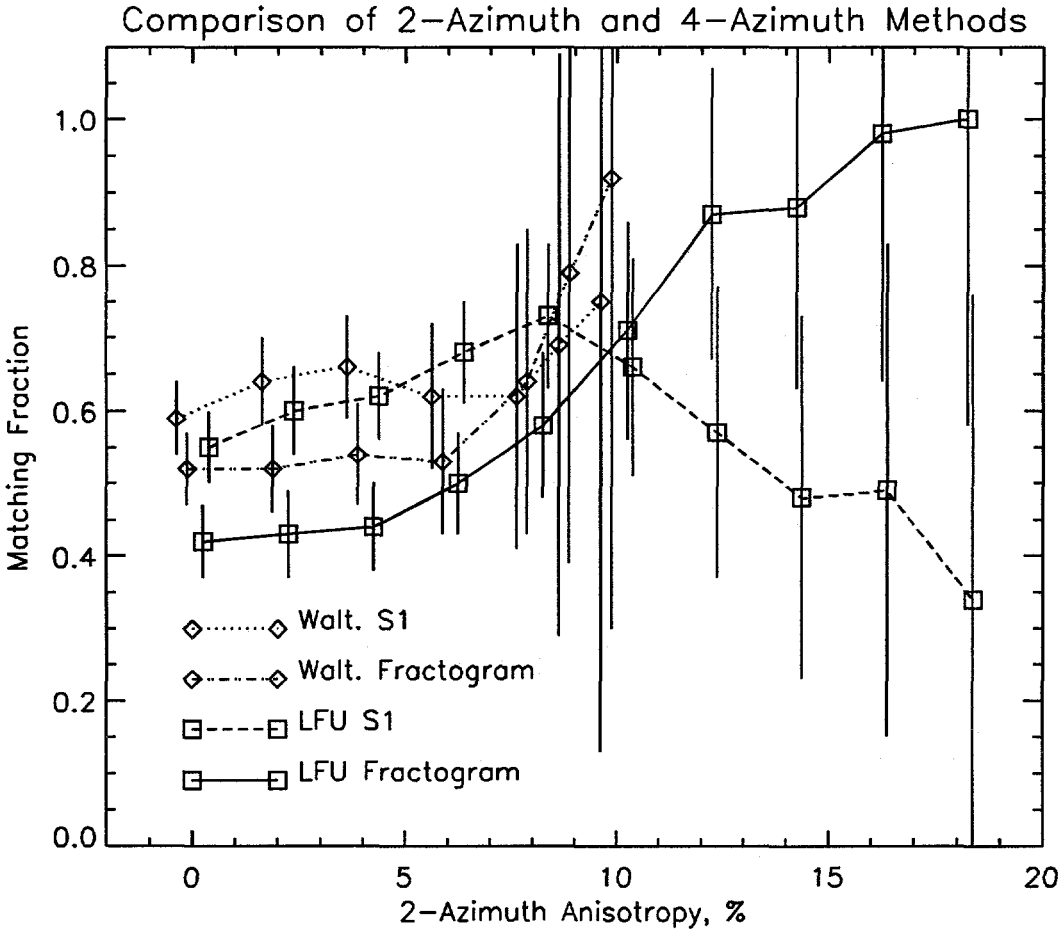
Comparison of 2–Azimuth and 4–Azimuth Methods
Matching Fraction
1.0
0.8
0.6
0.4
0.2
0.0
0
5
10
15
20
2–Azimuth Anisotropy, %
Walt. S1
Walt. Fractogram
LFU S1
LFU Fractogram

Figure 7-22

8. CONCLUSIONS AND RECOMMENDATIONS

We analyzed three groups of seismic experiments in order to characterize azimuthal anisotropy diagnostic of vertical fractures, which provide key permeability pathways for natural gas.

A simple measure of anisotropy is the ratio of P-wave interval velocities measured in two azimuth bins, each $\pm 45°$ around the chosen principal directions. These directions must be orthogonally oriented toward the regional minimum and maximum anisotropy, which can be determined from superbin azimuthal scans or independently inferred from geology. Two-azimuth binning maintains high fold, and hence high signal-to-noise, but is blind to anisotropy near $45°$ to the principal directions. In this study, the principal directions derived by more sophisticated methods had the greatest likelihood of being in the matching two-azimuth bin where the apparent two-azimuth anisotropy exceeded about 8%. In spite of these restrictions, the magnitude of velocity anisotropy inferred using the two-azimuth method correlated well with gas yield: greater anisotropy implies greater fracturing and hence greater gas production.

In addition to velocity, other seismic attributes can be analyzed for anisotropy in the two-azimuth method. Both reflectivity and frequency were found to be anisotropic in this study, and azimuthal differences in these parameters had better correlations with gas productivity than did velocity. Furthermore, reflectivity and frequency on raypaths traveling parallel to fractures are the attributes with the strongest association with gas. In the heterogeneous fluvial units of the reservoir, gas-charged sands may be forming "dim spots" that can be detected only when the scattering effects of fractures are finessed by examining fracture-parallel raypaths. Increases in frequency associated with gas yield may be the result of a "squirt flow" mechanism parallel to fractures. Neural networks are among several techniques that can be used to empirically determine the mapping from geophysical, geological, and engineering attributes to gas yield, and hence infer "prospectivity" over undrilled areas.

A small region within the larger P-wave study was reshot at higher density using three-component receivers. In addition to the two-azimuth approach, two techniques were used that split the data into four azimuths. The Fractogram fits a cosine curve to the four velocities and computes the fast P-wave direction (which can have an arbitrary direction) and the amplitude of the anisotropy. The horizontal geophones record S-waves formed from conversions of P-waves at layer interfaces. S-waves split into fast and slow waves in anisotropic media; the direction of maximum separation is called the fast or S1 direction. The fast P- and S-directions can be the same, although they are not required to be, and their relative magnitudes depend on the physical properties of the rock and fractures.

Both the Fractogram and S1 maps reveal significant anisotropy heterogeneity, that is, strong lateral variations in anisotropy. There are systematic differences in the methods; in particular, the Fractogram directions are more northerly than the S1 and regional fracture trends indicate. When compared to the two-azimuth method, the S-wave technique appears more reliable at low anisotropy, whereas the Fractogram matches better at high anisotropy. However, the Fractogram appears to be influenced by local dip of rock units, which could be a consequence of the lack of complete reflector repositioning (migration). The four-azimuth methods are more costly, requiring more than twice the processing, and for the same survey geometry have lower fold and signal-to-noise than the two-azimuth approach. They can, however, detect anisotropy with arbitrary orientation and smaller magnitude than when using two azimuths only.

All of the methods investigated here use isotropic processing of azimuth-limited volumes. An emerging alternative for measuring velocity anisotropy is to correct individual traces in a velscan gather for directionally variable velocity, i.e., to perform anisotropic NMO (e.g., Sena, 1991; Sayers, 1997; Tsvankin et al., 1997). This approach provides P-wave anisotropy and magnitude at each velscan location, as does the 4-azimuth Fractogram. Where signal-to-noise and azimuth distribution are good, however, anisotropic NMO will provide a more accurate measure. Similarly, continuos variations in azimuthal anisotropy of frequency and reflectivity can also be analyzed on a bin-by-bin basis (although "superbin" gathers even larger than those used for velocity analysis may be necessary to achieve sufficient S/N). Larger costs are associated with these methods, which require extensive prestack processing, some iterative. At this site, the two-azimuth method appears to be robust for apparent anisotropy exceeding 5-10%, levels that are also strongly indicative of commercially viable gas wells. Therefore simple, low-cost methods of anisotropy measurement may be sufficient for practical prediction of maximum gas yield. Although directional resolution is lost in the two-azimuth approach, the wide-angle averaging is less sensitive to variations in acquisition geometry, for example, when standard rectangular receiver patches are dictated by cost.

The two-azimuth P, four-azimuth P (Fractogram), and four-azimuth S analyses all had some measure of success in characterizing fracture anisotropy. Which of these methods, or others such as anisotropic NMO, are used in future surveys depends on the nature of the reservoir and the available funding and equipment. In general, for cost-effective characterization of fractured reservoirs, we recommend:

(1) Acquire full azimuth 3D P-wave survey with maximum offsets equal to target depth plus 20%, using azimuthally isotropic source and receiver arrays. Every effort should be made to obtain equal maximum offsets and fold in all azimuths.

(2) Calibrate with limited P-S or S-S data: a 9C-VSP or a live patch of 3C geophones while the 3D survey is recorded to document S-wave anisotropy.

(3) Process in as many azimuths as allowed by cost, with independent velocity analyses in each azimuth (in the limit of anisotropic NMO, the number of azimuths is equal to the number of traces in the gather). In contrast to conventional practice, errors on the interval velocities should be specified so that errors on the velocity anisotropy can be quantified. A higher density of velocity scan locations should also be supported, in order to accurately map anisotropy heterogeneity.

Improved theoretical understanding, tested with field experiments, is necessary to build a better conceptual framework for the seismic response of fractures and their contents. Such work should include:

(4) Theoretical modeling of P-wave response at large angles of incidence in fractured media, to determine if P-wave amplitudes or amplitude variations with offset (AVO) can be used to determine fracture contents directly (Grimm and Lynn, 1997). Improved parameterizations for AVO analysis will likely also be required.

(5) Theoretical studies of the effects of anisotropic media (TI, orthorhombic) and horizontal stress fields on P-P azimuthal velocity variations and the direction of the fast split S-wave (Tsvankin, 1997; Cruts et al., 1995).

(6) Physical modeling of dual-porosity systems (e.g, Furre and Holt, 1995), emphasizing the relationship of attenuation and permeability.

(7) P- and S-wave field experiment at a location where significant control is available for evaluating the presence and orientation of fractures, matrix porosity, gas/oil production in a fractured target layer in a relatively unstructured region.

In order to improve the performance of seismic data in integrated reservoir studies, we recommend:

(8) Assess seismic attributes in three dimensions. Empirical correlations with gas yield must be determined from breakdowns of Expected Ultimate Recovery of gas as a function of depth. New logging tools like nuclear magnetic resonance may significantly help this mapping by best distinguishing gas from water around the well.

This work and complementary DOE-sponsored studies confirm the viability and continued promise of advanced seismic methods to locate natural gas in naturally fractured reservoirs.

9. APPENDICES

9.1. References Cited

Akbar, N, Dvorkin, J. and Nur, A., 1993, Relating P-wave attenuation to permeability, Geophysics **58**, 20-29.

Asquith, G.B. and C.R. Gibson, 1982, Basic well log analysis for geologists, Amer. Assn. of Petrol. Geologists, Tulsa, OK.

Barton, C.C., 1995, Fractal analysis of scaling and spatial clustering in fractures: In: Fractals in the Earth Sciences (edited by Barton, C.C. and La Pointe. Plenum Press, New York, 141-178

Bruno, M.S. and Winterstein, D.F., 1994, Some influences of stratigraphy and structure on reservoir stress orientation, Geophysics **59**, 954-962.

Craft, K, Mallick, S., Meister, L., and Van Dok, R., 1997, Azimuthal anisotropy analysis from P-wave seismic traveltime data, 67th Ann. Internat. Mtg., Expanded Abstracts, in press.

Crampin, S., 1984, Effective anisotropic elastic constants for wave propagation through cracked solids, *Geophys. J. Roy. astr. Soc.* **76**, 135-145.

Crampin, S., 1985, Evaluation of anisotropy by shear-wave splitting, Geophysics **50**, 142-152.

Crampin, S., 1987, The geological and industrial implications of extensive-dilatancy anisotropy, Nature **328**, 491-496.

Crampin, S., 1994, The fracture criticality of crustal rocks, Geophysical Journal International **118**, 428-438.

Cruts, H. M. A., Groenenboom, J., Duijndam, A. J. W., Fokkema, J. T., 1995, Experimental verification of stress induced anisotropy, 65th Ann Mtg. SEG, Exp. Abstracts, 894-897.

Davis, John, Statistics and Data Analysis in Geology, Second Edition, John Wiley and Sons, New York, 1986.

Dunleavy, J.M. and Gilbertson, R.L., 1986, Madden anticline: growing giant, proceedings of Wyoming Geological Association 1986 symposium on Rocky Mountain Oil and Gas fields).

Dyke, C.G. and Milton-Taylor, D., 1995, Advances in characterizing natural fracture permeability from mud log data, SPE Journal **10**, 160-166.

Fagin, S., 1996, The fault shadow problem: its nature and elimination, The Leading Edge, **15**, nr. 8, 1005-1013.

Falconer, K., 1993, Fractal Geometry, Mathematical Foundations and Applications. John Wiley and Sons, 288 p.

Flores, R.M.; Keighin, C.W.; and Nichols, A.J., 1992. Sedimentology, conglomerate petrology, and pelynostratigraphy of the Fort Union Formation (Paleocene), Castle Gardens, Wind River Basin, Wyoming, in Sundell, K.A. and Anderson, T.C., editors, Road Log Volume for Rediscover the Rockies: Casper, Wyoming, Geological Association, p. 21-27.

Furre, A.K., Holt, R. M., 1995, Anisotropy of a synthetic layered medium, 65th Ann. Mtg. SEG, Exp. Abstracts, 898-901.

Gassmann, F., 1951, Elastic waves through a packing of spheres, Geophysics **16**, 673-685.

Gelinsky, S. and Shapiro, S.A., 1996, Anisotropic permeability: influence on seismic velocity and attenuation, *in* Seismic Anisotropy, Fjaer, Holt and Rathore, eds., SEG press.

Gelinsky, S., Shapiro, S.A., 1994, Poroelastic velocity and attenuation in media with anisotropic permeability, 64th Ann. Mtg. SEG, Exp. Abstr., 818-821.

Gough, D.I. and Bell, J.S., 1981, Stress orientation from oil well fractures in Alberta and Texas, Can. J. Earth Sci. **18**, 638-645.

Grimm, R.E. and Lynn, H.B., 1997, Effects of acquisition geometry, large-scale structure, and regional anisotropy on AVOA: an example from the Wind River Basin, submitted to 1997 SEG Ann. Internat. Mtg., Expanded Abstracts.

Heffer, K.J. and Koutsabeloulis, N.C., 1995, Stress effects on reservoir flow:-numerical modeling used to reproduce field data, *in* DeHaan, H.J. (ed.), New Developments in Improved Oil Recovery, Geological Society Special Publication No. 84, 81-88.

Heffer, K.J. and Lean, J.C., 1993, Earth stress orientation--a control on, and guide to, flooding directionality in a majority of reservoirs, *in* Linville, W. (ed.), Reservoir Characterization III, PennWell Books, Tulsa.

Hudson, J.A., 1981, Wave speeds and attenuation of elastic waves in material containing cracks, *Geophys. J. R. astr. Soc.* **64**, 133-150.

Johnson, R.C., Finn, T.M., Crovelli, R.A., and Balay, R.H., 1996: U.S.G.S. Open-File Report 96-264, p54-57).

Keefer, W.R., 1965, Stratigraphy and geologic history of the uppermost Cretaceous, Paleocene, and lower Eocene rocks in the Wind River Basin, Wyoming: U.S. Geological Survey Professional Paper 495-D, pp D1.-D35.

Lavely, Eugene, and C. R. Bates, 1996, Problems in the analysis of multicomponent VSP data, The Leading Edge, pp. 937-941.

Lynn, H.B. and Thomsen, L.A., 1990, Reflection shear-wave data collected near the principal axes of azimuthal anisotropy, Geophysics **55**, 147-156.

Mallick, S., Craft, K.L., Meister, L.J., Chambers, R.E., 1996, Computation of principal directions of azimuthal anisotropy from P-wave seismic data, 66th Ann SEG Mtg, Expanded Abstracts, 1862-1865.

Meissner, F., 1984, Cretaceous and lower Tertiary coals as sources for gas accumulations in the Rocky Mountain area: Rocky Mountain Association of Geologists guidebook - Hydrocarbon source rocks of the Greater Rocky Mountain Region, 401-432.

Mueller, M.C., 1991, Prediction of lateral variability in fracture intensity using multicomponent shear-wave surface seismic as a precursor to horizontal drilling in the Austin Chalk, Geophysical Journal International **107**, 409-415.

Ostrander, W.J., 1984, Plane-wave reflection coefficients for gas sands at nonnormal angles of incidence. Geophysics, **49**, 1637-1648.

Peterson, C., T. Rognvaldsson, and L. Lonnblad, 1993, JETNET 3.0 - A Versatile Artificial Neural Network Package. Univ. of Lund, Sweden. Available via anonymous ftp from ftp.thep.lu.se/pub/LundPrograms/Jetnet.

Pointer, T., Liu, E., Hudson, J.A., 1996, Seismic wave propagation in media with interconnected cracks and pores, 66th Ann Mtg. SEG Exp. Abstracts, 1846-1849.

Queen, J.H. and Rizer, W.D., 1990, An integrated study of seismic anisotropy and the natural fracture system at the Conoco Borehole Test Facility, Kay County, Oklahoma, Journal of Geophysical Research **95**, 11255-11273.

Queen, J.H., Rizer, W.D., Liu, E., Crampin, S., and Lines, L., 1992, A review of downhole source effects at the Conoco Borehole Test Facility: Proceedings of the cross-borehole geophysics in the petroleum industry symposium, Geophysical Society of Tulsa, Mar. 1992.

Sayers, C.M., 1997, Seismic traveltime analysis for azimuthally anisotropic media, SEG Expanded Abstracts.

Schmitt, G.T., 1975, Madden-Badwater field, Fremont and Natrona Counties, Wyoming: Rocky Mountain Association of Geologists guidebook, Deep drilling frontiers of the central Rocky Mountains, p.245-254.

Sena, A.G., 1991, Seismic traveltime equations for azimuthally anisotropic and isotropic media: estimation of interval elastic properties, Geophysics, **56**, 2090-2101.

Sheriff, R.E., and L.P. Geldart, 1995, Exploration Seismology, 2nd ed., Cambridge Univ. Press, Cambridge, 592 pp.

Shuey, R.T., 1985, A simplification of the Zoeppritz equations, Geophysics **50**, 609-614.

Thomsen, L., 1986a, Reflection seismology in azimuthally anisotropic media, SEG 56th Ann. Internat. Mtg., Expanded Abstracts, 468-470.

Thomsen, L., 1986b, Weak elastic anisotropy, Geophysics **51**, 1954-1966.

Thomsen, Leon, 1988, Reflection seismology over azimuthally anisotropic media, Geophysics.

Tsvankin, I. ,1997, Anisotropic parameters and P-wave velocity for orthorhombic media, Geophysics, 62, 1292-1309.

Tsvankin, I., V. Grechka, and J.K. Cohen, 1997, Generalized Dix equation and modeling of normal moveout in inhomogeneous anisotropic media, SEG Expanded Abstracts.

Van Dok, R.R., Gaiser, J.E., Jackson, A.R., 1997, 3-D converted-wave processing: Wind River Basin case history, to be presented @ 97SEG.

Wasserman, P., 1993. Advanced Methods in Neural Computing. Van Nostrand Reinhold, New York. 255 pp.

Winterstein, D. F. and Meadows, M.A., 1991, Shear-wave polarizations and subsurface stress directions at Lost Hills field, Geophysics **56**, 1331-1348.

Wyllie, R.J., Gregory, A.R. and Gardner, G.H.F., 1957, An experimental investigation of factors affecting elastic wave velocities in porous media, Geophysics **23**, 459-493.

Yielding, G., Needham, T., and Jones, H.; 1996, Sampling of fault populations using sub-surface data: a review. Journal of Structural Geology; Vol. 18, Nos. 2/3, 135-146.

Zoback, M.D., Moos, D., and Mastin, L., 1985, Well bore breakouts and in situ stress, J. Geophys. Res. **90**, 5523-5530.

9.2. List of Figures and Tables

9.3. The Present Role of Geophysics in Reservoir Engineering at the Study Site

We briefly describe how geophysics is presently used at the site, and suggest some areas for more full incorporation of these technologies in reservoir exploration and development there.

Surface geophysics figures prominently in well siting. Conventional two- and three-dimensional seismic reflection are used together with well control to determine the locations of target units. Drilling near or through large faults indicated on the seismic records is of particular interest at present. Some auxiliary indicators from the seismic data are also used. Variations in reflectivity are used as a qualitative guide to sand thickness. A decrease in coherence is an additional fault marker. Locally intense fracturing in part of a unit can lower the seismic velocity, displacing units beneath this zone to later times on the seismic record: an anomaly is then indicated by local "velocity sags" of underlying reflectors. Maps of interval velocity as a function of depth, described above as part of the present DOE contract, give essentially the same information.

Both surface and borehole geophysics are used to determine perforation intervals in wells. Surface seismic is used as discussed above, mostly to determine stratigraphic and structural position. The principal factor influencing completion intervals is gas show in the mud log. Lost circulation is a classic indicator of local high porosity, here likely due to fracturing. Recently, drill cuttings have been studied for shows of former fracture-lining crystals and cements. These three nongeophysical indicators follow directly from the drilling and are therefore comparatively cheap. A suite of wireline geophysical data complements the drilling tests, including formation microscanners, repeat- formation tests, and self-potential, resistivity, sonic, neutron, and density logs. New nuclear-magnetic resonance logs have particular promise to distinguish gas from water, which is of critical importance.

Little, if any, geophysics is presently used in reservoir management. When a pay interval is exhausted or begins to make too much water, that interval is sealed off and new perforations are made at the next higher selected level. Due to the limited extent of many sand bodies, it is difficult to predict the production longevity of individual units.

In conclusion, geophysics currently plays an important role in the gas-reservoir engineering of the DOE Wind River study area, but is underutilized because of cost and/or a lack of "ground-truth" correlation with historical data. Conventional interpretation of three-dimensional seismic reflection is important in well-site selection and completion. However, the heterogeneous nature of deposition resulted in multiple individual reservoirs with variable gas saturation that are often not fully resolved in surface-seismic data. Downhole geophysical methods can

provide detailed mapping of these units and their contents: offset vertical-seismic profiles can show the lateral extent of individual sand bodies, and nuclear-magnetic resonance or borehole gravity can distinguish gas from water. These investigations can be costly, however, and therefore quantitative correlations with surface seismic data would be invaluable. Such correlations would trade off some vertical resolution in favor of establishing lateral continuity of properties. Innovative seismic attributes, such as those developed for the present DOE project, must be better tied to borehole data in order to be widely accepted and fully exploited.

9.4. Numerical Modeling of AVO

(See attachment of Grimm and Lynn SEG abstract)

9.5. Near-Surface Seismic Characterization

(See attachment of Bates et al. SEG abstract)

submitted to *SEG 1997*

Effects of acquisition geometry, large-scale structure, and regional anisotropy on AVOA: an example from the Wind River basin

Robert E. Grimm, Blackhawk Geometrics Inc., and Heloise B. Lynn, Lynn Inc.*

Summary

Reflection-amplitude variations with offset and azimuth (AVOA) are being explored as indicators of crack density, orientation, and content in vertically fractured gas reservoirs. However, amplitudes are also sensitive to many other factors that could potentially bias such inferences. Using paraxial ray tracing, we have quantified the effects of several such factors in 3D data in a structurally complex, anisotropic environment. Elongated receiver patches result in different AVO gradients in the long vs. short directions because of the finite accuracy of the Shuey approximation used to compute AVO. Furthermore, calculated gradients are less robust in the short direction due to fewer samples and a smaller range of offsets. Scattering from faults reduces both reflection amplitude and gradient and introduces large variances to the estimates. Changes in AVO gradients due to anisotropy are consistent with those expected from variations in Poisson's ratio: for noncompliant (e.g, water-filled) fractures, gradients perpendicular to fracture strike on the top of a vertically fractured sand are more positive than the isotropic case. Conversely, layering anisotropy in the cap shale yields gradients more negative than in isotropy. When both anisotropies are present, the cap shale dominates due to the prevalence of ray paths traveling at high angles to the layering. Such variations are reversed for gas-filled fractures, suggesting that the azimuthal difference in AVO gradient (fracture-perpendicular minus fracture-parallel) can be used to discriminate fracture content: the difference will be positive for water and negative for gas. This sign change is independent of the contrast in impedance or Poisson's ratio across the reflector, but can be obscured by structural scattering and acquisition geometry, including a lack of sufficient offsets.

Introduction

Two 3D data volumes (a large conventional survey and a smaller three-component grid) were acquired in the Wind River basin in support of the U.S. Department of Energy's program to detect and characterize natural fractures in low-permeability gas formations (Lynn et. al, 1996a). These data are being used to examine the relationships between S-wave anisotropy—the most diagnostic but expensive fracture indicator—and various P-wave attributes (azimuth-dependent AVO, traveltimes, velocities, and frequencies). Earlier 2D, nine-component work in the Uinta basin (Lynn et al., 1996b) yielded a good correlation in some intervals between S-wave anisotropy and P-wave AVO. At the Wind River basin and Rulison field sites, azimuthal P-wave velocity anisotropy has shown better correlation with gas pay than has P-wave AVOA (Lynn et al., 1997). However, amplitudes are more sensitive than travel times to experiment and environment. In an attempt to improve AVOA performance in complex regions, we quantitatively examined three such influences—acquisition geometrical biases, large-scale structure, and regional anisotropy—on AVOA. We also performed several tests unrelated to the field data in order to obtain some general insights into anisotropy and gas effects.

The exploration target is a heterogeneous fluvial sequence of sand, silt, and clay at approximately 6500 ft depth. A lacustrine cap shale grades laterally into a coarser-grained marginal unit. Other continental sediments form the upper overburden. In the exploration area, the sequence has been deformed into an anticline with over 1600 ft of structural relief; east-west faults with displacements up to 200 ft parallel the anticline's axial plane. Borehole-televiewer and hydraulic data also indicate a dominant EW orientation to vertical fractures in the reservoir.

The 3D P-wave survey is the subject of this investigation. Long receiver lines—up to 30,000 ft—oriented perpendicular (NS) to the anticline were recorded for apertures sufficient to image targets much deeper than the formation studied here. Our data were processed with 10,000 ft NS and 5,000 ft EW offsets, but include two strips of 10,000 ft offsets in both azimuths.

Method

We calculated synthetic seismograms using the layout, representative velocity profile and anisotropy, and target reflector structure derived from the Wind River survey. In practice, both shots and receivers were decimated by a factor of ten for computational efficiency, yielding about 10^4 shot-receiver pairs. The adopted velocity profile monotonically increases with depth with the exception of the cap shale, which is a constant low velocity. Therefore the top of the reservoir sand is a positive impedance contrast. P-wave azimuthal anisotropy for the sand and layering anisotropy for the cap shale were taken to be 10% and 15%, respectively. These anisotropies are comparable to the observed rms deviations in interval velocity azimuthal ratios, but in fact represent upper bounds as we cannot separate heterogeneity from anisotropy. S-wave anisotropy was assumed to be twice that of the P-wave for the water-filled, reference case and half for the gas-filled reservoir. The overburden was assumed isotropic. The reflector was gridded at 125 ft intervals

(CMPs are 110 ft N x 220 ft E) which resolves well the large-scale fault structure.

Amplitudes were computed using paraxial ray tracing (Gibson et al., 1991). This code is applicable to media with arbitrary anisotropy and moderate structural complexity. Because the full elastodynamic (Zoeppritz) equations are solved implicitly, the solution for reflection amplitude is exact within the limitations of ray theory. The restricted-TI anisotropic stiffness matrices were calculated directly from the velocity anisotropies (Schoenberg and Sayers, 1995). In practice, time-domain seismograms were not computed; instead the transfer (Green's) function for the reflection can used directly, given bed thicknesses larger than the seismic wavelet. Geometrical spreading was neglected (the data have a t^2 correction) but the cumulative partitioning from overlying interfaces was retained. Reflections were binned on 1100x2200 ft centers (i.e., a CMP proportional to the data decimation); DMO/prestack partial migration of the data approximates such common-reflection point binning. The angle of incidence θ was calculated from the raypath and the unit normal to the reflector and was restricted to $\theta < 30°$. Rays were divided into NS (-45°E to +45°E; "fracture-perpendicular") and EW (45°E to 135°E; "fracture-parallel") azimuths. For each azimuth, we required at least 5 points per bin, and fit the Shuey approximation $R=A+B\sin^2\theta$ using an L1-norm.

Results

As a preliminary test, flat isotropic layers were modeled using the actual survey layout. This revealed an apparent difference of 30±70% in AVO gradient B between NS and EW azimuths. This bias is purely due to survey layout: the NS-elongated receiver patches lead to more long-offset sampling in this direction and therefore AVO fits are weighted differently in the long and short directions. Because $R=A+B\sin^2\theta$ is an imperfect model, with an error varying systematically with incidence angle (offset), the two azimuths show different AVO, with gradients smaller in the long direction. Figure 1 shows a simplified version of this effect, where amplitudes along a single hypothetical receiver line are fit separately in the near and far offsets. Furthermore, there is greater variance among the EW-binned data compared to NS: the fewer number of samples and smaller range of incidence angles in the near-offset direction yields less robust AVO estimates (Rolla, 1995).

The second experiment maintained isotropic layering, but included structure on both the target reflector and the top of the cap shale. Such rugosity scatters seismic energy, broadening the amplitude response at any incidence angle. This greater scatter in the AVO data tends to lower the estimated magnitudes of both A and B, but this difference is completely obscured by the large increase in variance: for the survey considered here, the combined effects of acquisition bias and structure yielded azimuthal differences in B of 2±160%. The acquistion geometry still resulted in higher variances EW than NS.

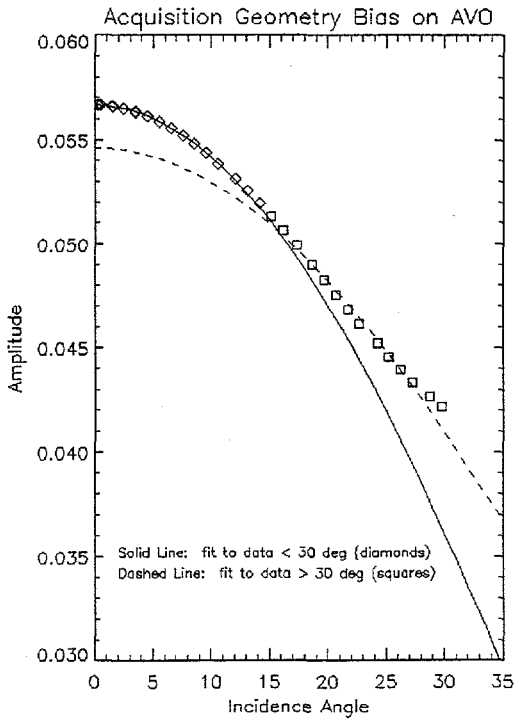

Figure 1. Illustration of AVO bias due to acquistion geometry. Symbols show exact reflection amplitudes; Shuey approximation $R=A+B\sin^2\theta$ gives smaller A and B in far offsets compared to near offsets.

Anisotropy has profound effects on AVO. Layering anisotropy (transversely isotropic with vertical symmetry axis, or TIV) in cap rocks has been studied extensively (Samec et al., 1990; Blangy, 1994; Hanitzsch et al., 1995; Waluyo et al., 1995; Kumar et al., 1996); AVO applications to azimuthal anisotropy (transversely isotropic with horizontal symmetry axis, or TIH) in the reservoir are more recent (Strahilevitz and Gardner, 1995; Rueger and Tsvankin; 1995; Ruger, 1996; Haugen and Ursin; 1996; Sayers and Rickett; 1997). We ran 18 test cases for all combinations of isotropy, TIV, and TIH in the cap shale and reservoir sand, for both positive and negative bulk impedance contrasts. For these generalized experiments, the anisotropy of the cap shale was set equal to that of the underlying sand and flat interfaces were used. However, the velocity profile and field layout from the actual experiment were retained. The results are most easily understood in terms of changes in Poisson's ratio σ as a function of incidence angle (Fig. 2). For noncompliant (e.g., water-filled) fractures or bedding planes (with S-exceeding P-anisotropy), σ increases for raypaths in the slow (crack-perpendicular) direction. Therefore overlying TIV will have a higher σ in this upper layer at near offsets, whereas overlying TIH will have a higher σ at far offsets. Both of

these cases are associated with a decrease in σ across the interface, which results in a more negative AVO gradient B (Ostrander, 1984). Of course, the AVO differs from a simple contrast in σ due to the offset-dependence. Conversely, underlying TIH or TIV are both associated with increases in σ and hence more positive B. Because actual reflection geometries are mostly near-vertical raypaths, TIV dominates the AVO response regardless of position with respect to the interface.

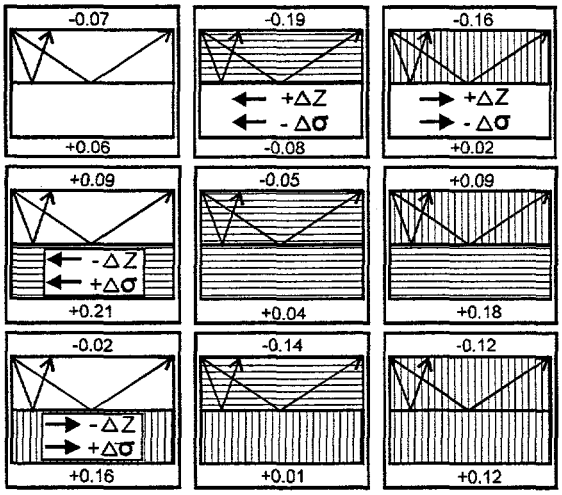

Figure 2. Effect of layering (horizontal ruling) and vertical-fracture (vertical ruling) anisotropy for water-filled cracks; AVO gradient B shown at top of panels for positive impedance contrast and bottom for negative impedance contrast. Arrows show lateral changes in interface contrast in Poisson's ratio $\Delta\sigma$ and impedance ΔZ as a function of offset. Changes in B are mostly determined by $\Delta\sigma$; for example, cap shale over isotropic sand (top center panel) has more negative B in near-offsets due to strongly negative $\Delta\sigma$ there. Overlying anisotropy causes more negative B, underlying anisotropy more positive B, regardless of impedance contrast; layering anisotropy exerts more influence due to prevalence of near-vertical rays. Schmatic rays are shown for illustration of offset-dependence only; actual calculation includes isotropic overburden.

These gradient changes are reversed, albeit with different magnitudes, when cracks are compliant (gas-filled), which suggests a method for distinguishing gas- from water-filled cracks in vertically-fractured reservoirs using azimuthal differences in AVO gradient (Fig. 3): compared to the reference case parallel to fractures, B is more positive in the perpendicular direction if fractures are water-filled and more negative if gas-fiilled. Subtracting the fracture-parallel from the fracture-perpendicular AVO gradient then yields a positive number for water and a negative number for gas. Although we have illustrated this approach specifically for the Wind River basin site, the model does not depend on the bulk contrast in impedance or Poisson's ratio across the interface.

Of course, this indicator will respond in principle to low (noncommercial) gas fractions as does conventional P-wave AVO. Furthermore, the signal-to-noise (S/N) is lower than conventional AVO, as we are looking at a differential attribute that is sensitive only to a small volume of the rock (the fractures). Structural scattering further obscures the signal. Because the sensitivity increases as ray inclinations become more perpendicular to vertical fractures, wide-angle reflections would be more diagnostic (Sayers and Rickett, 1997) but are rejected in processing as the S/N is lower and the Shuey approximation used in conventional AVO analysis is invalid. Combined, these noise sources prevented reliable recovery of this differential indicator in our full model experiments (incorporating field acquisition geometry, structure, strong TIV in cap shale and weaker TIH in reservoir sand). We are seeking to improve the performance of AVOA by restricting the analysis to the strips of equal azimuthal offset and considering AVO representations valid over a larger range of incidence angles (Aki and Richards. 1980; Johansen et al., 1995).

Conclusions

The influence of acquisition bias, structural scattering, and regional anisotropy on AVOA can be quantified by modeling. For the survey studied here, AVO gradients vary by azimuth by several tens of percent due to variable-offset sampling introduced by elongated receiver patches. Faults on the crest of the target anticline scatter seismic energy, introducing large variances to AVO parameters. Anisotropy causes AVO gradients to be more positive or more negative where the fracturing makes the contrast in Poisson's ratio across the reflector more positive or negative, respectively. The azimuthal difference in AVO gradient may be a useful indicator of fracture content, but requires high S/N and alternative AVO formulations applicable to wide-angle reflections.

Acknowledgements

This work was supported by the DOE Federal Energy Technology Center, Contract DE-AC21-94MC31224, Program Manager Bill Gwilliam. We thank Dave Phillips, Michele Simon, Rich Van Dok, and Stewart Squires for helpful discussions.

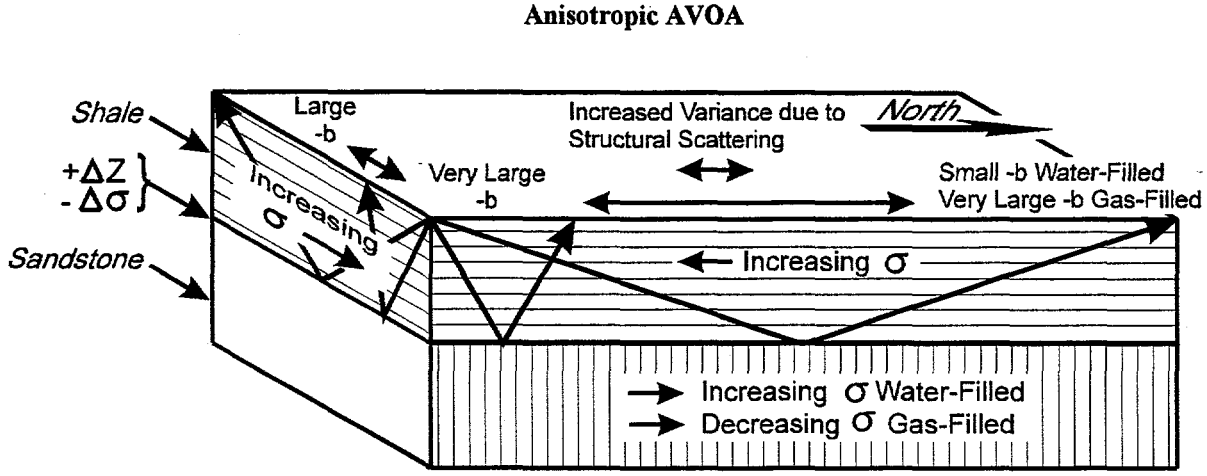

Figure 3. Conceptual model for AVOA at Wind River basin site. AVO gradient *B* perpendicular to vertical fractures in reservoir is more positive for water-filled and more negative for gas-filled fractures compared to fracture-parallel direction; predicted difference between NS (fracture-perpendicular) and EW (fracture-parallel) azimuths is therefore positive for water and negative for gas.

References

Aki, K., and P.G. Richards, 1980, Quantitative Seismology, Vol. 1, W.H. Freeman and Co., San Francisco, 558 pp.

Blangy, J.P., 1994, AVO in transversely isotropic mediaCa review. Geophys., 59, 775-781.

Gibson, R.L., A.G. Sena, and M.N. Toksoz, 1991, Paraxial ray tracing in 3D inhomogeneous, anisotropic media, Geophys. Prosp., 39, 473-504.

Hanitzsch, C.H., M.A.C. Tura, R.T. Coates, and W.B Beydoun, 1995, The effects of TI anisotropy on AVO inversion: a field-based study, 65th Ann. Internat. Mtg., Soc. Expl. Geophys., 336-339.

Haugen, G.U., and B. Ursin, 1996, AVO-A analysis of a vertically fractured reservoir underlying shale, 66th Ann. Internat. Mtg., Soc. Expl. Geophys., 1826-1829.

Johansen, T.A., L. Bruland, and J. Lutro, 1995, Tracking the amplitude versus offset (AVO) by using orthogonal polynomials, Geophys. Prosp., 43, 245-261.

Kumar, S., V. Singh, S.K. Chandola, and D. Dutta, 1996, Seismic wave propagation and AVO analyses in anisotropic media, 66th Ann. Internat. Mtg., Soc. Expl. Geophys., 1805-1808.

Lynn, H.B., K.M. Simon, C.R. Bates, and R. Van Dok, 1996a, Azimuthal anisotropy in P-wave 3-D (multiazimuth) data, The Leading Edge, Aug., 923-928.

Lynn, H.B., K.M. Simon, and C.R. Bates, 1996b, Correlation between P-wave AVOA and S-wave traveltime anisotropy in a naturally fractured gas reservoir, The Leading Edge, Aug., 931-935.

Lynn, H.B., et al., 1997, Fracture detection, mapping, and analysis of naturally fractured gas reservoirs using P-wave reflection seismic, 67th Ann. Internat. Mtg., Soc. Expl. Geophys., this volume.

Near surface variability in shear wave velocity anisotropy

C. R. Bates, D. Phillips, E. Lavely, Blackhawk Geosciences; and H. B. Lynn, Lynn Inc.*

MC 1.1

Summary

The weathered layer has been shown to contain some of the greatest values of shear wave velocity anisotropy in the earth (Lynn, 1991, Crampin, 1990). The cause of the shear wave velocity anisotropy is most often either due to particle layering in unconsolidated sediments and sedimentary rocks or due to aligned weaknesses commonly manifest as aligned open fractures. The aligned open fractures can be vertical and cross cut bedding in sedimentary rocks or can be horizontal to sub-horizontal and are aligned with bedding. The purpose of this study was to measure the variation in properties associated with the vertical or sub-vertical fractures as these fractures often provide preferential pathways to fluid migration and can also influence recording of deeper seismic shear wave reflection data for oil and gas exploration.

Introduction

Near vertical fractures are typically formed during diagenetic processes when a rock is subject to differential horizontal stress. After fractures have formed and opened they are often infilled or partially infilled by material with different properties than the surrounding host rock. Later, during uplift and exposure from weathering, the fractures are accentuated being either more or less competent than the host rock. It has been shown that the presence of these aligned fractures, their density and orientation can be measured using shear wave seismic techniques (for example Crampin, 1985, Winterstein and Meadows, 1990, Macbeth, 1995).

This presentation describes a technique designed to measure the variability in near surface shear wave velocity anisotropy. Furthermore, the variation in shear wave velocity anisotropy and the orientation of the fast shear wave direction is interpreted in terms of vertical aligned fractures that display a preferred orientation.

Field Procedure

During the acquisition of a 3D-3C (three component recording) dynamite reflection seismic survey a total of 30, three component geophones were deployed in shot holes across the 2 square mile receiver patch. Typically the explosive was loaded in a 60 foot deep hole with the down hole geophones attached below the charge. Seismic energy was then recorded from a surface impact source to the down hole 3C geophone. The geometry of the 3C borehole geophones is illustrated in Figure 1.

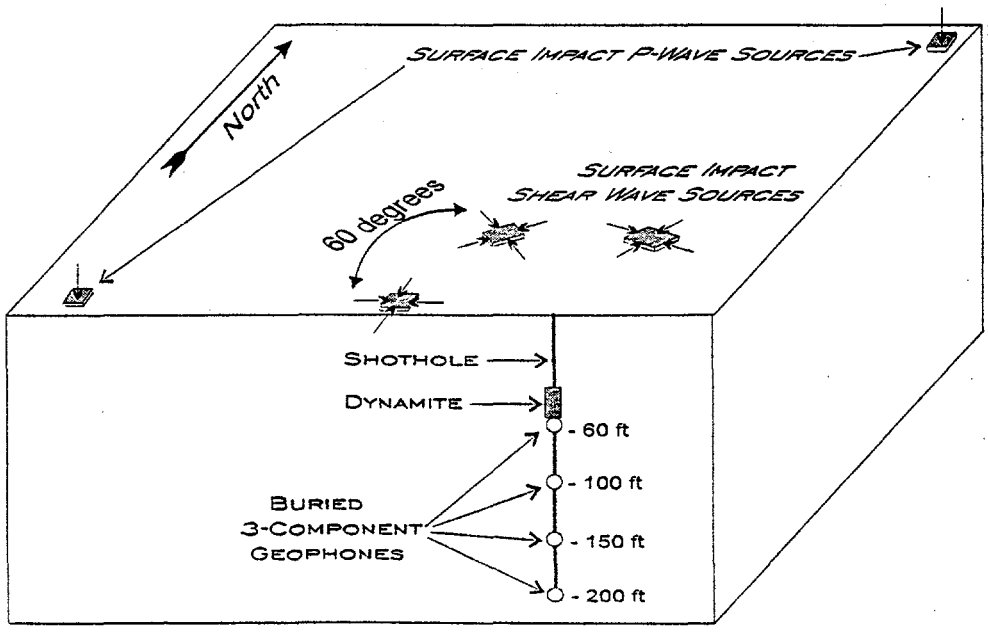

Figure 1. Acquisition geometry for collection of shear and compressional wave data for downhole receivers placed in shotholes.

The average depth over which the downhole impact surveys were made was 60 feet. At two locations in the field however, receivers were deployed at 60, 100, 150 and 200 feet. While the explosive detonation did destroy the downhole geophones, the method was more cost effective than drilling extra holes for the geophones. For 4D seismic acquisition, drilling of extra holes may be a more prudent long term method for measuring the near surface changes in shear wave velocity.

The down hole geophone assembly consisted of three single geophone elements arranged to be mutually orthogonal with two elements in the horizontal plane and one vertical. These were potted inside of an empty explosive sleeve in order that the geophone assembly could be screwed onto the bottom of the explosive charge. No attempt was made to orient the geophones down hole as it was intended to use a software rotation after recording the seismic energy to determine absolute azimuth.

For each buried phone location, three near offset shear and compressional wave source locations were surveyed. In addition, two far offset compressional wave source locations were used per hole for orienting the down hole assembly. The shear wave source consisted of a 60 lb. steel plate coupled to the ground using 6 inch spikes. This source was struck on each end to create shear waves with their polarization direction perpendicular to the propagation direction. By striking the source on both ends, a reversal in shear energy was achieved which aids in identification of the shear arrivals. The source was oriented both radial and transverse to the hole approximately 10 feet from the hole at each of the three locations. The compressional waves were created by striking the plate vertically.

The three source locations were compared to give an estimate of the error in this recording procedure. However, in future work only two locations should be sufficient as the measured velocity and azimuth from all three positions gave results within 5% of each other.

Data Processing

The compressional wave velocity was measured from picking the arrival time on the vertical geophone element. A close correlation was obtained between the compressional arrival time from down hole recording and the uphole time recorded by the shooter when the explosive charge was fired (Figure 2).

The following sequence was used in the processing of the shear wave records. First the data was sorted and geometry files written. A tool spin correction was applied using both the offset p-wave source locations. These results were compared for consistency in the corrections. The horizontal geophone elements were then rotated to be parallel and perpendicular to the shear wave source locations and a rotation analysis performed for the fast and slow shear waves following the method of Alford (1986). The resultant principal time series for the fast and slow shear waves were then used to re-create the original input data. If a close match was obtained with the original input data, the rotation was determined to be a success. From this the azimuth of the fast shear wave was noted. The fast and slow shear wave time series were then cross correlated to obtain the time delay between fast and slow waves. The final output was a measure of the azimuth of fast shear wave, the time difference between fast and slow shear waves and the magnitude of anisotropy in shear wave velocity.

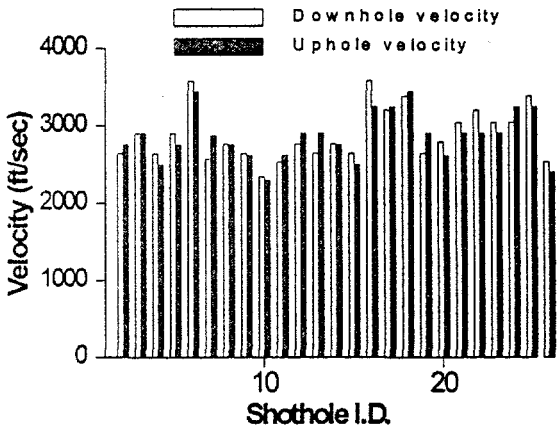

Figure 2. Compressional wave velocities calculated from surface sources and phones placed in the shotholes (Downhole), and from buried charges recorded by the uphole phones during the seismic survey (Uphole).

Results

The results for all 30 geophones are shown in a series of contour maps. In Figure 3, the VP/VS1 ratio is shown. Only at one place in the survey did the VP/VS1 ratio exceed 3 and therefore, following the work of Sipos and Marshall (1995) it may be inferred that this is the only location which truly belongs to a weathered layer case. Therefore, at this location the p-wave static solutions can not be used to construct shear wave static solutions in the absence of specific shear wave data. Thus, careful attention to static solutions, and the S1/S2 ratio, should be paid in this area. At all other locations the p-wave static solutions could be used with the VP/VS1 ratio to model shear wave static solutions and furthermore, the S1 static solution could be used to model the S2 solution.

Figure 4a illustrates the percent shear wave anisotropy and fast shear wave azimuth. The fast shear azimuth shows a consistent direction approximately East-West.

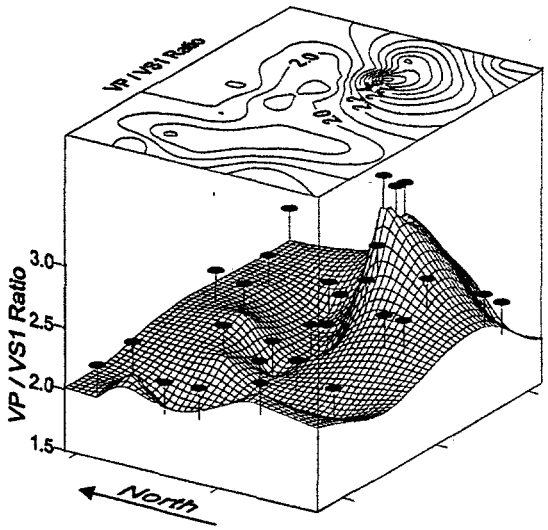

Figure 3. VP/VS1 ratio as measured by the buried geophone arrays. Black circles correspond to measurement locations.

This direction is plotted on a rose diagram in Figure 4b and is similar to that measured from air photography for faults, fractures and linear geomorphic trends. The fast direction is parallel to the long axis of an open fracture with the slow direction perpendicular to this or across the open fractures. Thus the fast and slow shear directions are interpreted to indicate a predominant weakness direction aligned approximately East-West in the surface rocks. The magnitude of shear wave anisotropy is a measure of the difference between fast and slow shear waves and is greatest in the northern half of the survey where values greater than 10% are observed. For most deeper seismic studies in the US, background shear wave velocity anisotropy is recorded at 4% or less and therefore the values of anisotropy recorded here are interpreted to be anomalously high. Crampin (1994) has indicated that values of shear wave velocity anisotropy over 8 to 10% represent a state of competency in the rock mass where fracturing is so severe that a breakdown in shear strength occurs and enhanced permeability results. Thus, vertical hydraulic conductivity is also greater at this location. This has implications for engineering, hydrogeologic and environmental assessment of the site.

It is also worth noting here that the location that contained the problem area for seismic static solutions is not the area that most concern should be paid for the environmental and engineering surveys. Nonetheless, the technique described here simultaneously addresses both problem areas. The variation in shear wave velocity anisotropy across the survey area is significant and indicates the potential for rapid variations in similar geologic settings.

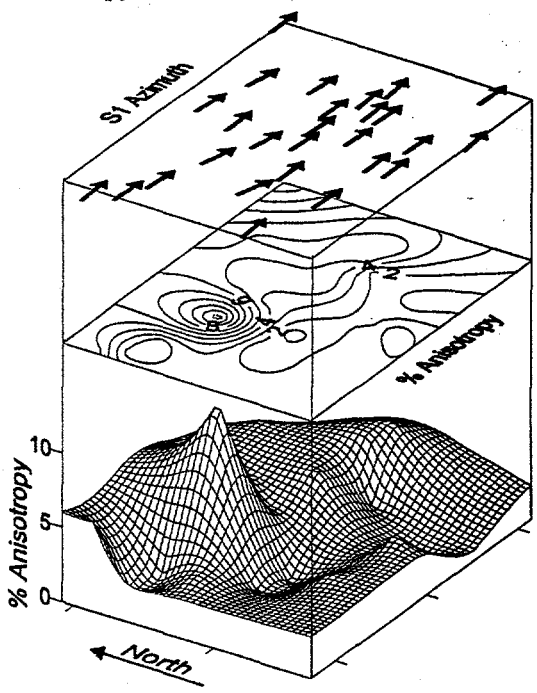

Figure 4a. Percent shear wave anisotropy and azimuth of the fast shear wave. Azimuth arrows correspond to measurement locations.

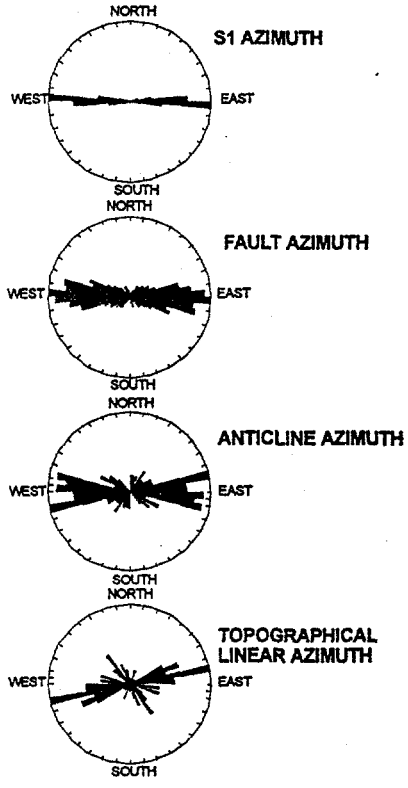

Figure 4b. Rose diagrams generated from fast shear wave azimuth, local fault azimuth, anticlinal azimuths and topographical azimuths.

On observing this variability the question remains whether closer sampling would have identified even greater variation in shear wave velocity anisotropy and if these near surface lateral variations are also seen at depth. These issues will be the focus of the next phase of investigation.

Acknowledgments

This research was carried out as part of a Department of Energy project, DE-AC21-94MC31224. We thank the industry partner for access to the field for this work.

References

Crampin, S., 1990. Alignment of Near Surface Inclusions and Appropriate Crack Geometries for Geothermal Hot-dry-rock Experiment. Geophysical Prospecting, v38, p.621-631.

Crampin, S., 1994. The Fracture Criticality of Crustal Rocks. Geophysical Journal International, v. 118, p.428-438.

Lynn, H.B., 1991. Field Measurements of Azimuthal Anisotropy: First 60m, San Francisco Bay Area, and Estimations of Horizontal Stress Ratios from V_{S1}/V_{S2}. Geophysics, v56, p.822-832.

MacBeth, C., 1995. How can Anisotropy be used for reservoir Characterization? First Break, v13, p.31.

Sipos, Z. & Marshall, R., 1995. Remarks on Static corrections for S-waves. Journal of Seismic Exploration, v.4, p.199.

Winterstein, D.F. & Meadows, M.A., 1991. Shear Wave Polarizations and Subsurface Stress Directions at Lost Hills Field. Geophysics, v56, p.1349-1364.